NASA TECHNICAL NOTE
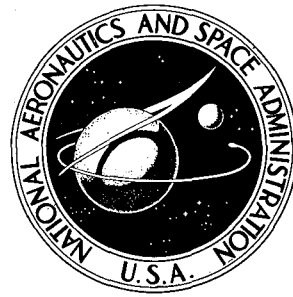
NASA TN D-4983

NASA TN D-4983

FULL-SCALE WIND-TUNNEL INVESTIGATION OF STATIC LONGITUDINAL AND LATERAL CHARACTERISTICS OF A LIGHT TWIN-ENGINE AIRPLANE

by Marvin P. Fink and Delma C. Freeman, Jr.

Langley Research Center
Langley Station, Hampton, Va.

FULL-SCALE WIND-TUNNEL INVESTIGATION OF

STATIC LONGITUDINAL AND LATERAL CHARACTERISTICS OF A

LIGHT TWIN-ENGINE AIRPLANE

By Marvin P. Fink and Delma C. Freeman, Jr.

Langley Research Center
Langley Station, Hampton, Va.

FULL-SCALE WIND-TUNNEL INVESTIGATION OF
STATIC LONGITUDINAL AND LATERAL CHARACTERISTICS OF A
LIGHT TWIN-ENGINE AIRPLANE

By Marvin P. Fink and Delma C. Freeman, Jr.
Langley Research Center

SUMMARY

An investigation has been conducted in the Langley full-scale tunnel to determine the static longitudinal and lateral stability and control characteristics of a full-scale light twin-engine airplane. Hinge moments were also measured for all control and flap surfaces during the investigation. The investigation was made over an angle-of-attack range of -4° to 18° at various angles of sideslip between $\pm 8^{\circ}$ for various power and flap settings. The thrust coefficients were 0, 0.20, and 0.44, which correspond to either a low-power or a high-speed condition, to a climb condition, and to a take-off or a wave-off condition, respectively, for an airplane having installed horsepower of 200 per engine.

The investigation showed that, in general, the airplane has stick-fixed longitudinal stability through the stall, but stick-fixed instability could be encountered at some lift coefficients with rearward center-of-gravity location, particularly at a thrust coefficient of 0.44 and flaps deflected 27°. The airplane has stick-free stability through the stall, however, for all power, flap, and center-of-gravity conditions investigated. At angles of attack below the stall, the airplane is directionally stable, has positive effective dihedral, and the variation of the lateral coefficients is fairly linear. At angles of attack above the stall, the airplane is directionally stable, and has positive effective dihedral for all conditions except at a thrust coefficient of 0; however, rolling and yawing moments greater than those produced by full opposite control occur at zero sideslip, particularly at a thrust coefficient of 0.20, because of asymmetrical wing stall. Aileron and rudder effectiveness is maintained through the stall.

INTRODUCTION

For the past several years the NASA Flight Research Center has been conducting a program to evaluate the flying qualities of a number of general-aviation aircraft. The results of these investigations have been reported in reference 1. As a part of the continuing investigation, one of the airplanes investigated in reference 1, a light twin-engine configuration, has been tested in the Langley full-scale tunnel. The investigation was

made to determine the static longitudinal and lateral stability and control characteristics with various power (up to 200 horsepower per engine) and flap settings over a range of angles of attack from -4° to 18° and over a range of sideslip angles of ±8°. All of the tests except those at a thrust coefficient of 0.44 were made at a tunnel speed of about 93 feet per second (28.35 meters per second) giving a Reynolds number of approximately 2.96×10^6 based on a mean aerodynamic chord of 5 feet (1.52 meters). Tests at 0.44 thrust coefficient were made at a tunnel speed of about 63 feet per second (19.2 meters per second).

SYMBOLS

Figure 1 shows the stability-axis system used in the presentation of the data and the positive direction of forces, moments, and angles. The data are computed about the moment center (see fig. 2) which is at airplane longitudinal station 85 or 10.0 percent of the mean aerodynamic chord. All areas used in determining hinge-moment coefficients are defined as the area back of the hinge line.

Measurements for this investigation were made in the U.S. Customary System of Units. Equivalent values are indicated herein in the International System (SI) in the interest of promoting the use of this system in NASA reports. Factors relating the two systems of units used in this paper may be found in the appendix.

b wing span, 35.98 feet (10.97 meters)

C_D drag coefficient, $\dfrac{\text{Drag}}{qS}$

$C_{h,a}$ aileron hinge-moment coefficient, $\dfrac{\text{Hinge moment}}{qS_a \bar{c}_a}$

$C_{h,f}$ flap hinge-moment coefficient, $\dfrac{\text{Hinge moment}}{qS_f \bar{c}_f}$

$C_{h,r}$ rudder hinge-moment coefficient, $\dfrac{\text{Hinge moment}}{qS_r \bar{c}_r}$

$C_{h,t}$ horizontal-tail hinge-moment coefficient, $\dfrac{\text{Hinge moment}}{qS_t \bar{c}_t}$

$C_{h,tab}$ horizontal-tail tab hinge-moment coefficient, $\dfrac{\text{Hinge moment}}{qS_{tab} \bar{c}_{tab}}$

$C_{h\delta,a}$ aileron hinge-moment parameter, $\dfrac{\partial C_h}{\partial \delta,a}$, per degree

C_L lift coefficient, $\dfrac{\text{Lift}}{qS}$

C_{L_α} lift-curve slope

C_l rolling-moment coefficient, $\dfrac{\text{Rolling moment}}{qSb}$

C_{l_β} lateral stability parameter; effective dihedral parameter, $\dfrac{\partial C_l}{\partial \beta}$, per degree

$C_{l_{\delta,a}}$ aileron effectiveness parameter $\dfrac{\partial C_l}{\partial \delta,a}$, per degree

C_m pitching-moment coefficient, $\dfrac{\text{Pitching moment}}{qS\bar{c}}$

$C_{m_{\delta,t}}$ horizontal-tail effectiveness parameter, $\dfrac{\partial C_m}{\partial \delta,t}$, per degree

C_n yawing-moment coefficient, $\dfrac{\text{Yawing moment}}{qSb}$

C_{n_β} directional stability parameter, $\dfrac{\partial C_n}{\partial \beta}$, per degree

$C_{n_{\delta,r}}$ rudder effectiveness parameter, $\dfrac{\partial C_n}{\partial \delta,r}$, per degree

C_Y side-force coefficient, $\dfrac{\text{Side force}}{qS}$

$\bar{c}$ mean aerodynamic chord, 5 feet (1.53 meters)

$\bar{c}_a$ aileron mean chord, 1.0 foot (0.30 meter)

$\bar{c}_f$ flap mean chord, 1.16 feet (0.35 meter)

$\bar{c}_r$ rudder mean chord, 1.2 feet (0.37 meter)

$\bar{c}_t$ tail mean chord, 2.7 feet (0.82 meter)

$\bar{c}_{tab}$ tab mean chord, 0.5 foot (0.15 meter)

D propeller diameter, 6.0 feet (1.83 meters)

N_β yawing-moment parameter, foot-pounds per degree (newton-meters per degree)

n	rotational speed, revolutions per second
q	free-stream dynamic pressure, pounds force/foot^2 (newtons/meter^2)
S	wing area, 178 feet^2 (16.50 meters^2)
S_a	area of one aileron, 5.8 feet^2 (0.548 meter^2)
S_f	area of one flap, 7.65 feet^2 (0.71 meter^2)
S_r	area of rudder, 5.2 feet^2 (0.482 meter^2)
S_t	area of horizontal tail, 19.5 feet^2 (1.81 meters^2)
S_{tab}	area of tail tab, 5.0 feet^2 (0.464 meter^2)
T	effective thrust, $\text{Drag}_{\text{propellers removed}} - \text{Drag}_{\text{propellers operating}}$
T'_c	thrust coefficient, $\dfrac{T}{qS}$
V	free-stream velocity, feet/second (meters/second)
X	longitudinal axis
α	angle of attack of fuselage reference line, degrees
β	angle of sideslip, positive when nose is to left, degrees
δ_a	total aileron deflection, positive when right aileron is down, $\delta_{aL} - \delta_{aR}$, degrees
δ_f	flap deflection, positive when trailing edge is down, degrees
δ_r	rudder deflection, positive when trailing edge is left, degrees
δ_t	horizontal-tail deflection, positive when trailing edge is down, degrees
δ_{tab}	horizontal-tail tab deflection, degrees
ϵ	average downwash angle, degrees

4

Subscripts:

L   left

max   maximum

R   right

The gearing constants at zero control deflection for the three controls are as follows:

Aileron . . . . 0.80 radian/foot (0.24 radian/meter)

Elevator . . . . 0.42 radian/foot (0.13 radian/meter)

Rudder . . . . 0.93 radian/foot (0.25 radian/meter)

AIRPLANE

The airplane tested was a light twin-engine low-wing monoplane. Figure 2 gives the principal dimensions and figure 3 shows the airplane mounted in the tunnel test section. The airplane had a wing span of 35.98 feet (10.97 m), a wing area of 178 feet^2 (16.50 m^2), an aspect ratio of 7.3, and a mean aerodynamic chord of 5 feet (1.53 m) based on projection of the outboard leading edge of the wing through the fuselage. The wing airfoil section was a modified NACA 64$_2$A215 airfoil with the trailing-edge cusp faired out. The wing leading edge was modified as shown in figure 2(b) for some tests. The wing had 5° of dihedral and no twist and was at 2^O positive incidence with respect to the fuselage reference line. The thrust axes were parallel to the reference line. The airplane had the standard three-control system. The horizontal tail was of the all-movable type with a control deflection range of 4° to -14°. The tail had a trailing-edge tab which moved in the same direction as the tail with a deflection ratio (tab deflection to tail deflection) of 1.5. The control deflection range on each aileron was from 14° to -18°. The rudder control deflection range was limited to ±20° because of restrictions imposed by remotely controlled actuators that were installed for these tests. The airplane normally would have ±27° of rudder deflection.

TESTS

The tests were made to determine the static longitudinal and lateral stability and control characteristics of the airplane over a wide range of flight conditions. Hinge moments were also measured for all control and flap surfaces during the investigation. The airplane was tested over an angle-of-attack range of -4° to 18°, over a sideslip range of ±8° for the clean condition (δ_f = 0°; gear up), and for flap deflections of 15° and 27°

with the gear down. A range of tail incidence angles from 4° to -14° was investigated at zero sideslip, and the aileron and rudder effectiveness was measured over the sideslip range. Although the airplane has engines with 160-rated horsepower, power conditions of up to 200 horsepower were simulated with thrust coefficients of 0, 0.20, and 0.44 representing flight conditions of low power or high speed, a climb at about 90-percent power, and a climb at full power as in take-off or wave-off conditions, respectively. The climb and take-off thrust coefficients with the 160-horsepower engines are 0.14 and 0.35, respectively. Several tests were made with asymmetric power to simulate an engine-out condition for either engine with the inoperative engine in a windmilling condition and a feathered-propeller condition. The running engine had full power ($T_c' = 0.44$) for the asymmetric power test. The propeller blade angle and consequently the advance ratio for each thrust coefficient were set at fixed values which were representative of those for flight conditions at which the particular value of thrust coefficient could be achieved. The values of V/nD were 0.78, 0.64, and 0.44 for values of T_c' of 0, 0.20, and 0.44, respectively.

PRESENTATION OF DATA

The data from these tests have been corrected for airstream misalinement, buoyancy effects, and mounting strut tares. Wind-tunnel jet-boundary corrections derived according to references 2 and 3 have been applied.

The data are presented in the following figures:

<div align="right">7</div>

RESULTS AND DISCUSSION

The basic data obtained during the wind-tunnel investigation are presented in figures 4 to 66 without analysis. Summary plots have been prepared from some of these data to illustrate the general static stability and control characteristics of the airplane. Only the summary plots are discussed.

Longitudinal Characteristics

Symmetric power.- The longitudinal characteristics of the airplane with symmetric power are presented in figure 67 for flap deflections of 0°, 15°, and 27°. As might be expected, increasing power results in a large increase in lift-curve slope and maximum lift coefficient because of the increased slipstream velocity over the wing. This effect of power on the lift characteristics is summarized in figure 68 where lift-curve slope and maximum lift coefficient are shown as functions of thrust coefficient.

The pitching-moment curves shown in figure 67 remain virtually linear through the stall ($\alpha = 15^O$; power on) and do not exhibit the nose-down pitching moment usually associated with a straight-wing airplane. The variation of the pitching-moment curves with angle of attack indicates that an increase in the thrust coefficient to 0.20 apparently has little effect on the longitudinal characteristics. An increase in the power to $T'_c = 0.44$, however, reduces the slope of the pitching-moment curve, particularly at low angles of attack. These power effects are further illustrated by the variation of static margin dC_m/dC_L with thrust coefficient in figure 69. These data are a measure of the stick-fixed stability and show that power is destabilizing, particularly for the condition where the flap deflection is 27°. It is possible for the airplane to become longitudinally unstable in this condition for some thrust and lift coefficients if the center of gravity is at or near the aft limit.

The stick-free static stability characteristics, determined from the pitching- and hinge-moment curves, are shown in figure 70. These data show that the airplane has stick-free stability in the normal operating angle-of-attack range for all flap and power conditions tested. The effect of thrust coefficient on the stick-free stability at a lift coefficient of 1.0 is shown in figure 70(c). These data show that power has a destabilizing effect, as it did for the stick-fixed case (fig. 69), but the airplane has stick-free stability even at the most rearward center-of-gravity location.

The variation of the horizontal-tail effectiveness with angle of attack is presented in figure 71 for flap deflections of 0°, 15°, and 27°. These data show that the tail effectiveness is reduced in the higher angle-of-attack range, but effectiveness is still maintained through the stall. The tail effectiveness is presented as a function of thrust coefficient in figure 72 for each flap deflection tested. These data show that power generally increased the tail effectiveness.

8

Presented in figure 73 is the variation of the average downwash angle at the tail with angle of attack for $T'_c = 0$ and 0.44 and flap deflections of 0°, 15°, and 27° calculated from tail-effectiveness data. These data show that the rate of change of downwash with angle of attack is highest for the flap deflection of 0° and is higher with power on $(T'_c = 0.44)$ than it is with power off $(T'_c = 0)$.

Asymmetric power.- The longitudinal characteristics of the airplane with symmetric and asymmetric power are shown in figure 74. These data show that the lift-curve slope and the maximum lift coefficient are reduced with one engine out because of the reduction in slipstream velocity over the engine-out wing. The pitching-moment variation with angle of attack is not greatly affected by the loss of an engine.

Lateral Characteristics

Symmetric power.- The variation of the effective-dihedral parameter C_{l_β} with angle of attack is shown in figure 75 for the various flap and power conditions tested. These data show that below the stall the airplane has positive effective dihedral $-C_{l_\beta}$ for all conditions. Above the stall the airplane has positive effective dihedral for all conditions except $T'_c = 0$ where the dihedral effect becomes negative beyond the stall. While the effective dihedral is positive below the stall, the value of $-C_{l_\beta}$ varies considerably with change in power or flap setting. Therefore, the response of the airplane to gusts or to rudder inputs to raise a wing could vary with the airplane configuration.

The variation of the directional stability parameter C_{n_β} with angle of attack is shown in figure 76 for the various flap and power conditions tested. These data show that the airplane is directionally stable in all conditions over the entire angle-of-attack range tested, including angles above the stall. As was the case for the effective dihedral, the value of C_{n_β} varies considerably for the different conditions. The directional stability parameter C_{n_β} increased at the stall for most conditions, and this point is illustrated further in figure 77 where the yawing moment in foot-pounds per degree of sideslip is presented against angle of attack. These data show that an increase actually occurs in the restoring moment at the higher angles of attack, and thus indicates an increase in dynamic pressure over the aft end of the airplane.

The variation of the aileron and rudder effectiveness with angle of attack is presented in figure 78 for the three power conditions tested and for flap deflections of 0° and 27°. These data show that, in general, the aileron effectiveness remains at a relatively constant level up to about the stall for most of the conditions tested. Although the effectiveness decreases at angles of attack near and above the stall, effectiveness is still maintained to the highest angles of attack tested. The rudder effectiveness is essentially constant through the stall and is relatively unaffected by changes in power or configuration.

The basic lateral characteristics of the airplane, as shown by the variation of the lateral coefficients C_l and C_n with angle of attack for 0° sideslip, are presented in figure 79 for the various power and flap conditions tested. The data show that below the stall the variation of the coefficients is generally fairly linear. At the stall, large rolling and yawing moments occur, particularly at $T_c' = 0.20$. The reason for these large moments was determined from tuft studies which showed that a large part of the left wing, outboard of the nacelle, stalled at an angle of attack about 2^O lower than the right wing, and thus created an asymmetrical stall and the resulting moments. The stall appeared to start fairly far back on the wing and was believed to be associated with the right-hand, or clockwise from the cockpit, direction of propeller rotation. (Left-hand rotation on both propellers would probably create a rolling asymmetry to the right.)

The data of figure 79 also show that the rolling and yawing moments are reduced as the angle of attack is increased beyond the stall. This reduction in the moments occurs in the wind-tunnel tests because the airplane is rigidly mounted on the strut system, and the further increase in angle of attack results in the right wing stalling, and thereby reduces the asymmetric moments. Under flight conditions, where the airplane is unrestrained, the asymmetric rolling and yawing moments might build up to even higher values as the left wing drops and the airplane rolls off.

The relatively small radius of the leading edge of the wing might be a factor in the magnitude of the stall asymmetry. Therefore, a few tests were made with the wing modification shown in figure 2(b). The variations of the lateral coefficients C_l, C_n, and C_Y with angle of attack obtained in these tests are compared with those of the basic wing in figure 80. These data show that the modified leading edge did reduce the magnitude of the asymmetric rolling and yawing moments at the stall somewhat, particularly with the flaps up, but did not eliminate the asymmetry. The reason for the decrease in moments is seen in the lift curves presented in figure 12 where, with flaps up, the lift curve of the modified wing breaks at a lower angle of attack and has a less abrupt stall than does the basic wing. With flaps down the stall is more like that of the basic wing and is reflected in the rolling and yawing moments in that they are not as greatly reduced by the wing modifications as were those for the flaps-up condition.

An attempt has been made to determine whether the controls are powerful enough to overcome the asymmetric moments at the stall, and the results of the analysis are presented in figure 81. In this figure are plotted the variations of the rolling and yawing moments with angle of attack at 0° sideslip for $T_c' = 0.20$ and a flap deflection of 27°. Added to these curves are the moments available from full opposite aileron and rudder deflection (including the adverse yaw of the ailerons and the roll due to rudder deflection). These data show that, based on the static wind-tunnel results, the rolling and yawing moments generated by the asymmetrical stall are larger than the corrective moments

10

produced by ailerons and rudder at 0° sideslip. If the airplane is allowed to sideslip, the yawing moment is reduced, but the rolling moment is increased.

A similar exercise was done for the airplane with the modified wing, and these results are presented in figure 82. The control characteristics were not measured with the modified wing; therefore, the corrective control moments measured for the basic airplane were used. Figure 82 shows that the asymmetric rolling moments could be overcome at all angles of attack and the asymmetric yawing moments could be overcome up to angles of attack slightly above the stall.

The results of these brief exploratory tests show that the large asymmetric moments might be reduced by a change in wing section. Perhaps these moments could also be reduced by the use of a properly sized and positioned stall strip.

The wind-tunnel investigation has apparently revealed the reason for the flight behavior of this airplane at the stall with power on. A number of pilots thought that as the airplane approached a power-on stall, the directional stability decreased, and/or the rudder power decreased, or rudder deflection was insufficient. The wind-tunnel investigation has shown that the directional stability actually increases at the stall (fig. 76) and that the rudder effectiveness is maintained through the stall (fig. 78). The behavior of the airplane at the stall seems to be the result of the rolling and yawing moments produced by the asymmetric stall. These moments are greater than the corrective moments produced by the controls.

Asymmetric power.- The variations of the effective dihedral parameter C_{l_β} and the directional stability parameter C_{n_β} with angle of attack for asymmetric power conditions are presented in figure 83. The values of C_{l_β} and C_{n_β} for the symmetric power condition are also given for comparison purposes. In general, there is little difference in the derivatives between the right- or left-engine operating conditions. The main effect of an asymmetric power condition occurs for C_{l_β} with flaps up where the dihedral effect becomes highly negative below the stall. Also, with flaps down, single-engine operation results in a large increase in $-C_{l_\beta}$ in the lower angle-of-attack range.

Aileron effectiveness was not measured in the asymmetric power condition because it was assumed that since the ailerons were well outside the slipstream, their effectiveness would not be appreciably affected by power changes. Rudder effectiveness was determined, however, and these data are presented in figure 84. Again, data obtained for the symmetric power condition are presented for comparison. These data show that the rudder was effective over the angle-of-attack range tested and that the level of effectiveness was relatively unaffected by which engine was operating or by flap deflection. Also, the rudder effectiveness was generally about the same as that measured for the symmetric power condition.

11

CONCLUSIONS

A full-scale wind-tunnel investigation has been made to determine the static longitudinal and lateral stability and control characteristics and control hinge moments of a light twin-engine airplane. The following conclusions were drawn from the results of the investigation:

1. The airplane has stick-fixed longitudinal stability through the stall for all configurations tested with the center of gravity located at airplane station 85. Power is destabilizing, particularly at a thrust coefficient of 0.44 (take-off thrust coefficient for 200-horsepower engines) and flaps deflected 27°, and the airplane could become longitudinally unstable in this condition at some lift coefficients if the center of gravity is at or near the aft limit.

2. The airplane has stick-free longitudinal stability in the normal operating angle-of-attack range for all flap and power conditions tested. Power is destabilizing, but the airplane has stick-free longitudinal stability even with the center of gravity at the aft limit.

3. Below the stall, the airplane is directionally stable, has positive effective dihedral, and the variation of the lateral coefficients is fairly linear.

4. Aileron and rudder control effectiveness is maintained through the stall.

5. Above the stall, the airplane is directionally stable, and has positive effective dihedral for all conditions except at a thrust coefficient of 0.

6. Above the stall, rolling and yawing moments larger than those produced by full opposite control occur at zero sideslip, particularly at a thrust coefficient of 0.20, because of asymmetrical wing stall.

Langley Research Center,
 National Aeronautics and Space Administration,
  Langley Station, Hampton, Va., September 25, 1968,
   736-01-00-01-23.

12

APPENDIX

CONVERSION FACTORS – U.S. UNITS TO SI UNITS

The following conversion factors from reference 4 are included in this paper for convenience:

Physical quantity	U.S. Customary Unit	Conversion factor (*)	SI Unit
Area	ft^2	0.0929	meters^2 (m2)
Density	slugs/ft^3	5153.8	kilograms/meter^3 (kg/m3)
Force	lbf	4.448	newtons (N)
Length	in.	0.0254	meters (m)
	ft	0.3048	meters (m)
Moment	lbf-ft	1.356	newton-meters (N-m)
Pressure	lbf/ft^2	47.88	newtons/meter^2 (N/m2)
Velocity	ft/sec	0.3048	meters/second (m/sec)

*Multiply value given in U.S. Customary Unit by conversion factor to obtain equivalent value in SI Unit.

13

REFERENCES

1. Barber, Marvin R.; Jones, Charles K.; Sisk, Thomas R.; and Haise, Fred W.: An Evaluation of the Handling Qualities of Seven General-Aviation Aircraft. NASA TN D-3726, 1966.

2. Heyson, Harry H.: Linearized Theory of Wind-Tunnel Jet-Boundary Corrections and Ground Effect for VTOL-STOL Aircraft. NASA TR R-124, 1962.

3. Heyson, Harry H.: Equations for the Applications of Wind-Tunnel Wall Corrections to Pitching Moments Caused by the Tail of an Aircraft Model. NASA TN D-3738, 1966.

4. Mechtly, E. A.: The International System of Units — Physical Constants and Conversion Factors. NASA SP-7012, 1964.
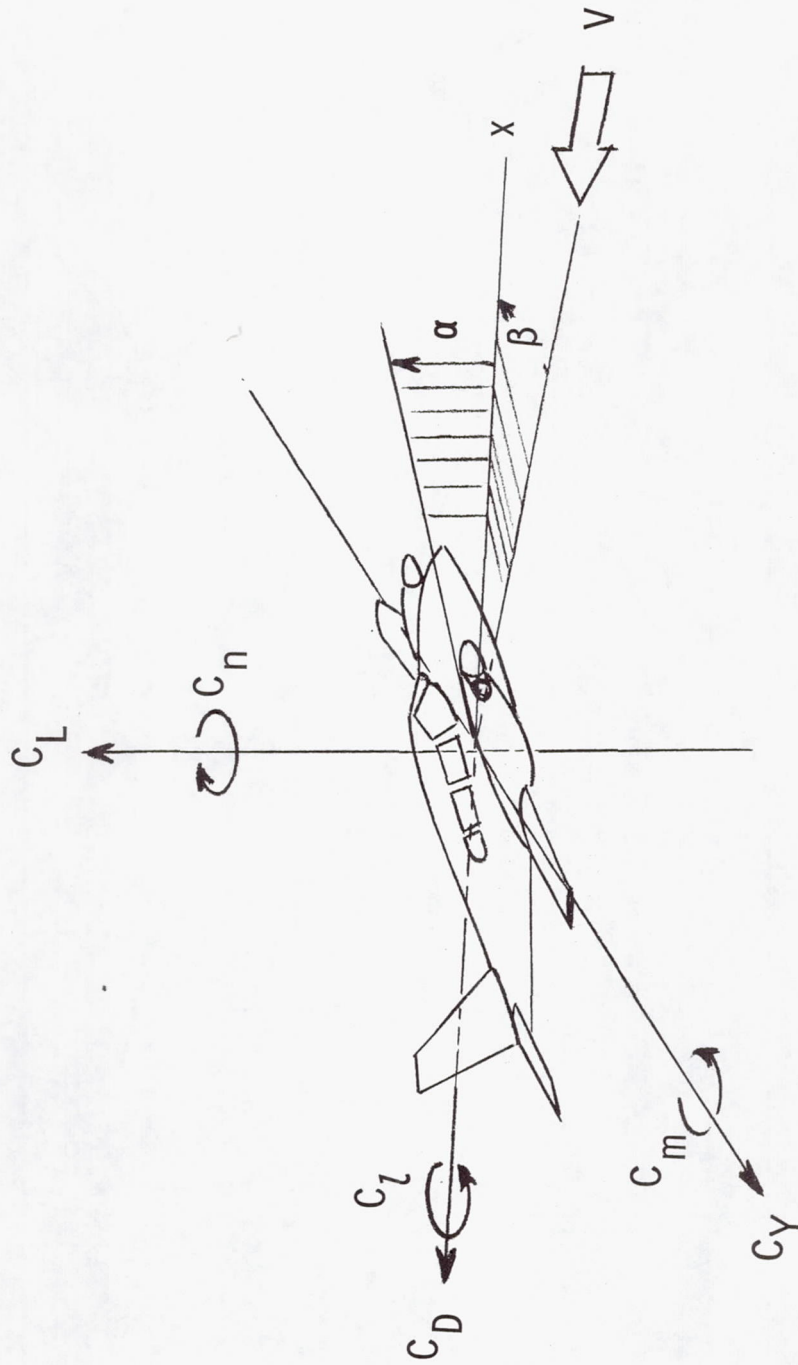
Figure 1.- System of axes and positive sense of angles, forces, and moments.

15
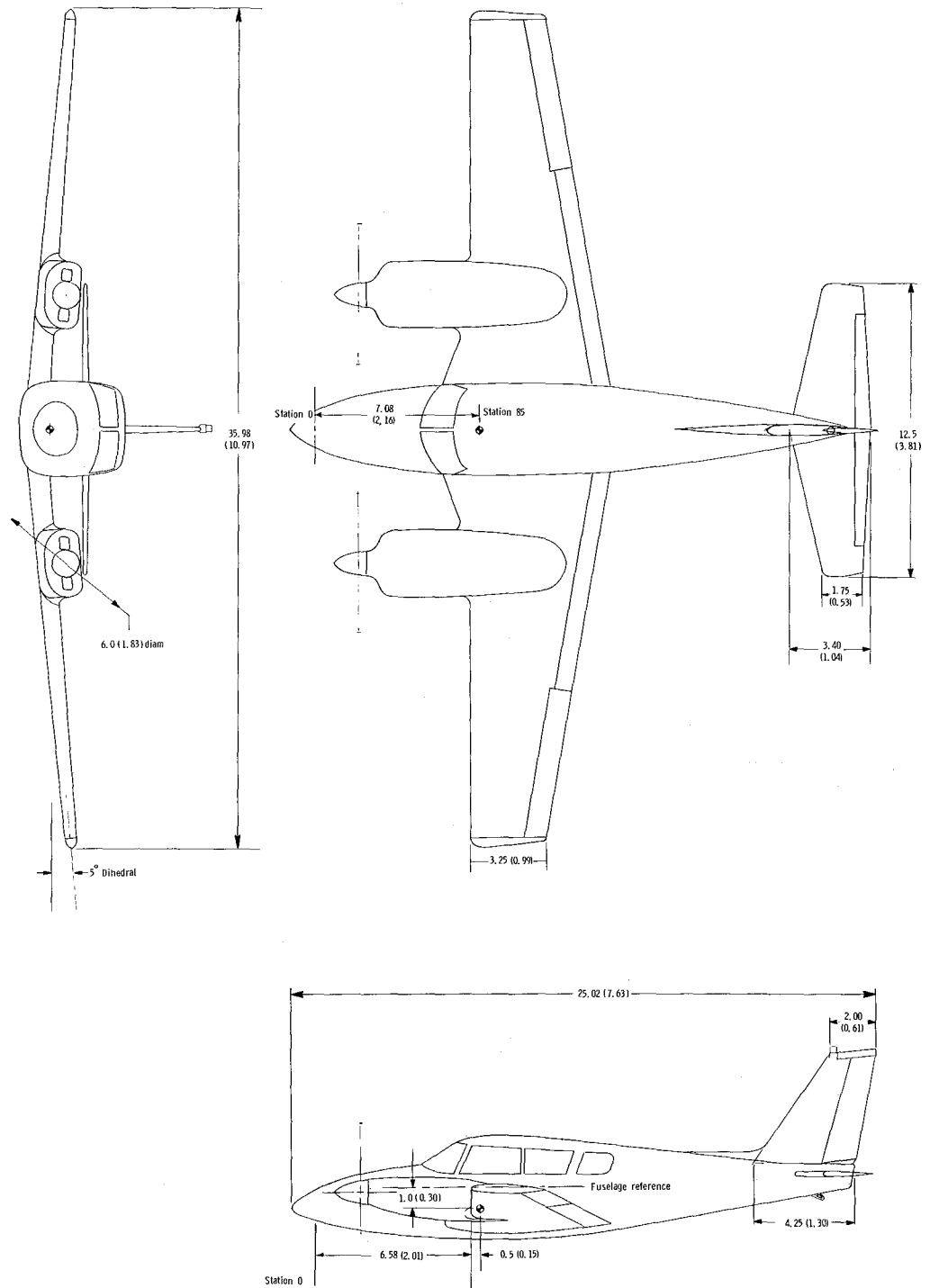
(a) Three-view drawing of airplane. All dimensions are in feet (meters).

Figure 2.- Three-view drawing of airplane and cross section of leading-edge radius increase.
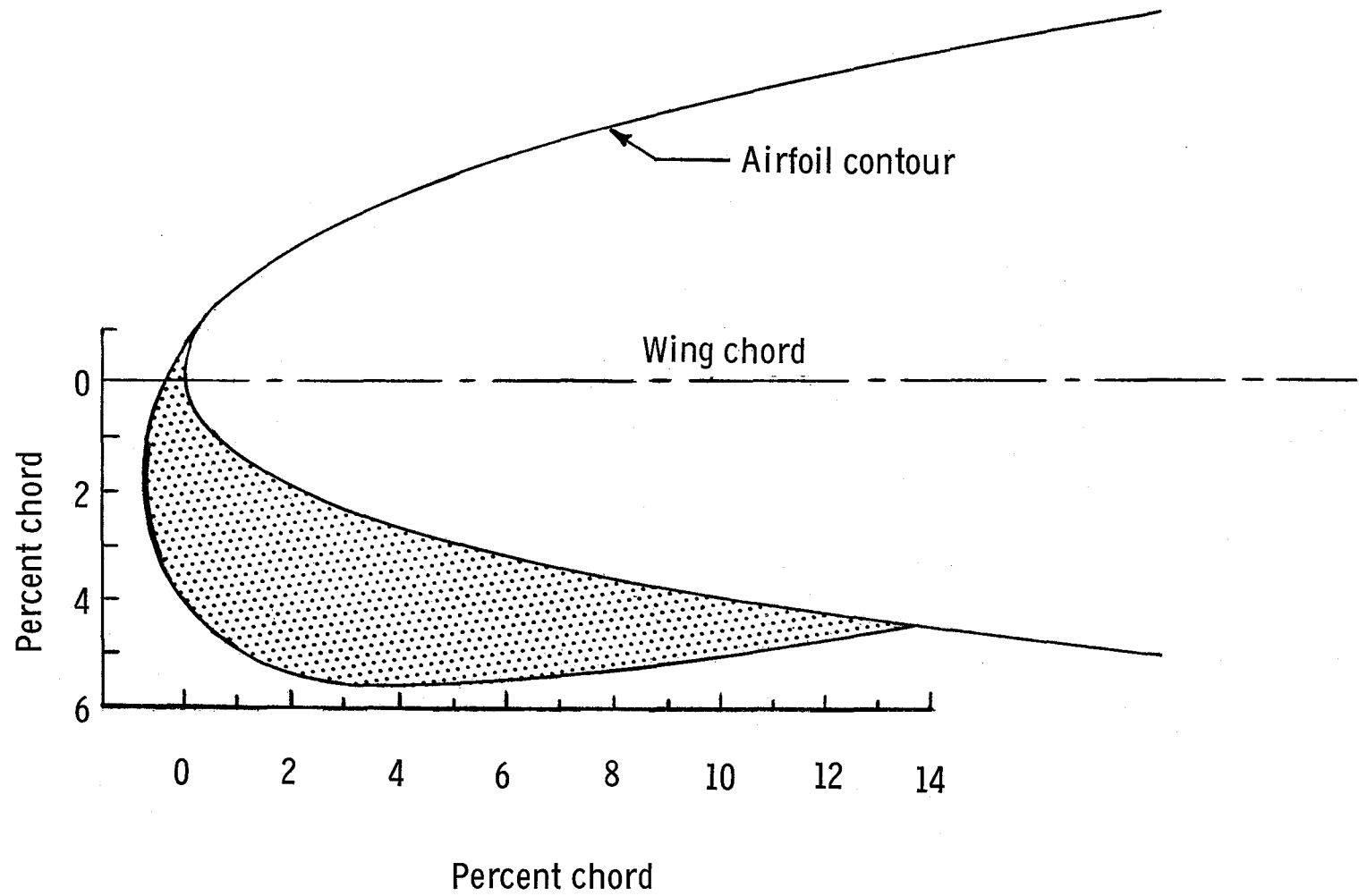
(b) Cross section of leading-edge radius modification.

Figure 2.- Concluded.

Figure 3.- Photograph of airplane mounted in Langley full-scale tunnel.

L-68-8599
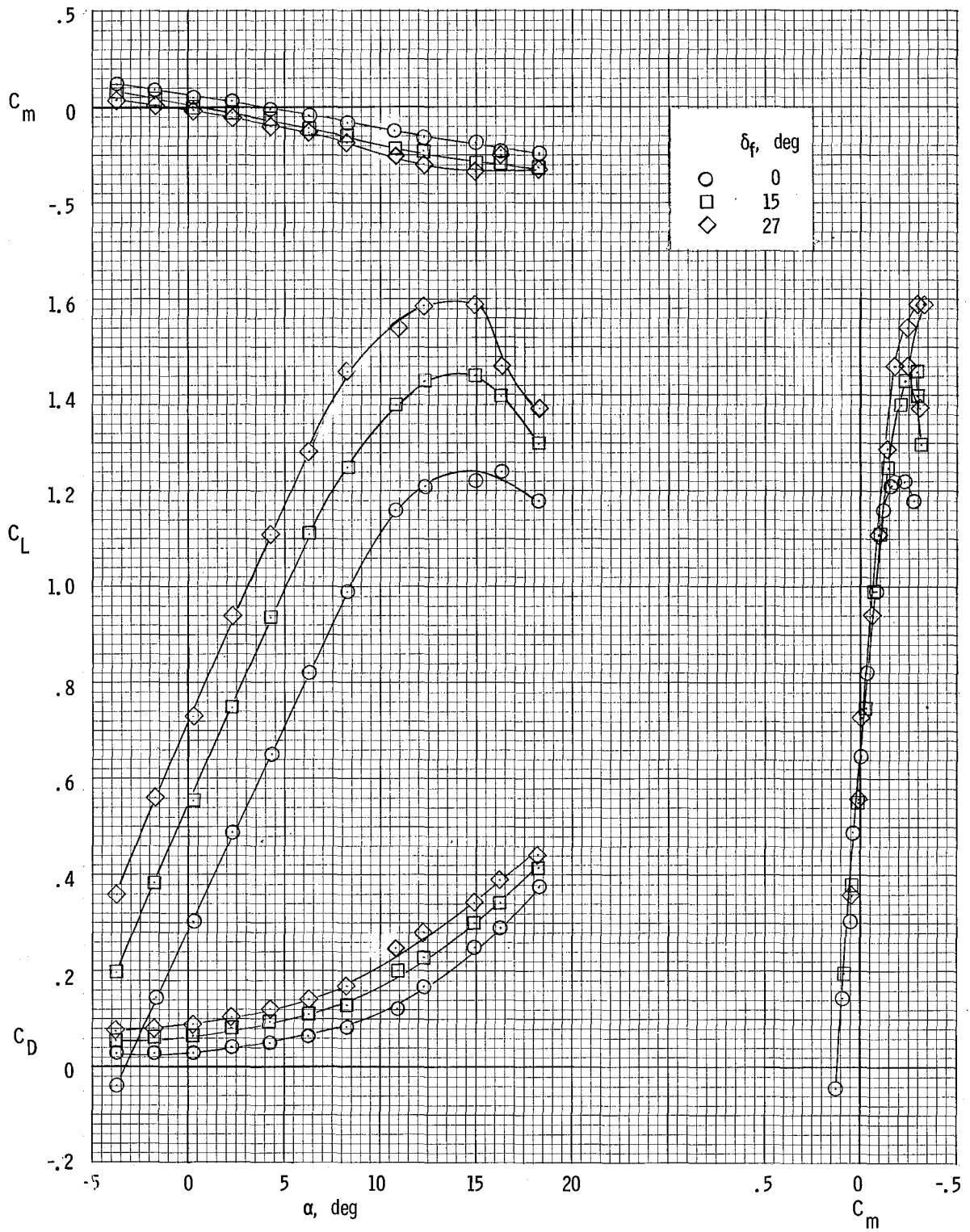
Figure 4.- Longitudinal aerodynamic characteristics of airplane with propellers removed for several flap deflections.

(a) $\delta_f = 0^o$.
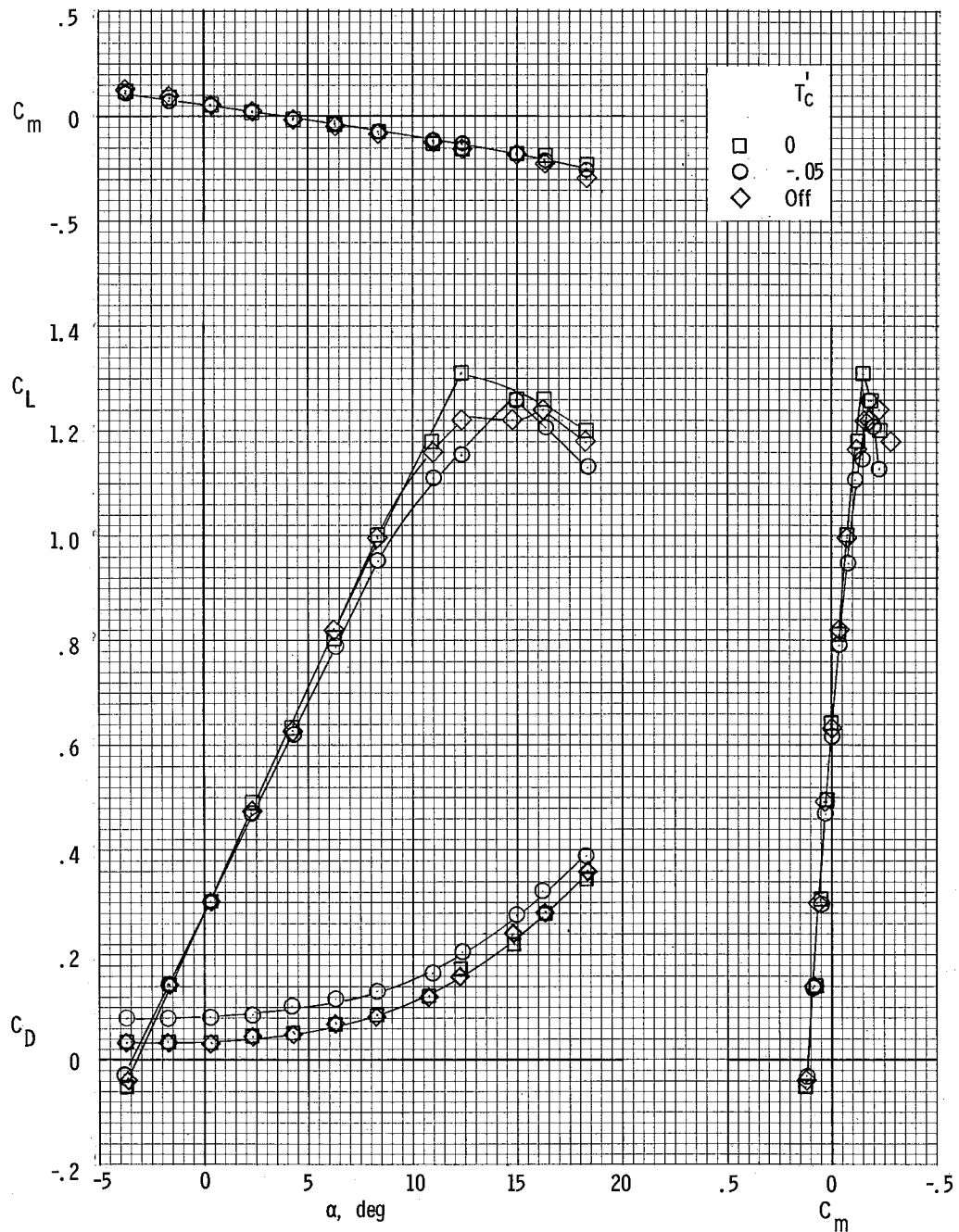
Figure 5.- Comparison of longitudinal aerodynamic characteristics of airplane with windmilling propellers $(T_c' = -0.05)$, zero thrust, and propellers removed.

(b) $\delta_f = 27^o$.
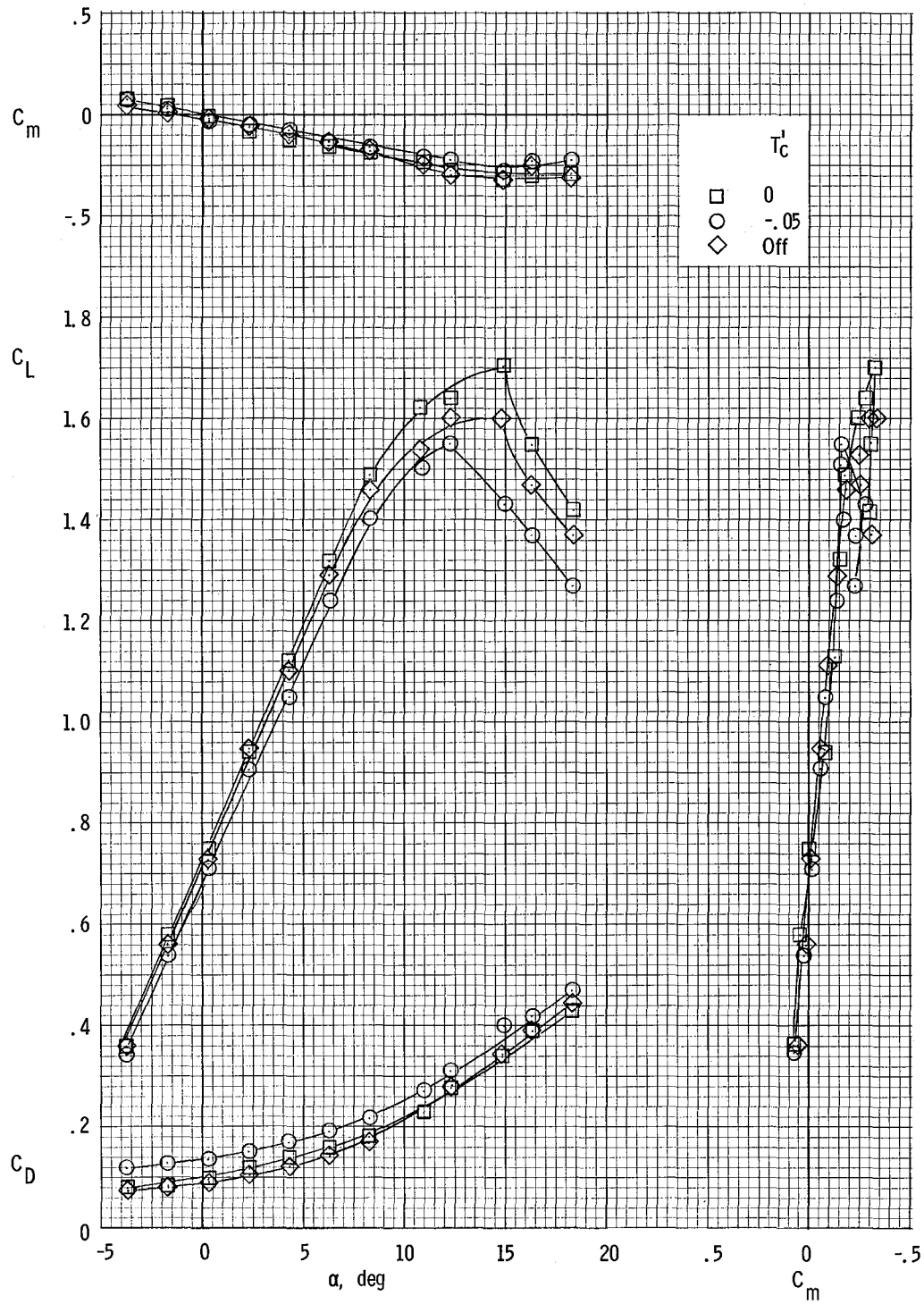
Figure 5.- Concluded.
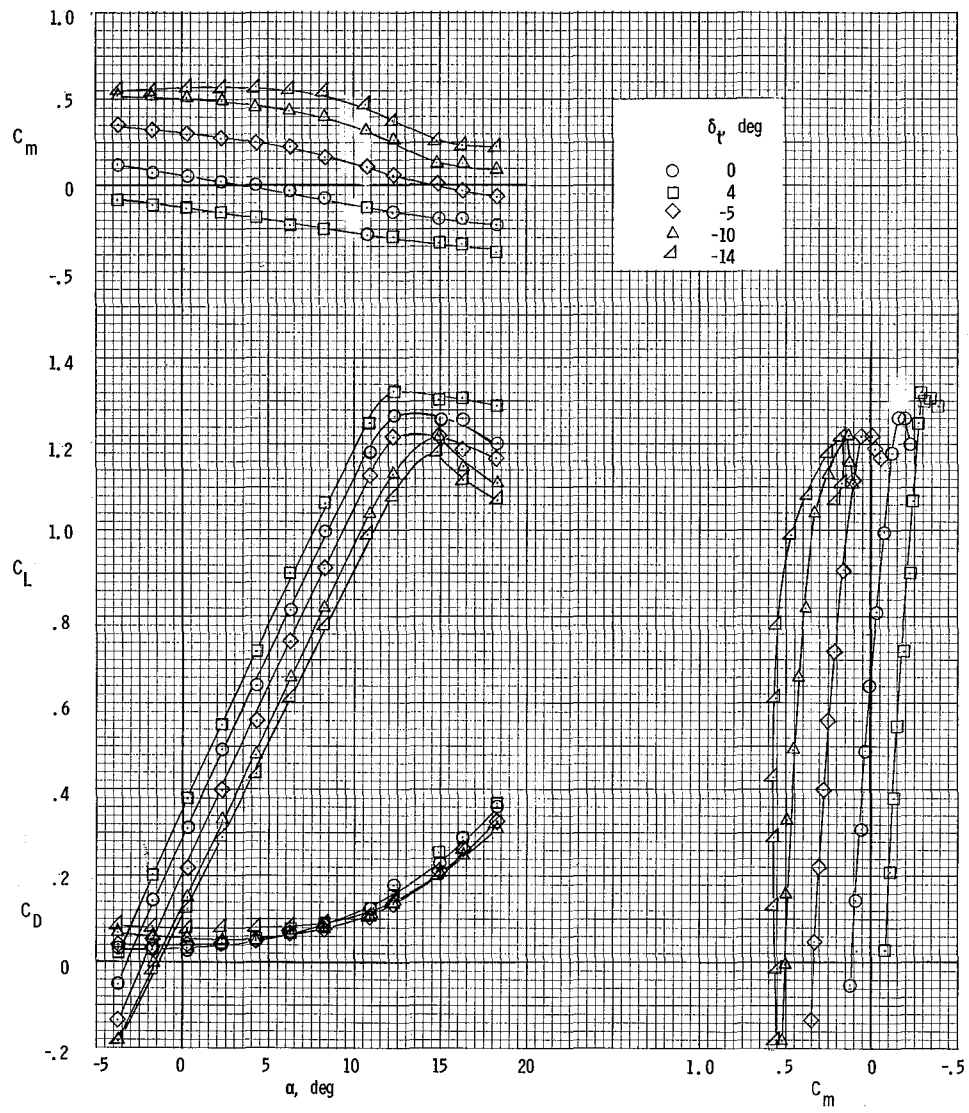
(a) $T'_c = 0$.

Figure 6.- Longitudinal aerodynamic characteristics of airplane for several thrust coefficients for $\delta_f = 0^0$.
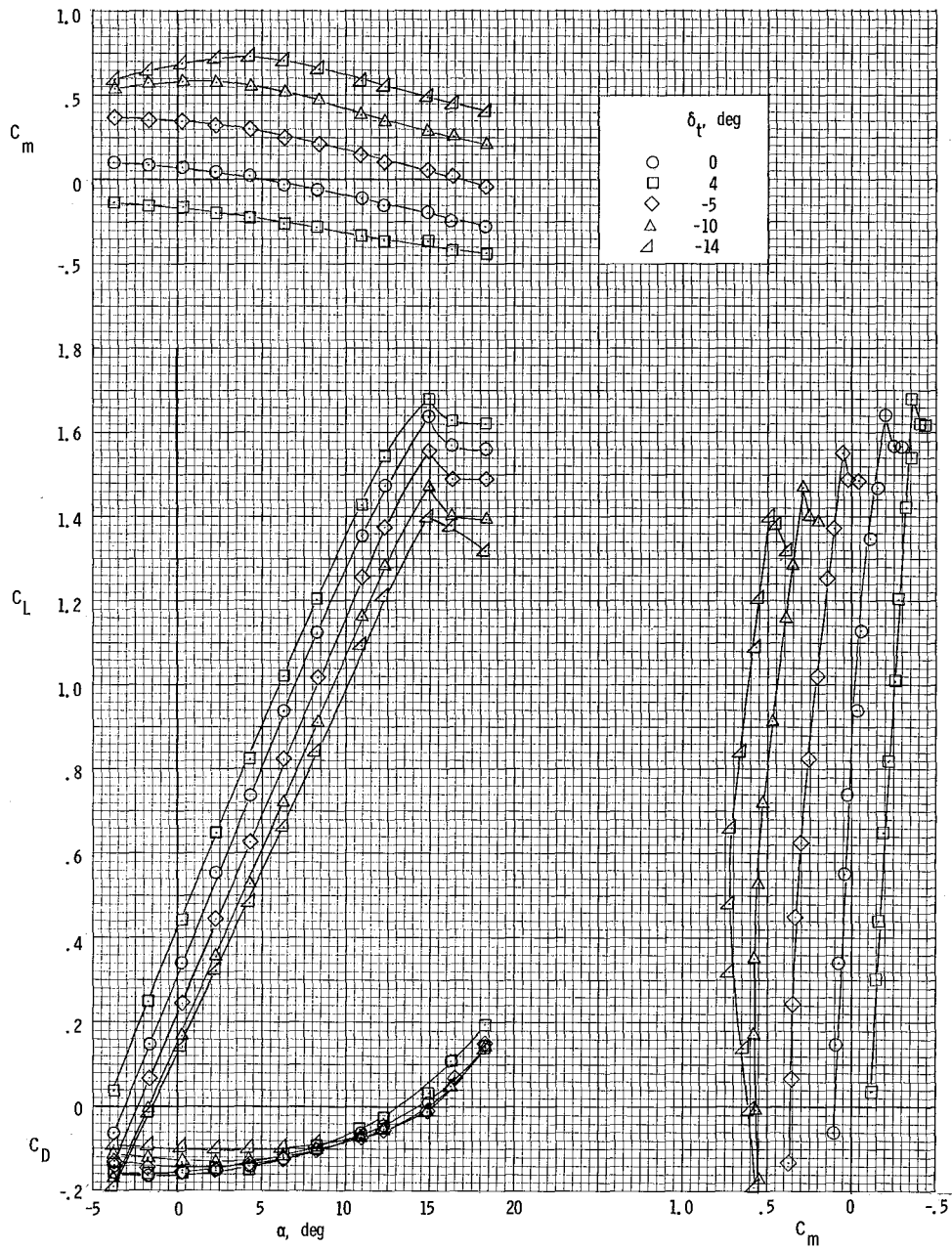
(b) $T_c^t = 0.20$.

Figure 6.- Continued.
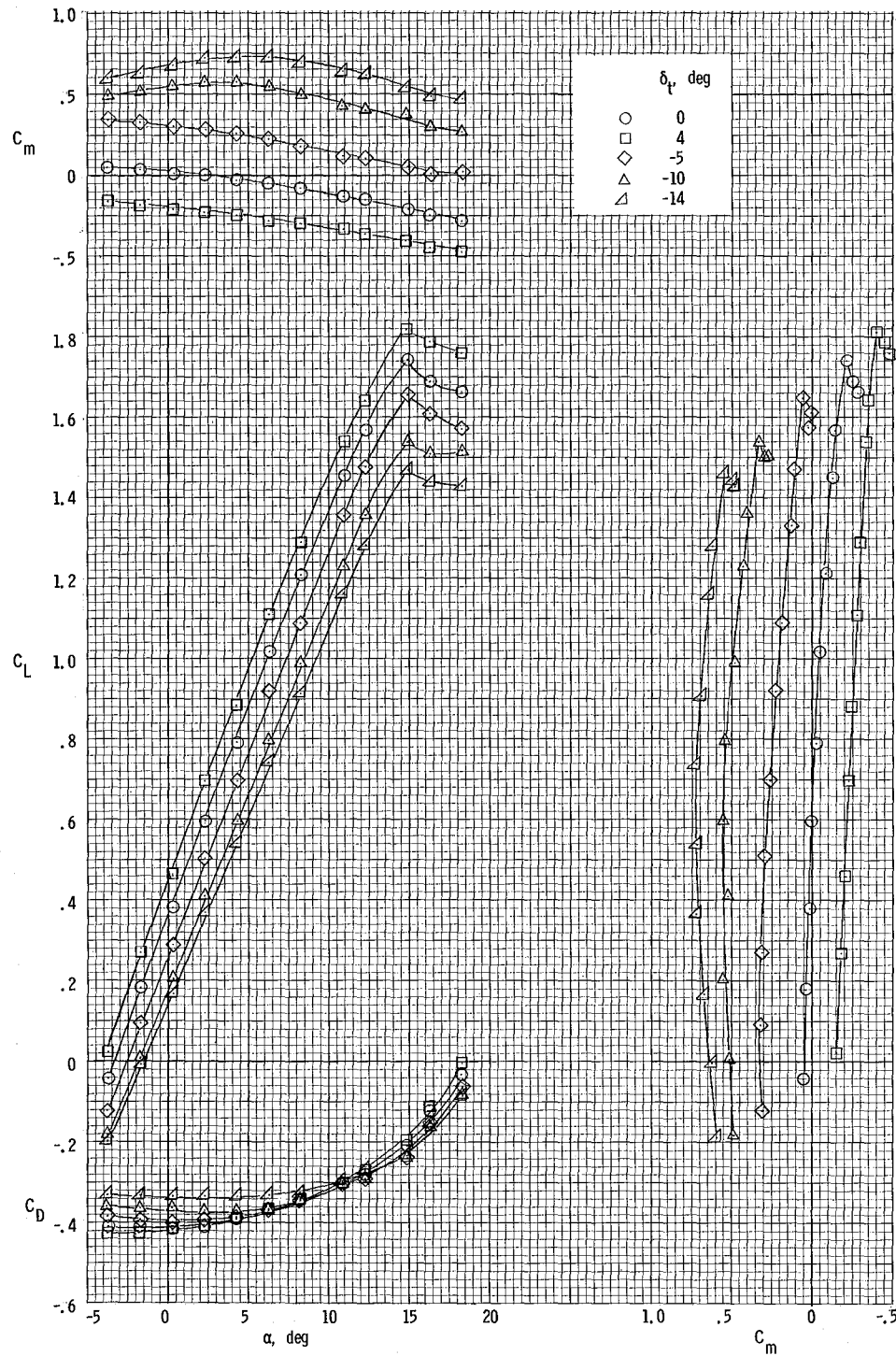
(c) $T_c' = 0.44$.

Figure 6.- Concluded.
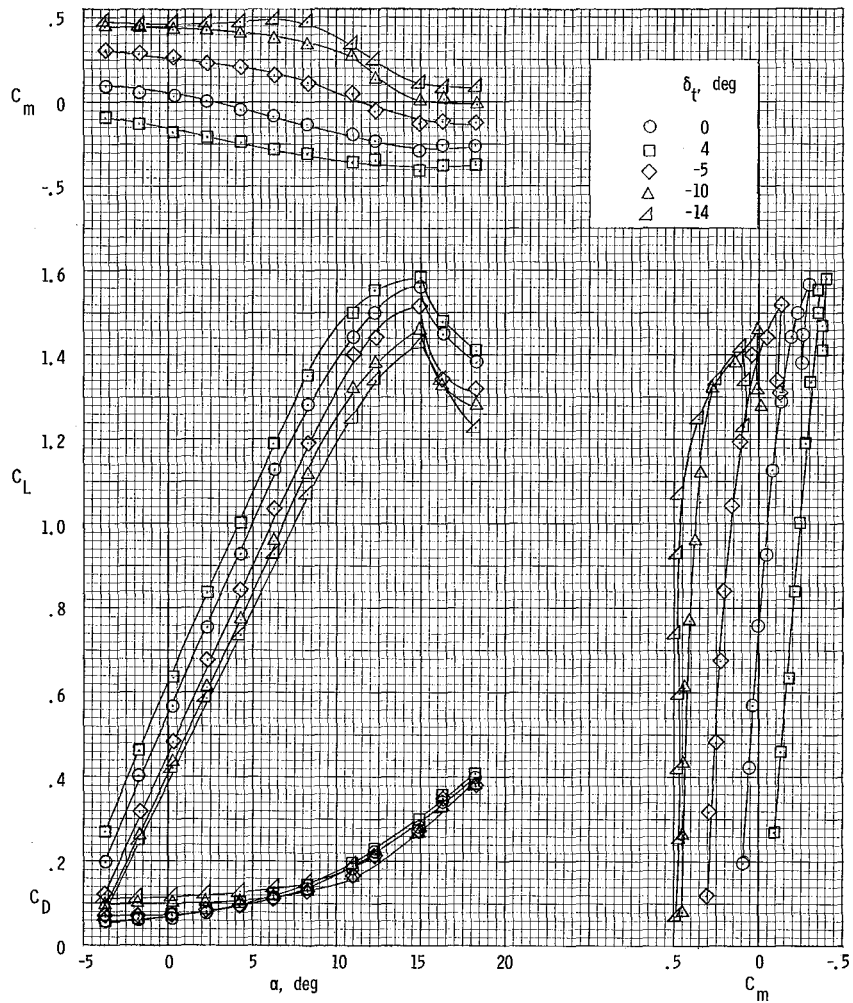
(a) $T_c' = 0$.

Figure 7.- Longitudinal aerodynamic characteristics of airplane for several thrust coefficients for $\delta_f = 15^0$.
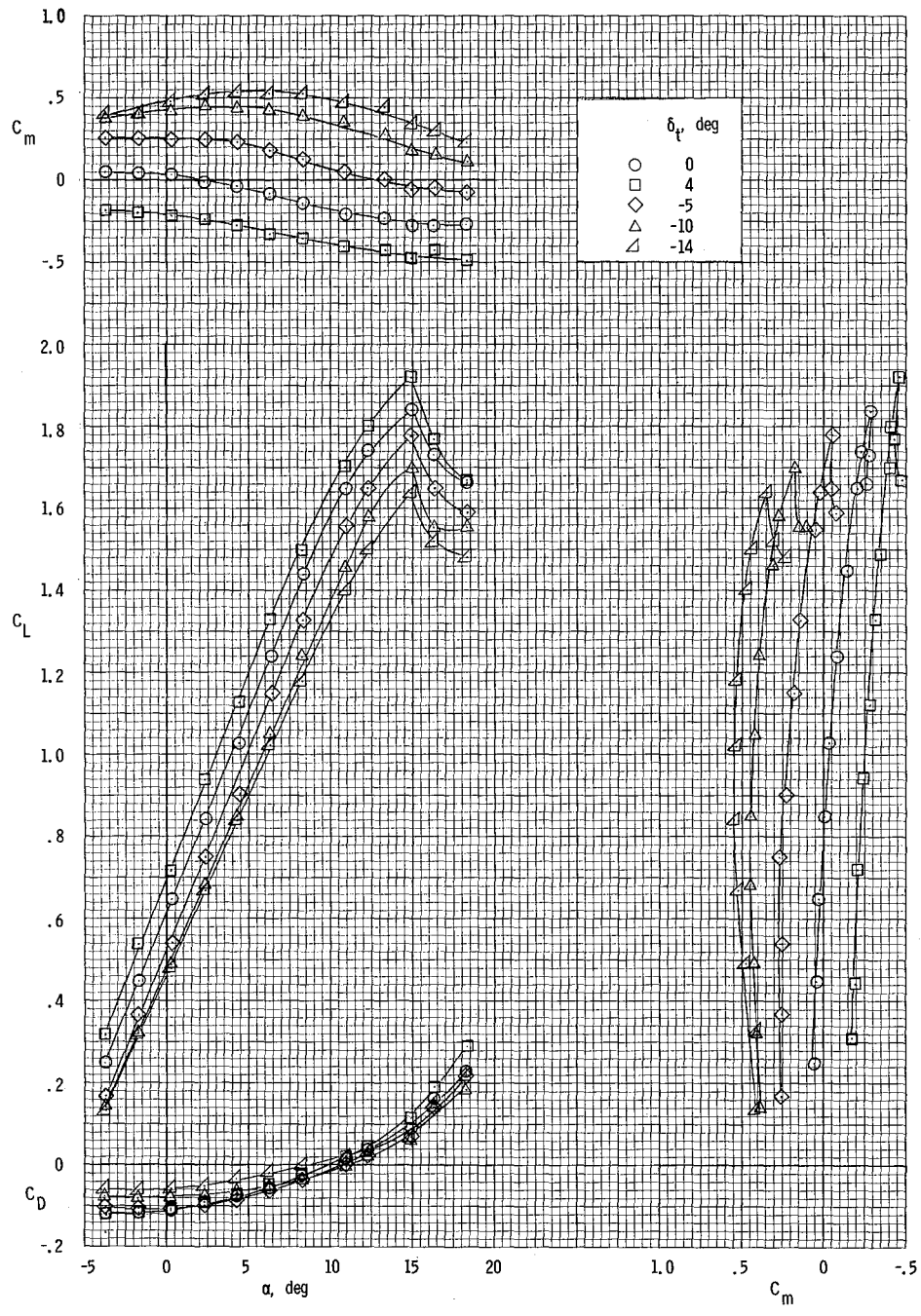
(b) $T_C' = 0.20$.

Figure 7.- Continued.
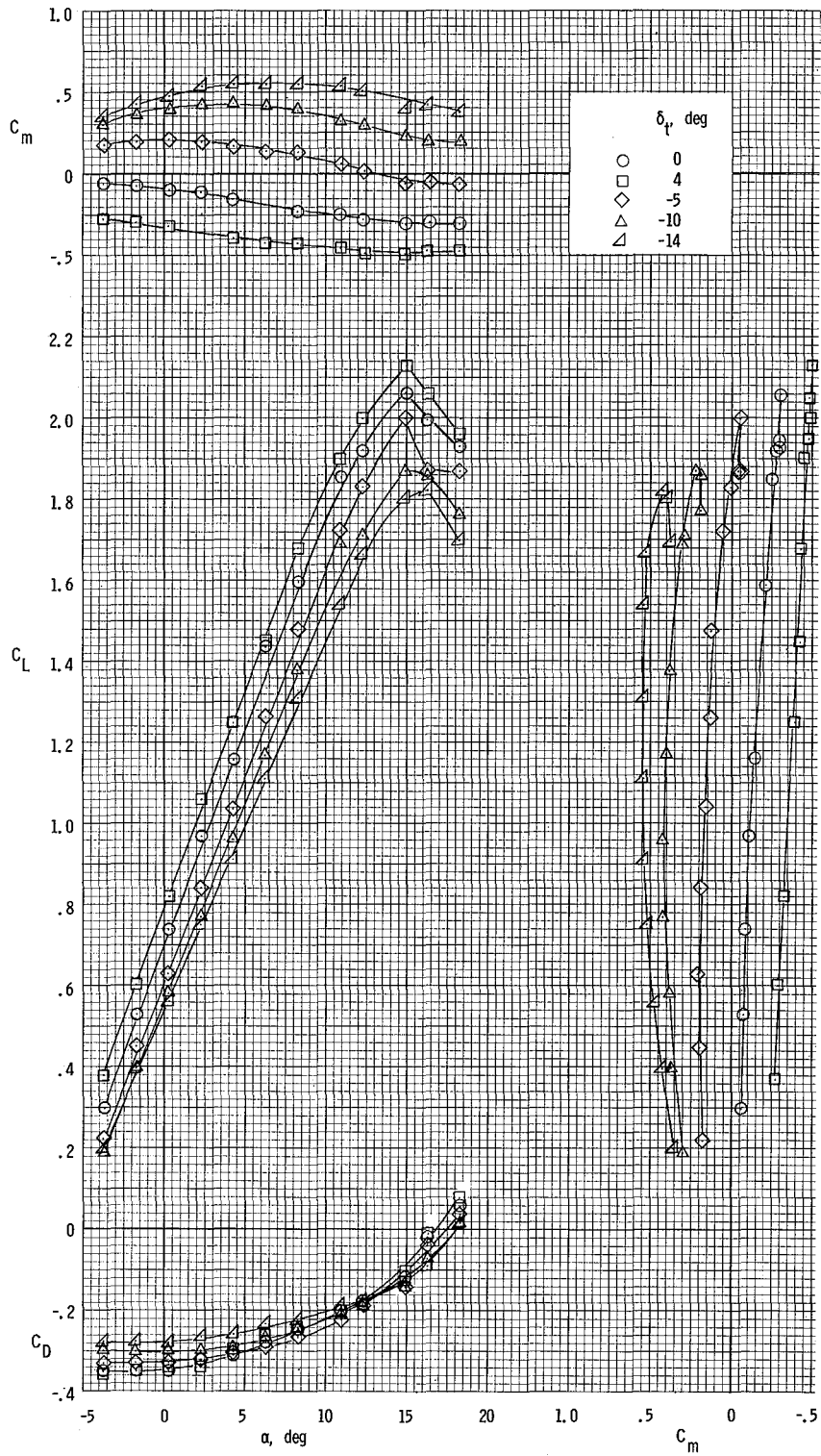
(c) $T_C' = 0.44$.

Figure 7.- Concluded.
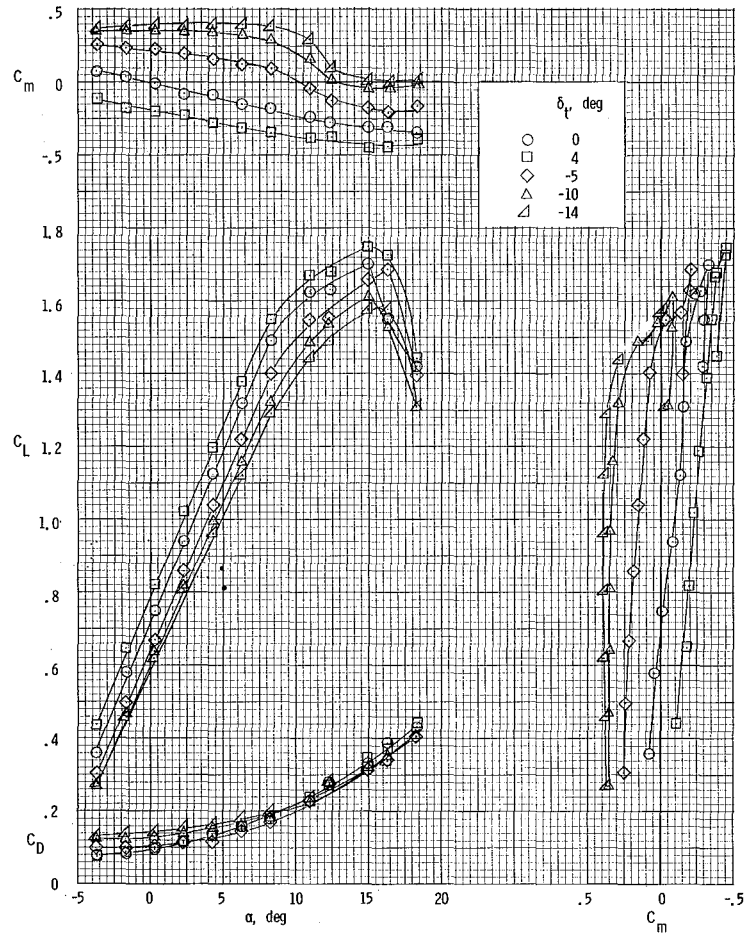
(a) $T_C' = 0$.

Figure 8.- Longitudinal aerodynamic characteristics of airplane for several thrust coefficients for $\delta_f = 27^0$.

28
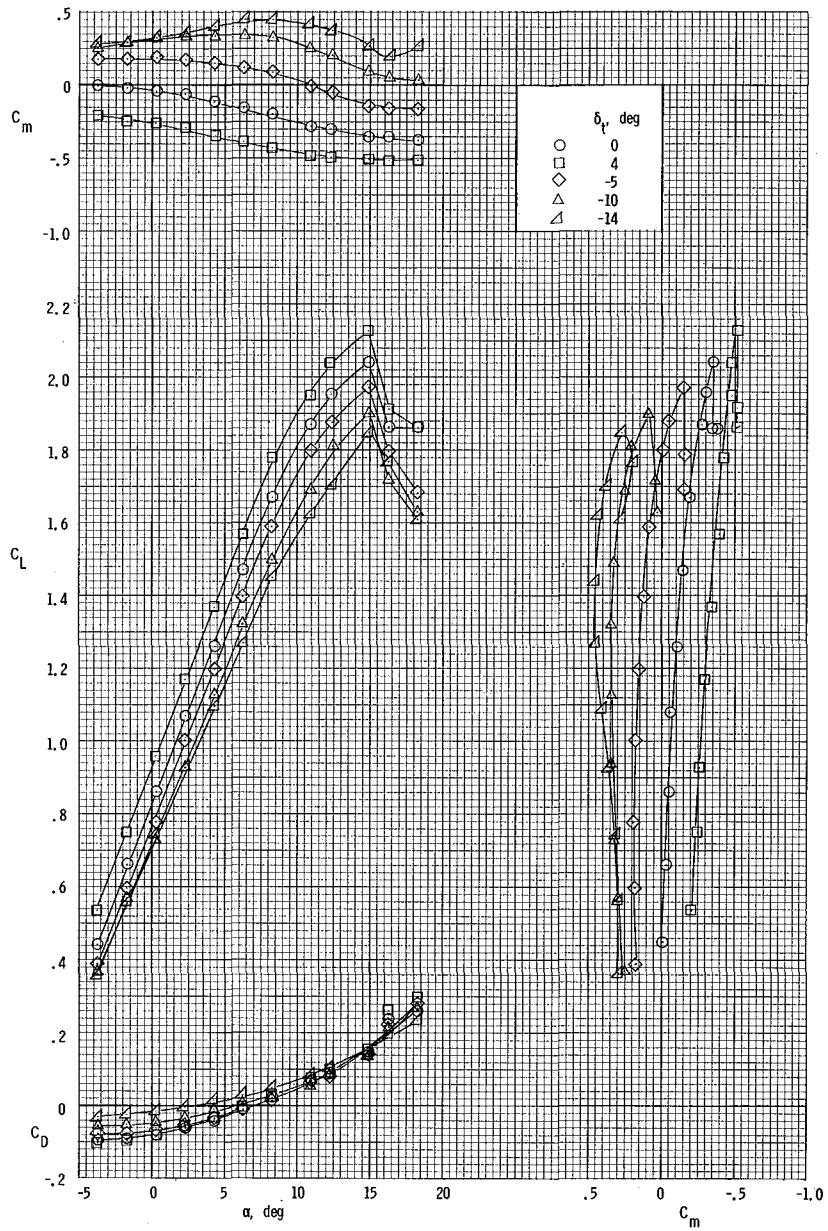
(b) $T_C^t = 0.20.$

Figure 8.- Continued.
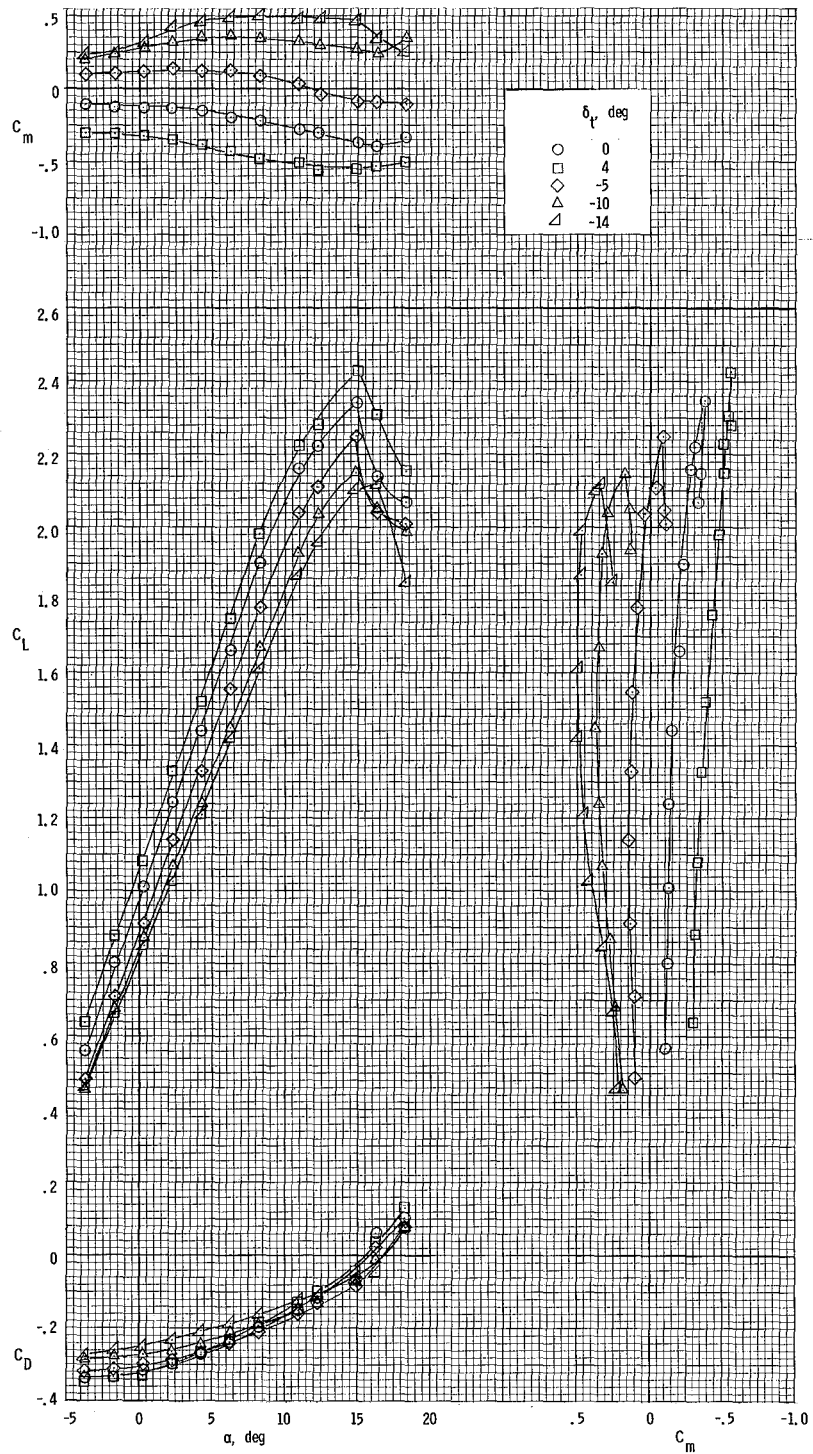
(c) $T_C' = 0.44$.

Figure 8.- Concluded.
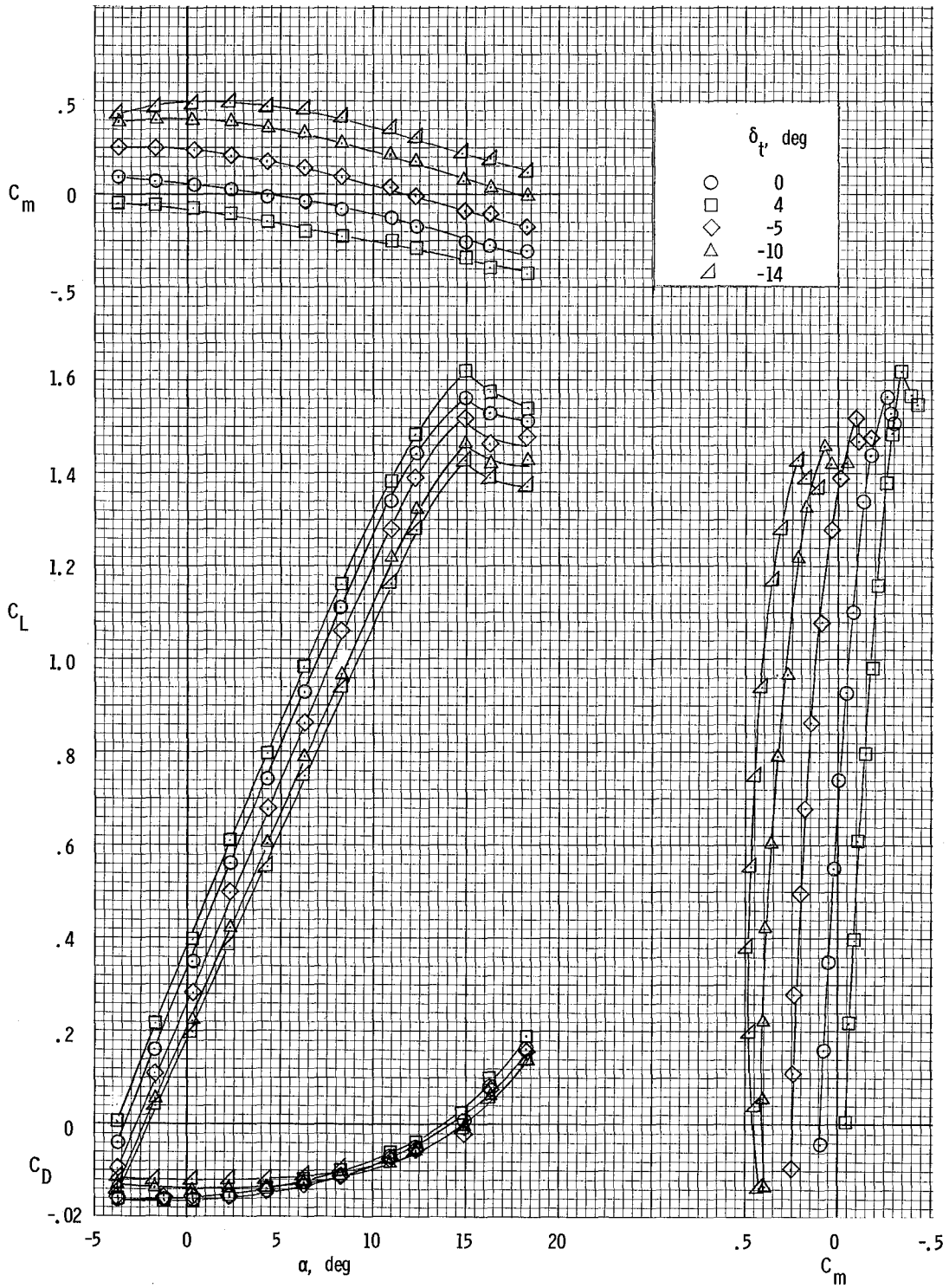
Figure 9.- Longitudinal aerodynamic characteristics of airplane with horizontal-tail tab fixed. $\delta_f = 0^0$; $T'_c = 0.20$.
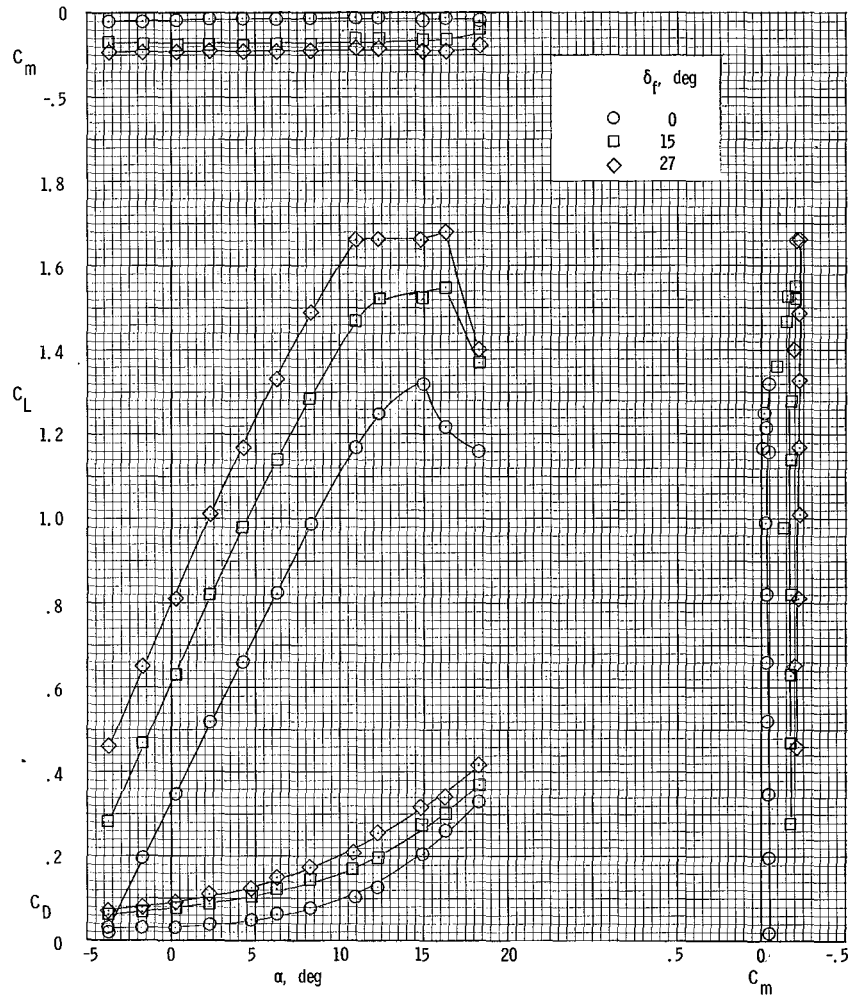
(a) $T'_c = 0.$

Figure 10.- Longitudinal aerodynamic characteristics of airplane with horizontal tail removed.
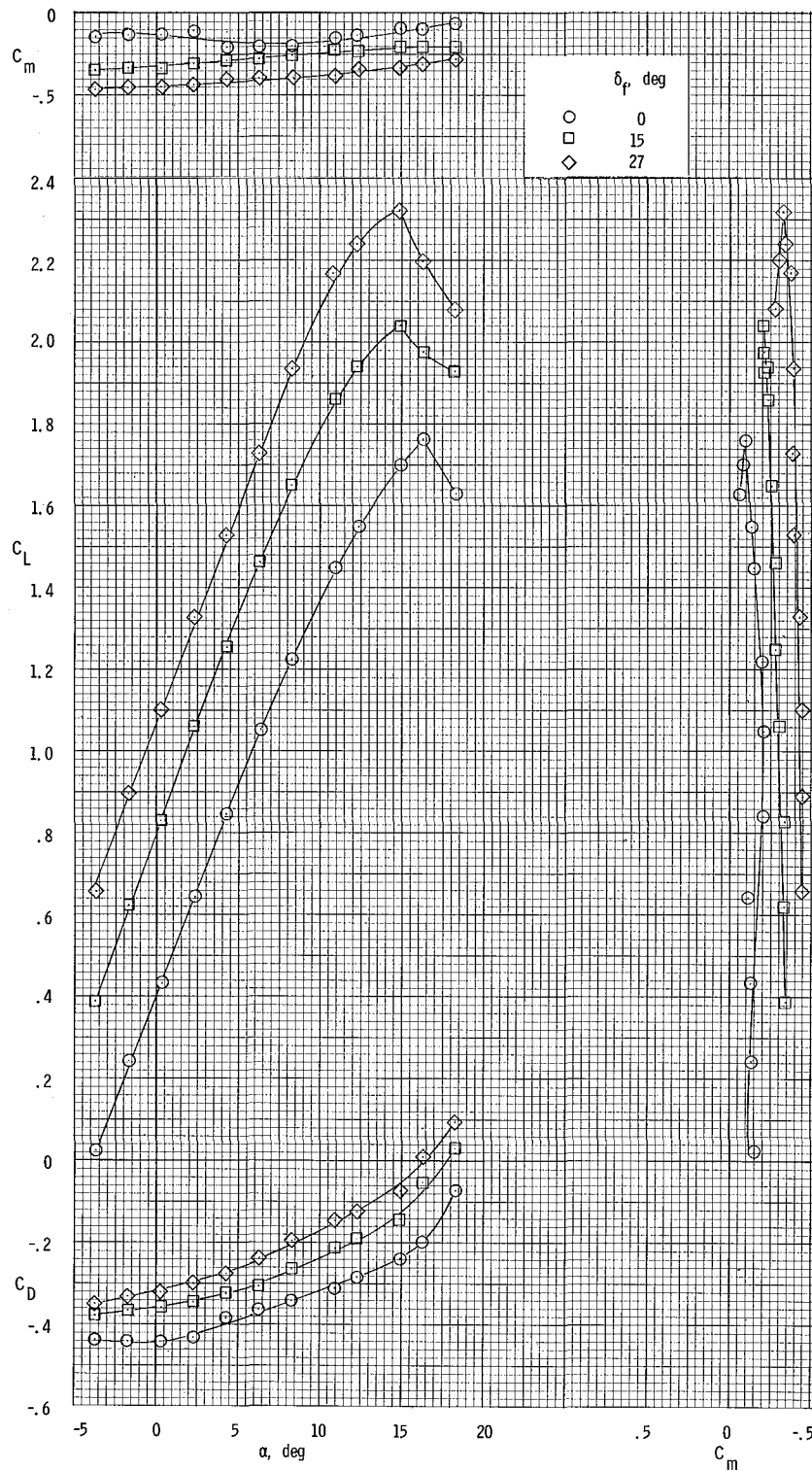
(b) $T_c' = 0.44$.

Figure 10.- Concluded.
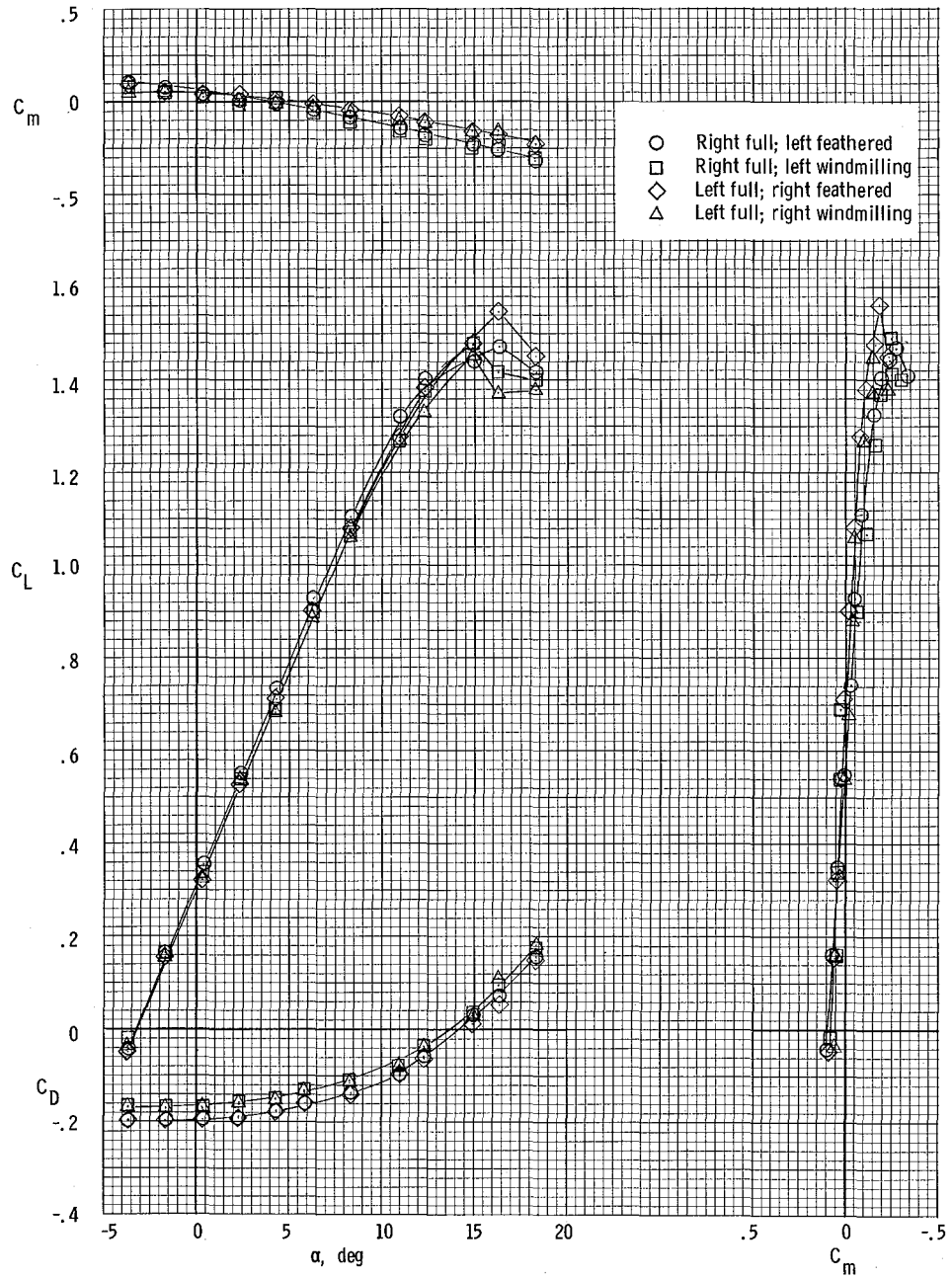
(a) $\delta_f = 0^0$.

Figure 11.- Longitudinal aerodynamic characteristics of airplane with asymmetric power.

(b) $\delta_f = 27^0$.
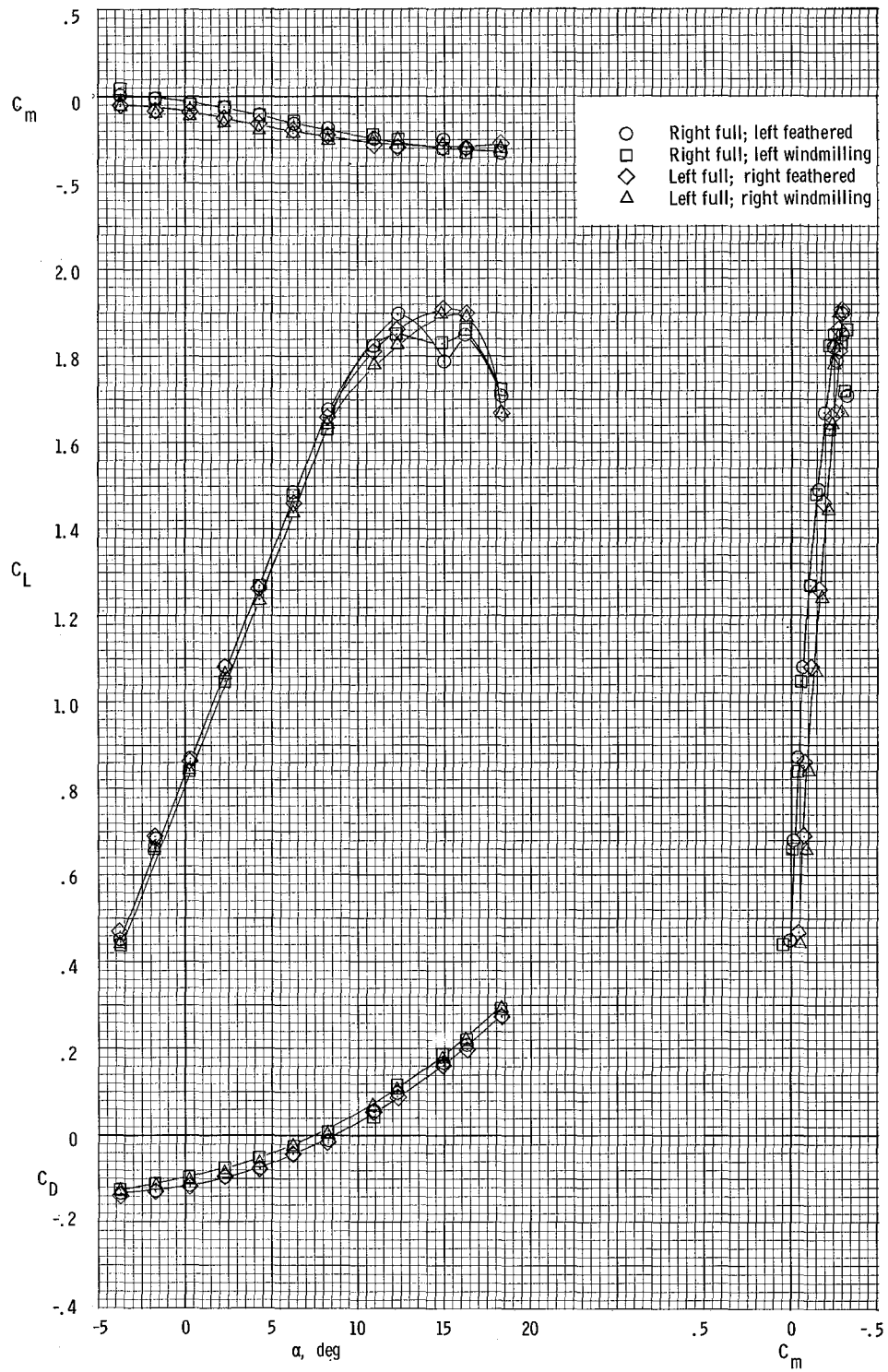
Figure 11.- Concluded.
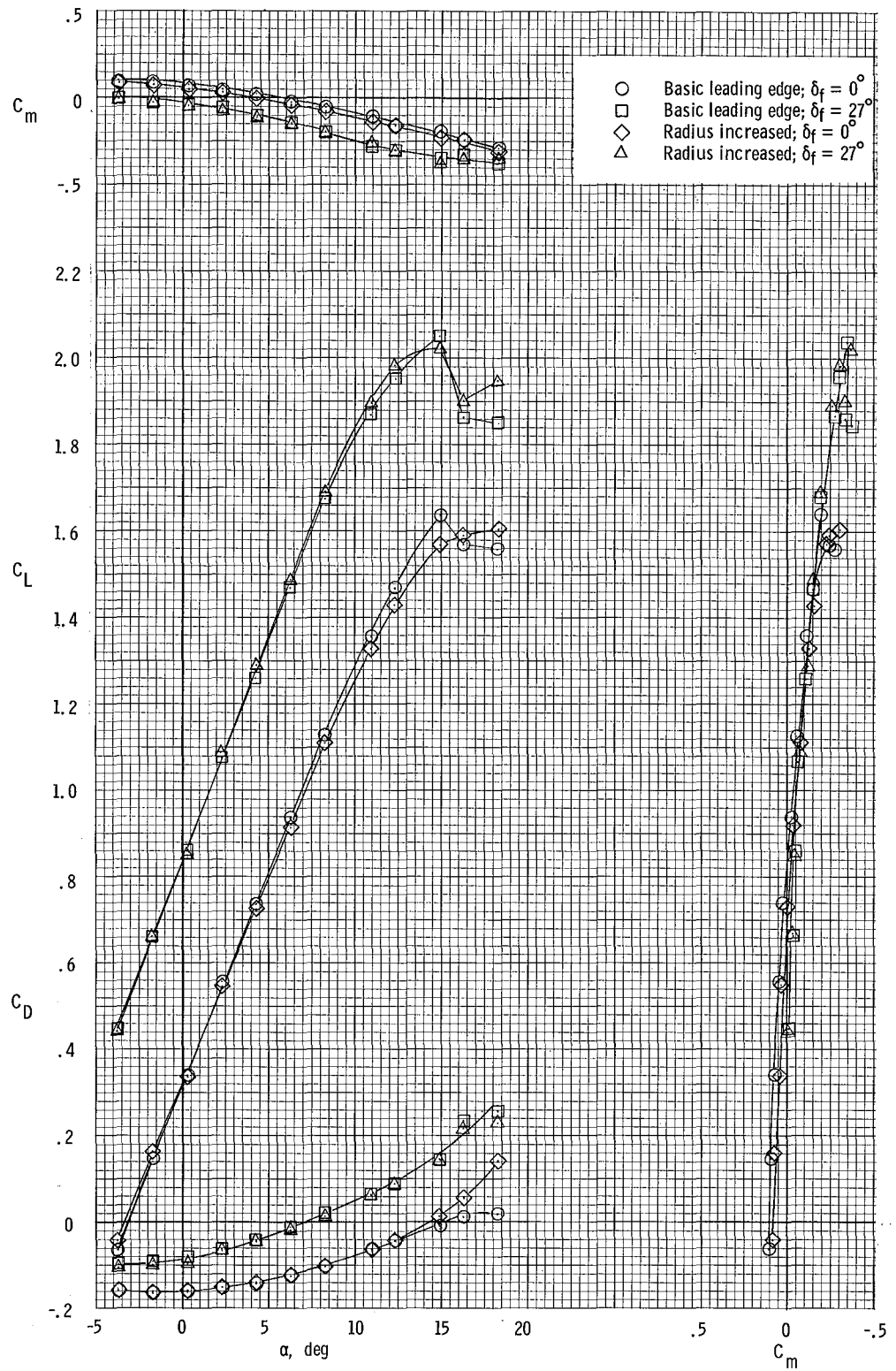
Figure 12.- Effect of leading-edge radius increase on longitudinal characteristics. $T'_c = 0.20$.
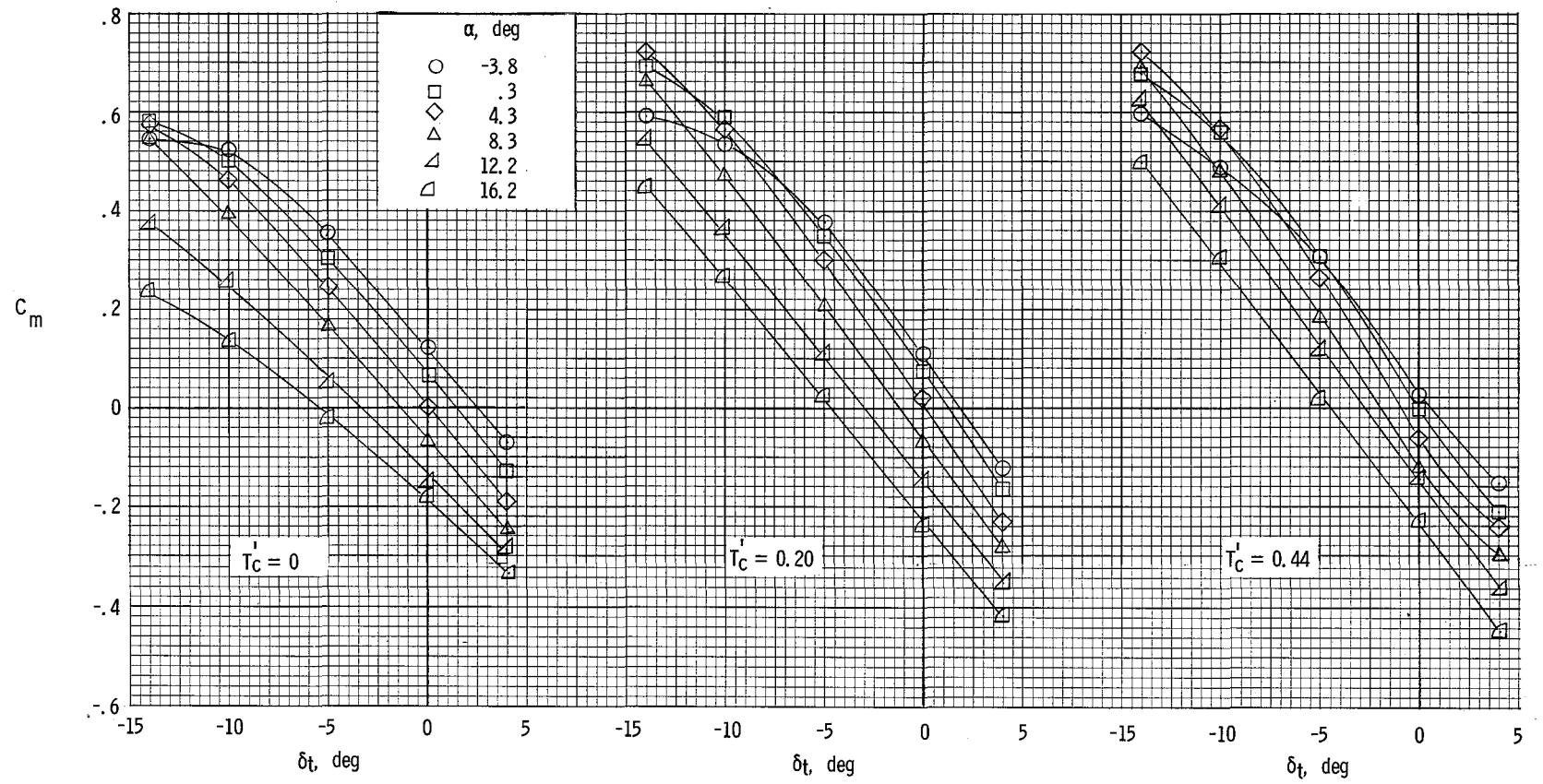
(a) $\delta_f = 0^0$.

Figure 13.- Variation of pitching-moment coefficient with horizontal-tail deflection for several power and flap settings.
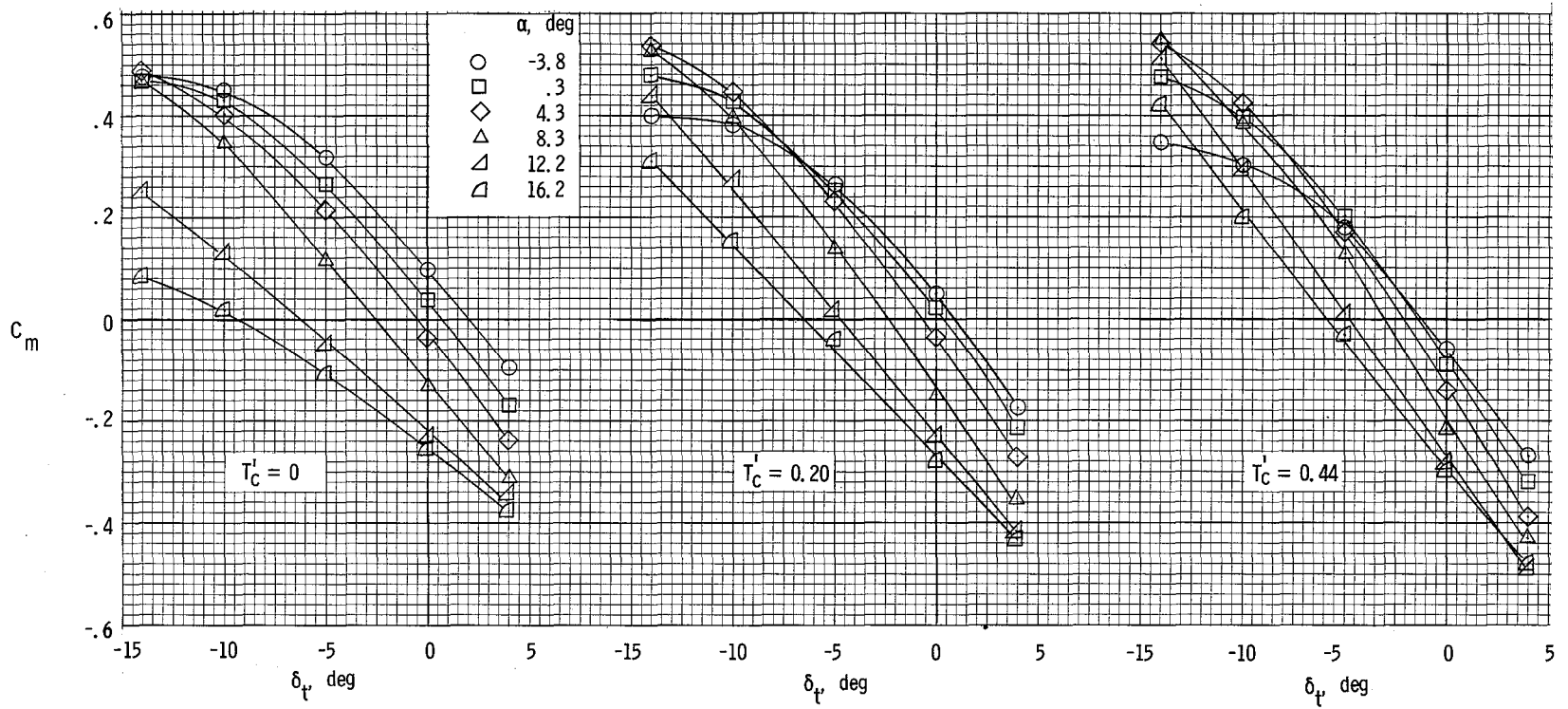
(b) $\delta_f = 15^\circ$.

Figure 13.- Continued.

(c) $\delta_f = 27^0$.
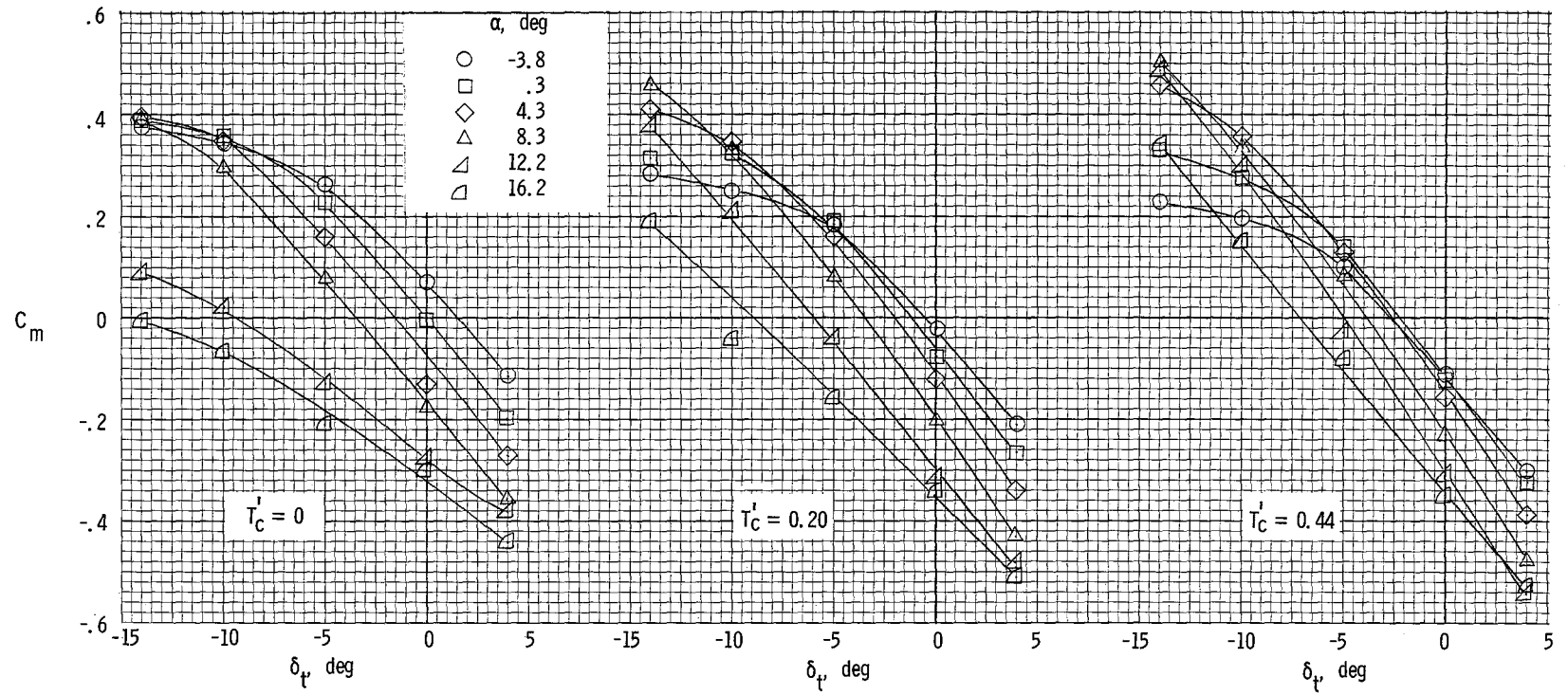
Figure 13.- Concluded.
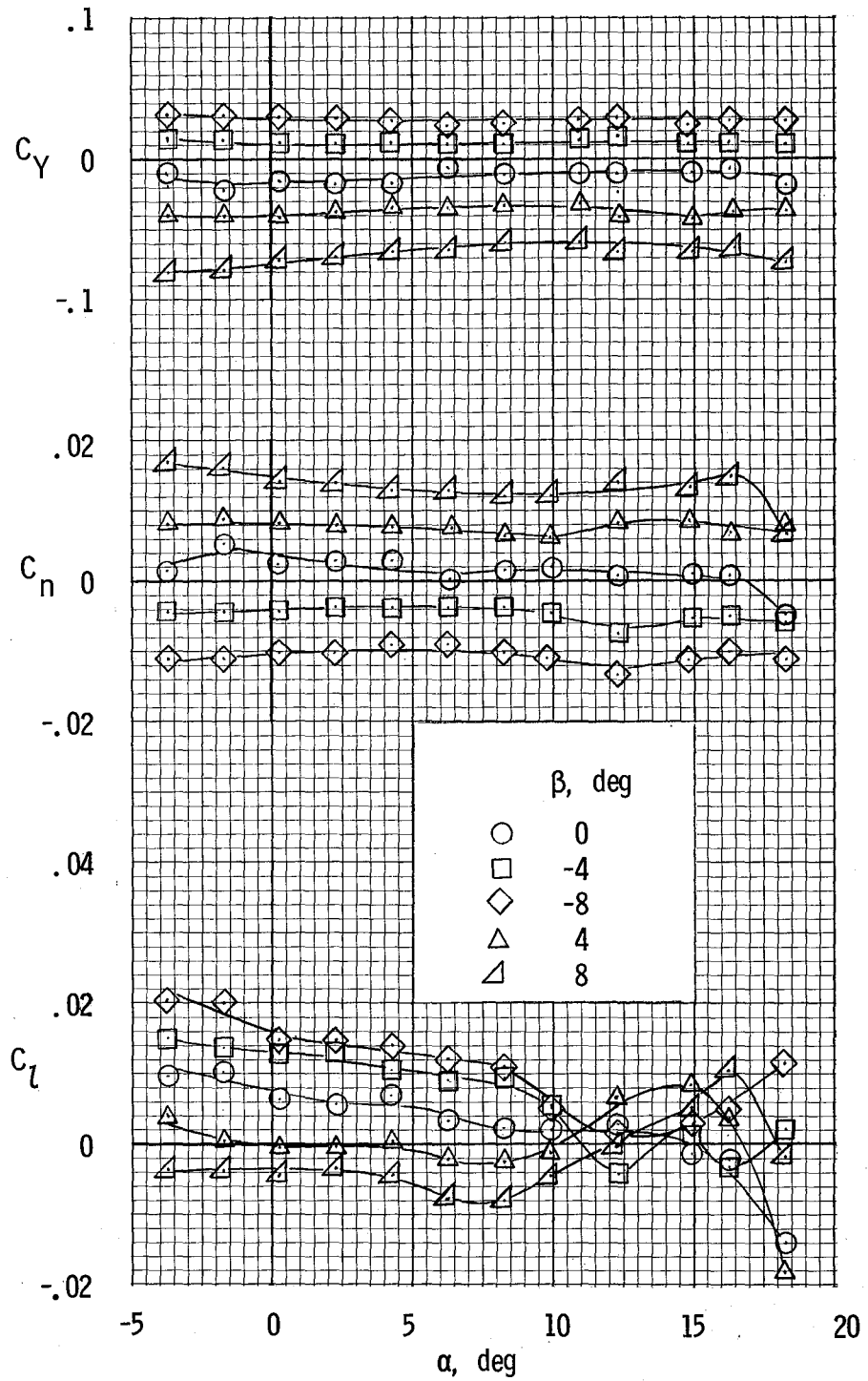
(a) $\delta_f = 0^0$.

Figure 14.- Lateral characteristics of airplane with propellers removed for several flap deflections.

(b) $\delta_f = 15^0$.
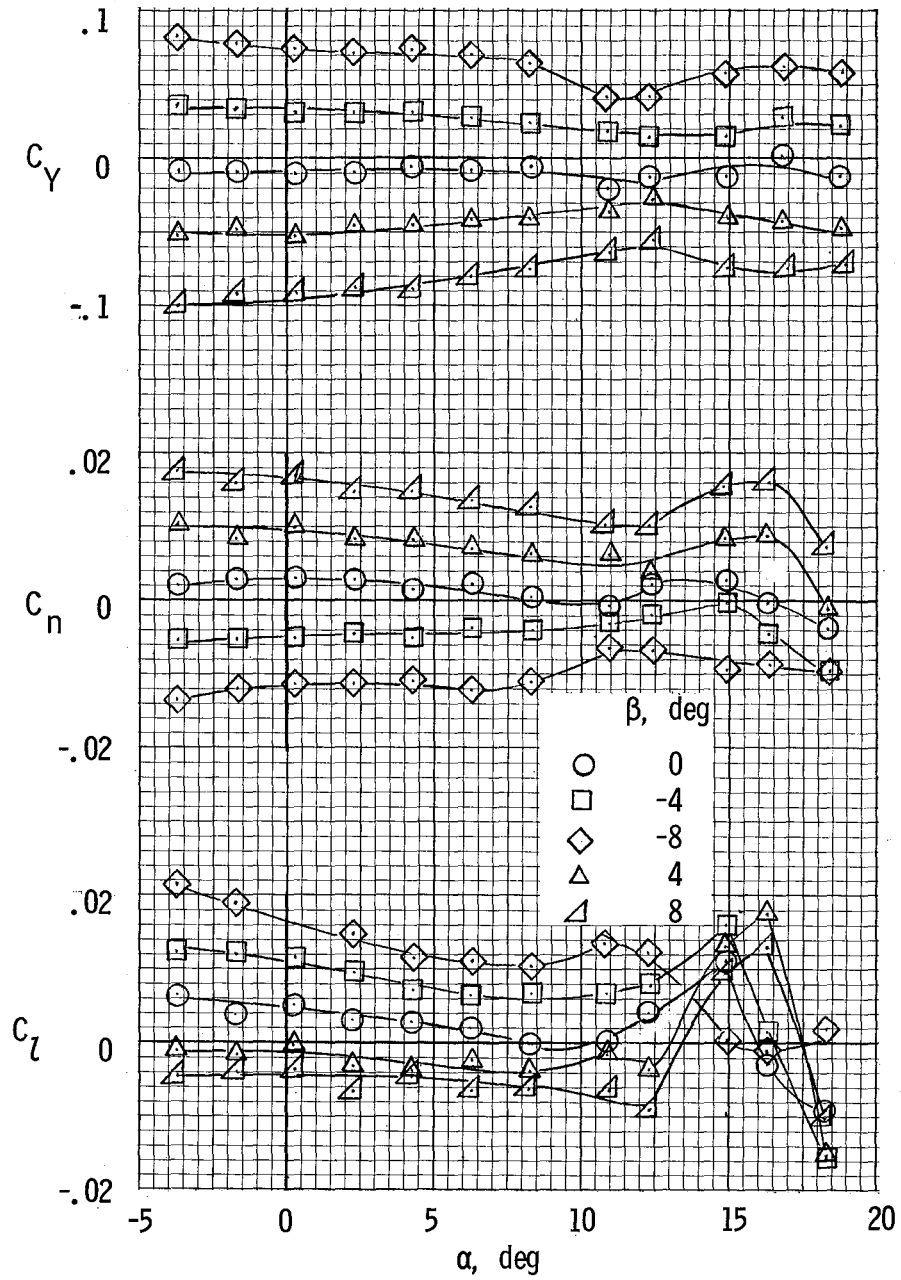
Figure 14.- Continued.

(c) $\delta_f = 27^o$.
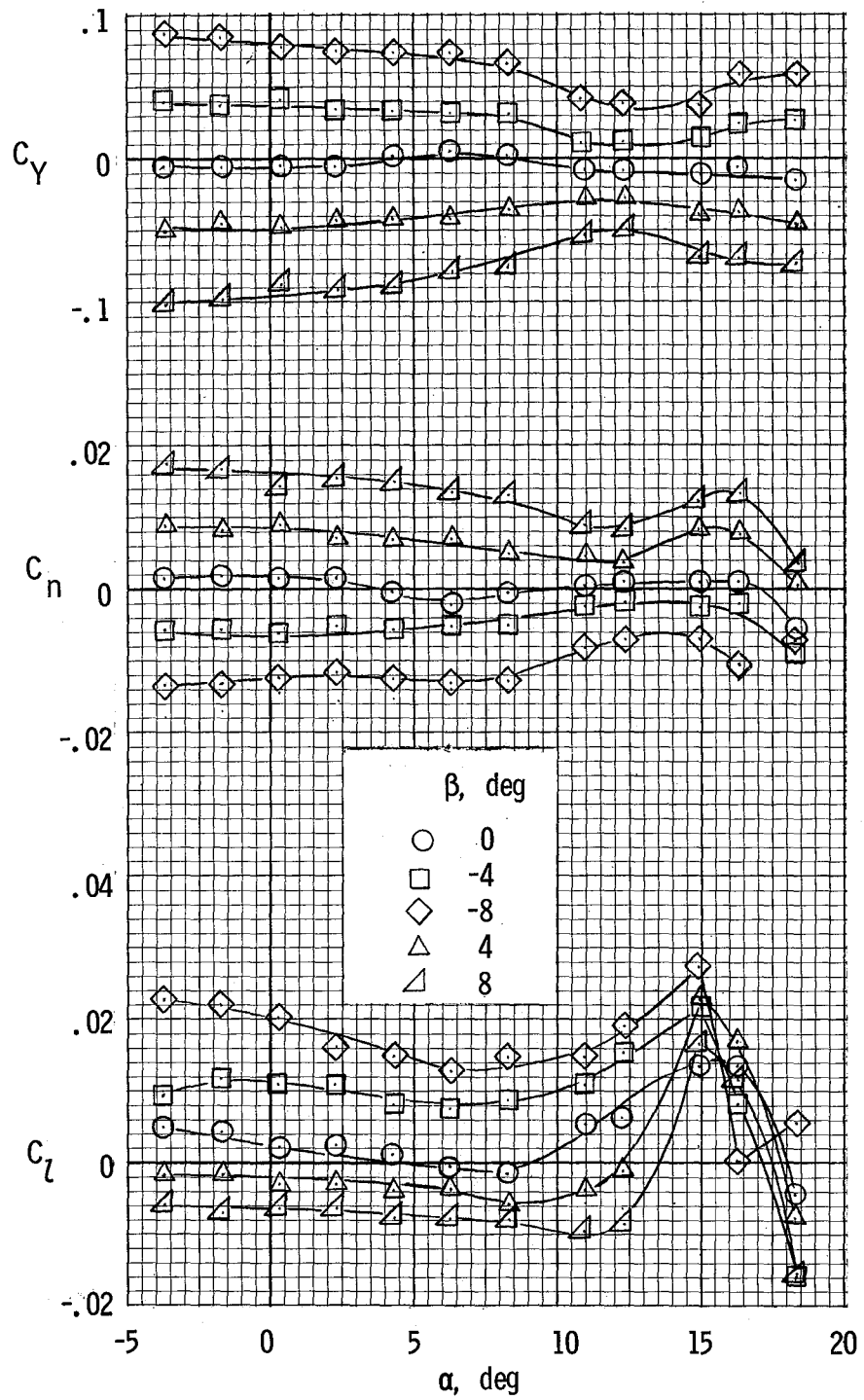
Figure 14.- Concluded.
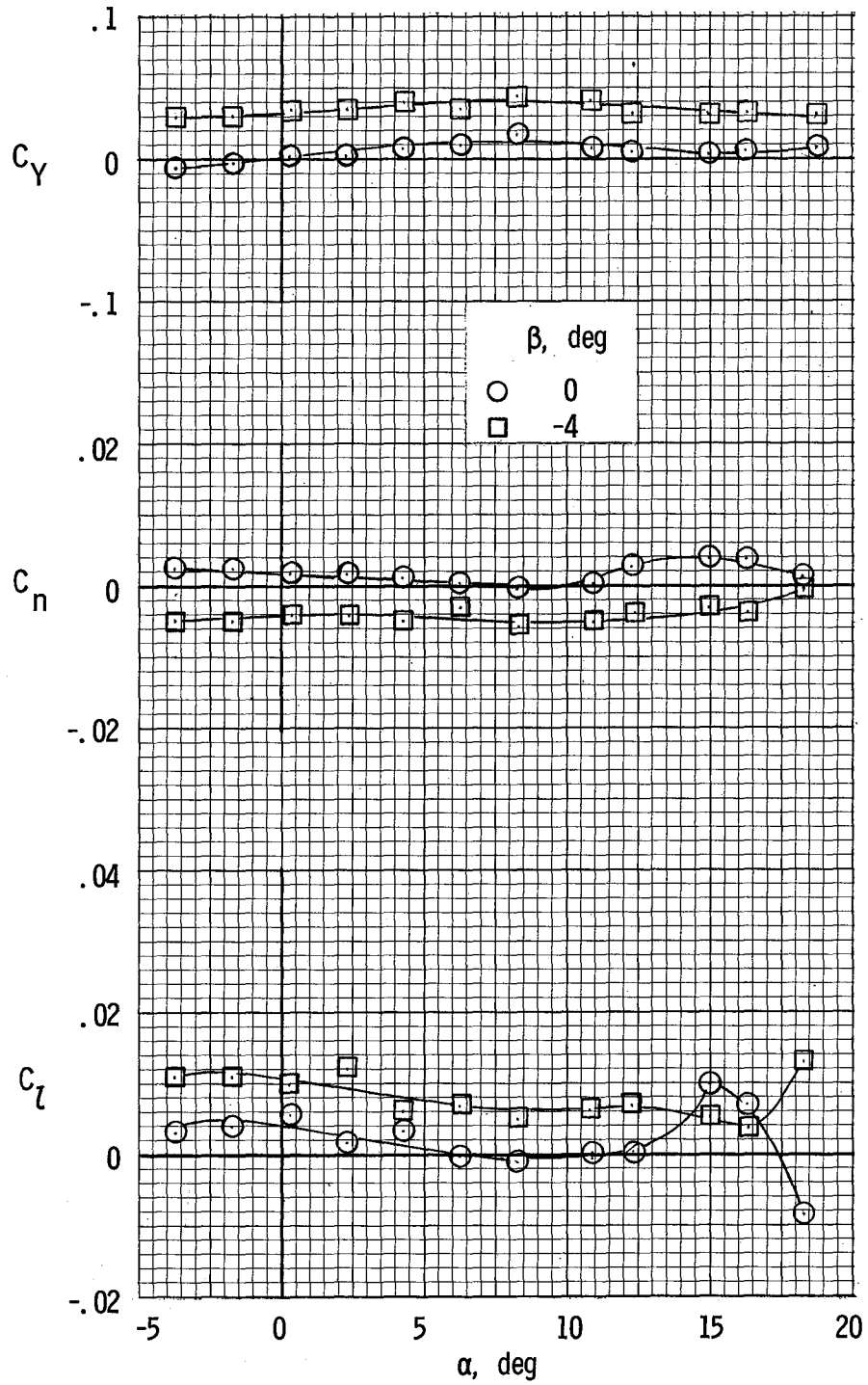
(a) $\delta_f = 0^0$.

Figure 15.- Lateral characteristics of airplane with windmilling propellers. $T_c' = -0.05$.

43

(b) $\delta_f = 27^o$.
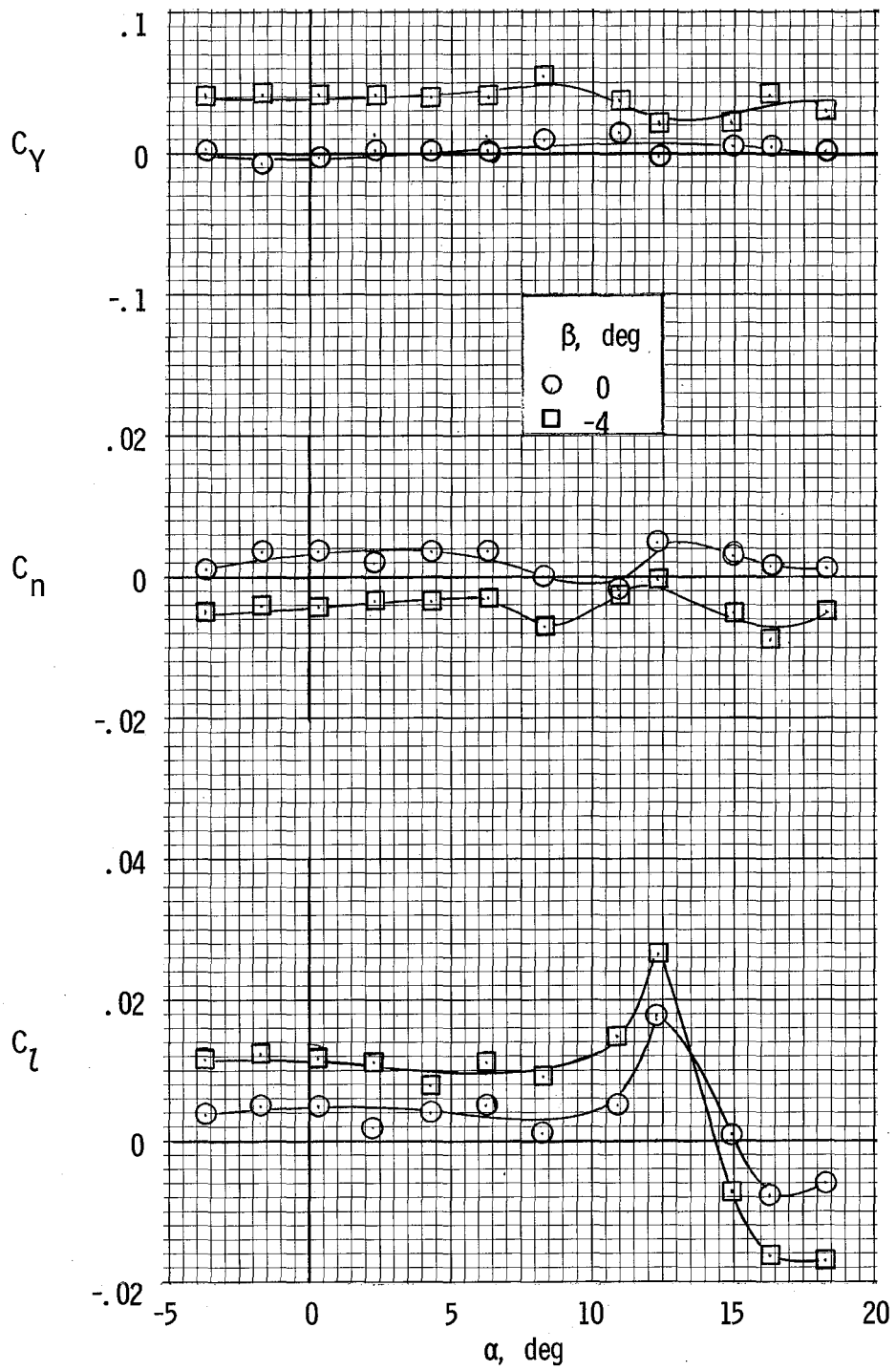
Figure 15.- Concluded.
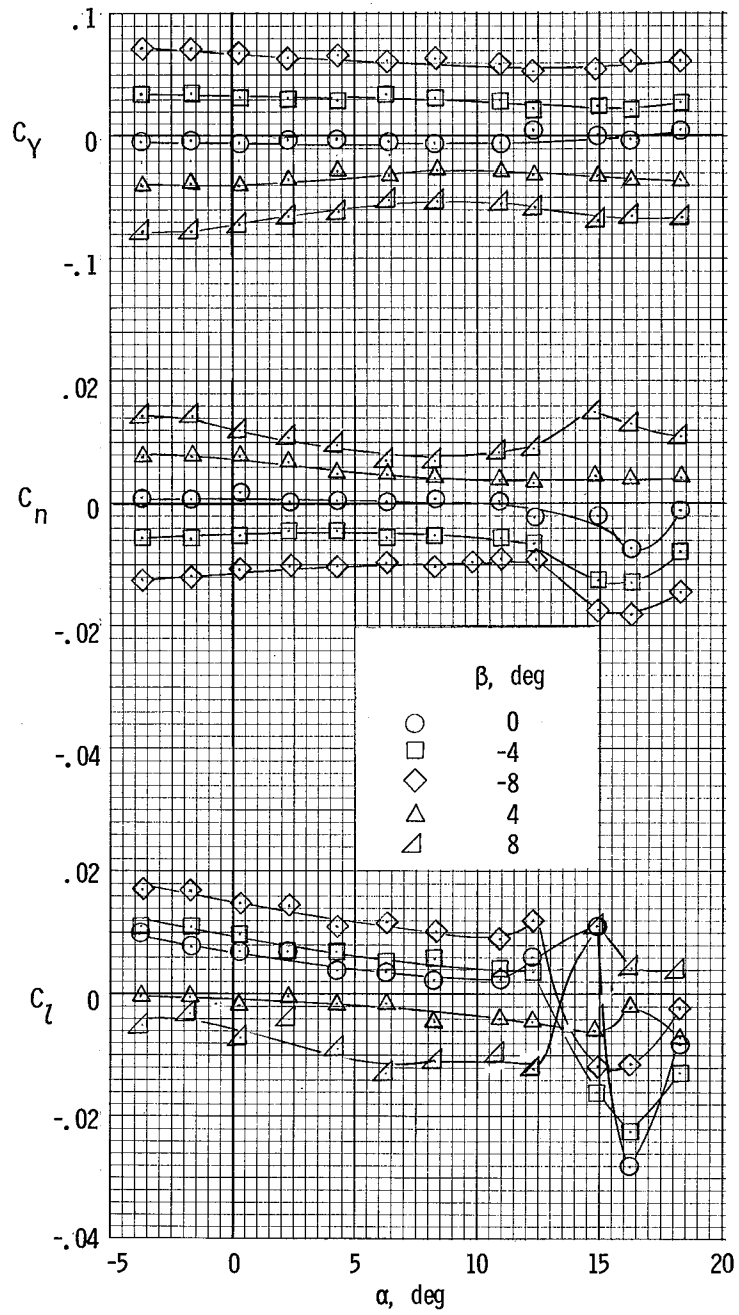
(a) $T'_c = 0$.

Figure 16.- Lateral characteristics of airplane for several sideslip angles and thrust coefficients for $\delta_f = 0^0$.
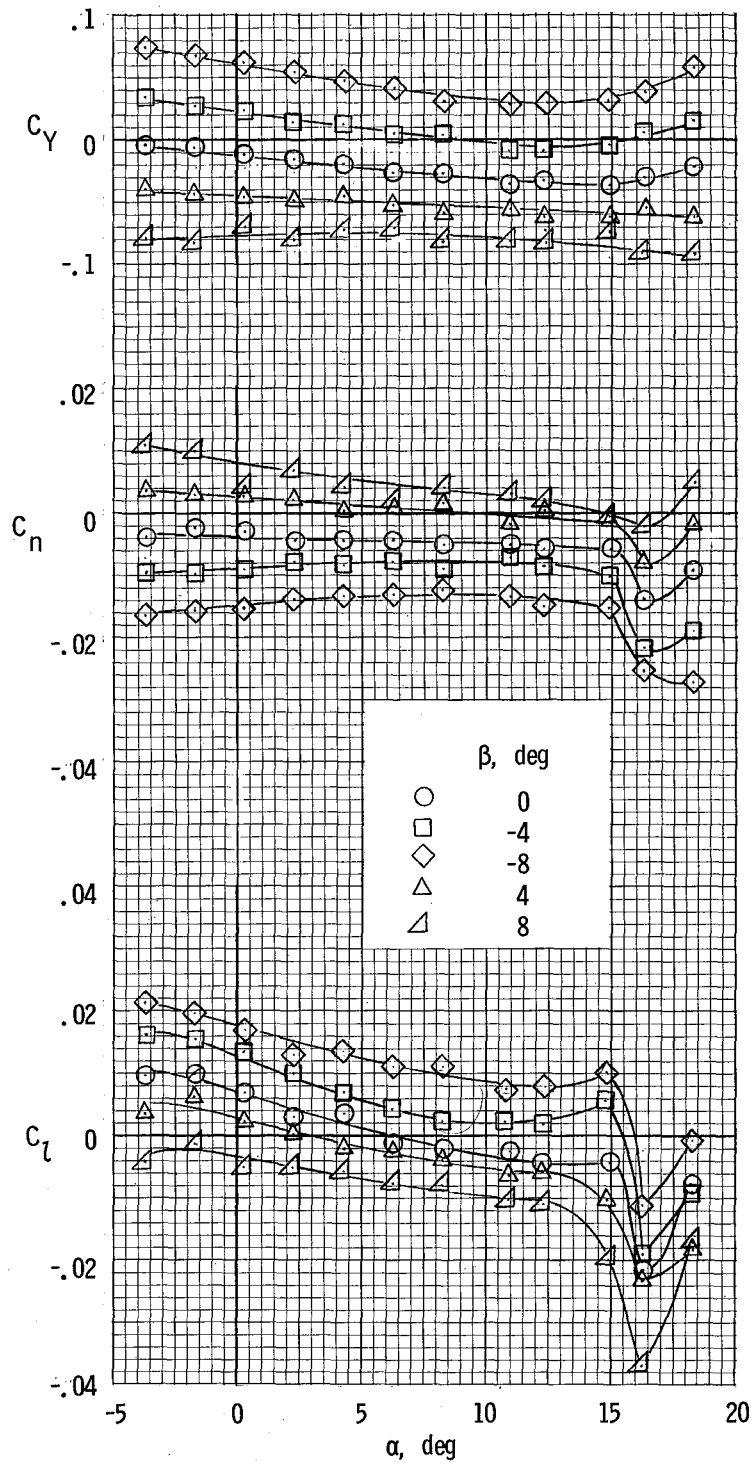
(b) $T_C' = 0.20$.

Figure 16.- Continued.
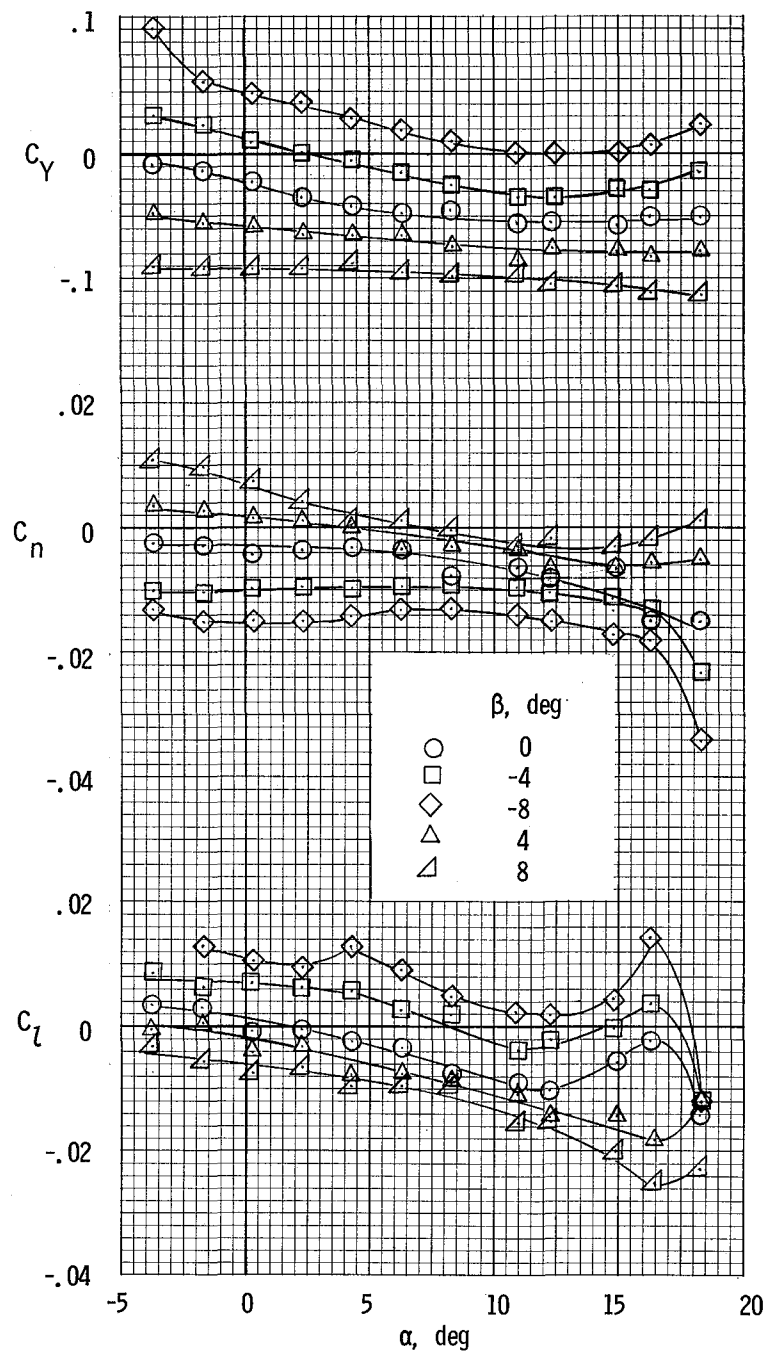
(c) $T'_c = 0.44$.

Figure 16.- Concluded.
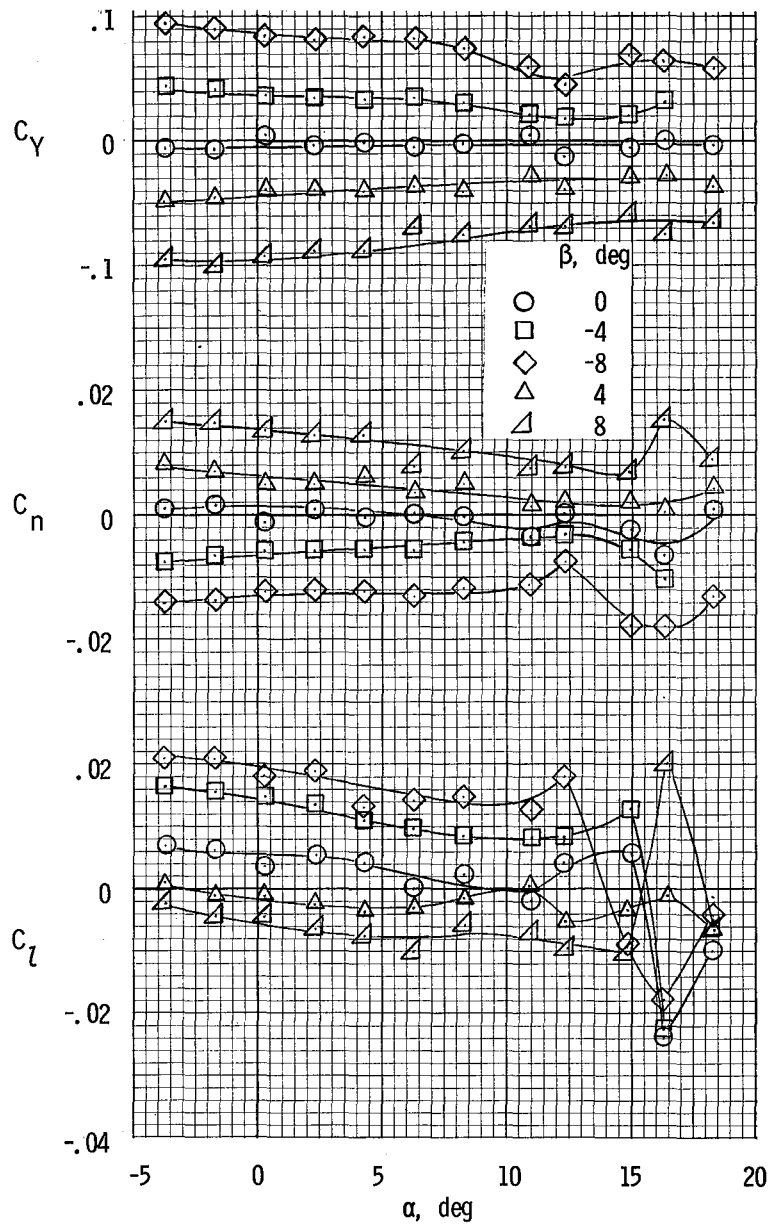
(a) $T_c' = 0$.

Figure 17.- Lateral characteristics of airplane for several sideslip angles and thrust coefficients for $\delta_f = 15^0$.
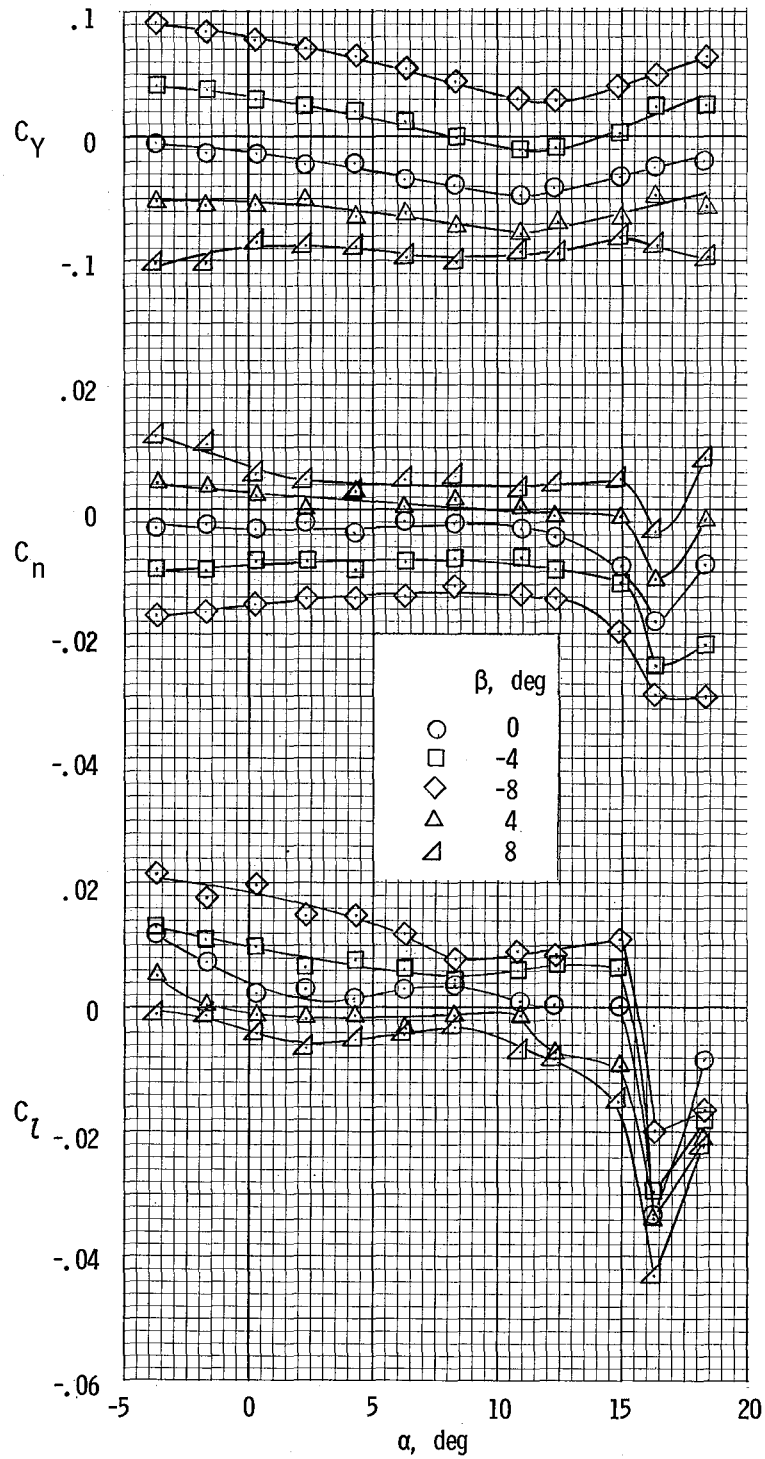
(b) $T_c' = 0.20$.

Figure 17.- Continued.
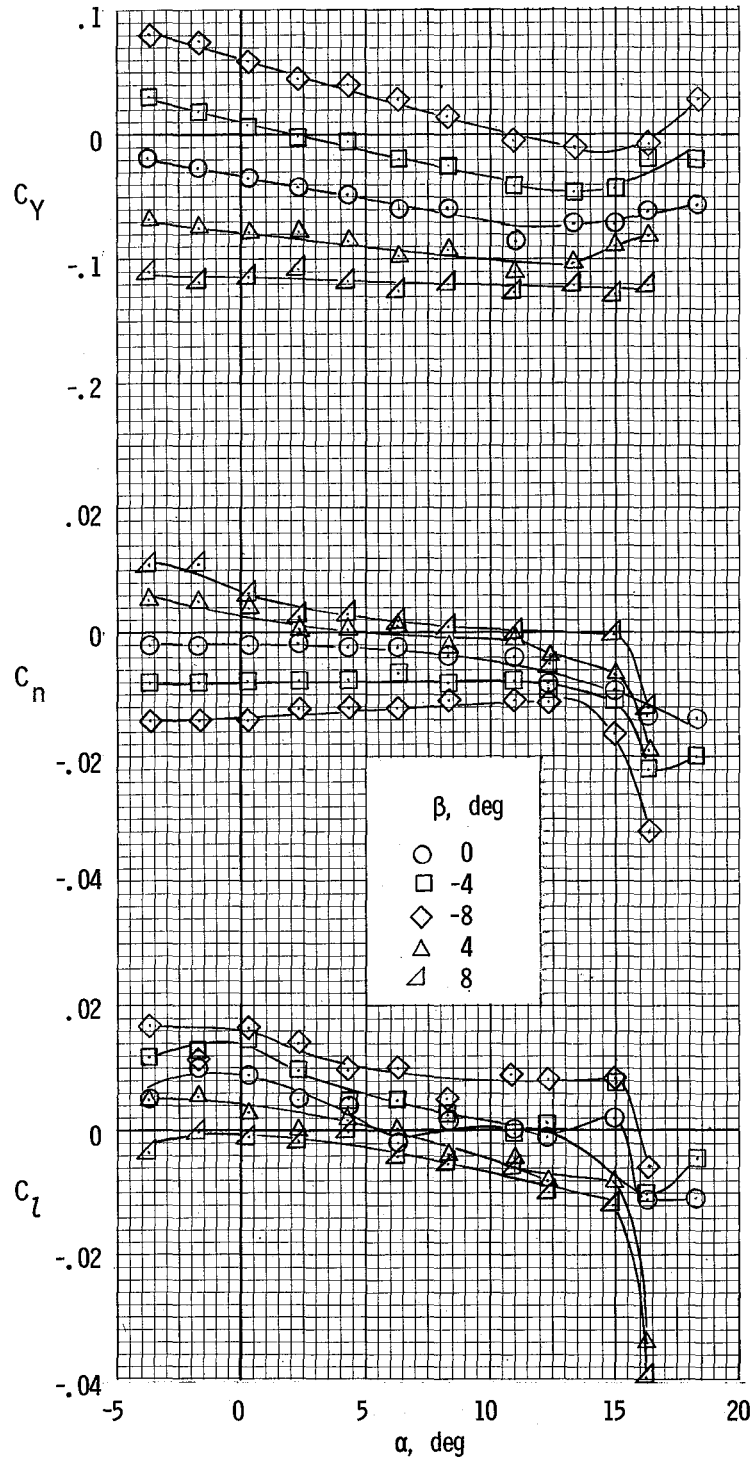
(c) $T'_C = 0.44$.

Figure 17.- Concluded.
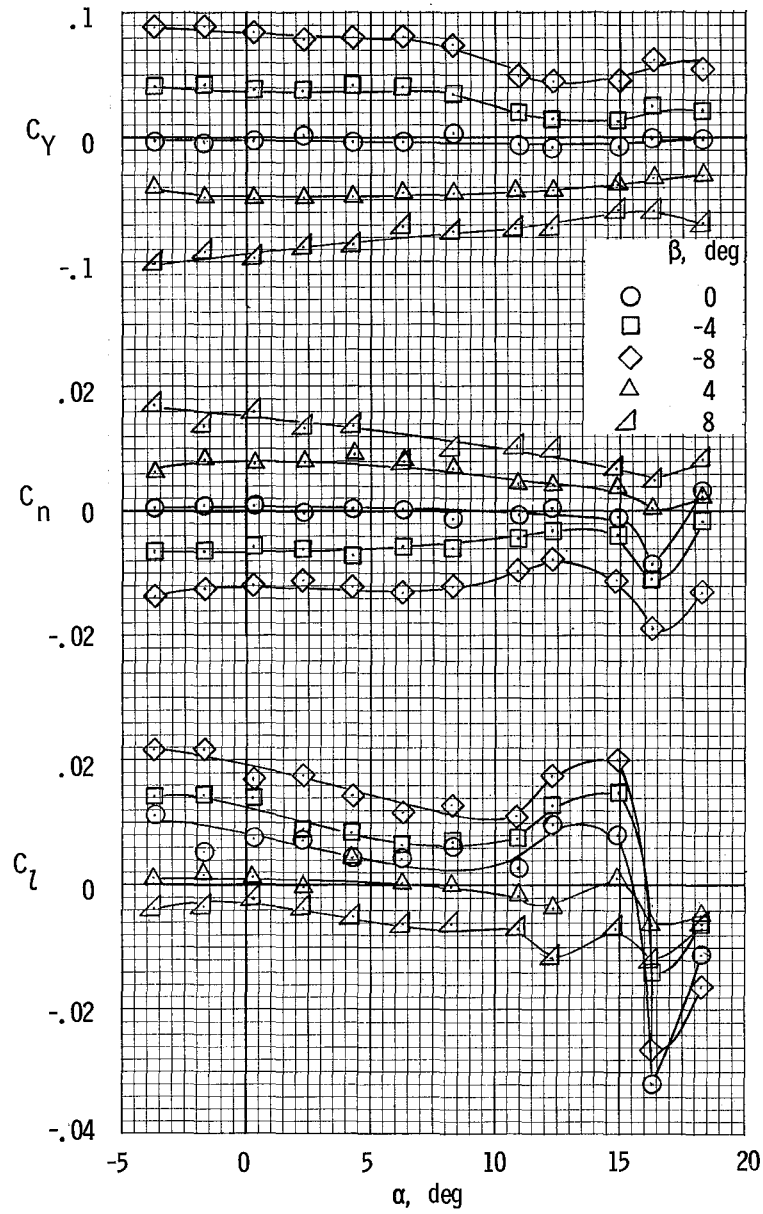
(a) $T_c' = 0$.

Figure 18.- Lateral characteristics of airplane for several sideslip angles and thrust coefficients for $\delta_f = 27^o$.
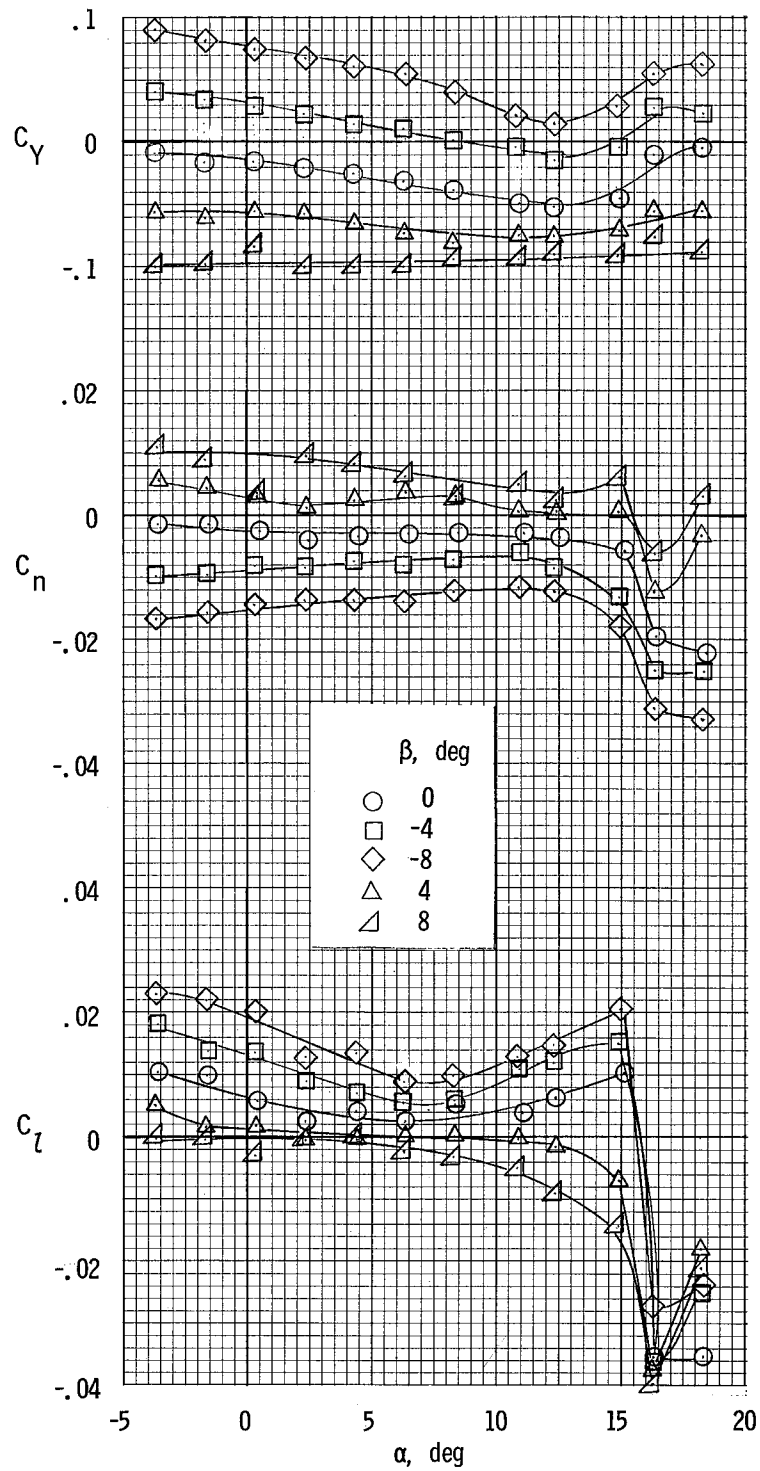
(b) $T_c^i = 0.20$.

Figure 18.- Continued.
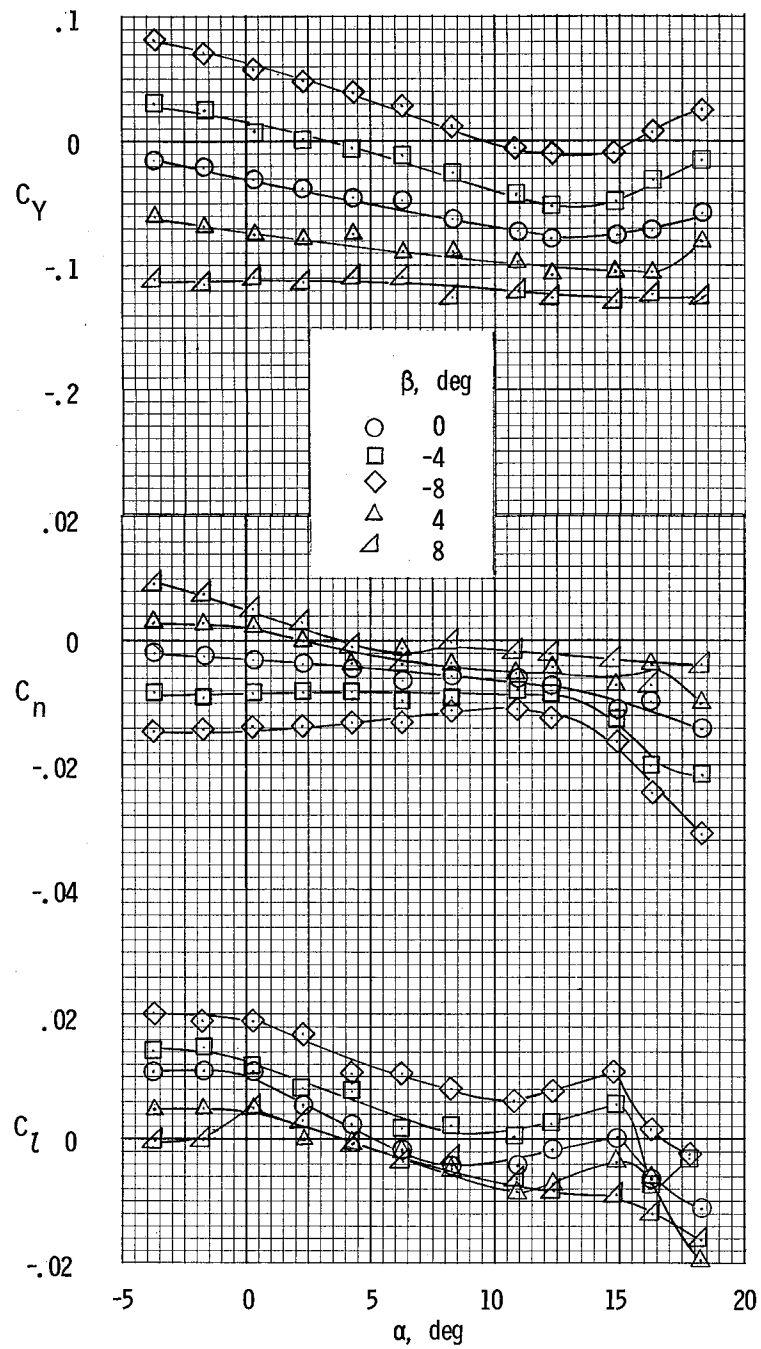
(c) $T_c' = 0.44$.

Figure 18.- Concluded.
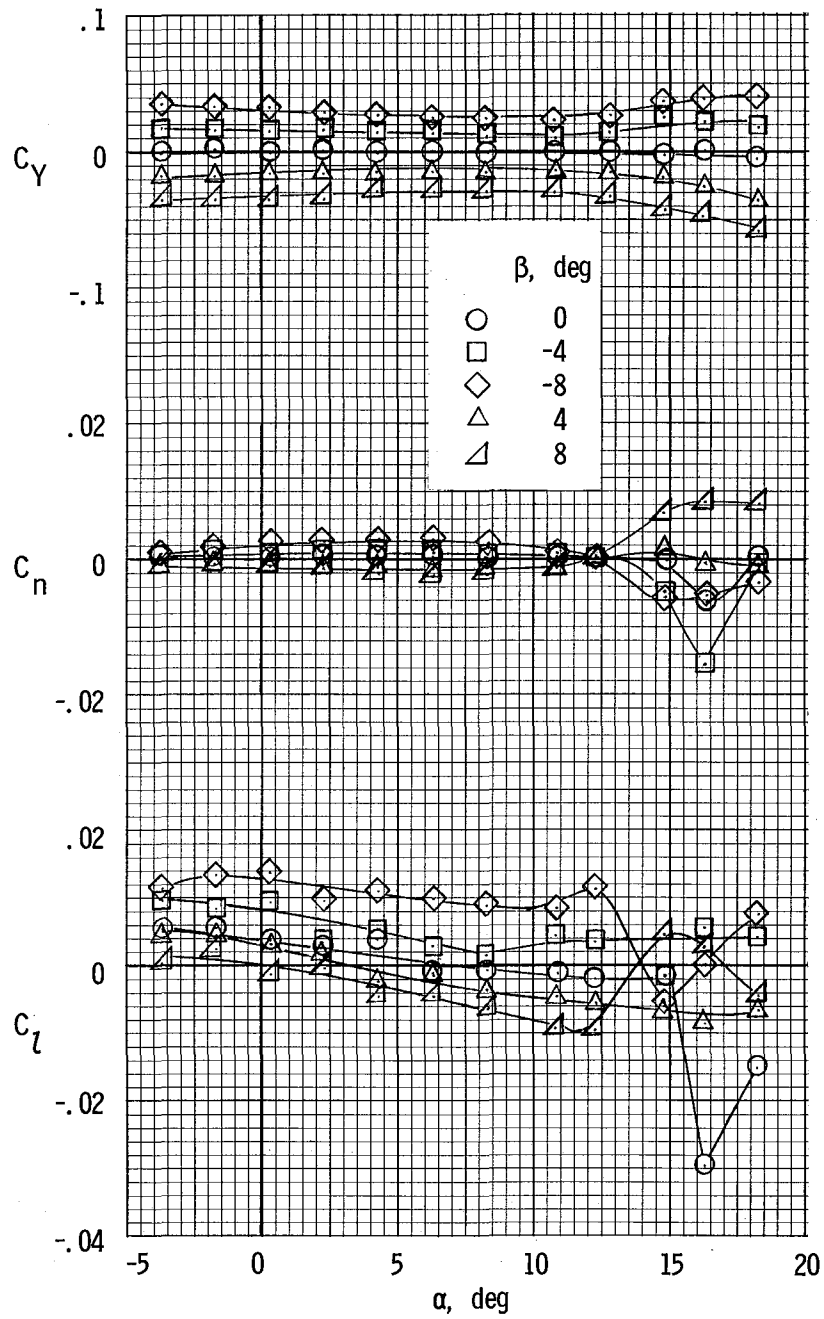
(a) $T'_c = 0$.

Figure 19.- Lateral characteristics of airplane with vertical tail removed. $\delta_f = 0^0$.
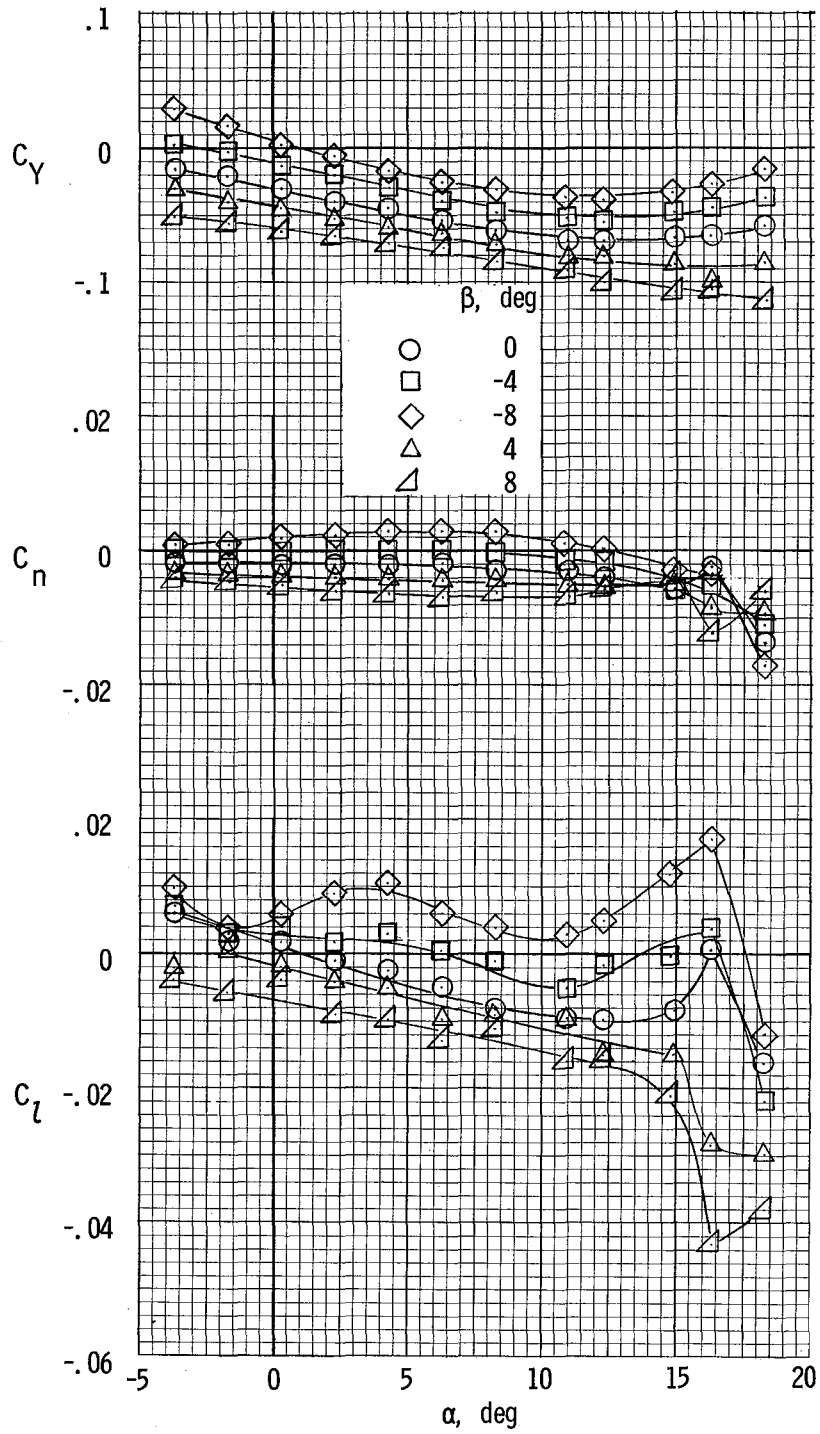
(b) $T'_c = 0.44$.

Figure 19.- Concluded.
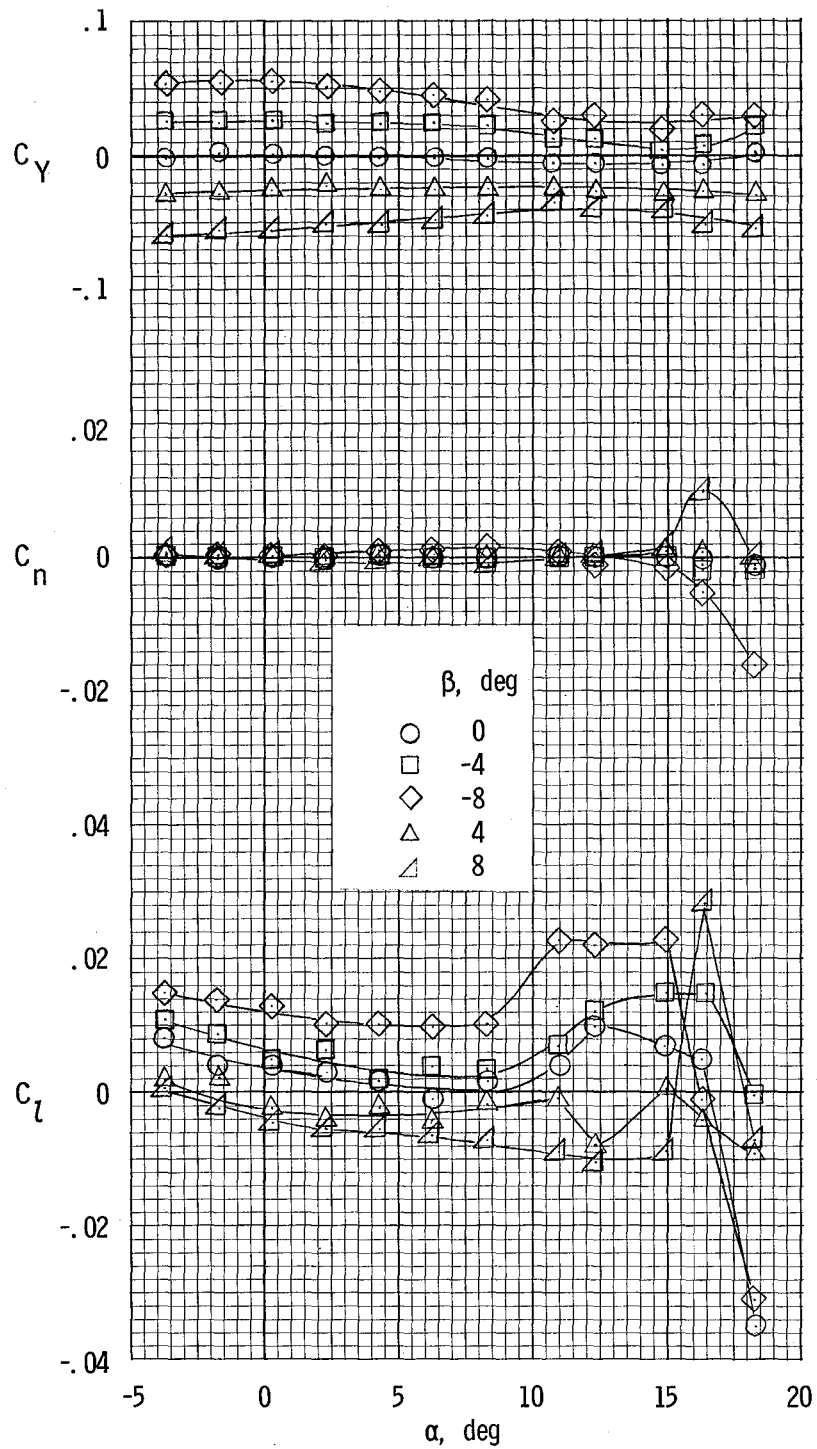
(a) $T_C' = 0$.

Figure 20.- Lateral characteristics of airplane with vertical tail removed. $\delta_f = 27^0$.
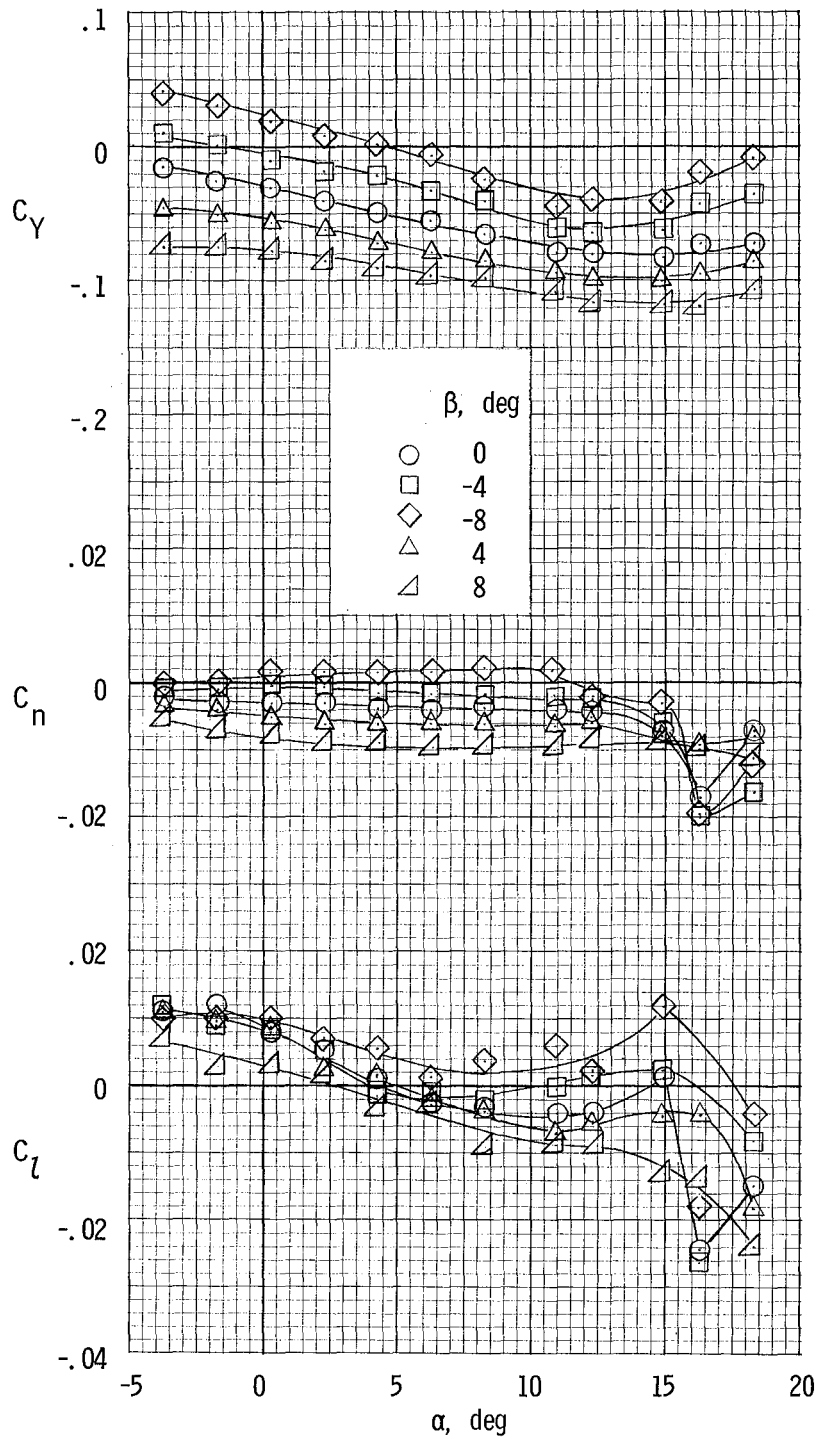
(b) $T_c' = 0.44$.

Figure 20.- Concluded.
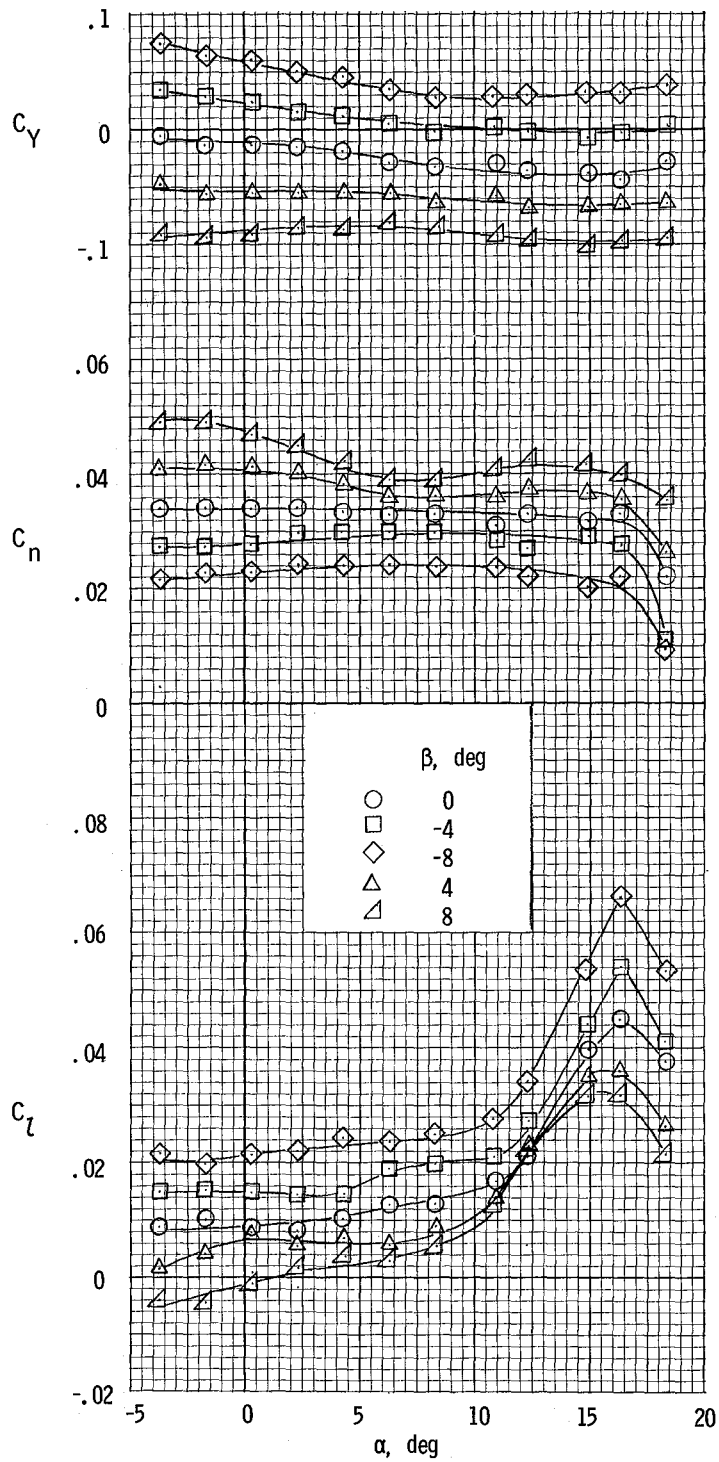
(a) Left engine full; right engine feathered.

Figure 21.- Lateral characteristics of airplane with asymmetric power. $\delta_f = 0^0$.
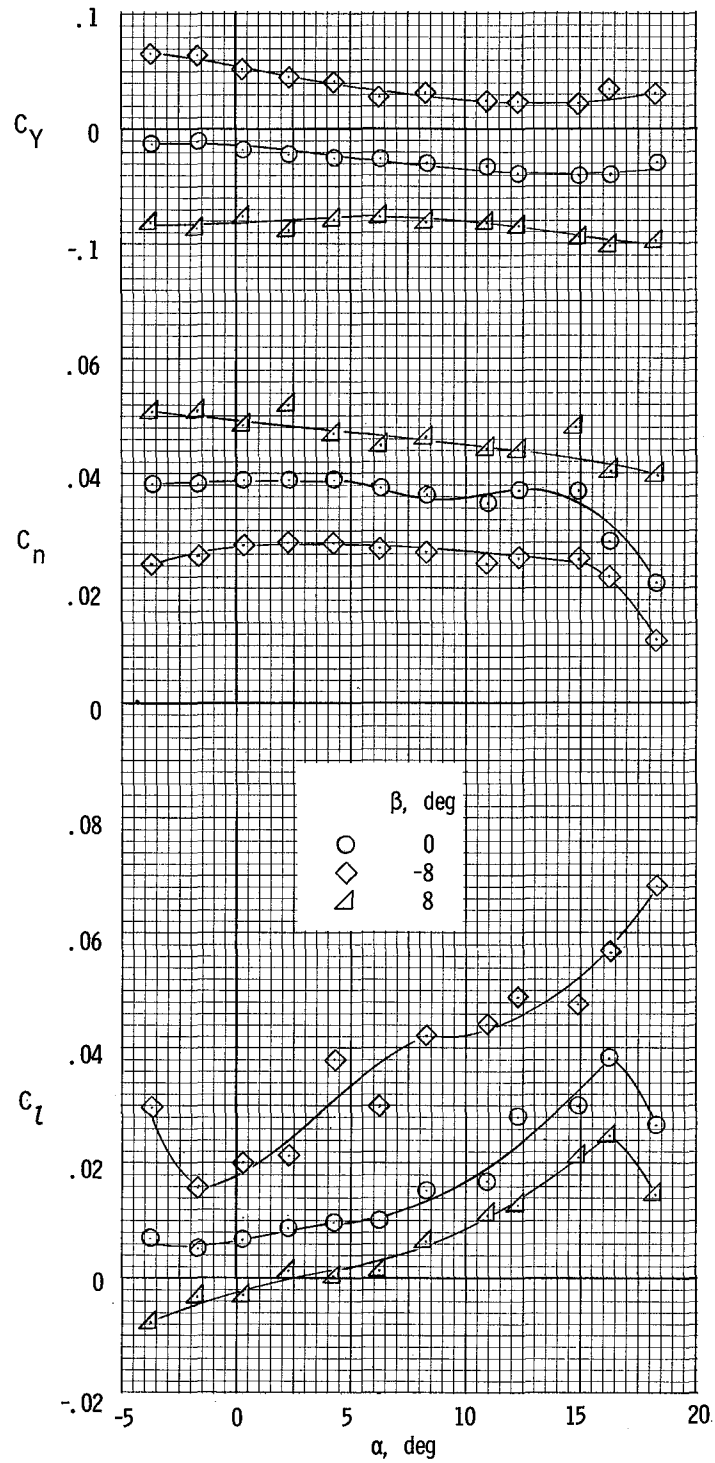
(b) Left engine full; right engine windmilling.

Figure 21.- Concluded.
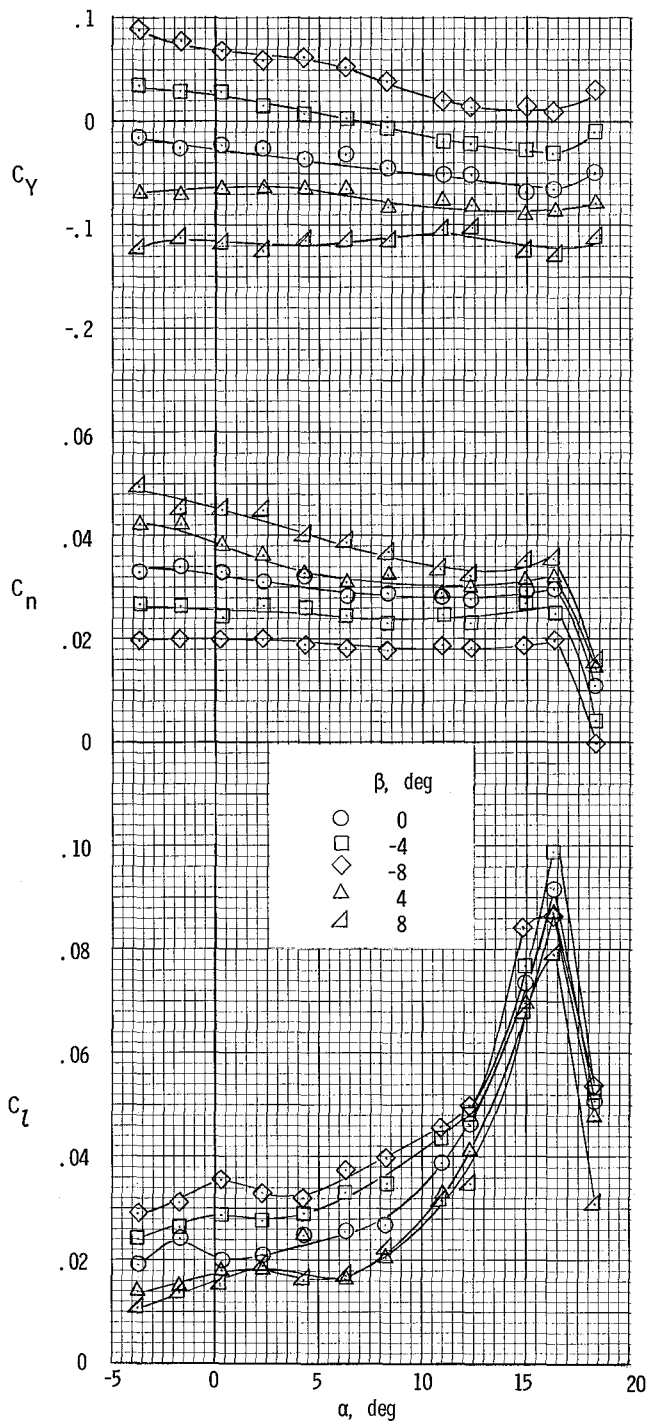
(a) Left engine full; right engine feathered.

Figure 22.- Lateral characteristics of airplane with asymmetric power. $\delta_f = 27°$.
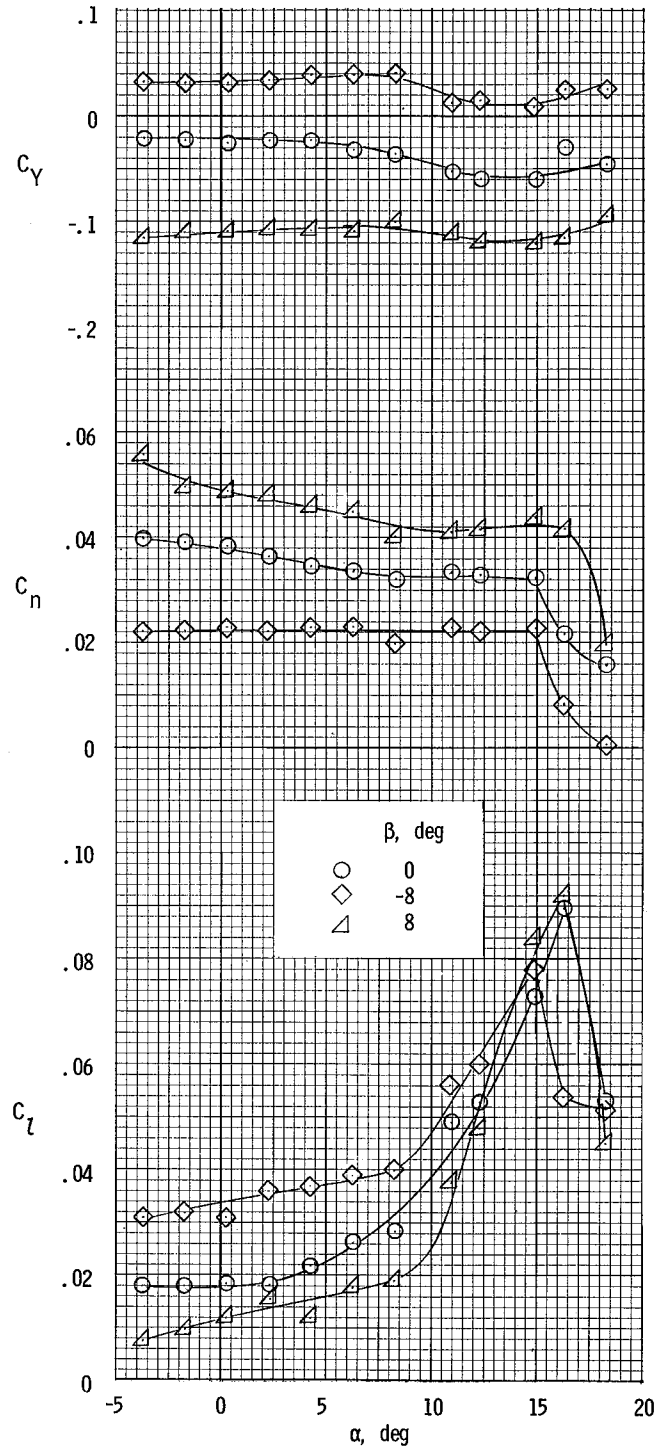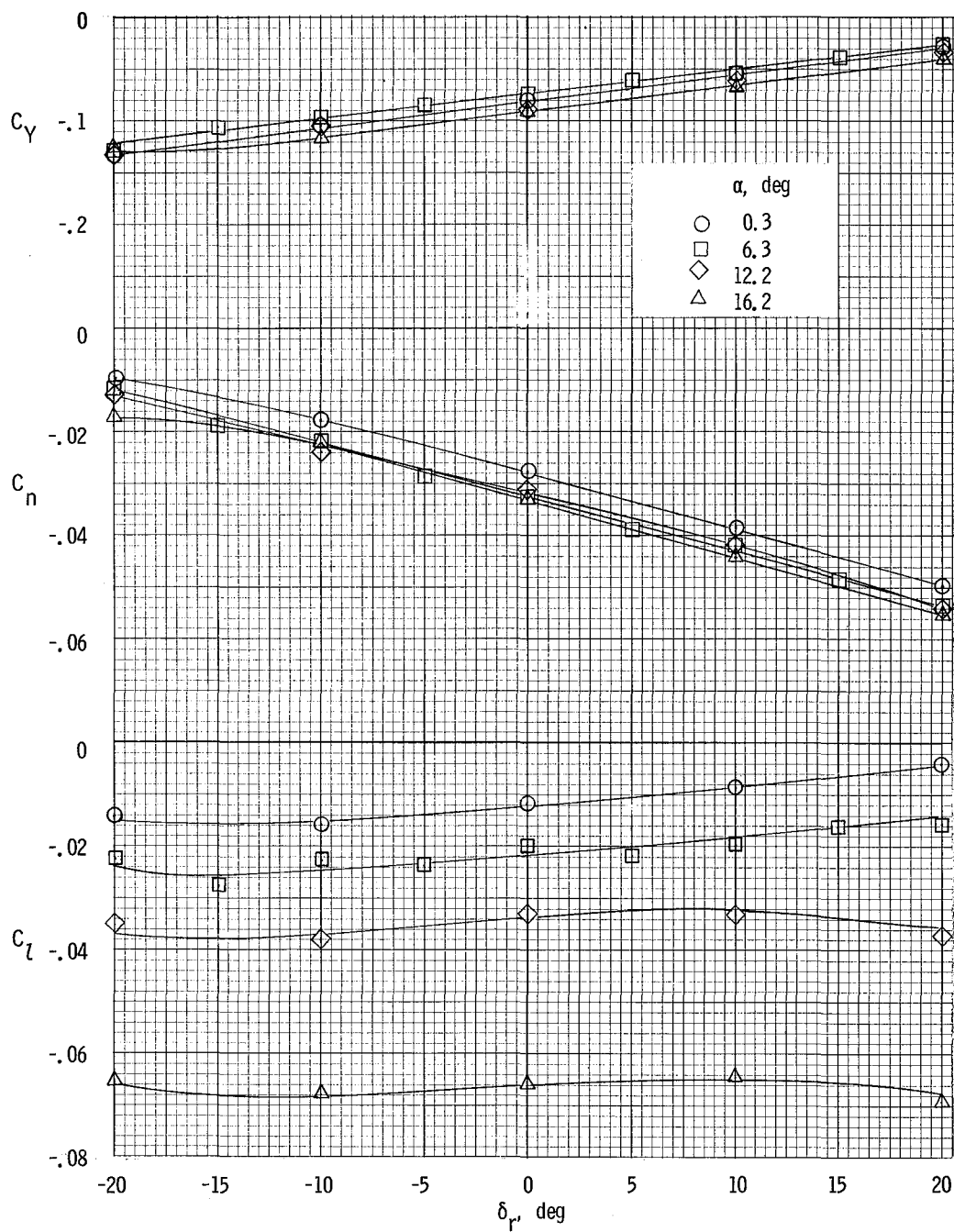
(b) Left engine full; right engine windmilling.

Figure 22.- Concluded.
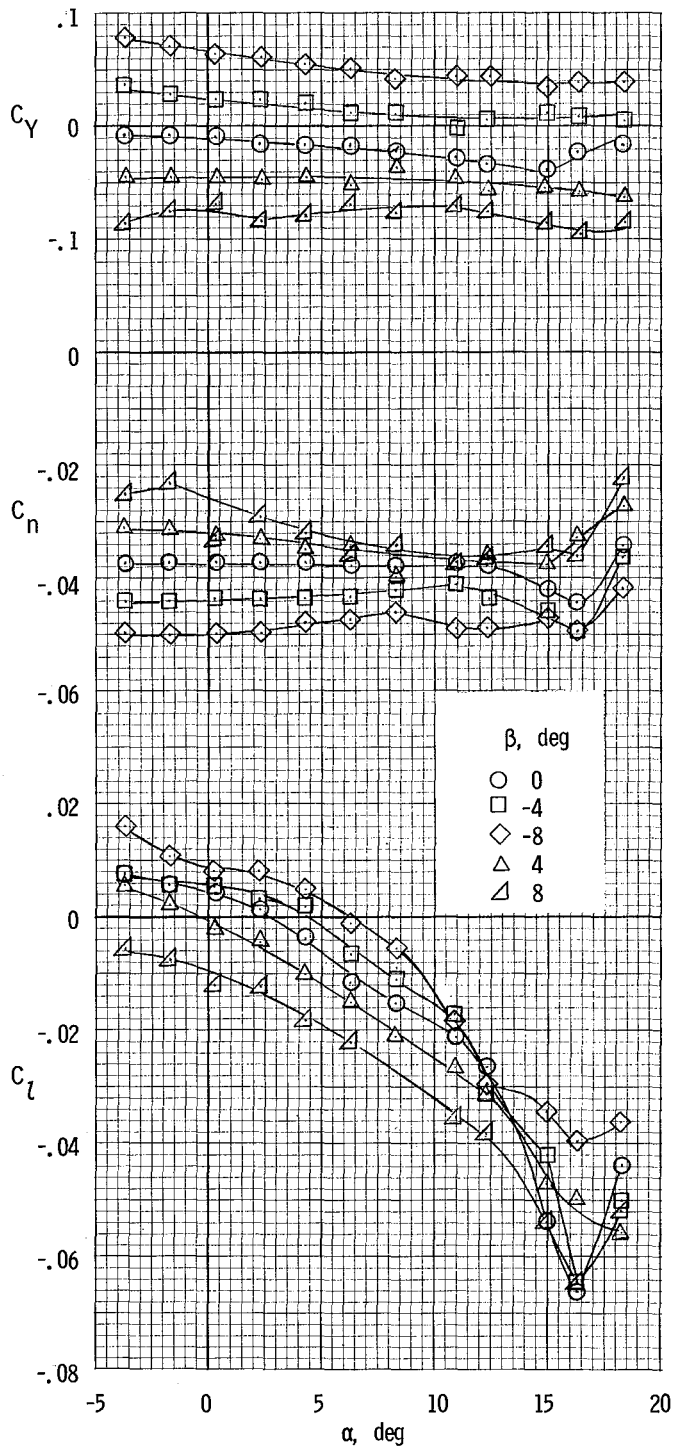
(a) Right engine full; left engine feathered.

Figure 23.- Lateral characteristics of airplane with asymmetric power. $\delta_f = 0^0$.
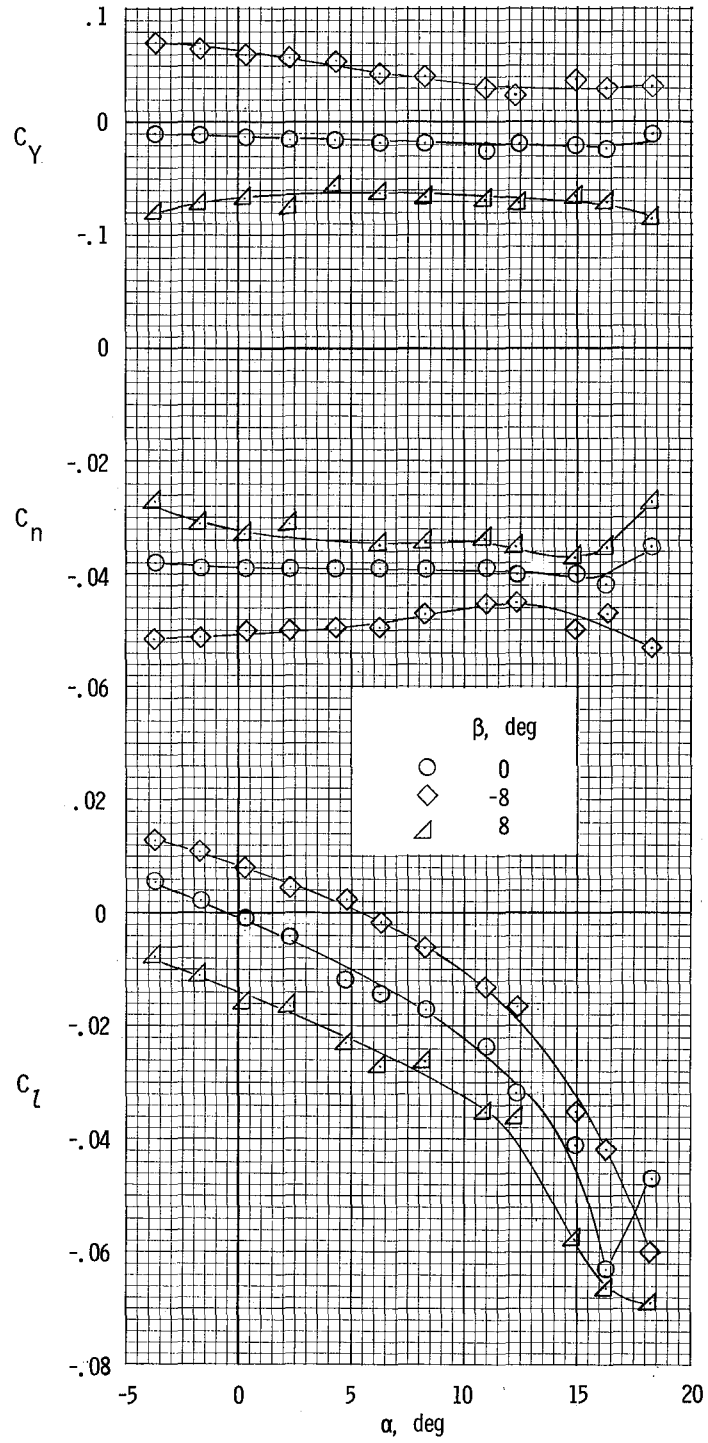
(b) Right engine full; left engine windmilling.

Figure 23.- Concluded.
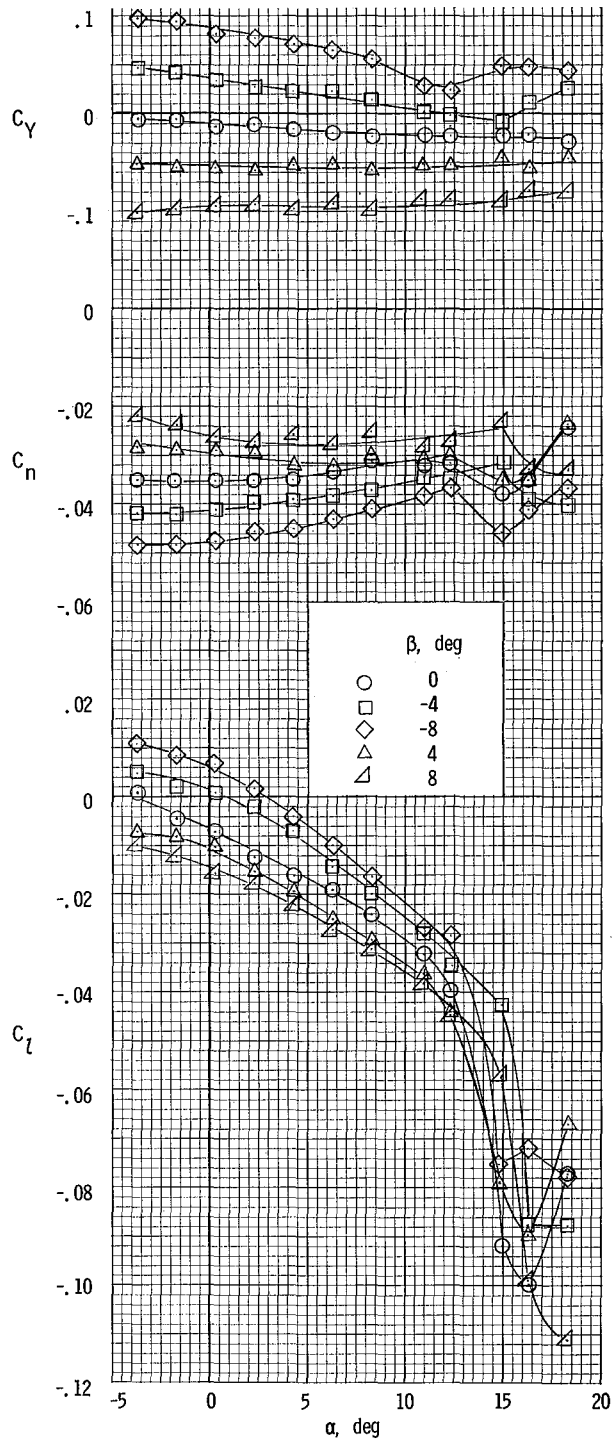
(a) Right engine full; left engine feathered.

Figure 24.- Lateral characteristics of airplane with asymmetric power. $\delta_f = 27^0$.
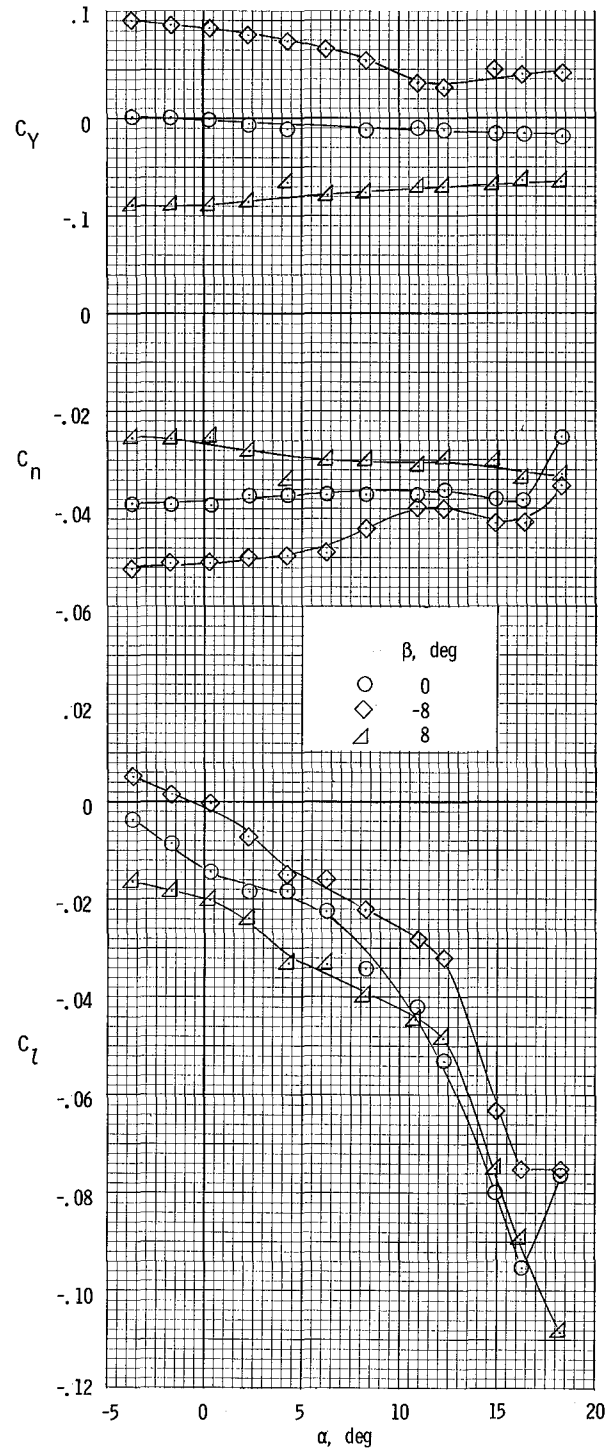
(b) Right engine full; left engine windmilling.

Figure 24.- Concluded.

(a) $\beta = 8^0$.
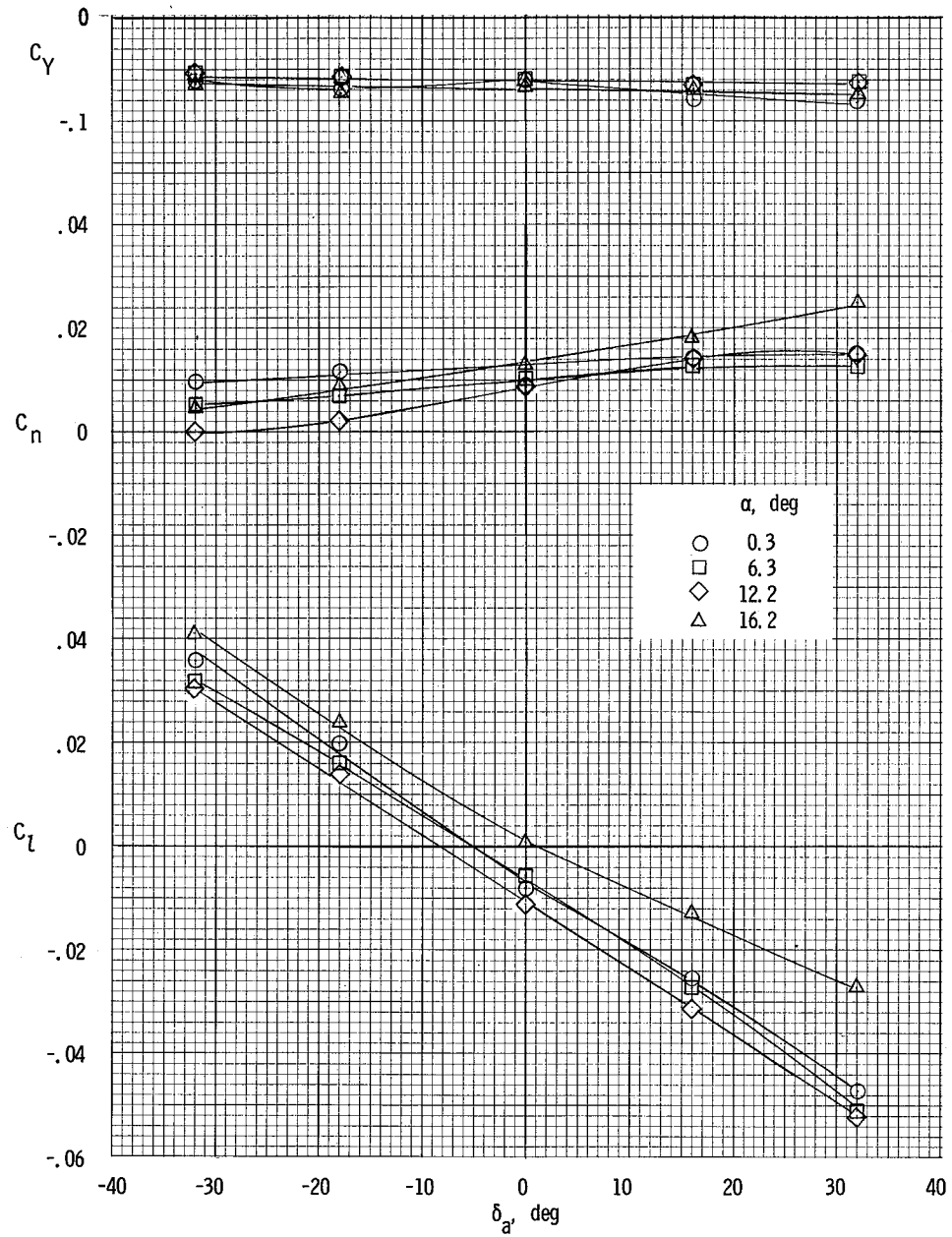
Figure 25.- Variation of lateral characteristics of airplane with aileron deflection. $\delta_f = 0^0$; $T'_c = 0$.
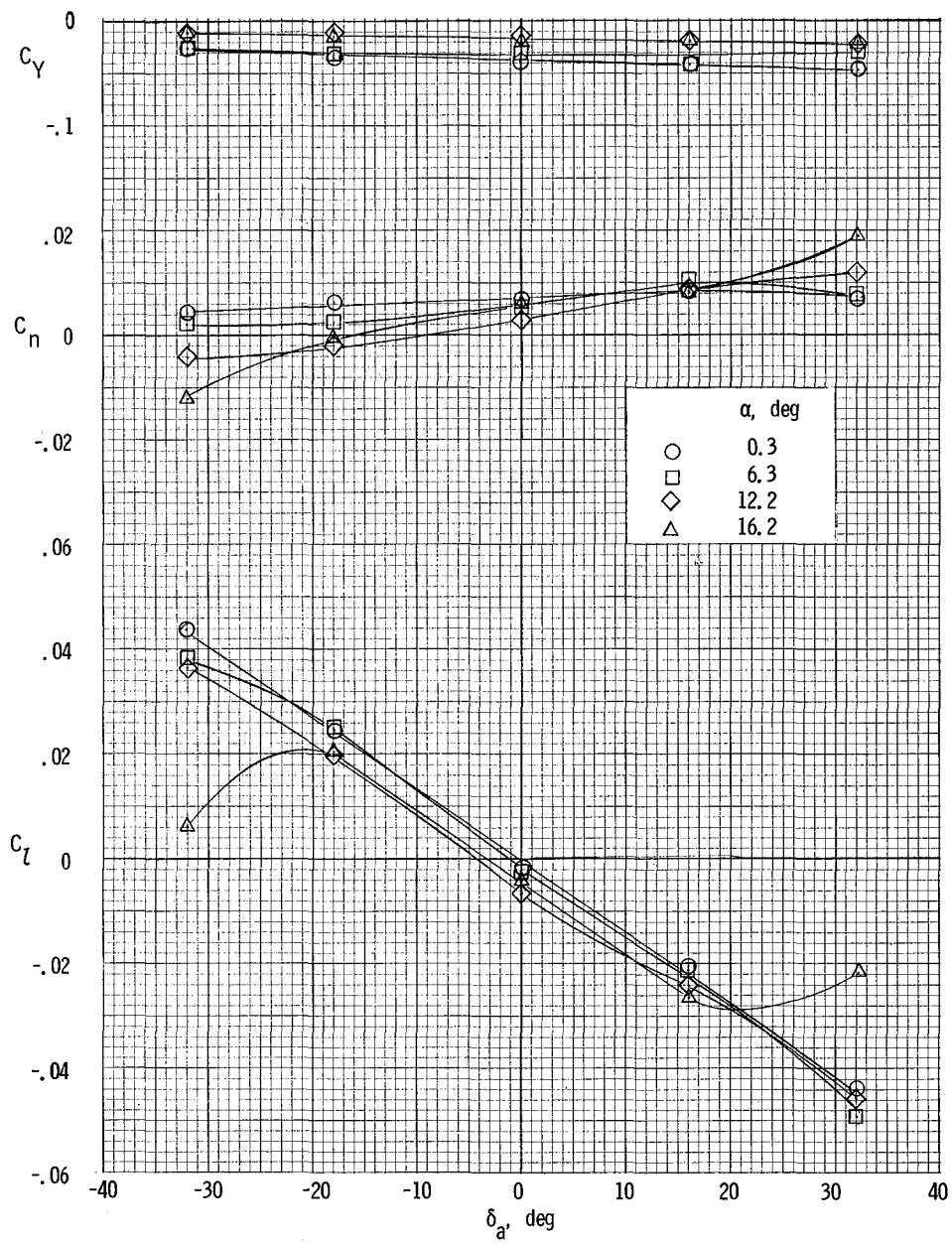
(b) $\beta = 4°$.

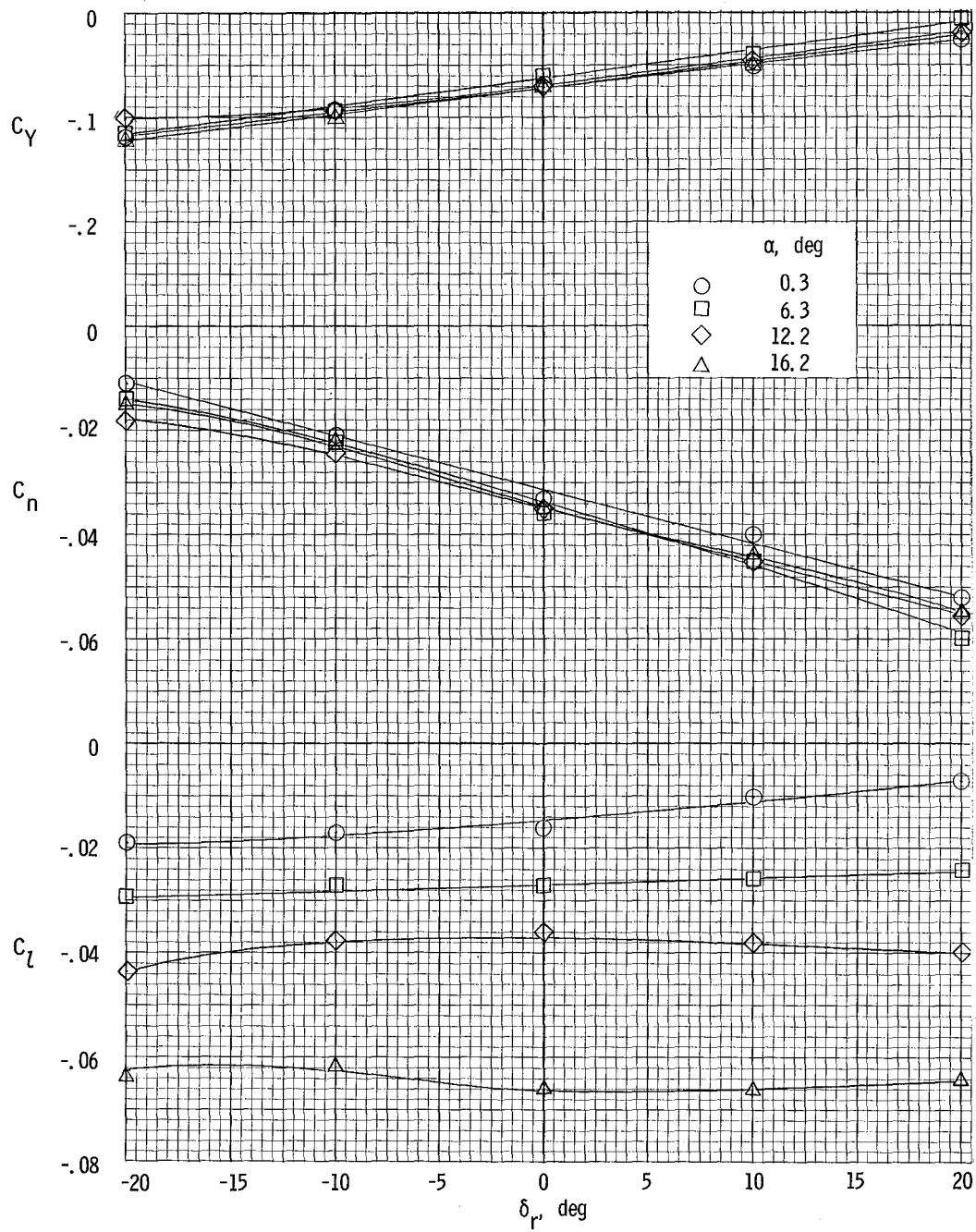Figure 25.- Continued.
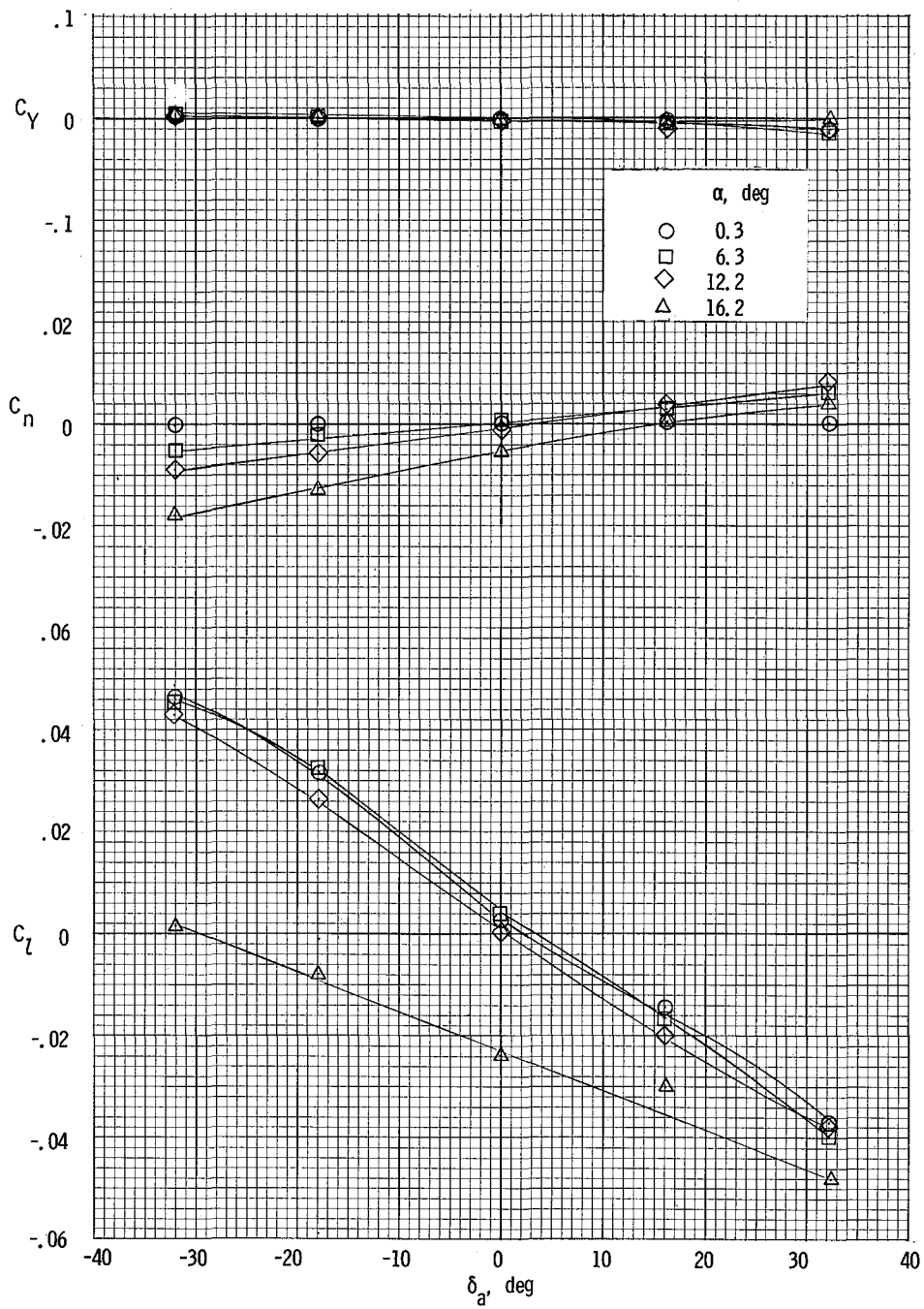
(c) $\beta = 0°$.

Figure 25.- Continued.

(d) β = -4°.
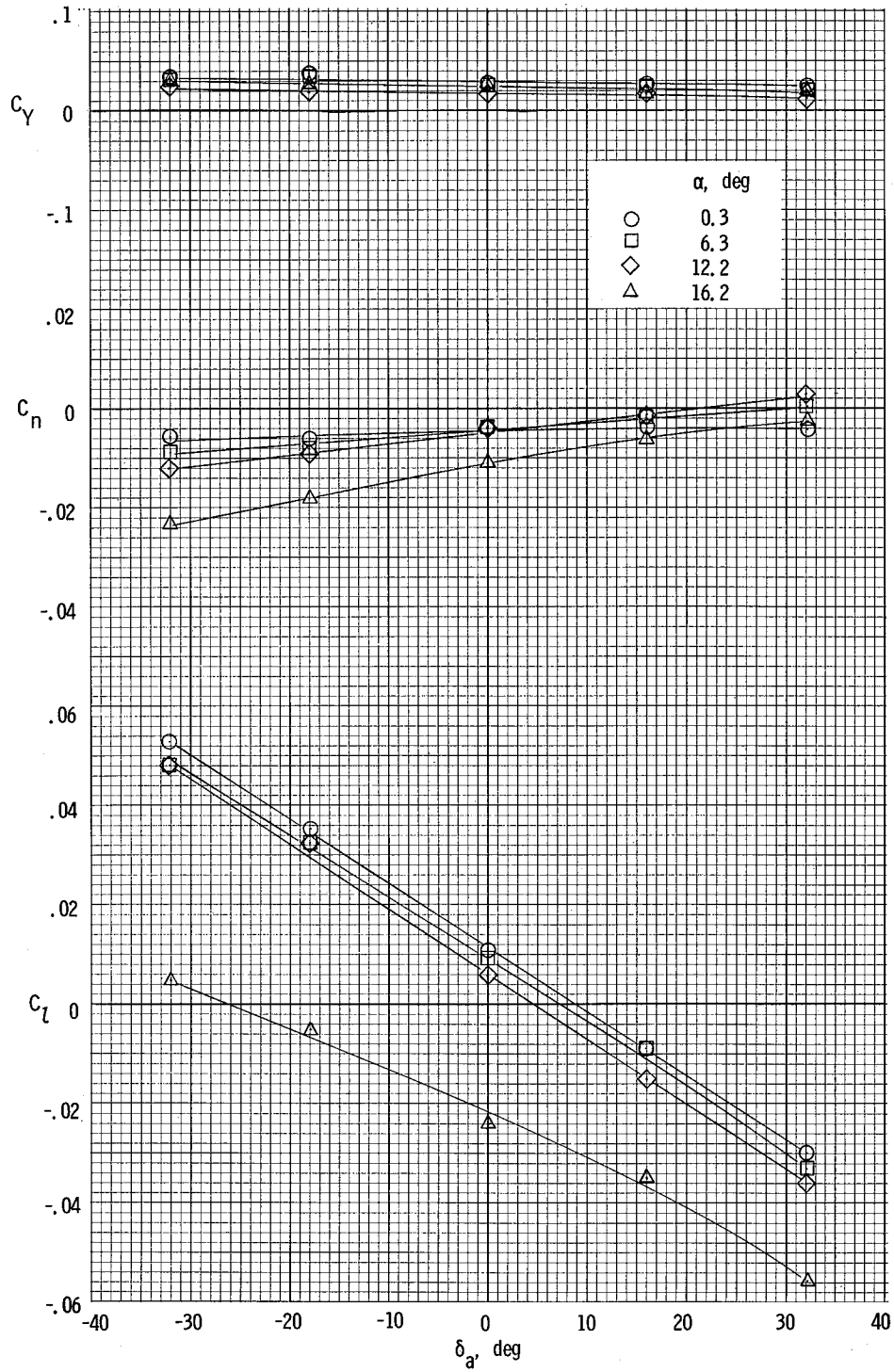
Figure 25.- Continued.
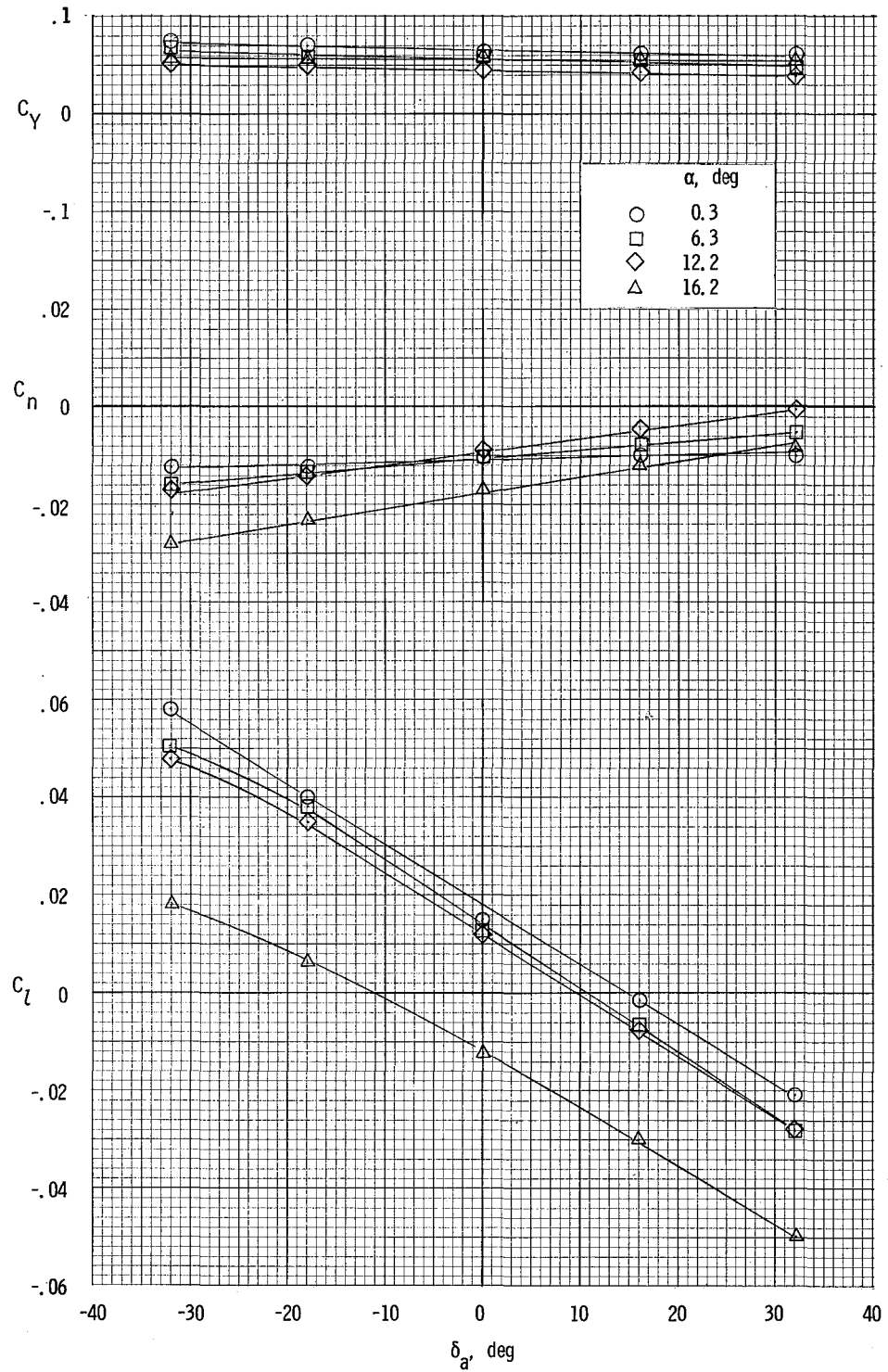
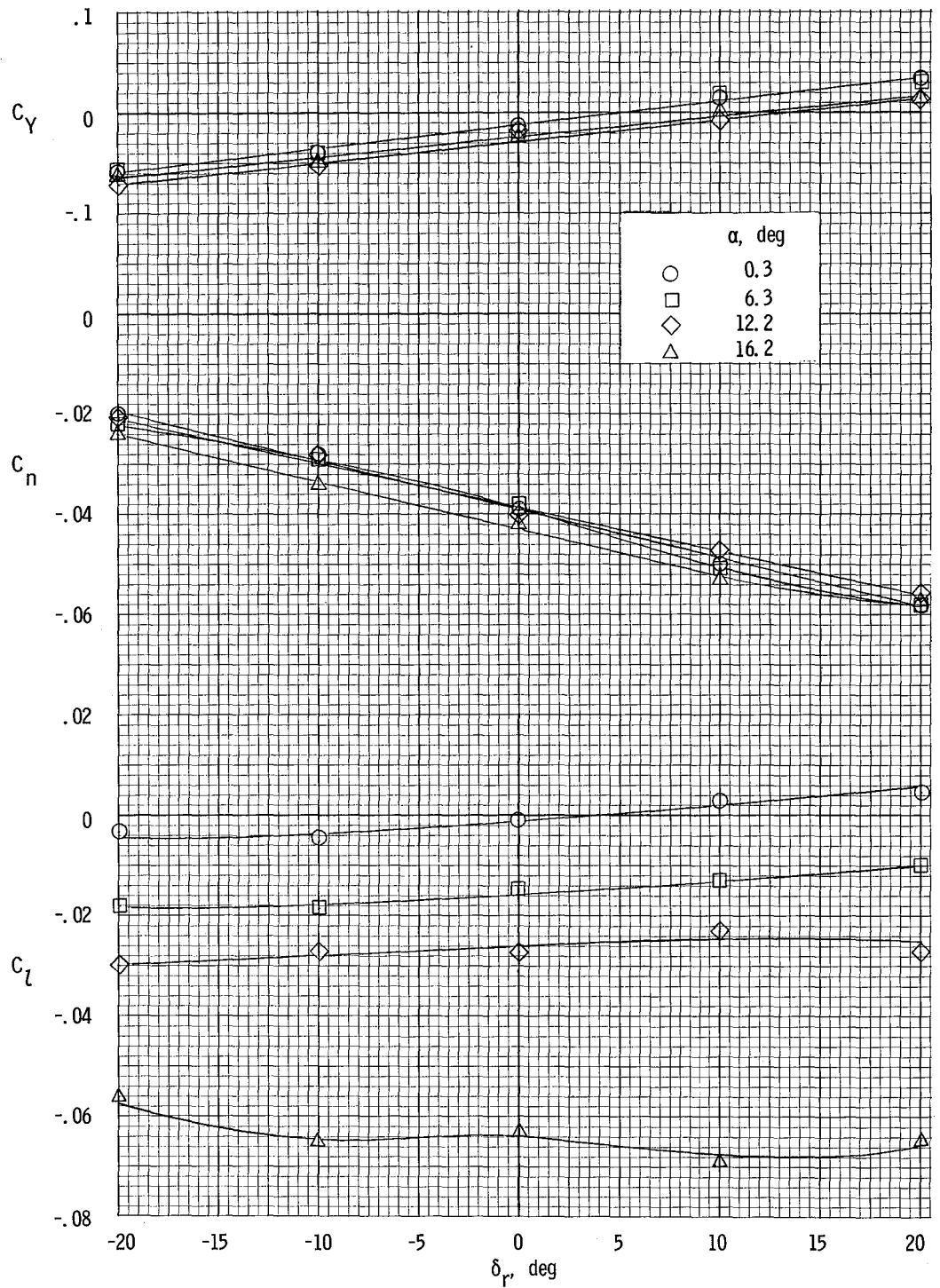(e) $\beta = -8^{\circ}$.

Figure 25.- Concluded.

(a) $\beta = 8^0$.
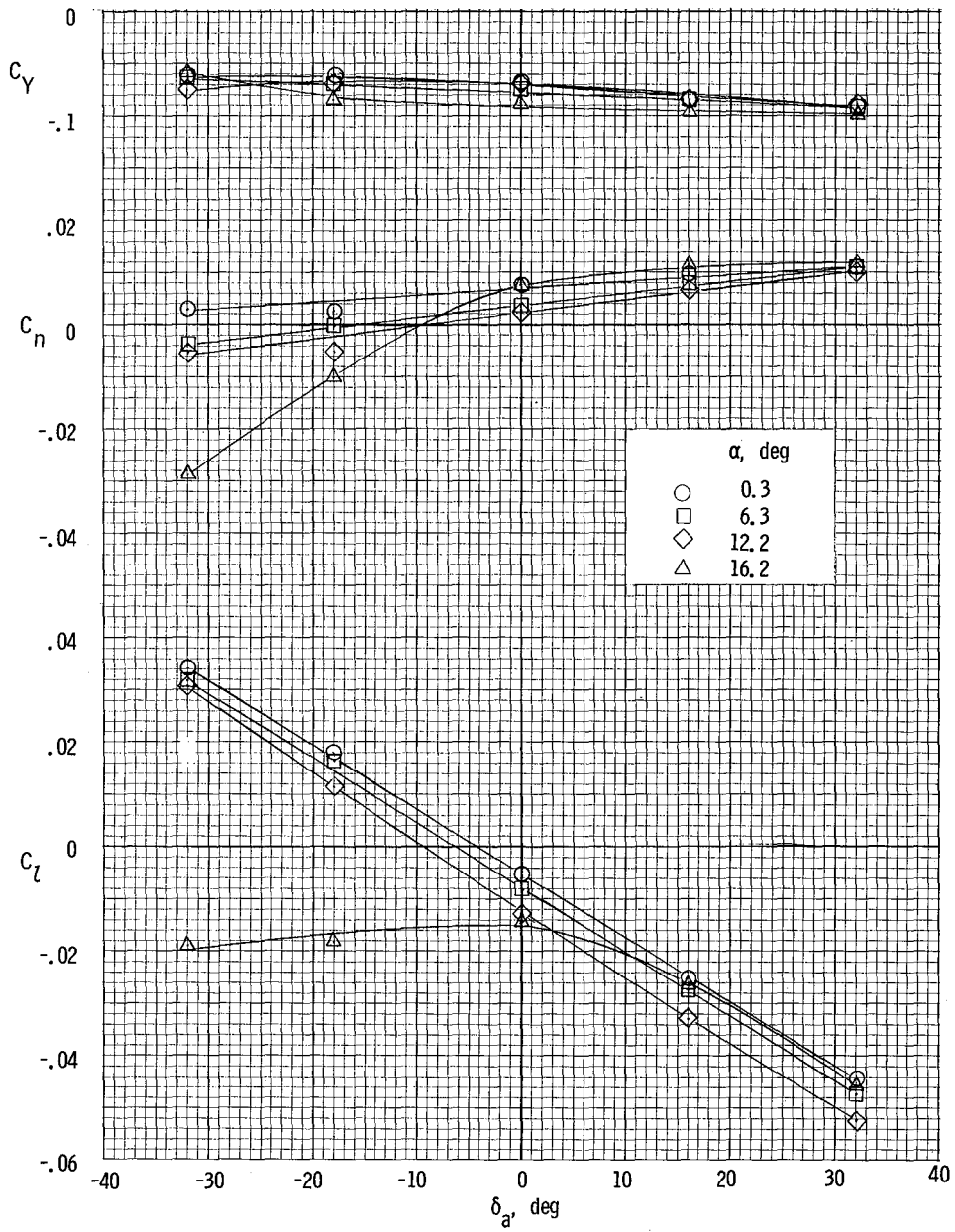
Figure 26.- Variation of lateral characteristics of airplane with aileron deflection. $\delta_f = 0^0$; $T'_c = 0.20$.

(b) $\beta = 4^0$.
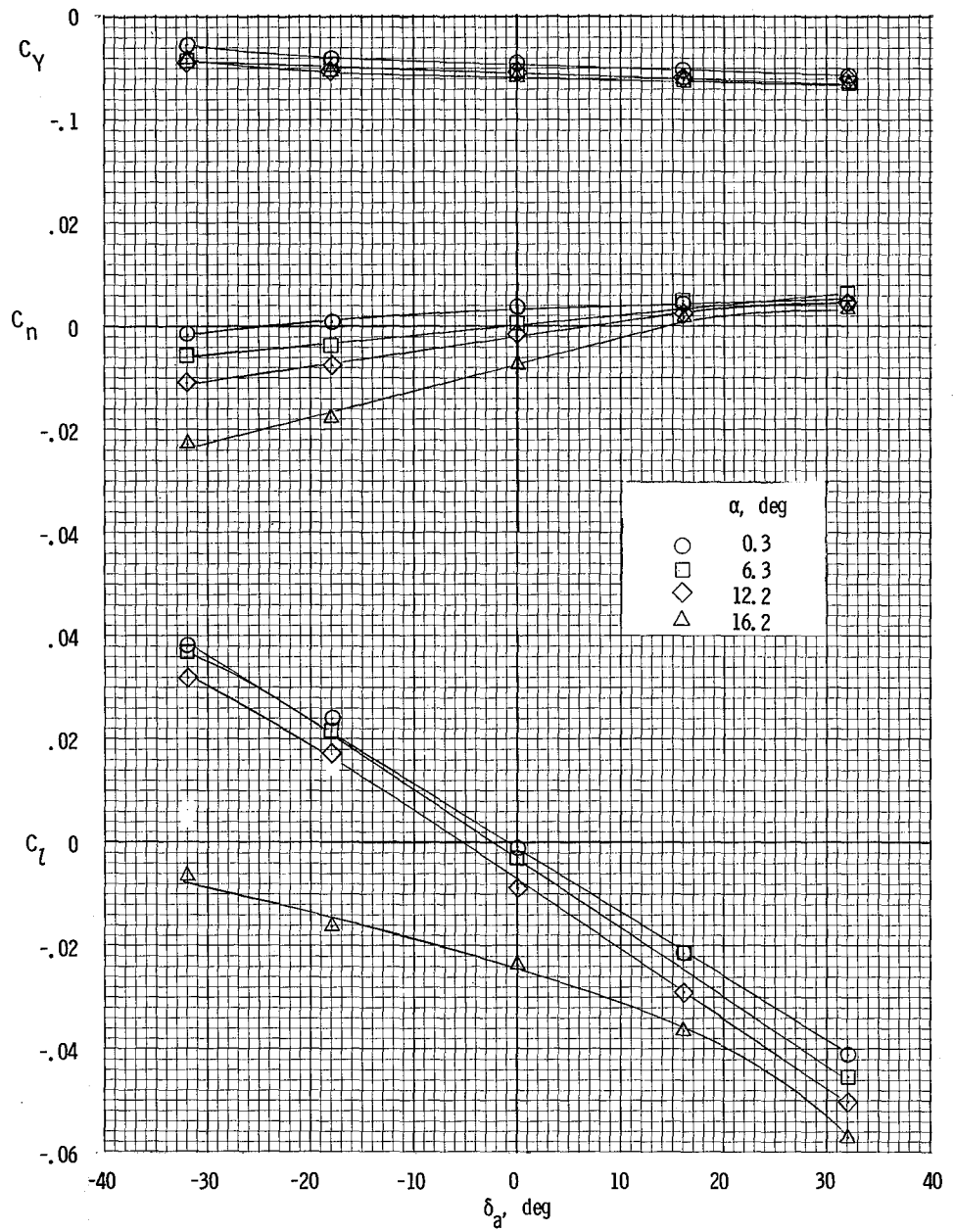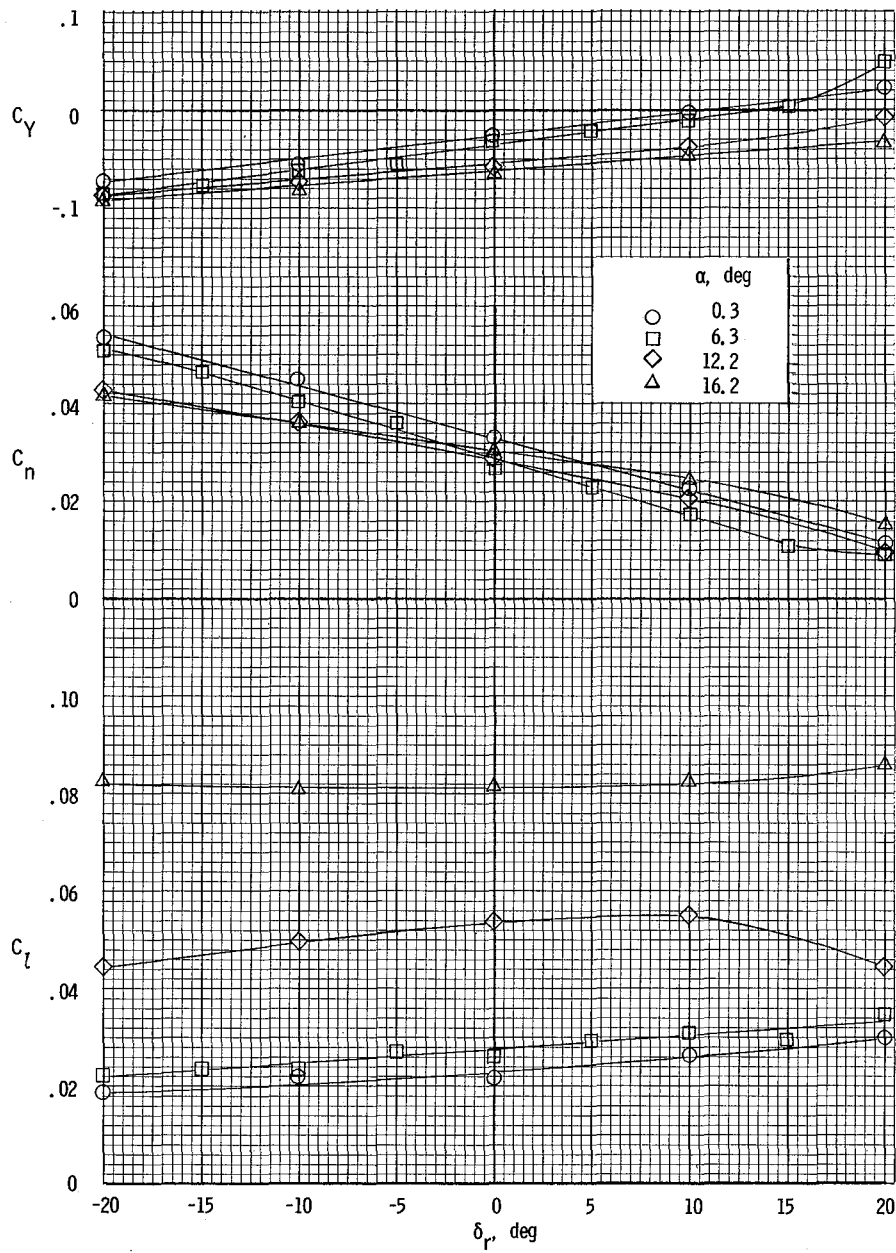
Figure 26.- Continued.

(c) β = 0°.
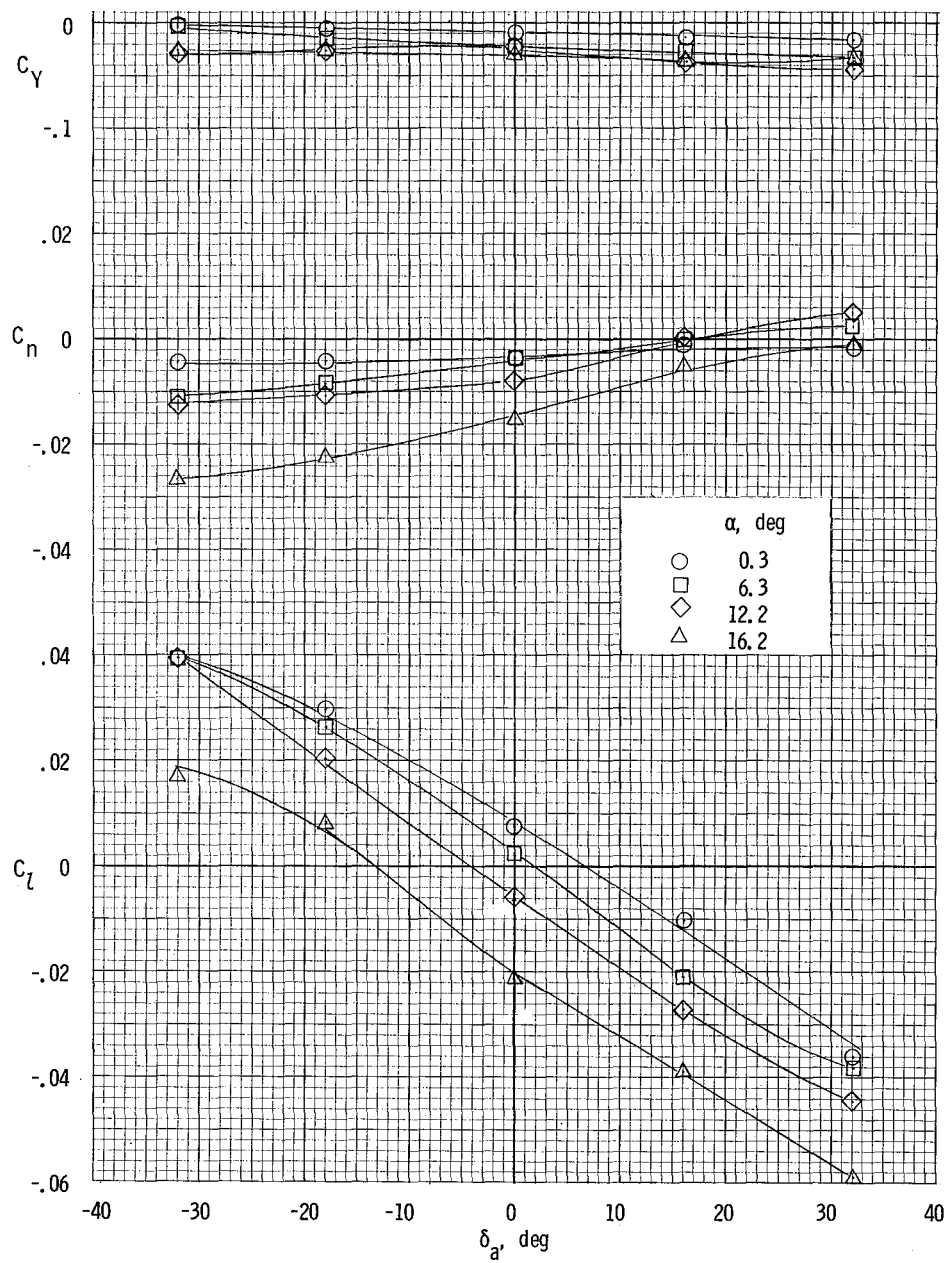
Figure 26.- Continued.
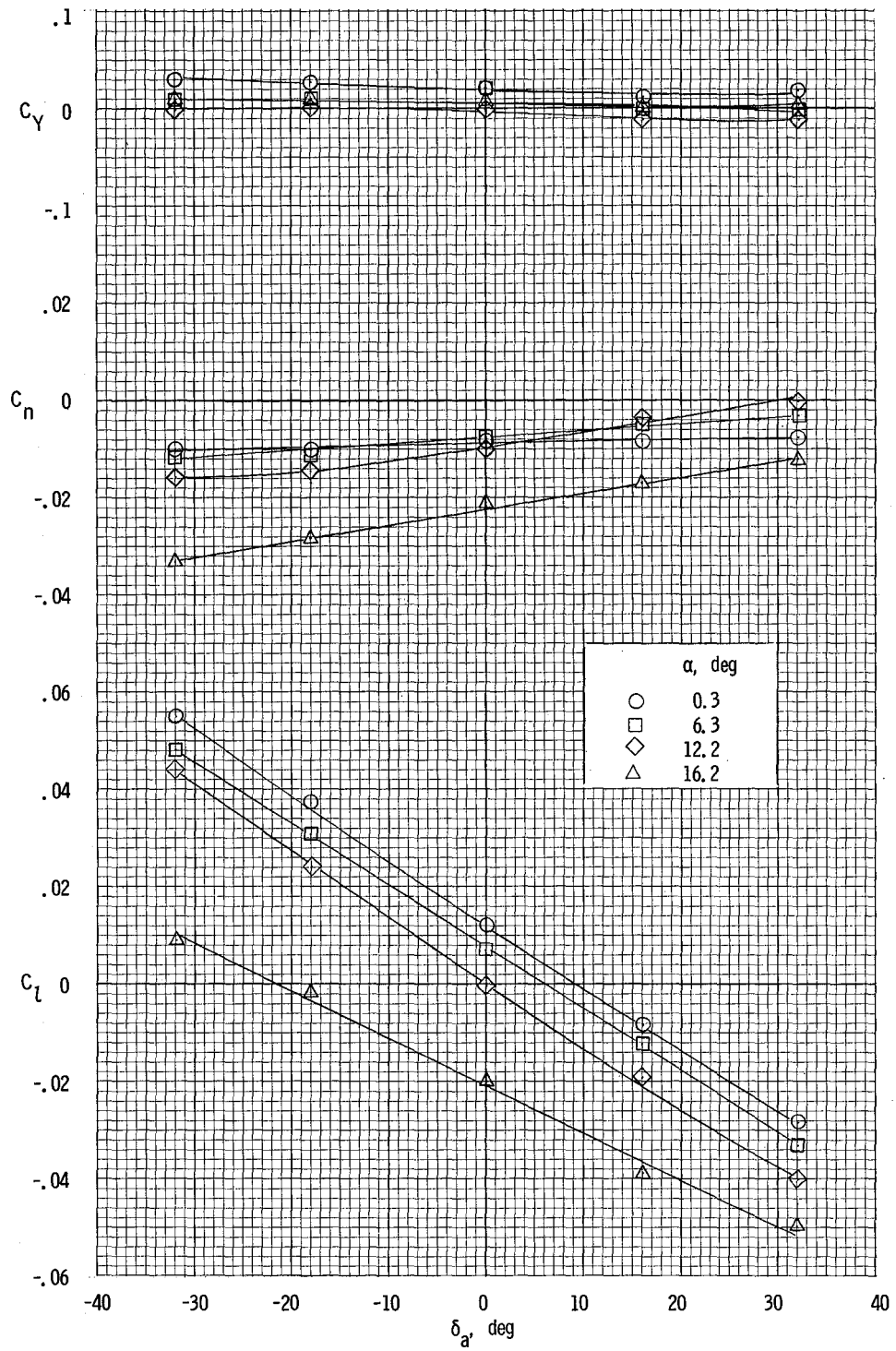
(d) $\beta = -4^{\circ}$.

Figure 26.- Continued.

74

(e) $\beta = -8^0$.
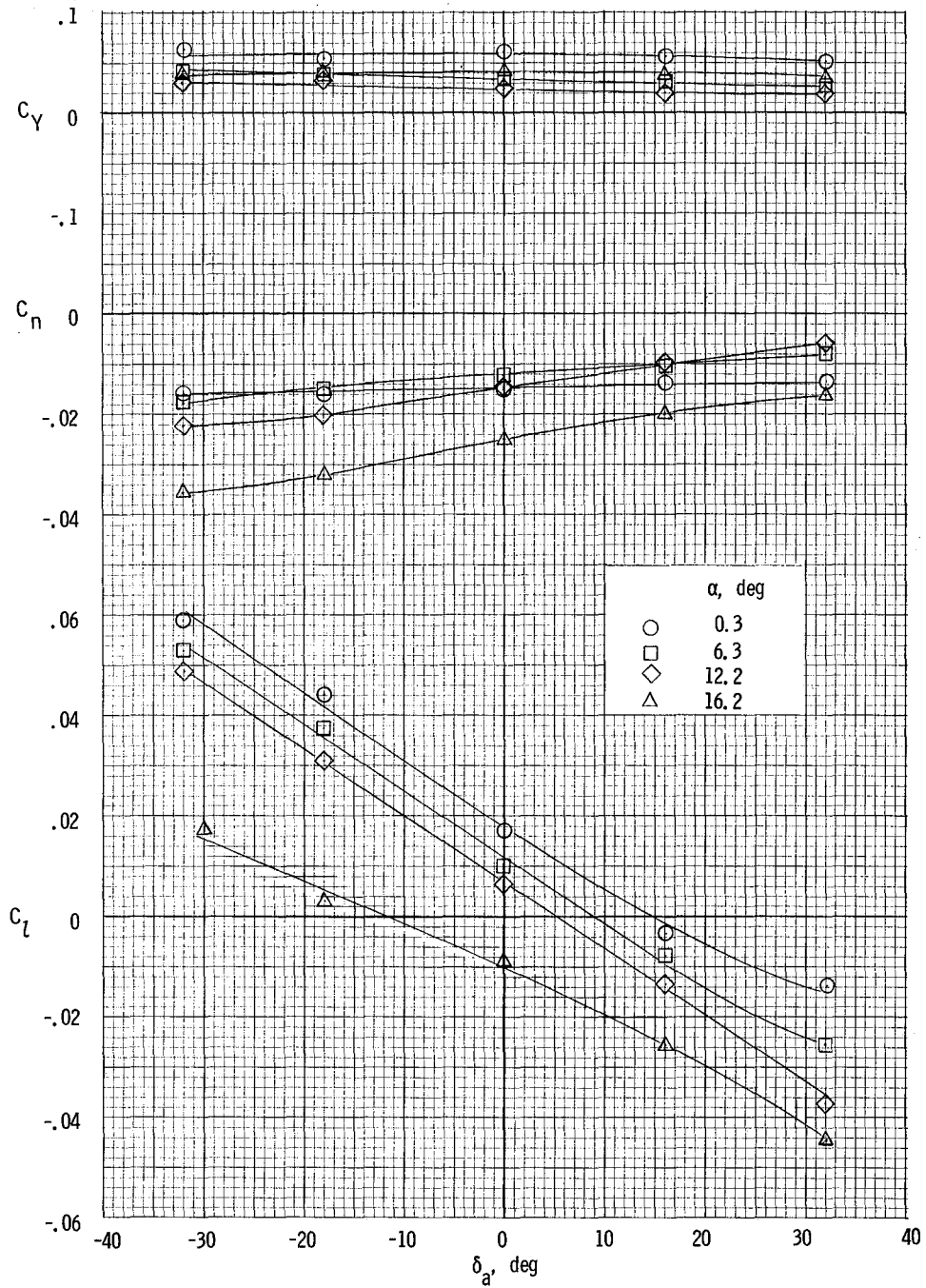
Figure 26.- Concluded.
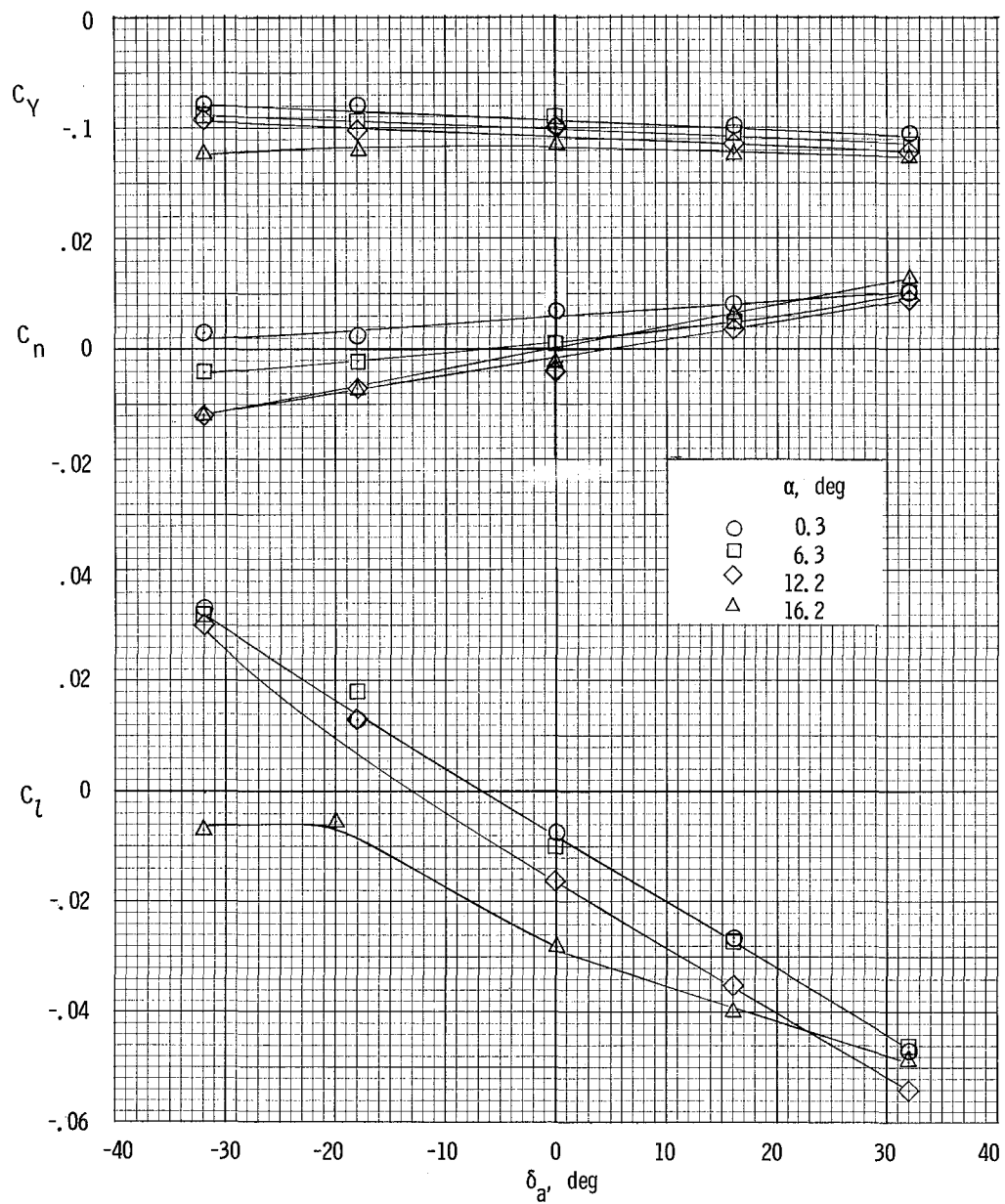
(a) β = 8°.

Figure 27.- Variation of lateral characteristics of airplane with aileron deflection. $\delta_f = 0°$; $T'_c = 0.44$.

(b) β = 4°.
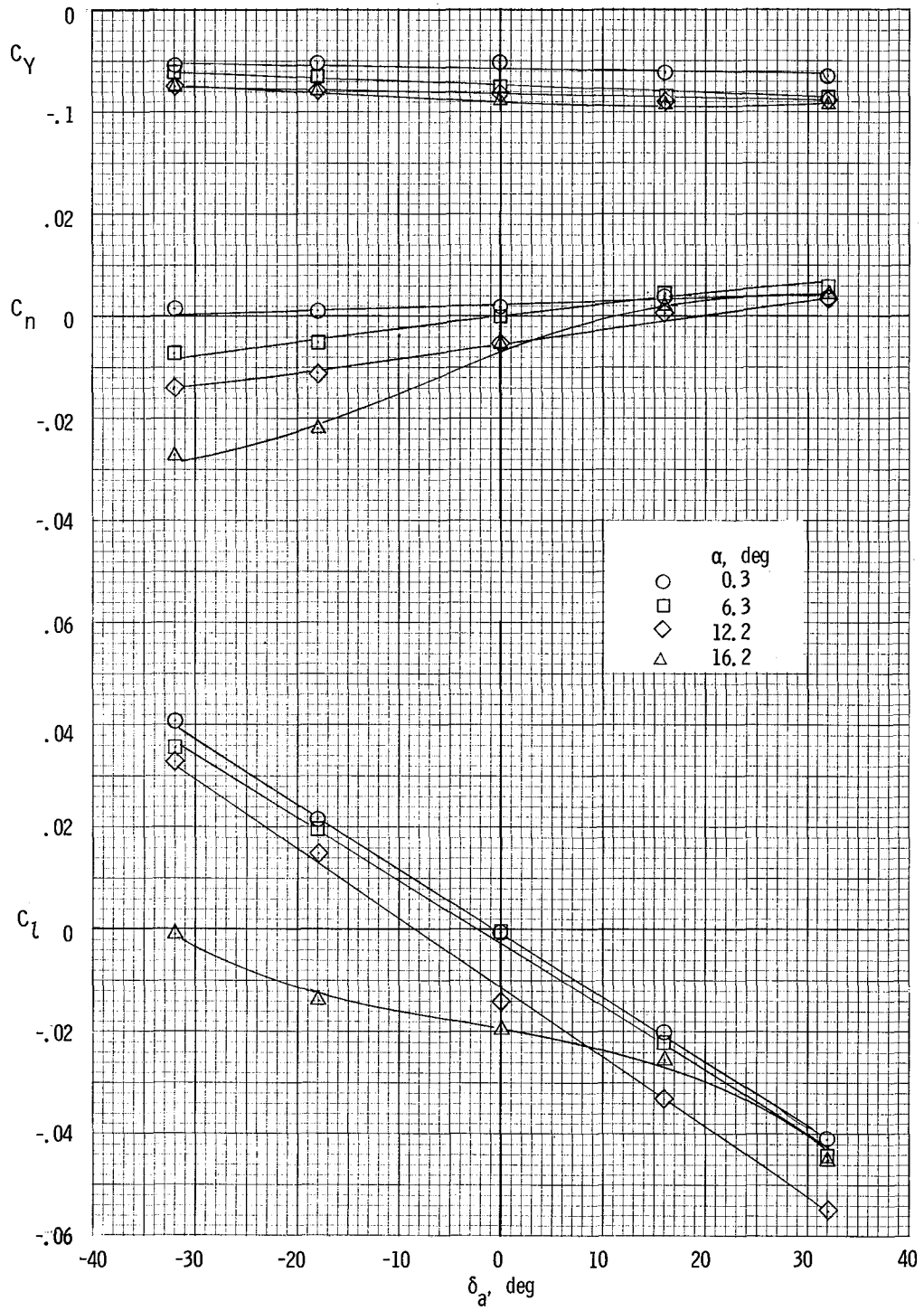
Figure 27.- Continued.
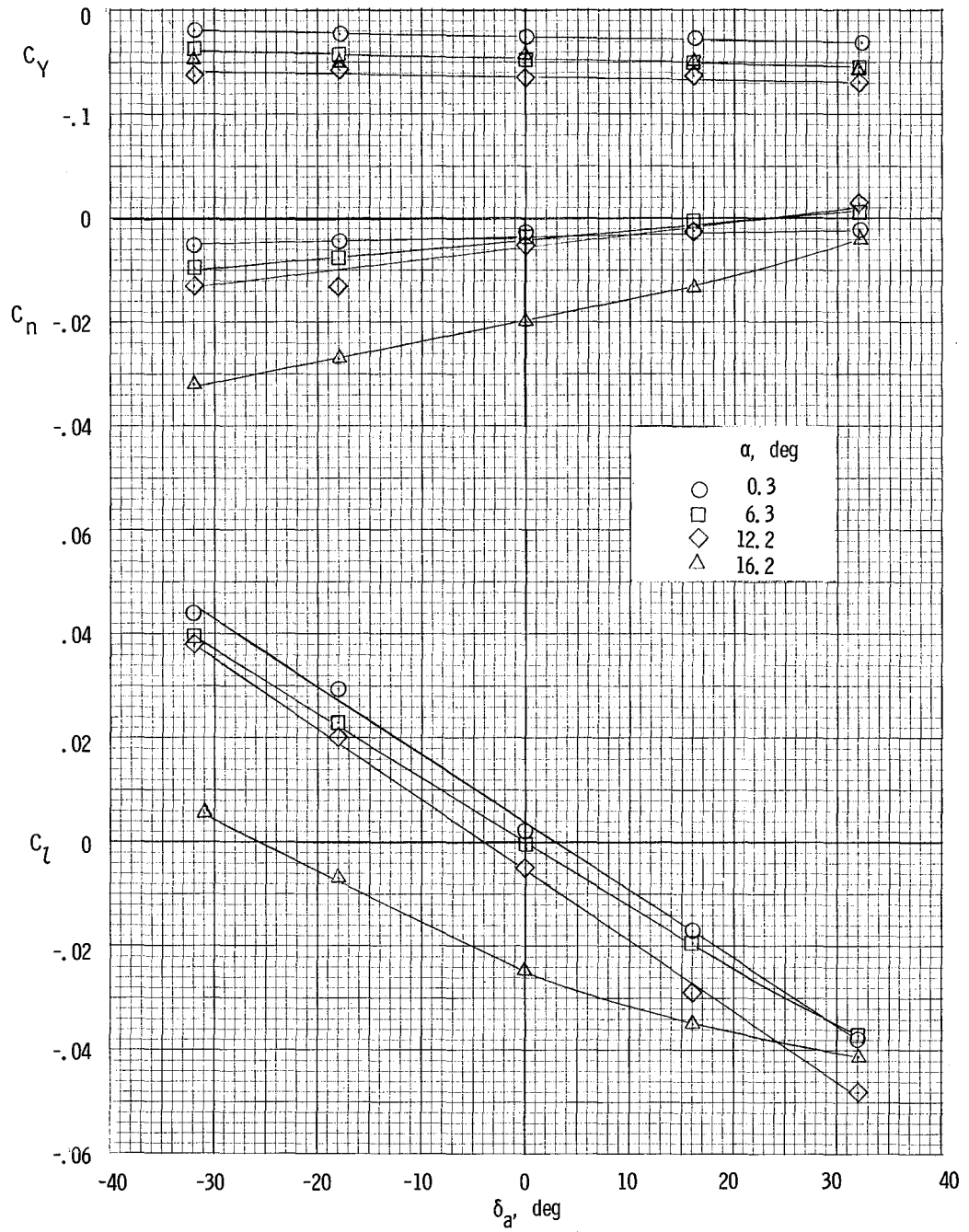
(c) β = 0⁰.

Figure 27.- Continued.
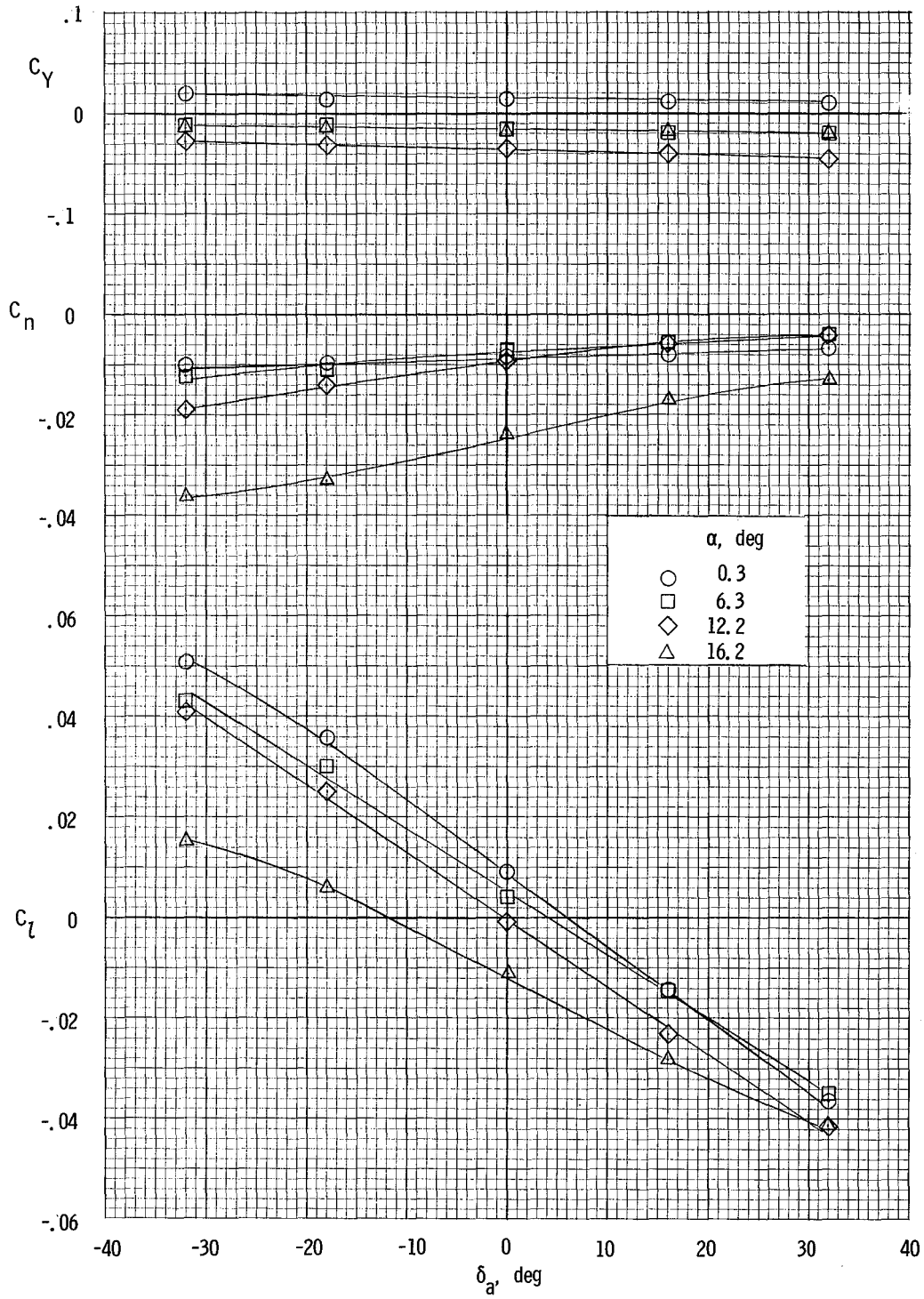
(d) $\beta = -4^\circ$.
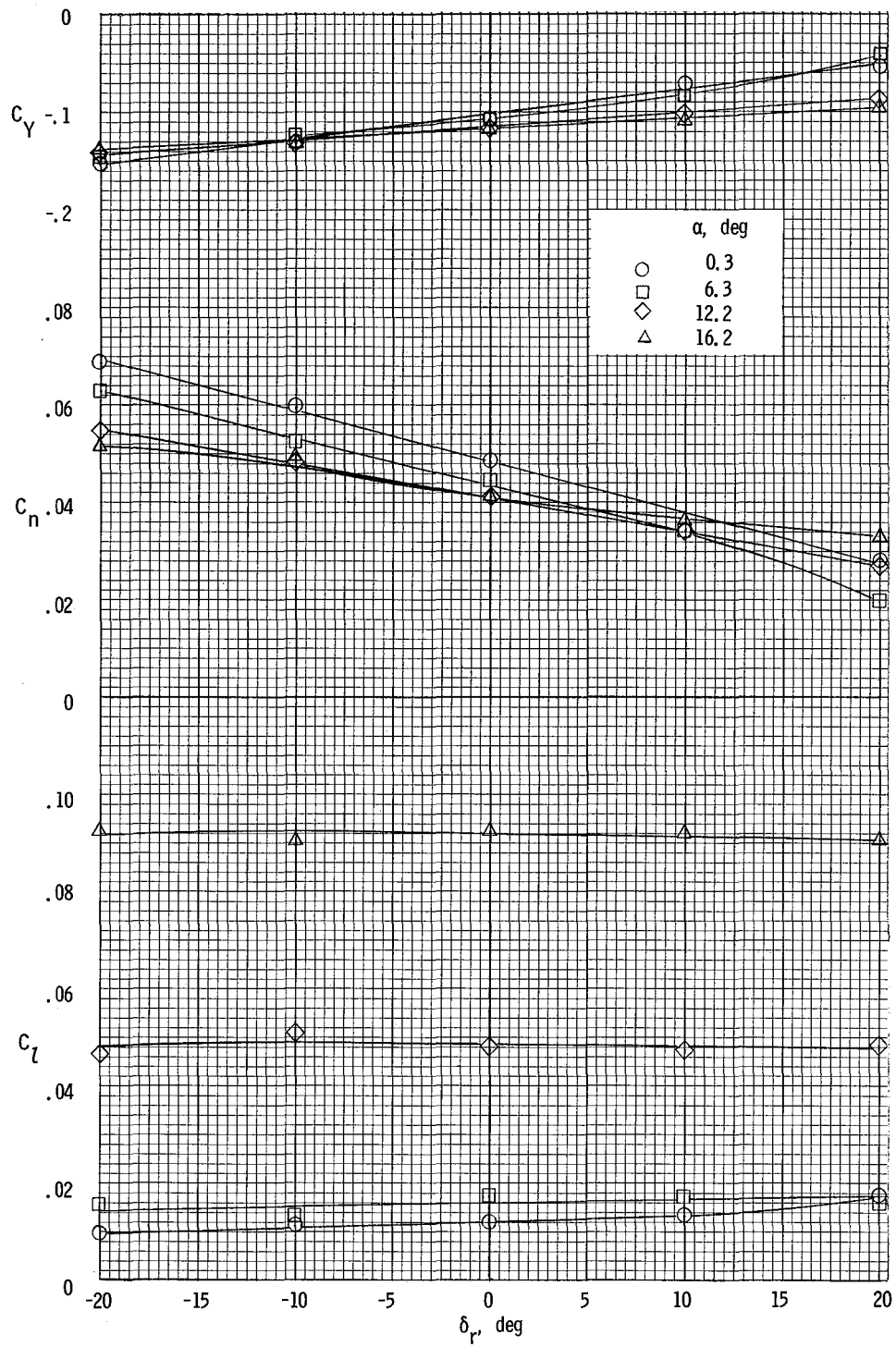
Figure 27.- Continued.

79
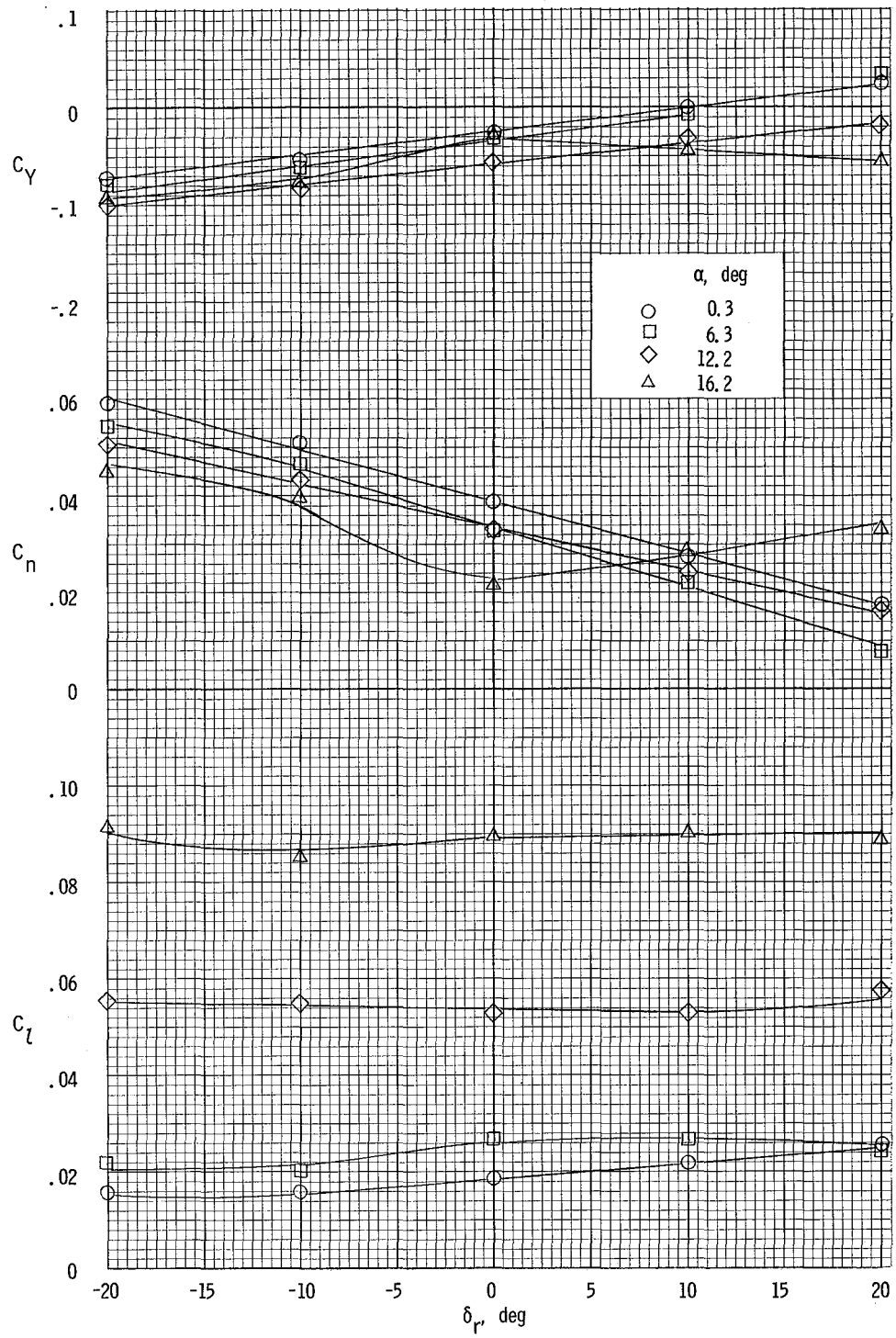
(e) $\beta = -8^0$.
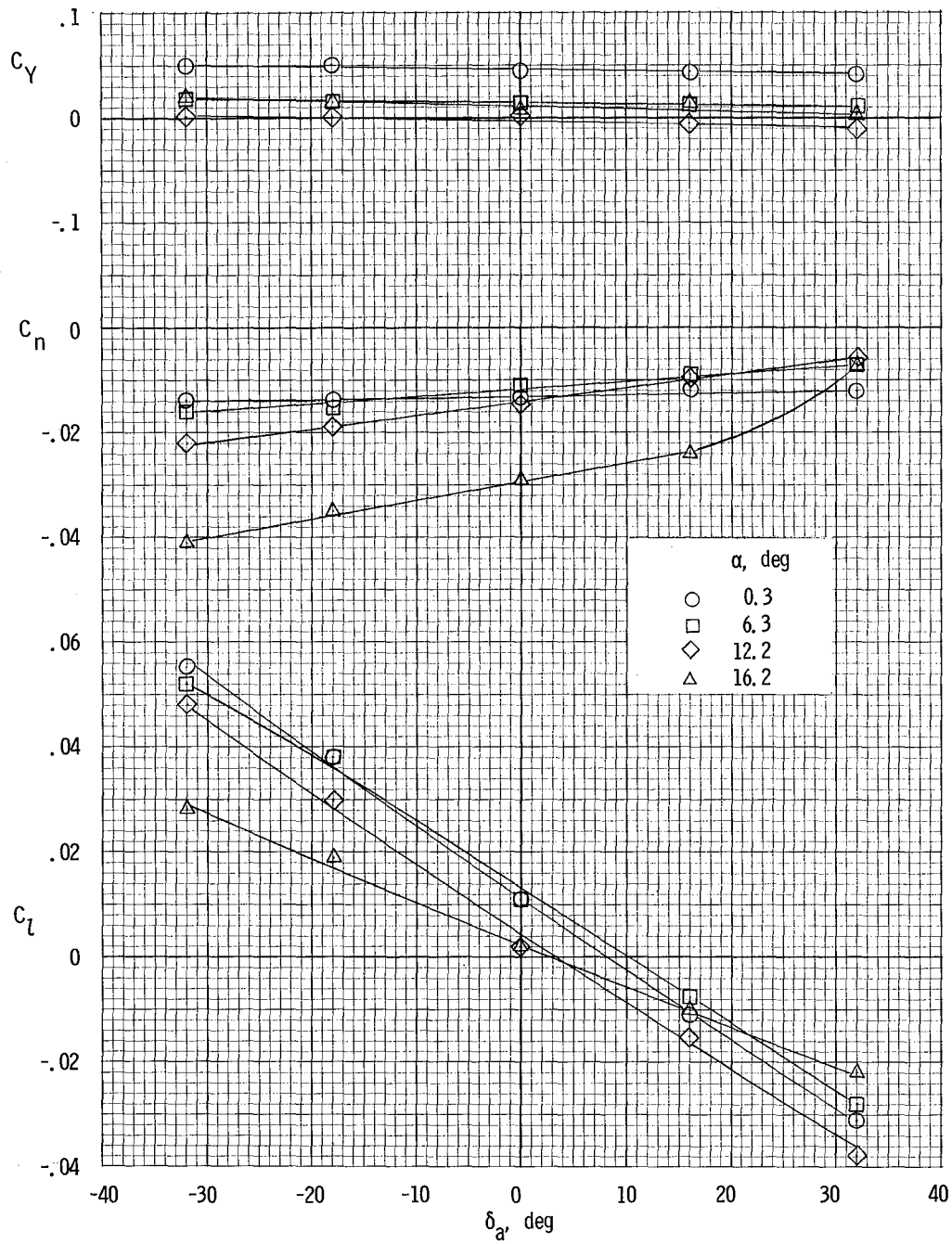
Figure 27.- Concluded.

(a) $\beta = 8^0$.
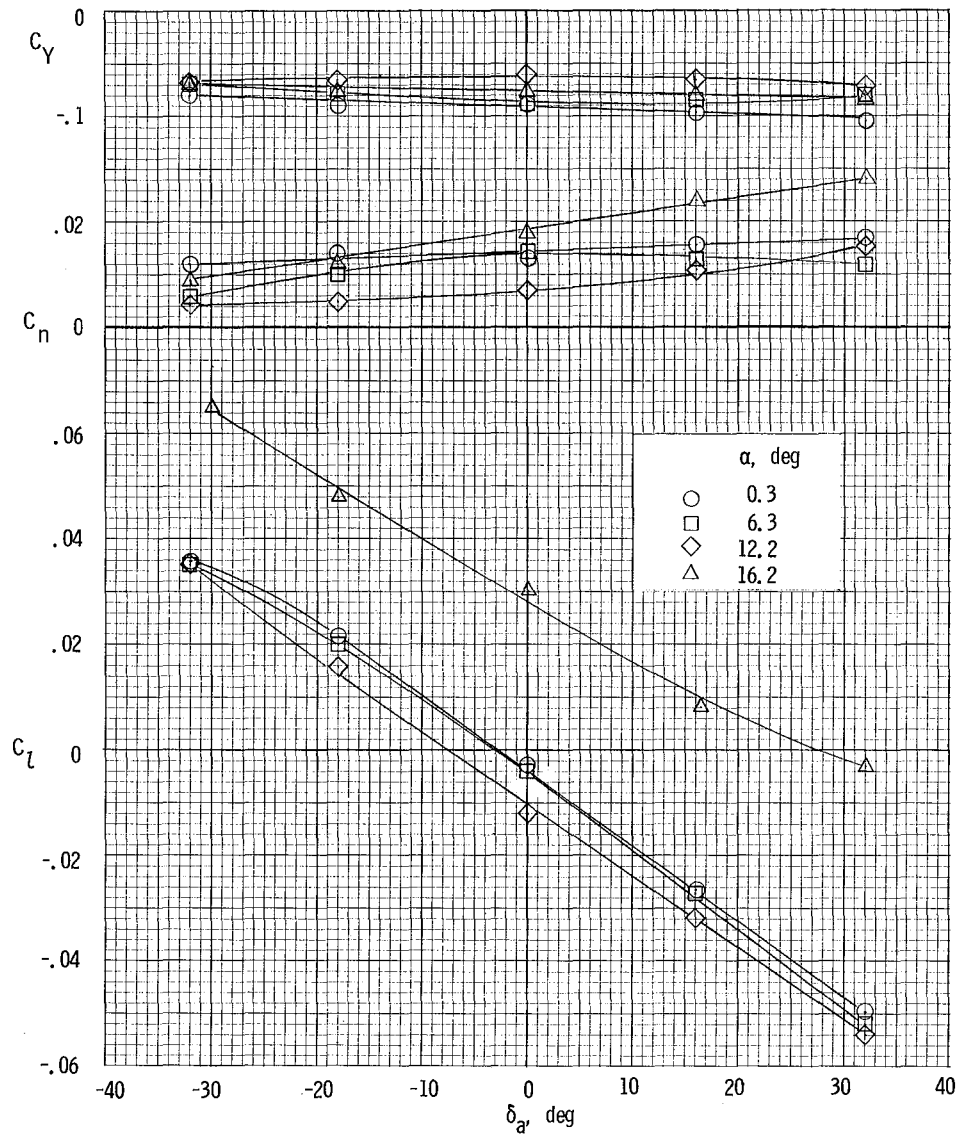
Figure 28.- Variation of lateral characteristics of airplane with aileron deflection. $\delta_f = 27^0$; $T_c' = 0$.

(b) $\beta = 4^0$.
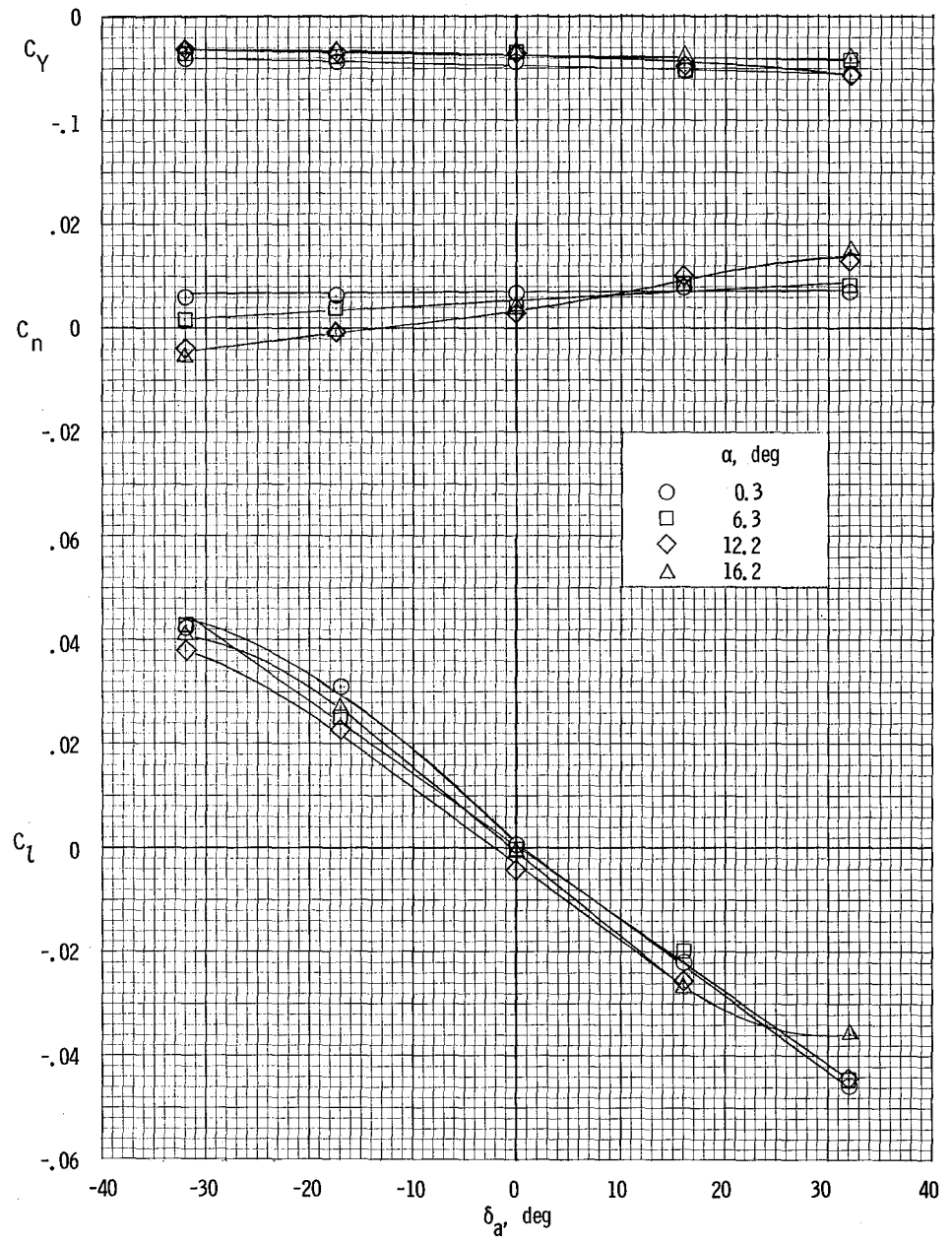
Figure 28.- Continued.

(c) $\beta = 0^0$.
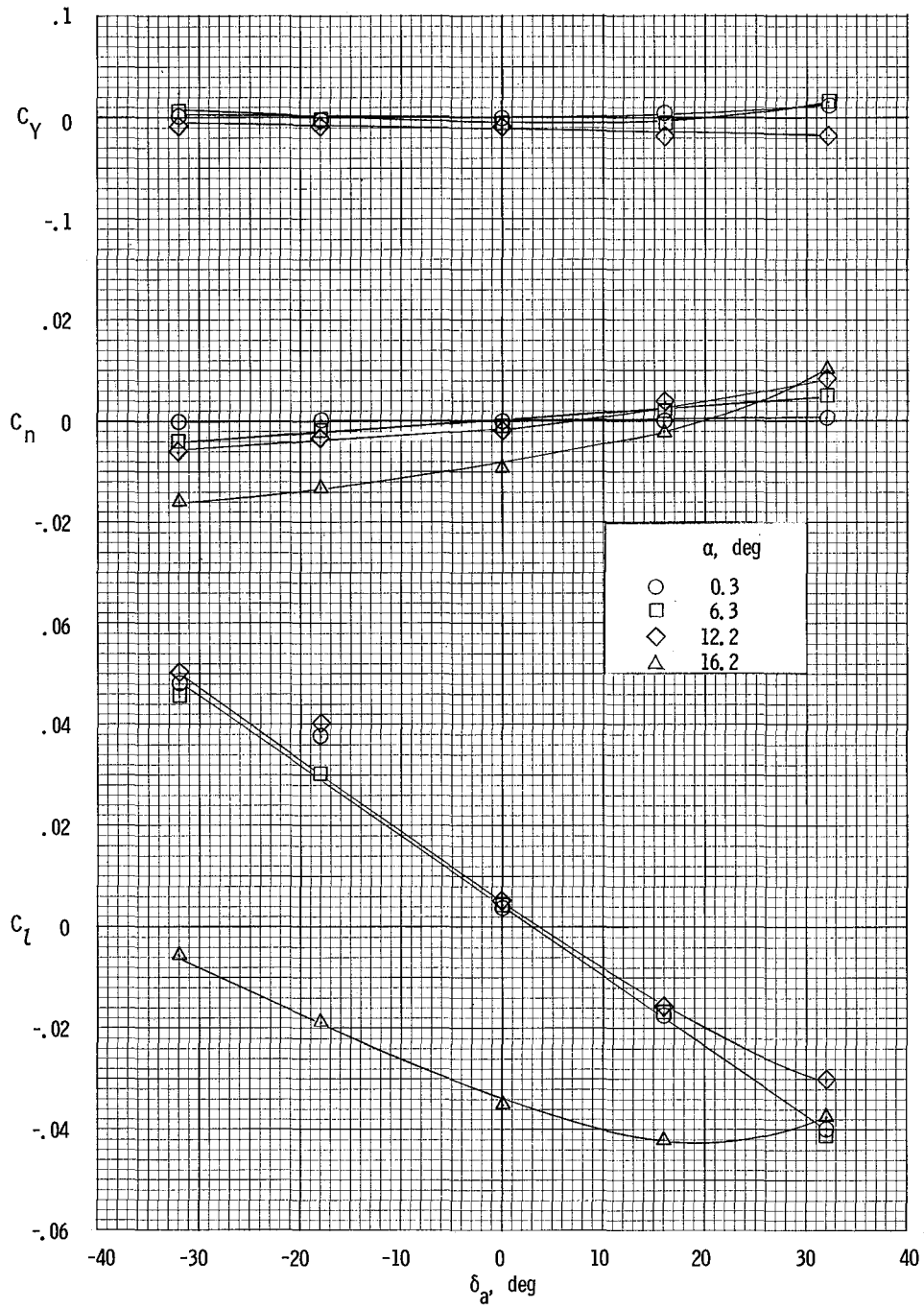
Figure 28.- Continued.
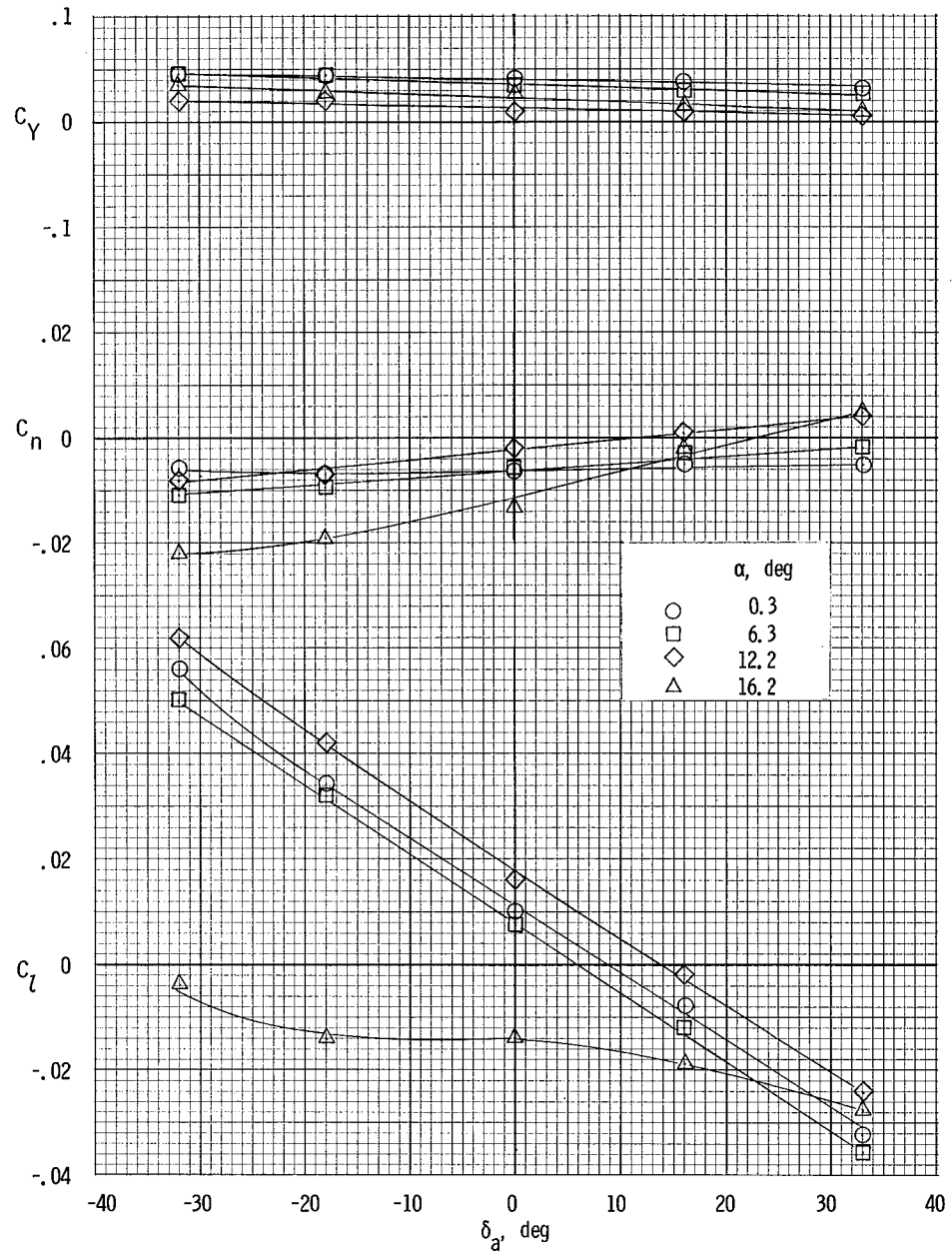
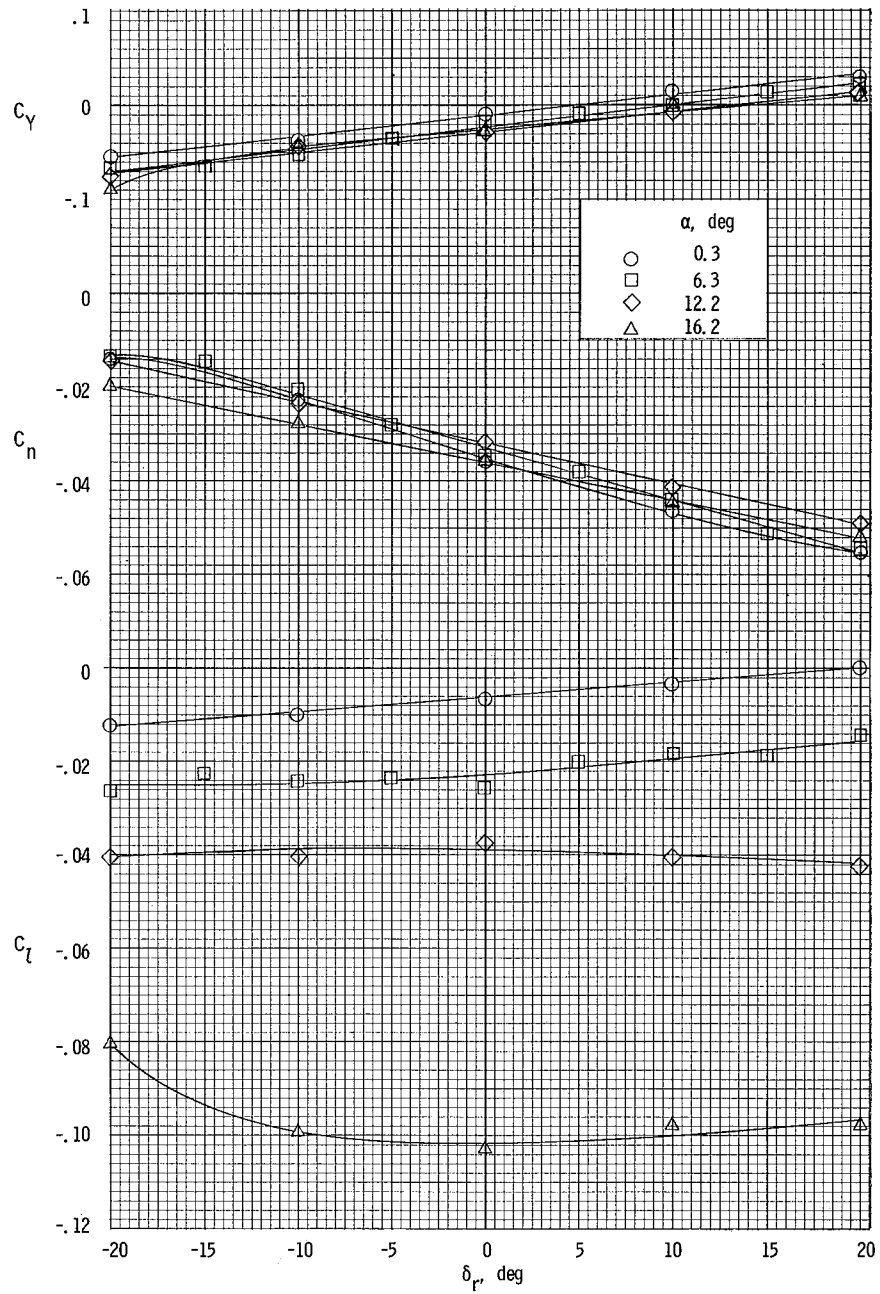(d) $\beta = -4^{\circ}$.

Figure 28.- Continued.
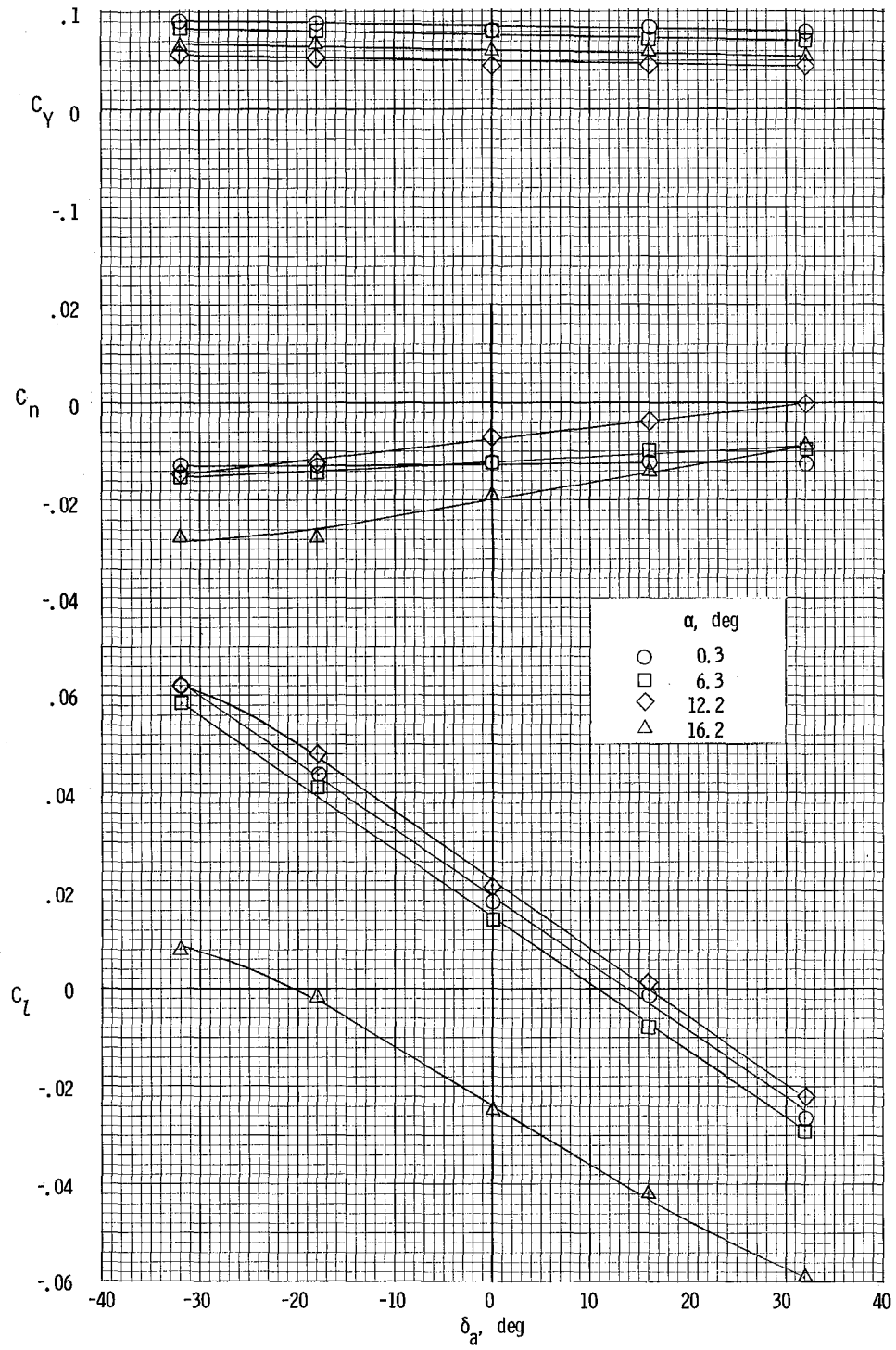
(e) $\beta = -8^\circ$.

Figure 28.- Concluded.

(a) $\beta = 8^0$.
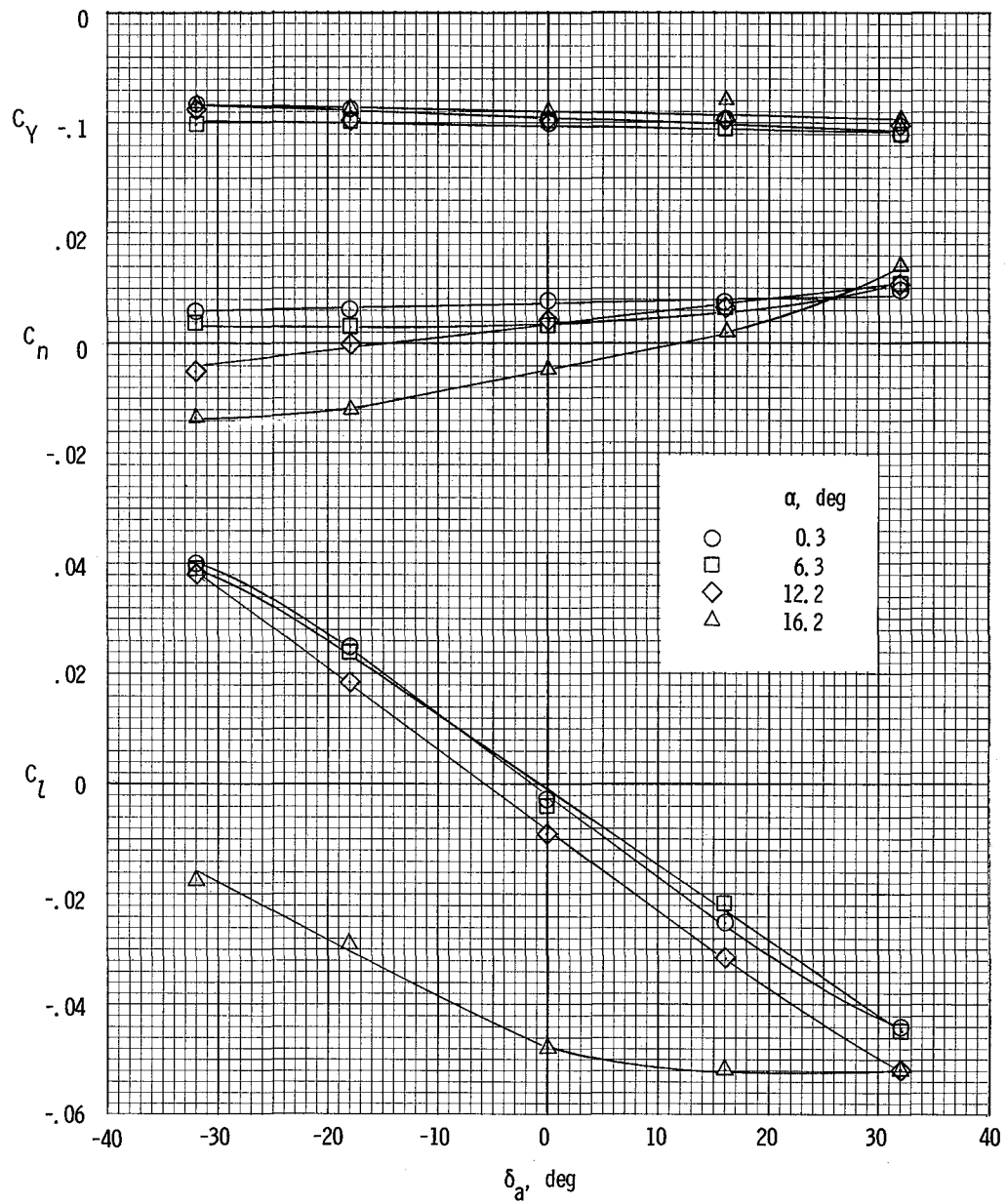
Figure 29.- Variation of lateral characteristics of airplane with aileron deflection. $\delta_f = 27^0$; $T_C^1 = 0.20$.

(b) β = 4°.
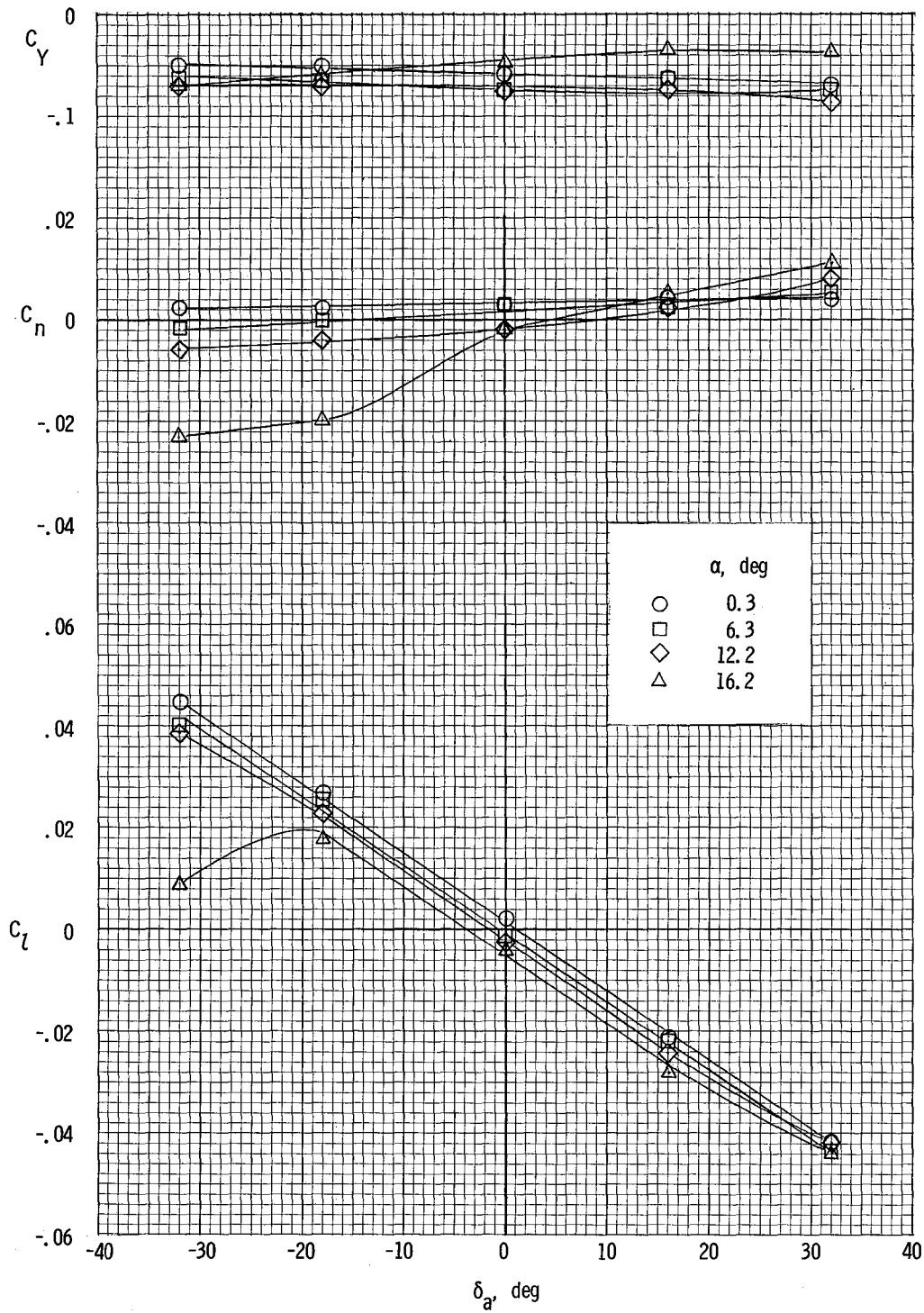
Figure 29.- Continued.
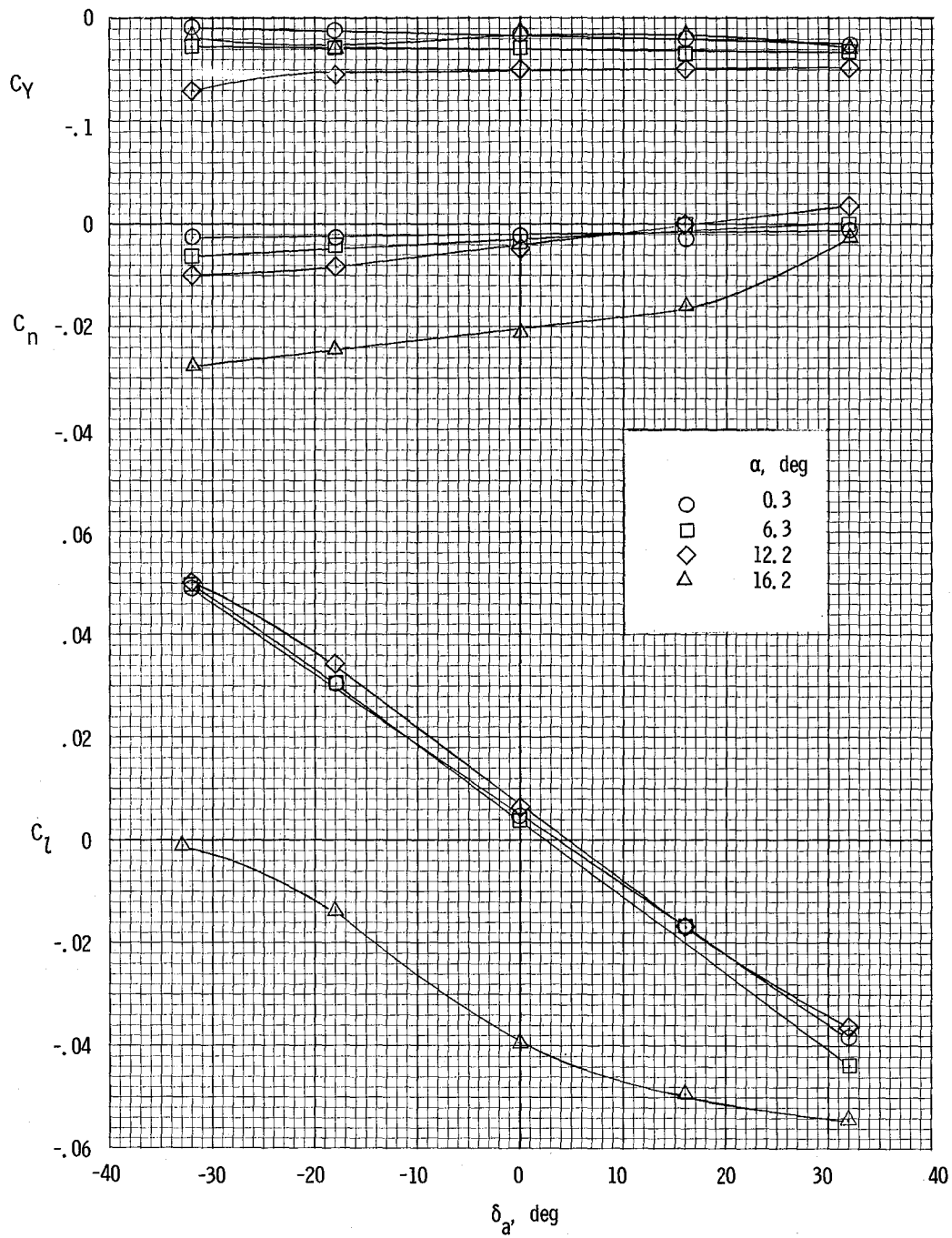
(c) $\beta = 0^0$.

Figure 29.- Continued.
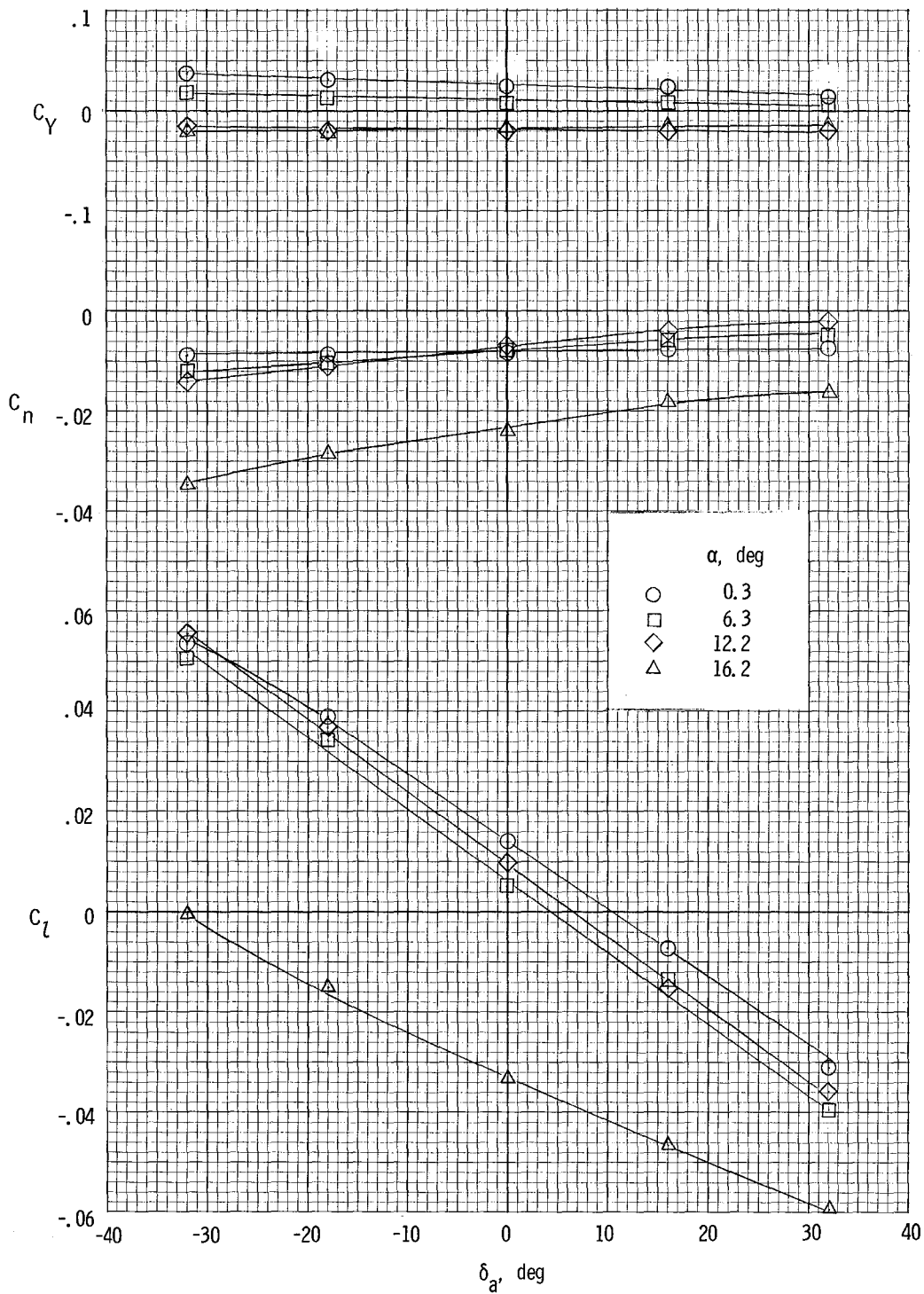
(d) $\beta = -4^{\circ}$.

Figure 29.- Continued.

(e) $\beta = -8^o$.
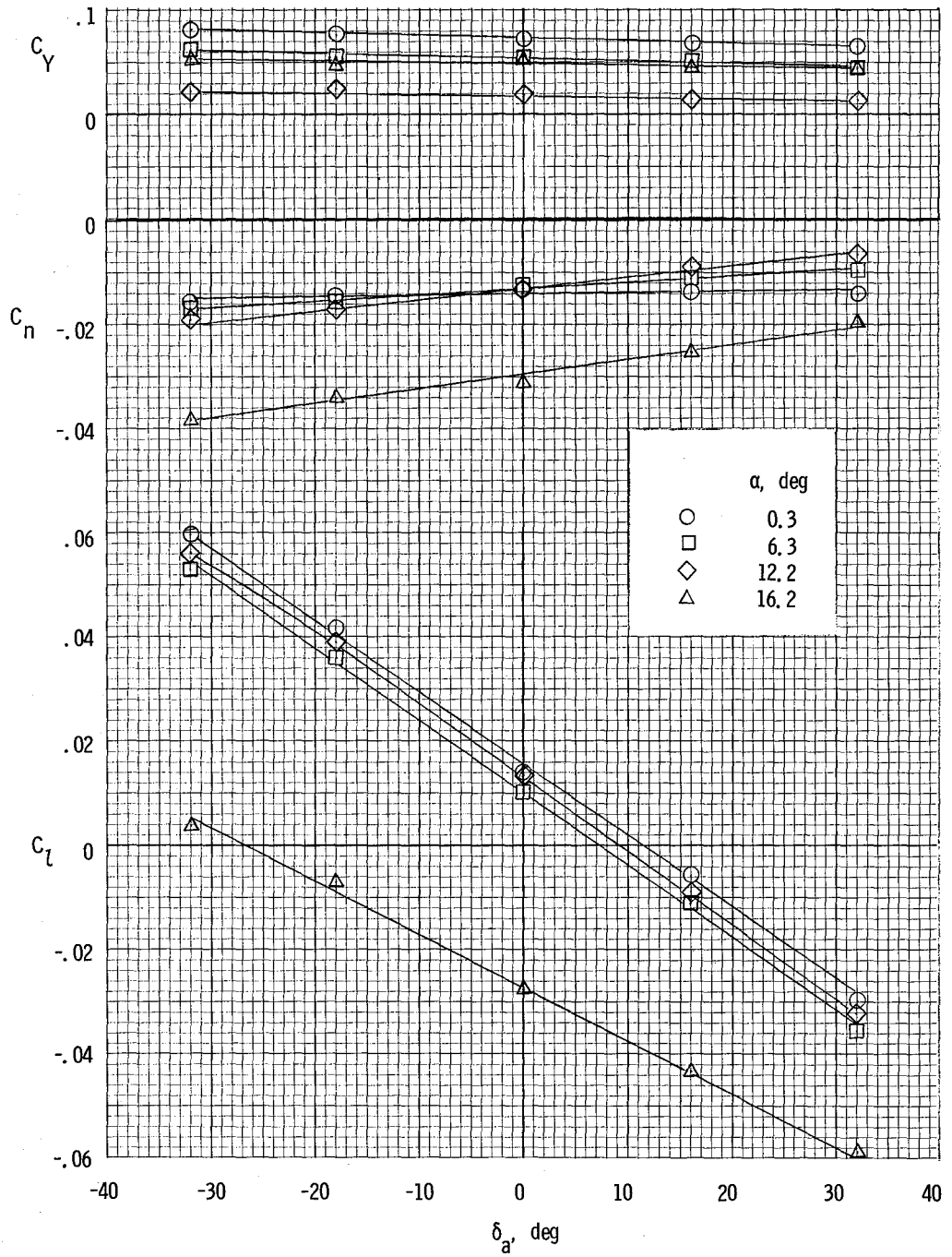
Figure 29.- Concluded.
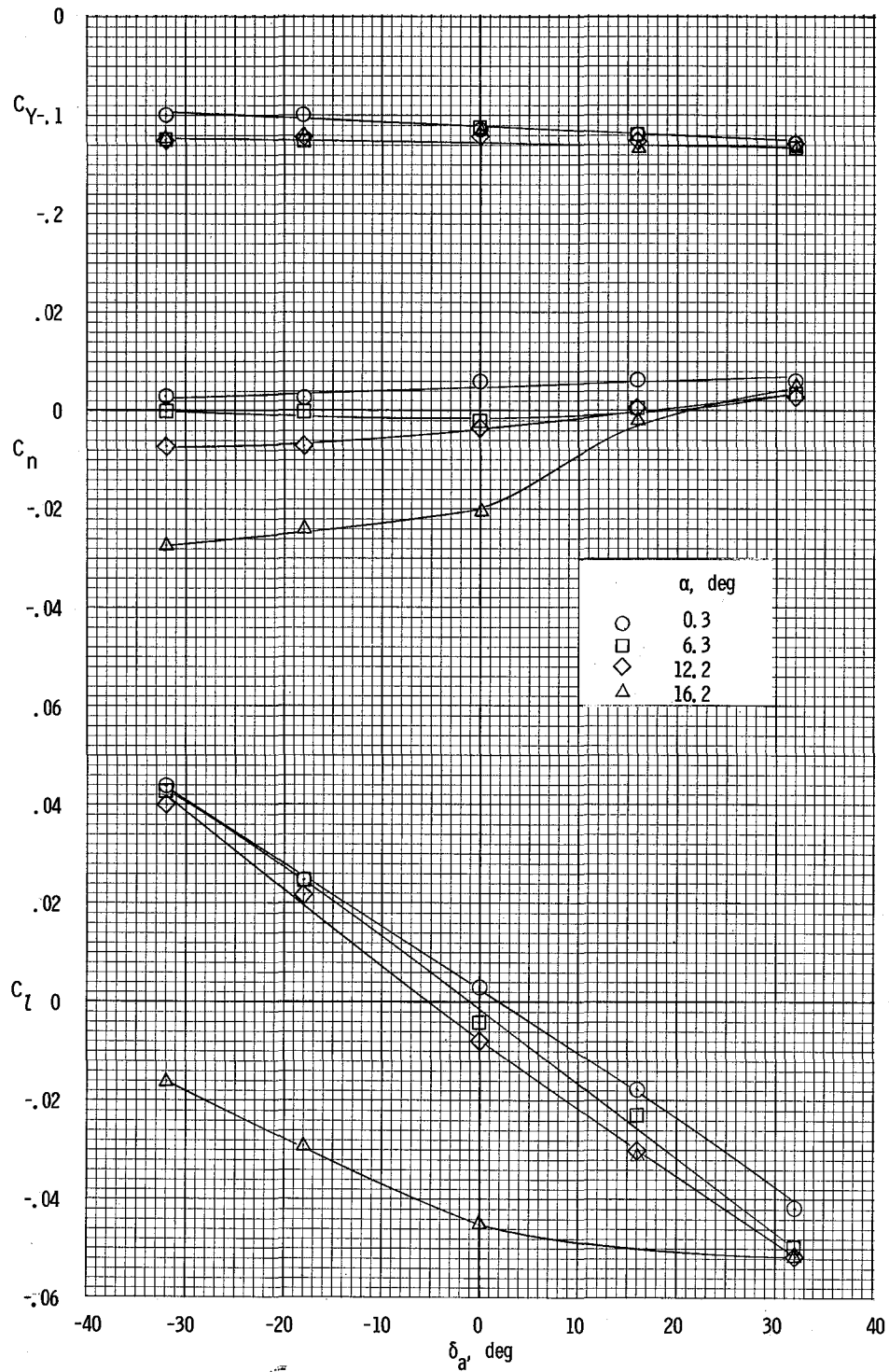
(a) β = 8°.

Figure 30.- Variation of lateral characteristics of airplane with aileron deflection. $\delta_f = 27°$; $T_c' = 0.44$.
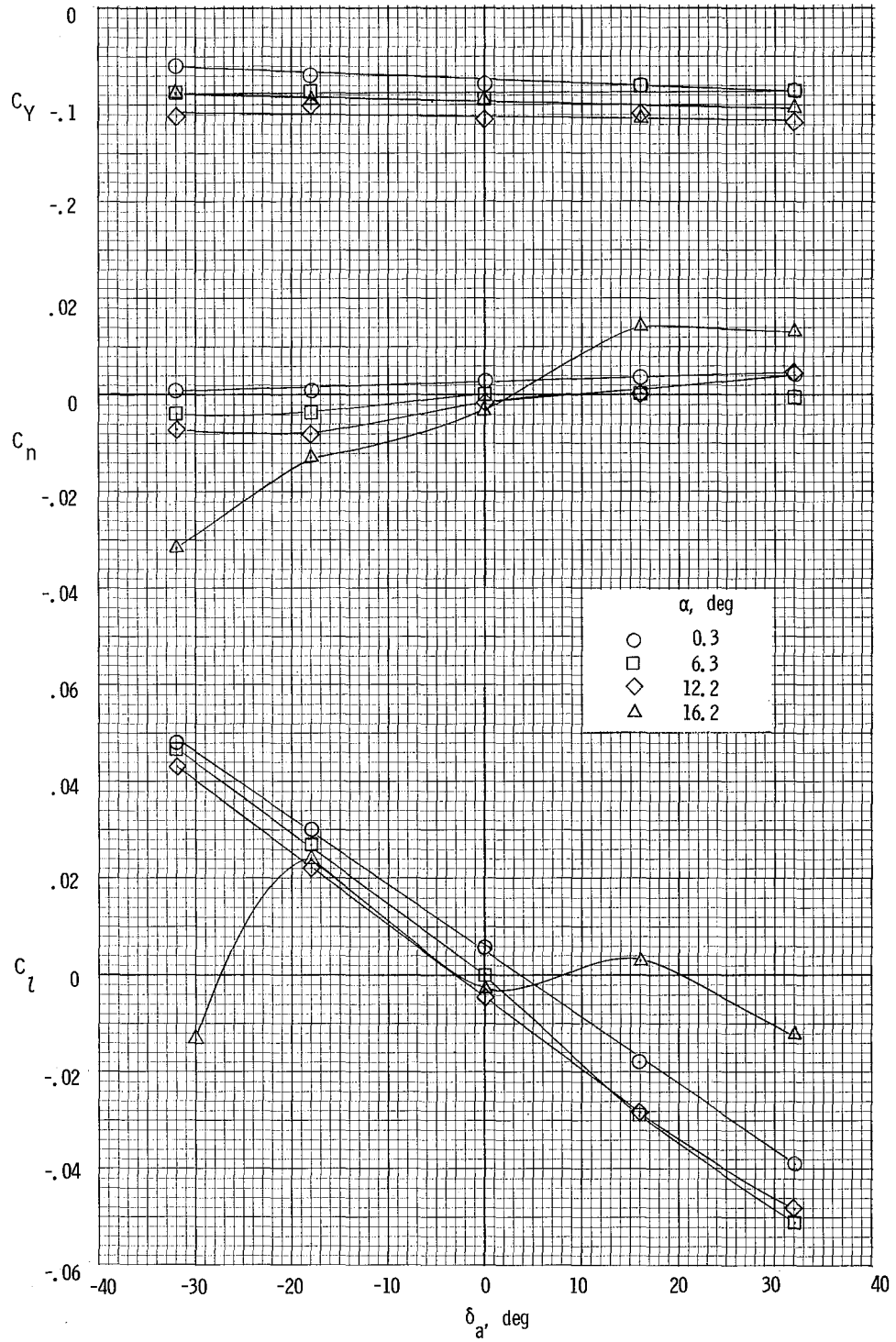
(b) β = 4°.

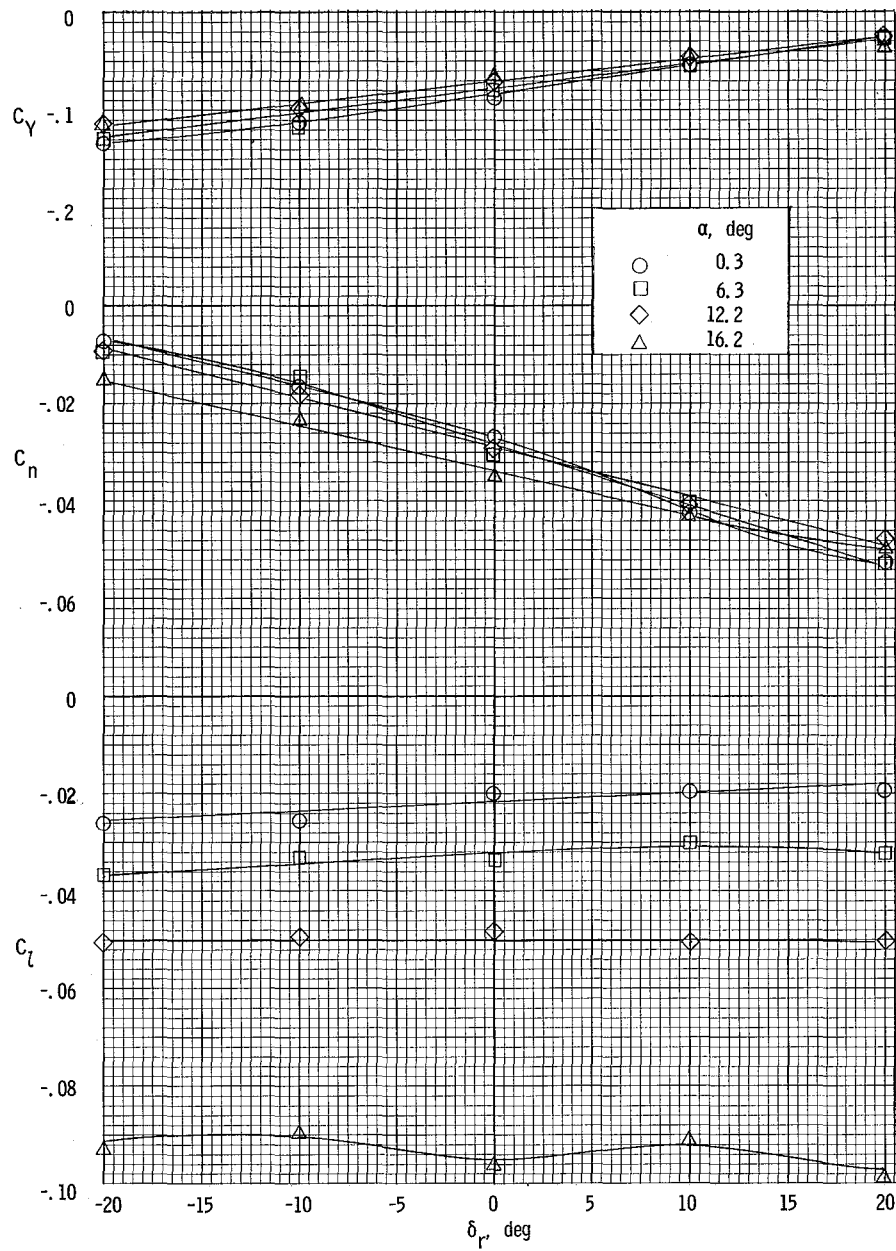Figure 30.- Continued.

92
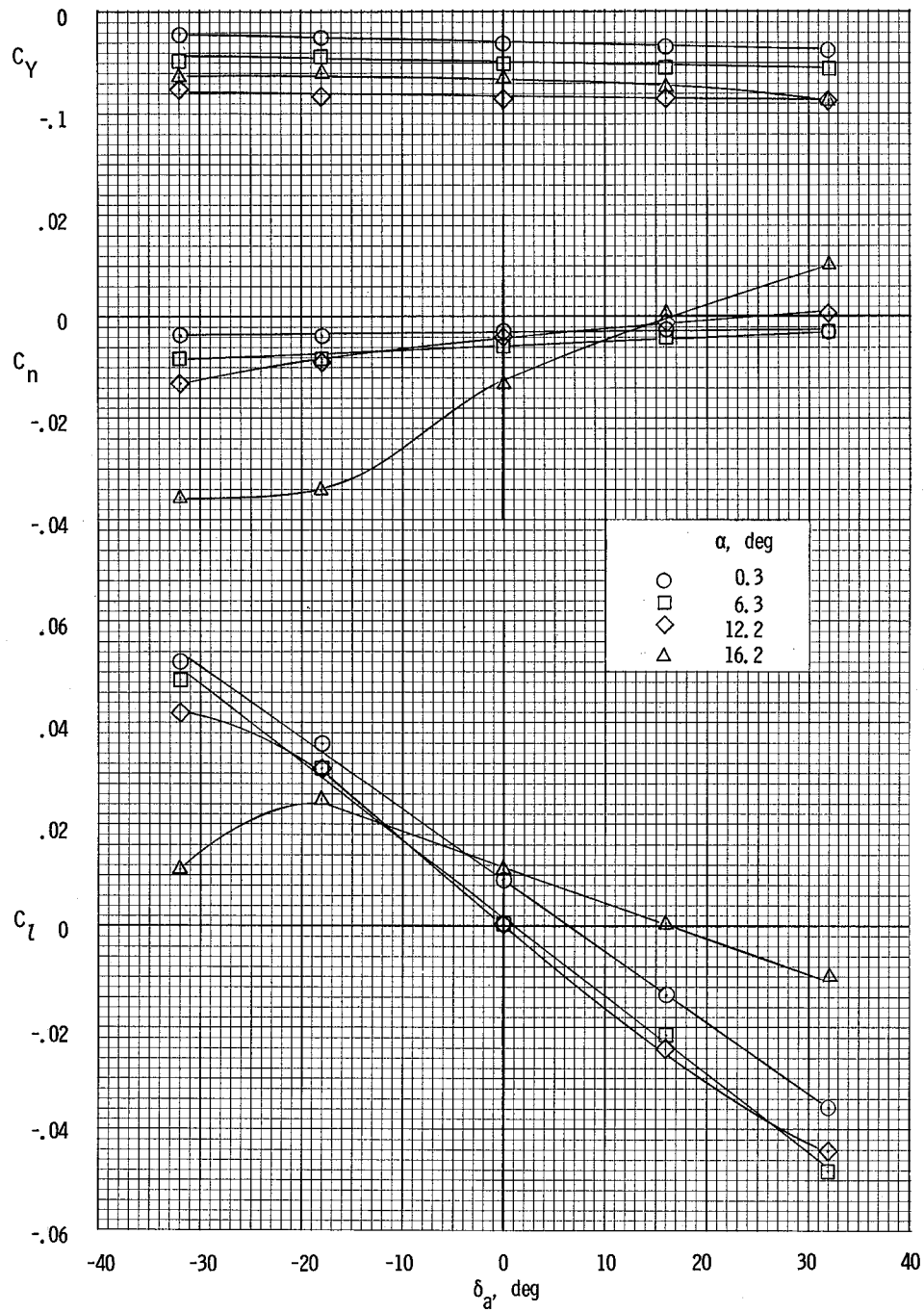
(c) $\beta = 0^0$.

Figure 30.- Continued.

(d) $\beta = -4^o$.
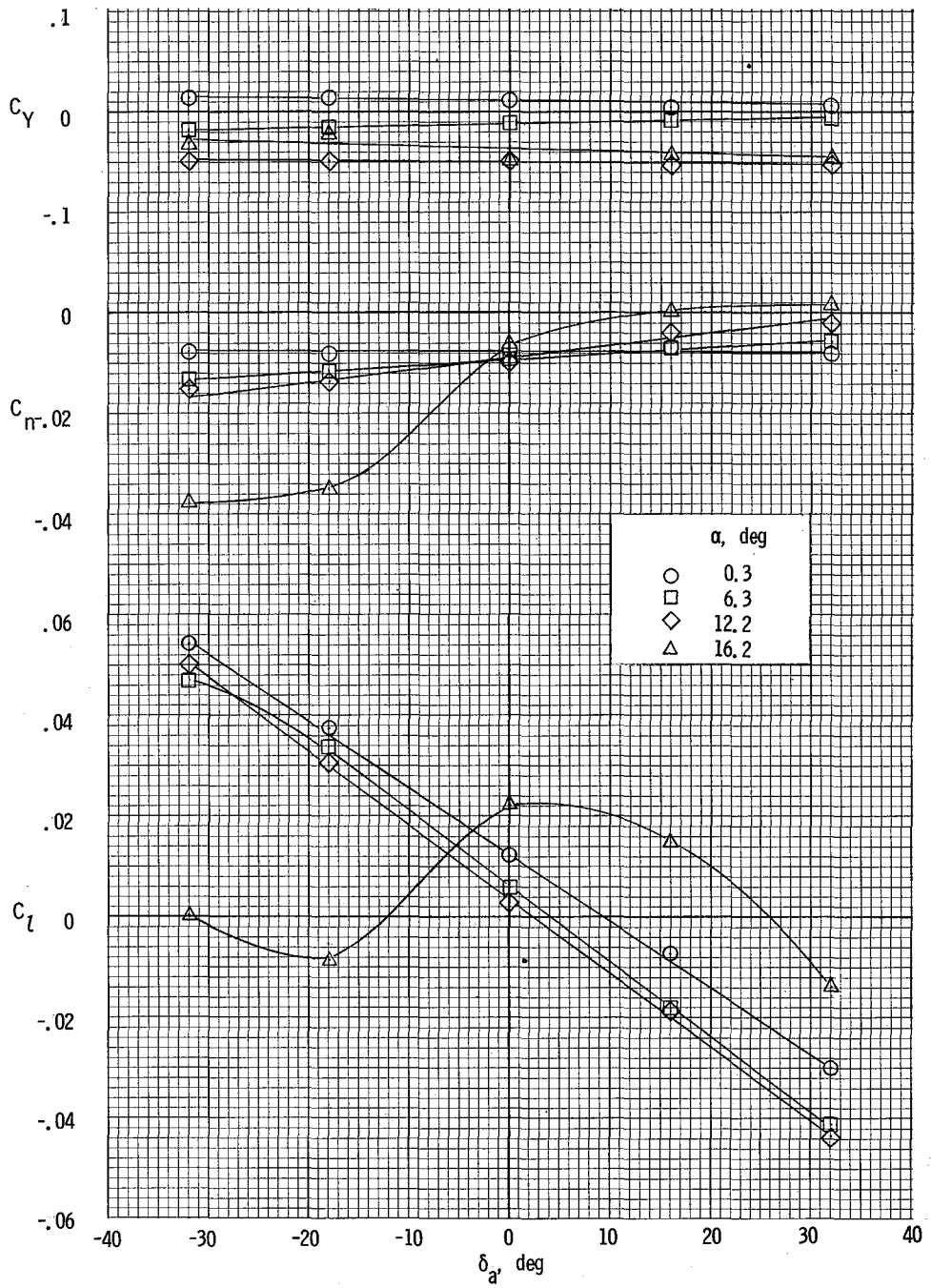
Figure 30.- Continued.

(e) $\beta = -8^0$.
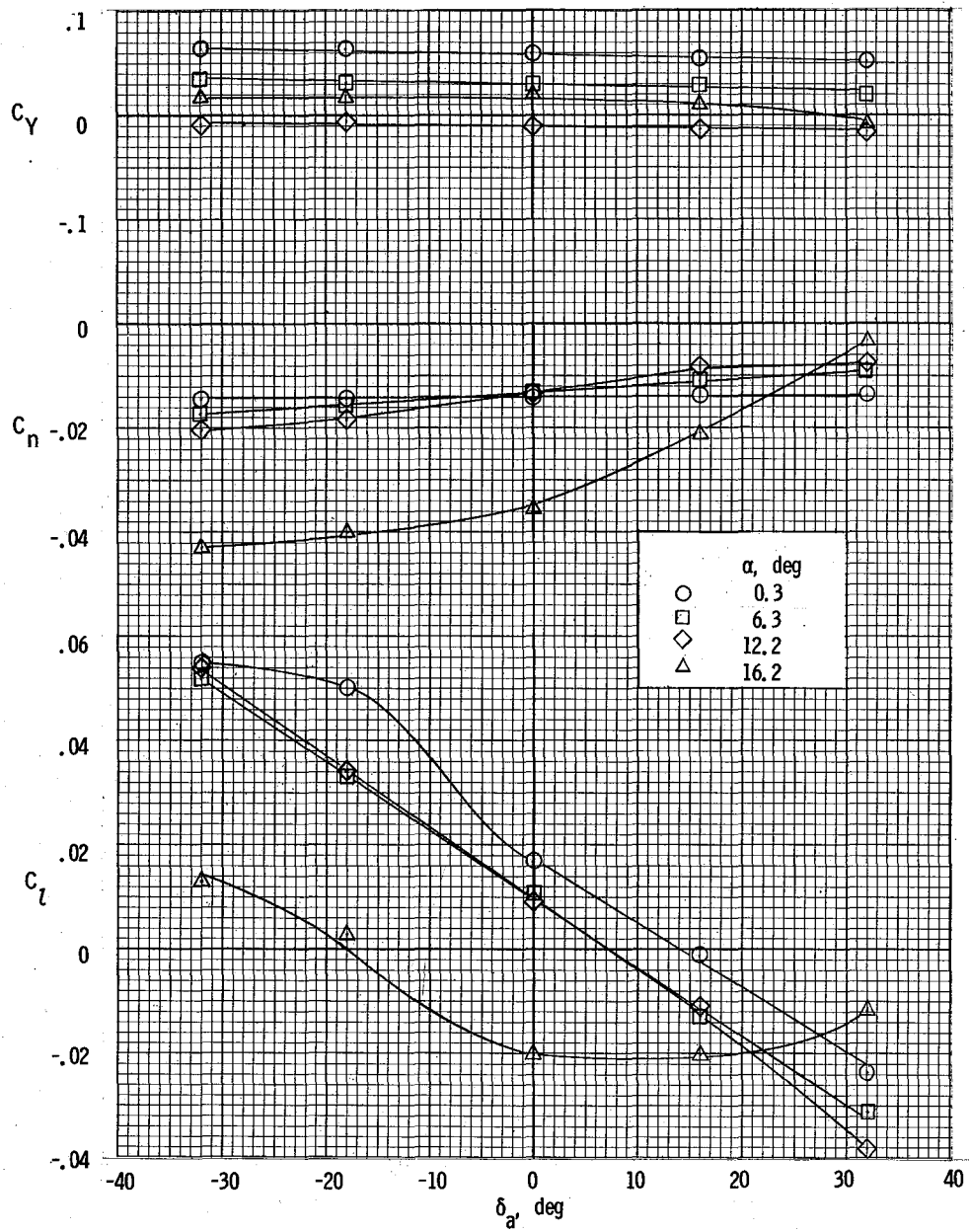
Figure 30.- Concluded.

(a) $\beta = 8^o$.
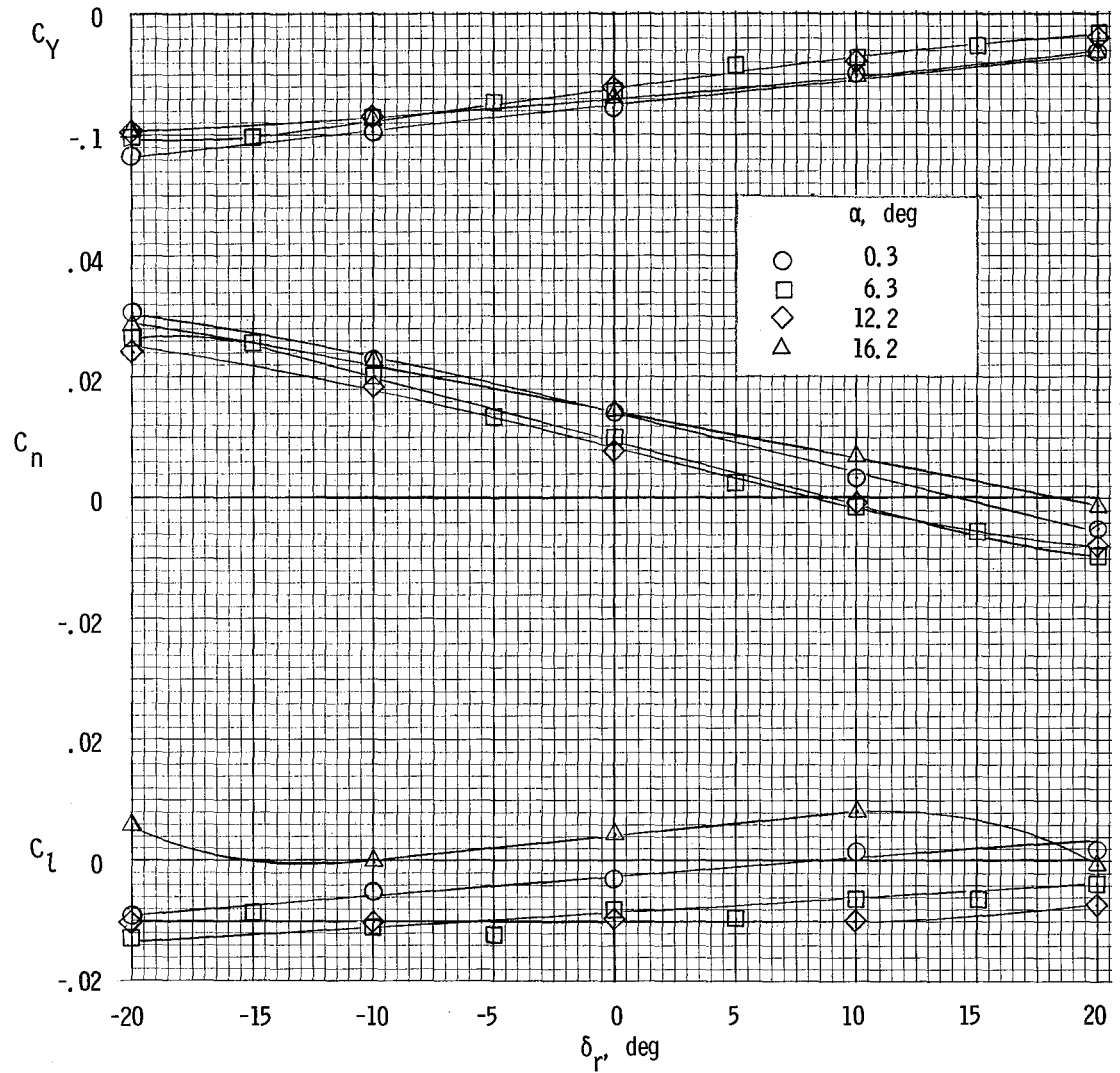
Figure 31.- Variation of lateral characteristics of airplane with rudder deflection. $\delta_f = 0^o$; $T'_c = 0$.
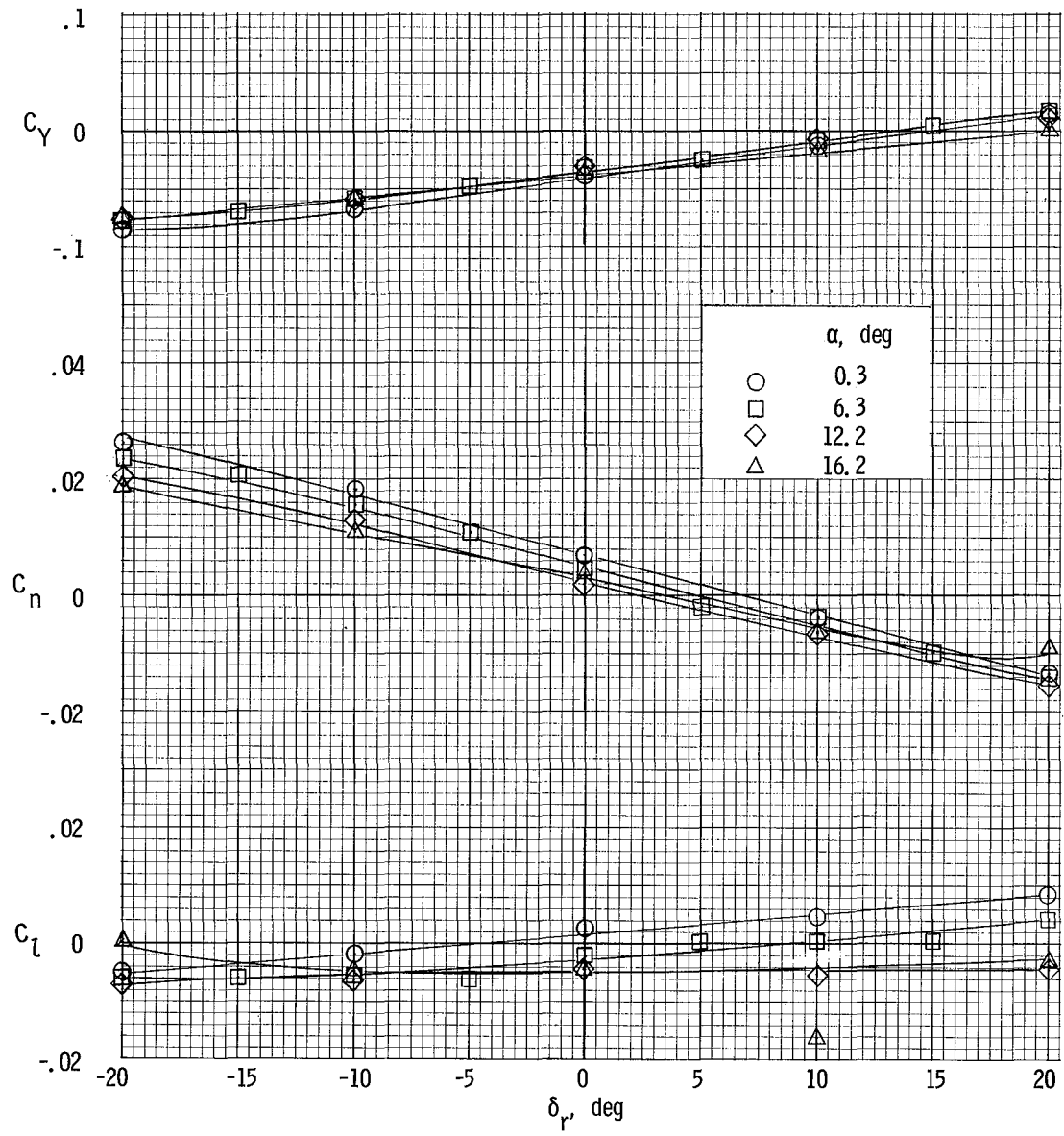
(b) β = 4°.

Figure 31.- Continued.
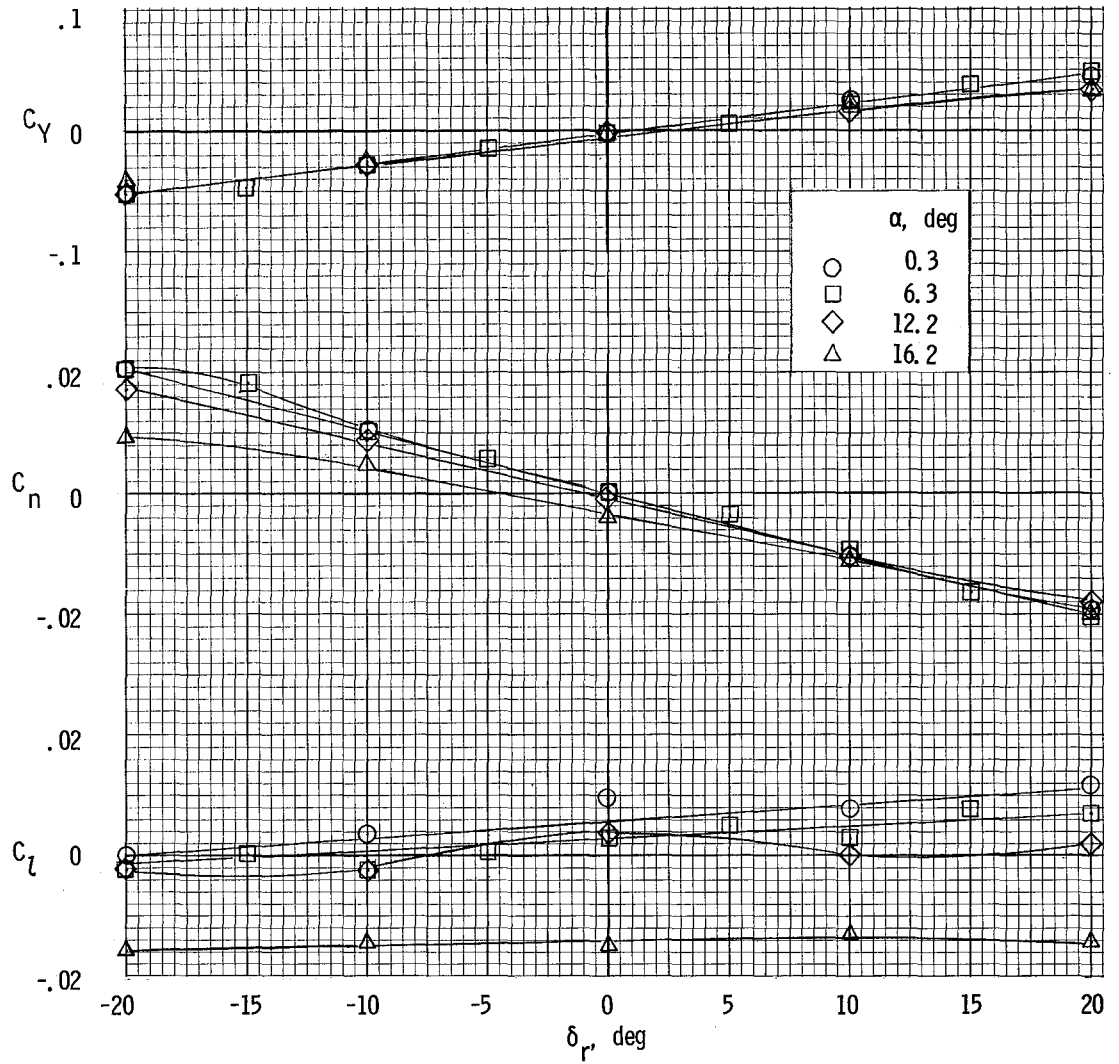
(c) $\beta = 0^0$.

Figure 31.- Continued.

(d) $\beta = -4^o$.
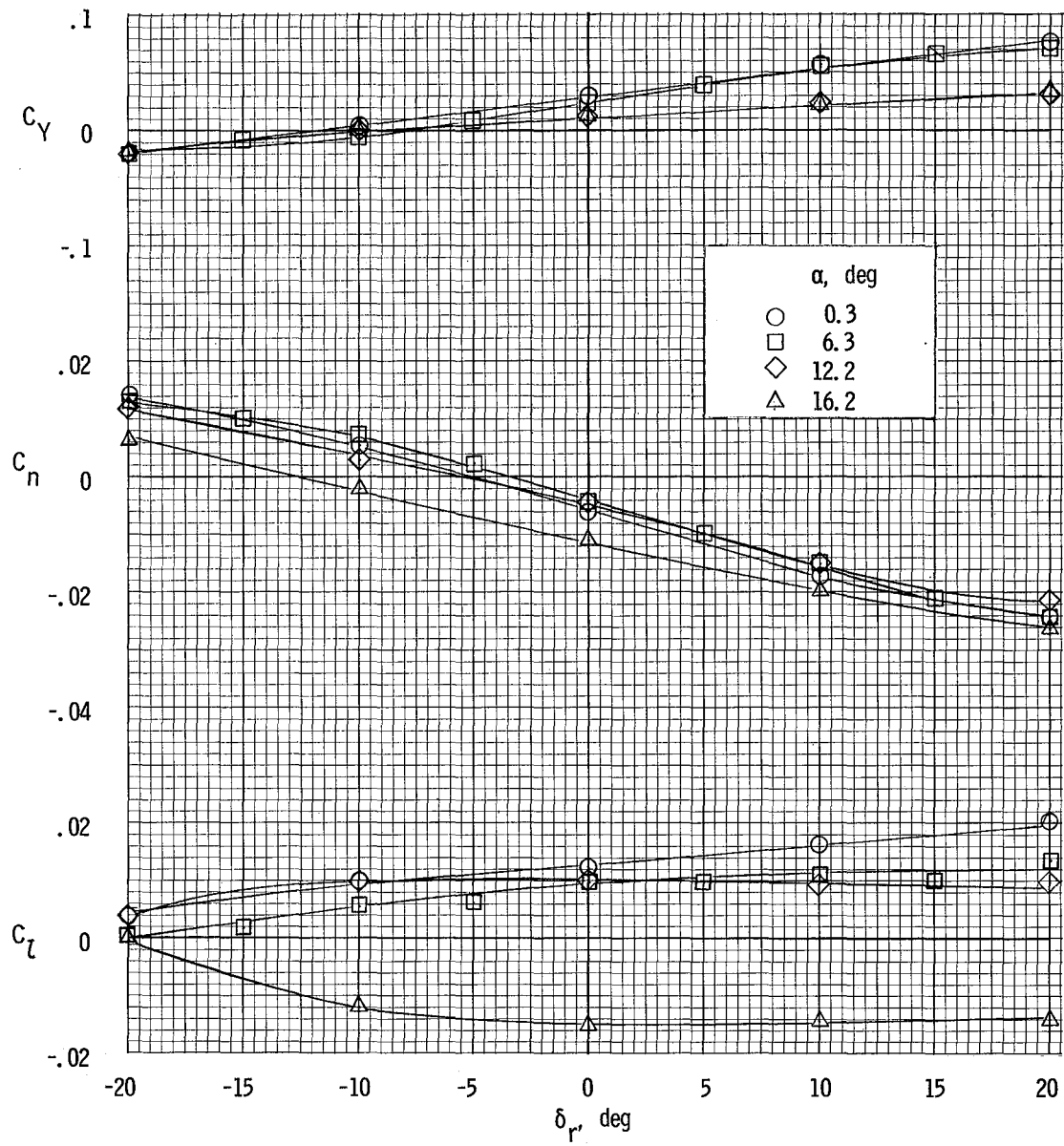
Figure 31.- Continued.
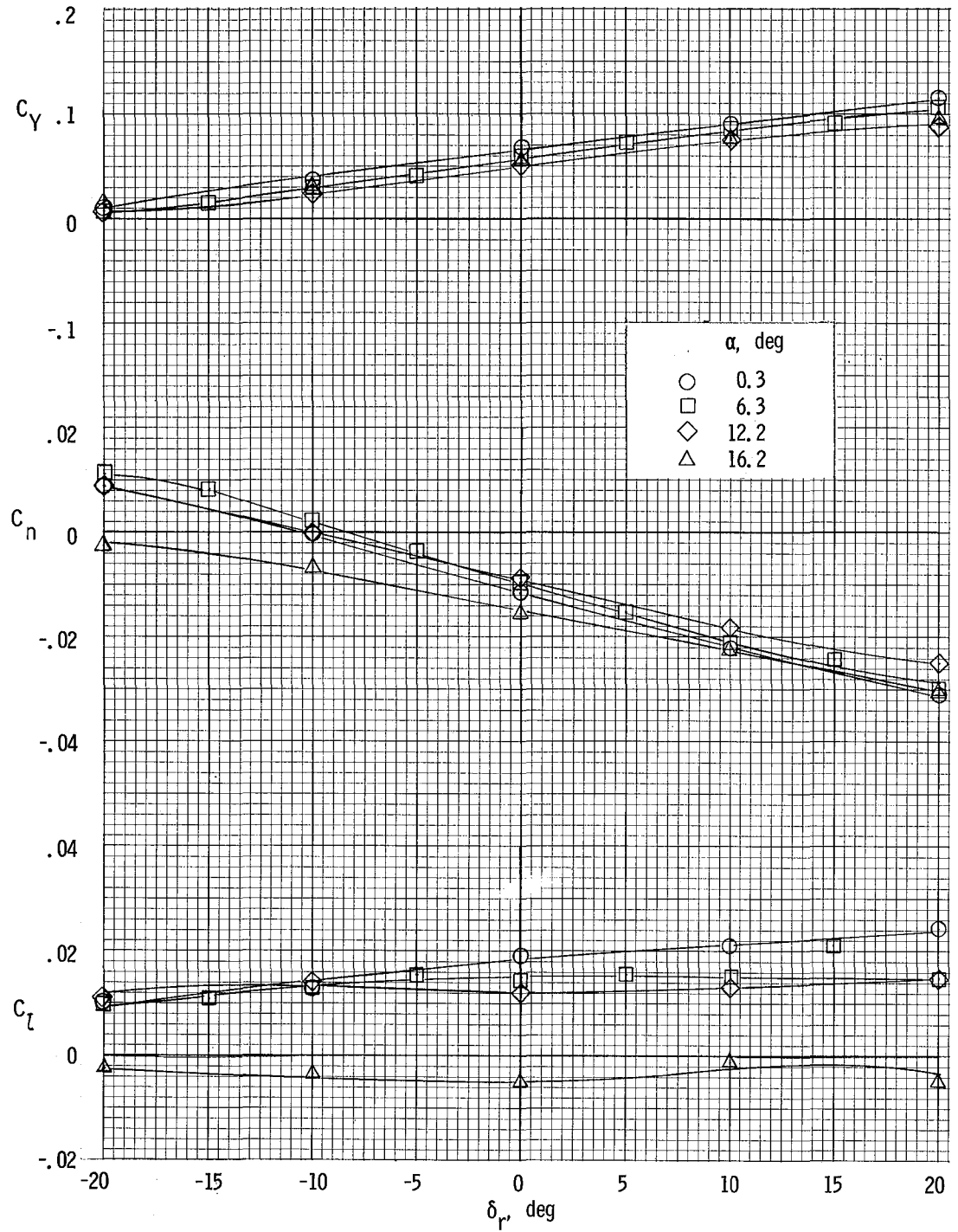
(e) $\beta = -8°$.

Figure 31.- Concluded.

(a) $\beta = 8^0$.
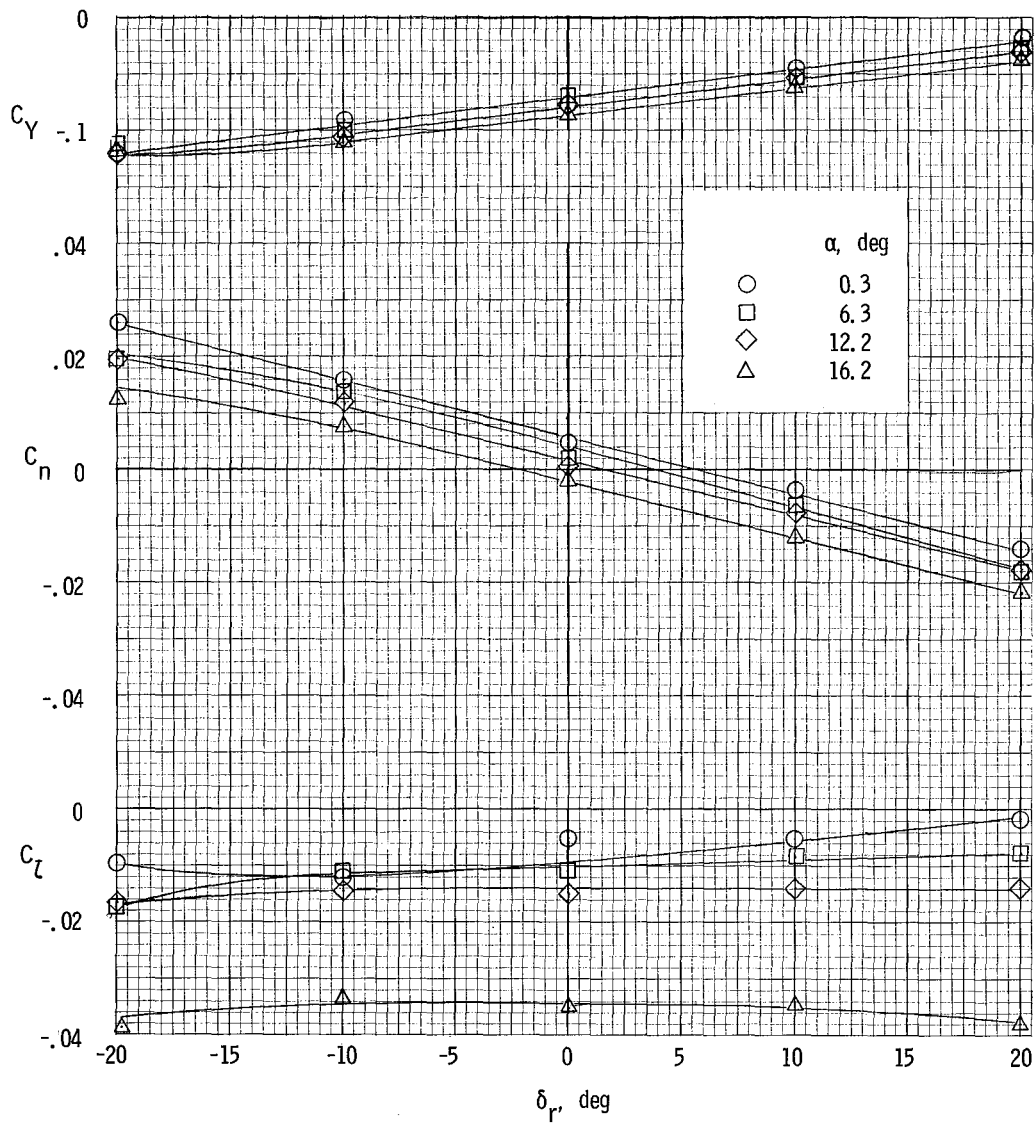
Figure 32.- Variation of lateral characteristics of airplane with rudder deflection. $\delta_f = 0^0$; $T'_c = 0.20$.
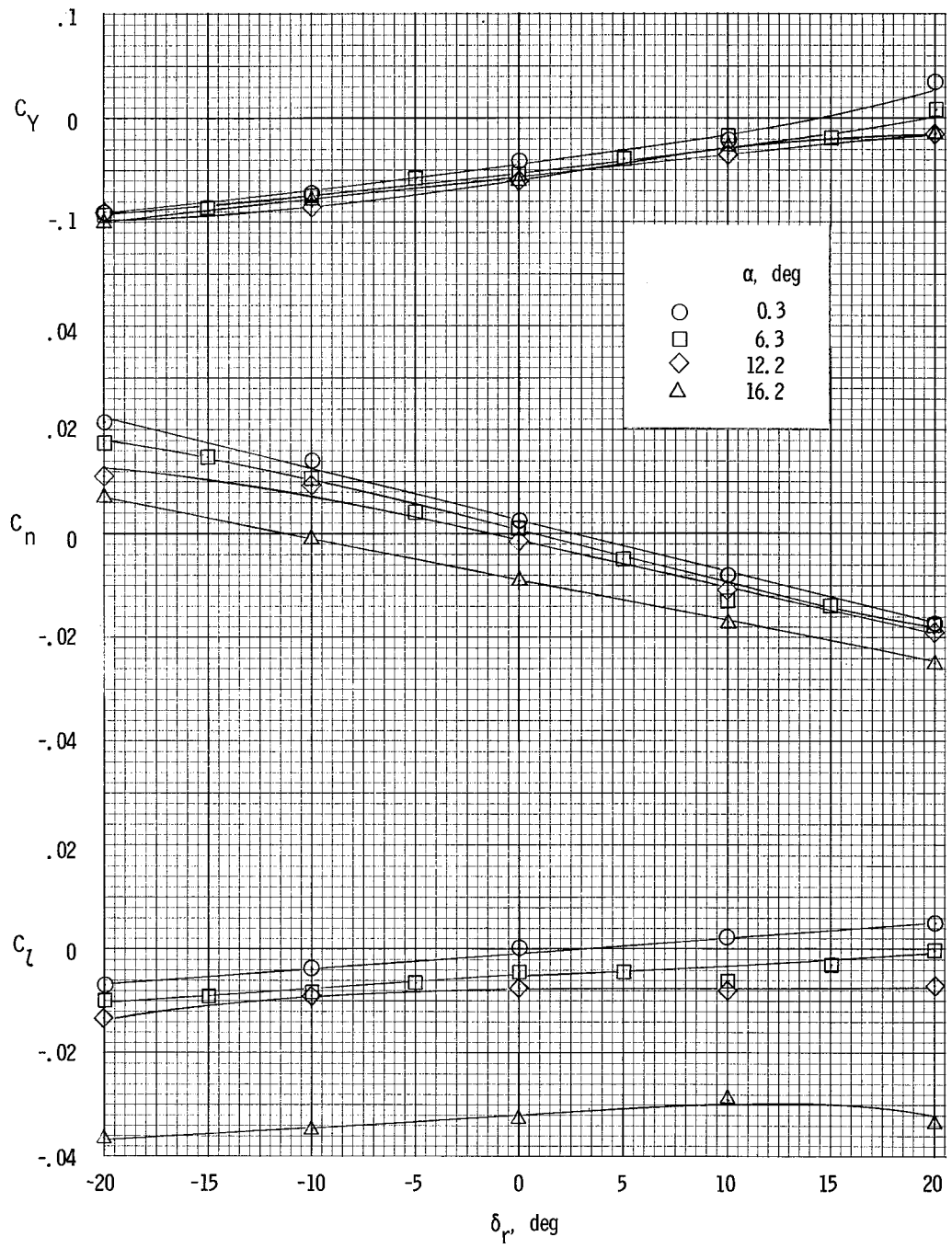
(b) β = 4°.

Figure 32.- Continued.

102
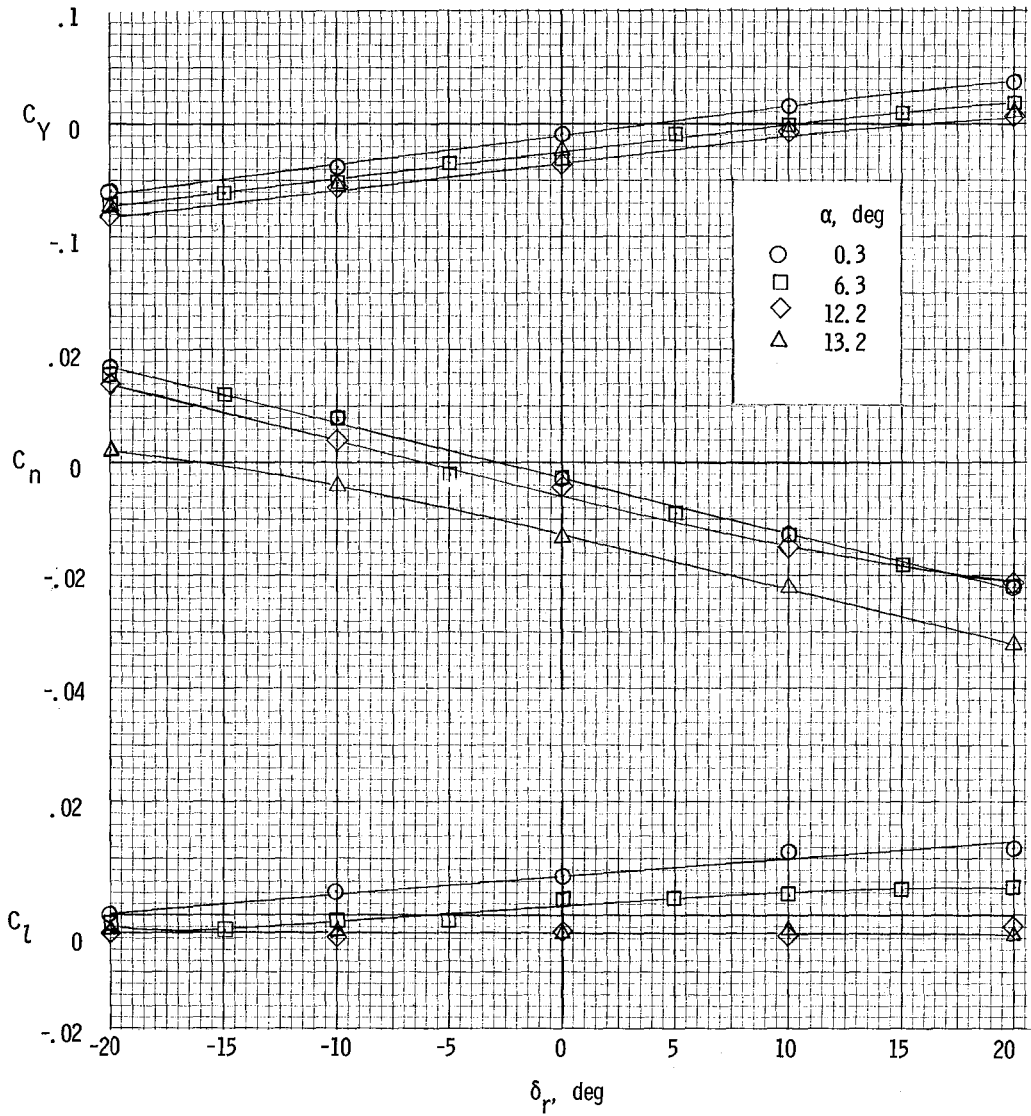
(c) $\beta = 0^0$.

Figure 32.- Continued.

(d) $\beta = -4^o$.
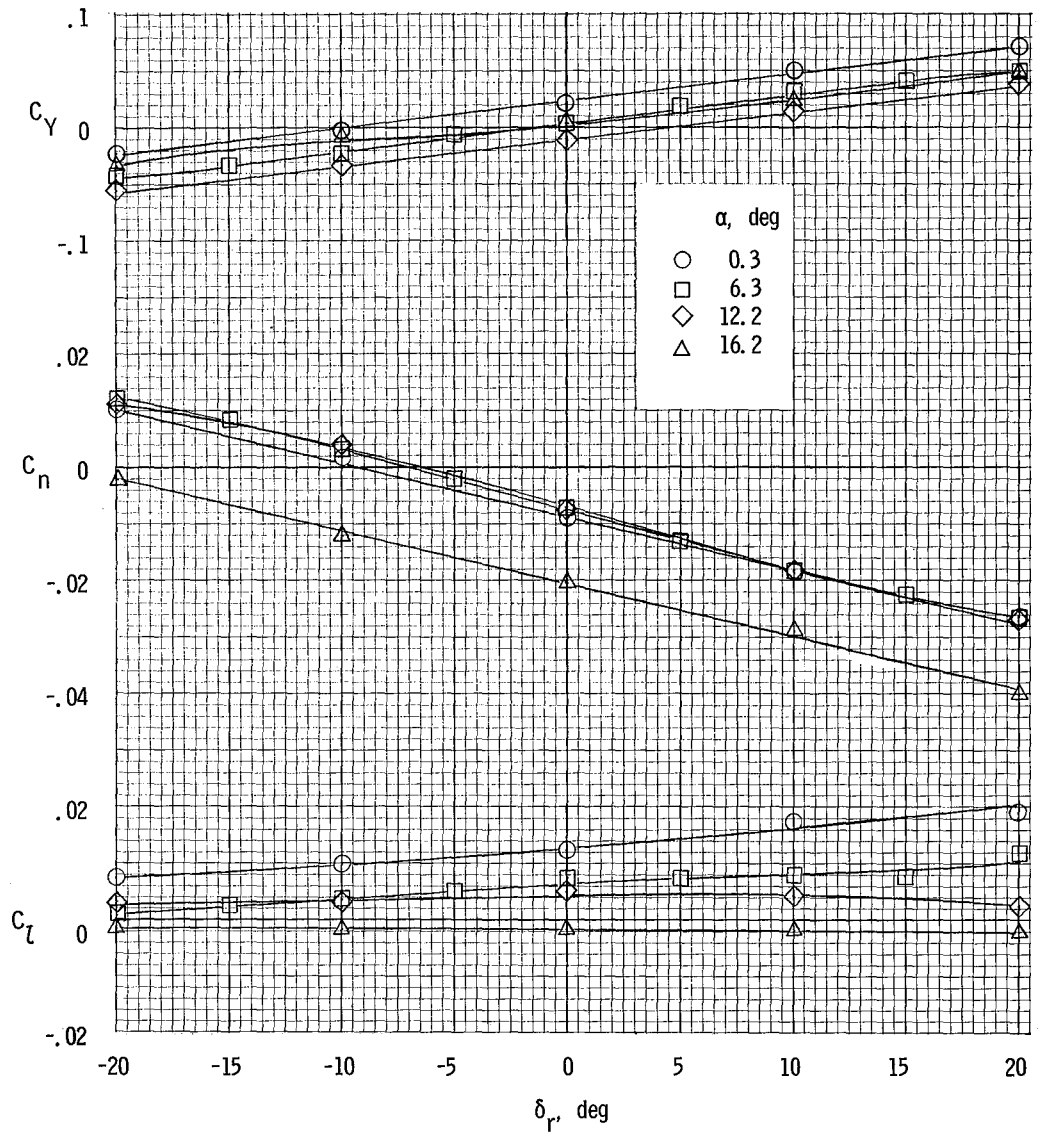
Figure 32.- Continued.

(e) $\beta = -8^0$.
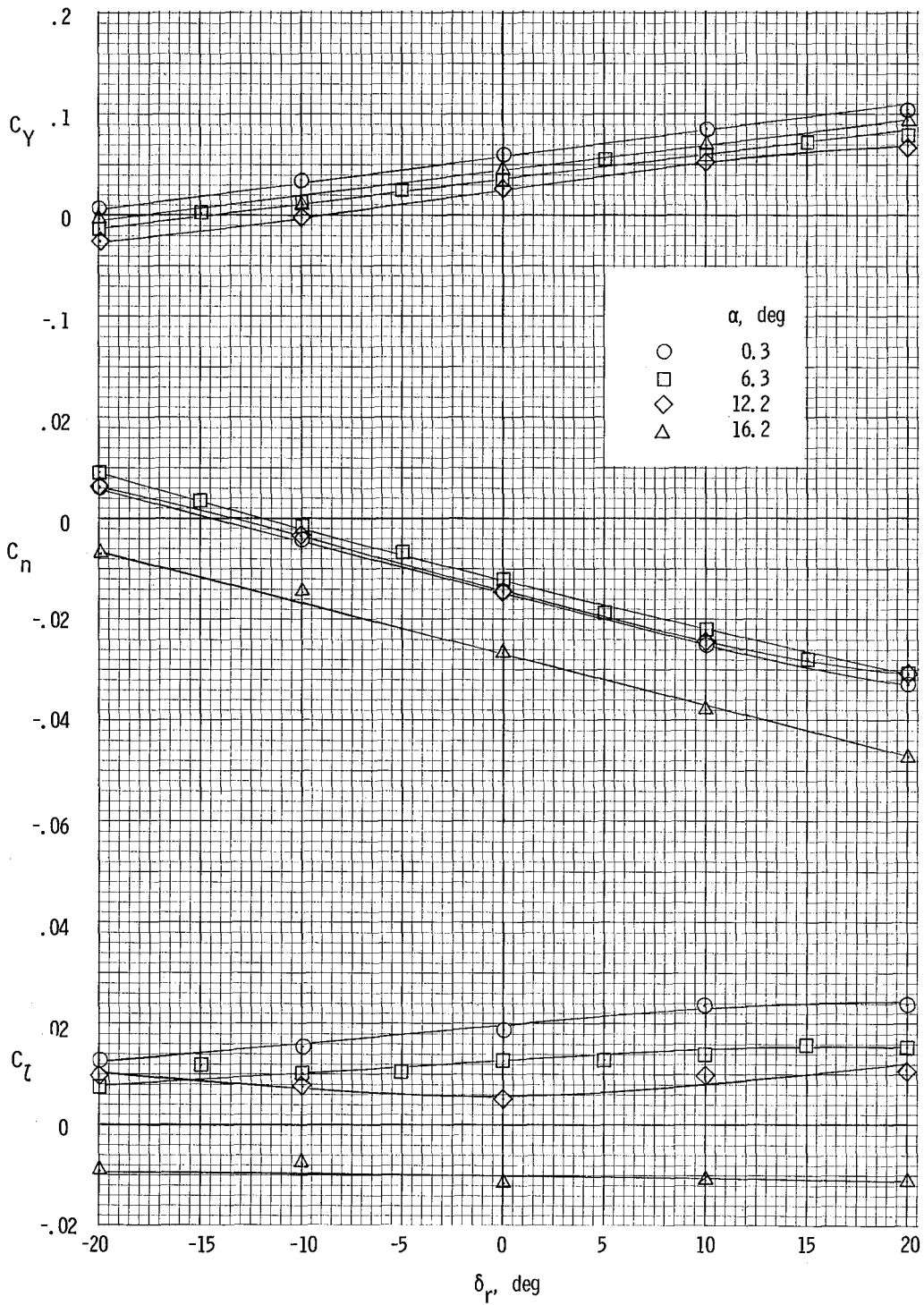
Figure 32.- Concluded.

(a) β = 8⁰.
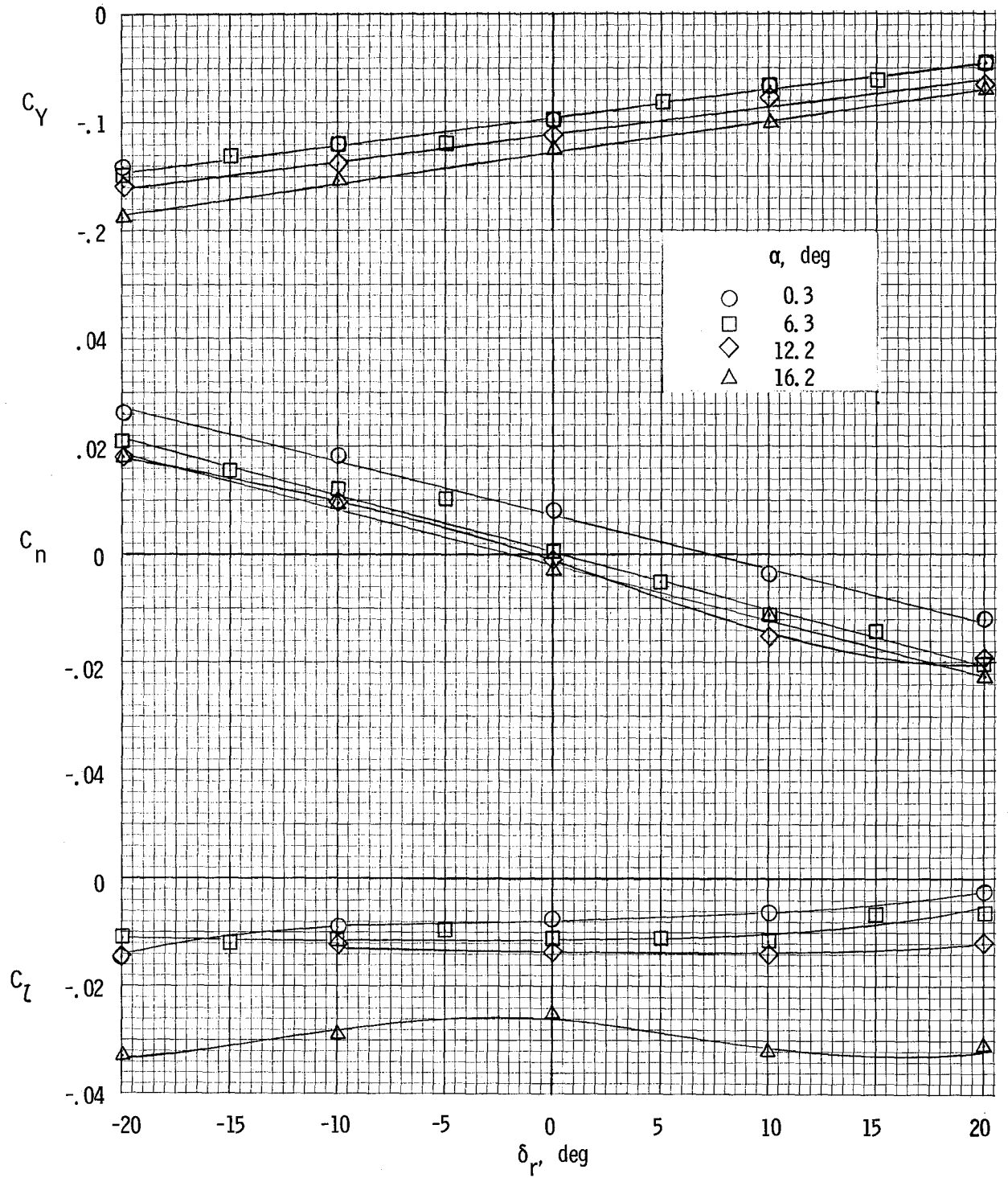
Figure 33.- Variation of lateral characteristics of airplane with rudder deflection. $\delta_f = 0^0$; $T'_c = 0.44$.
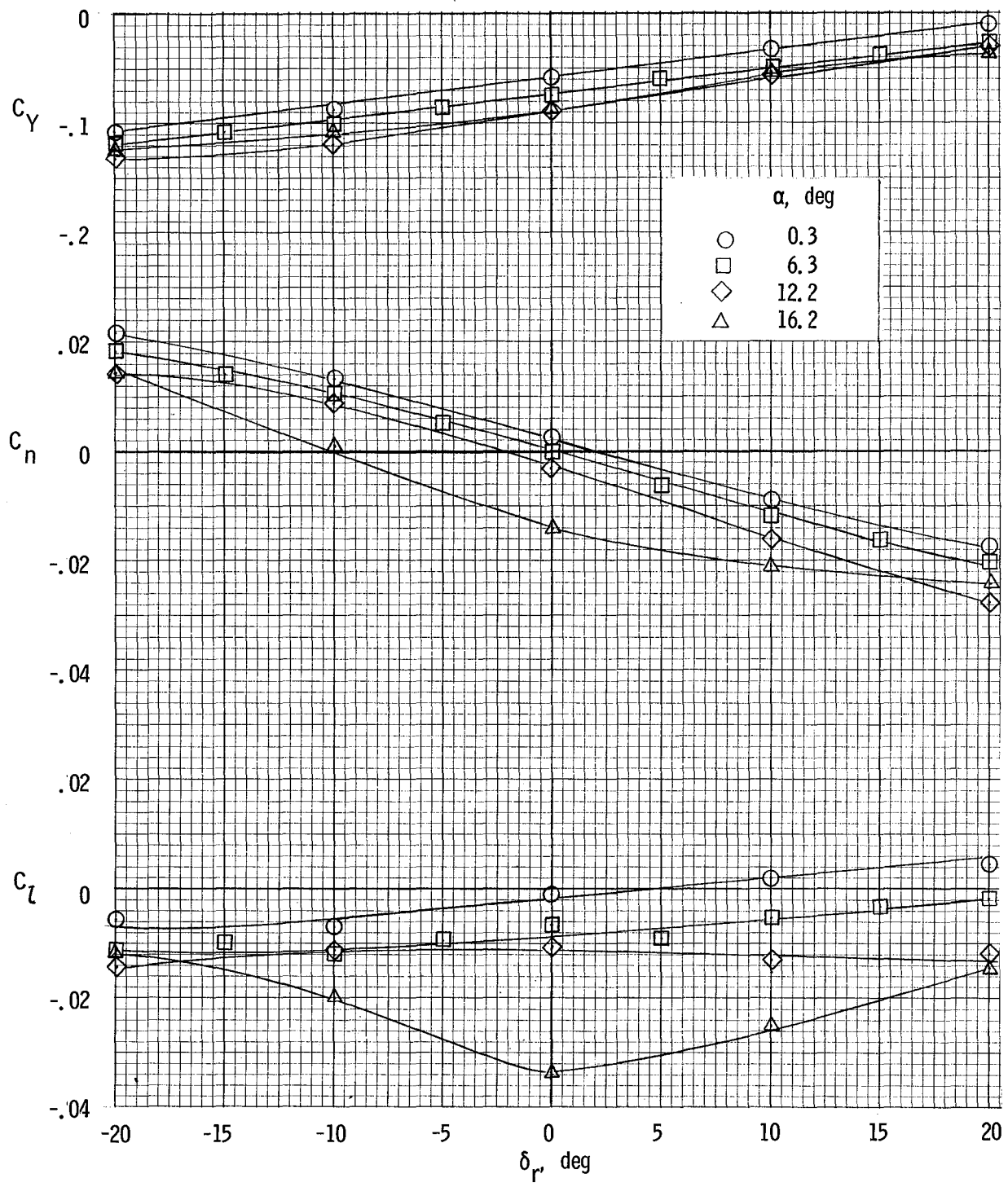
(b) β = 4°.

Figure 33.- Continued.
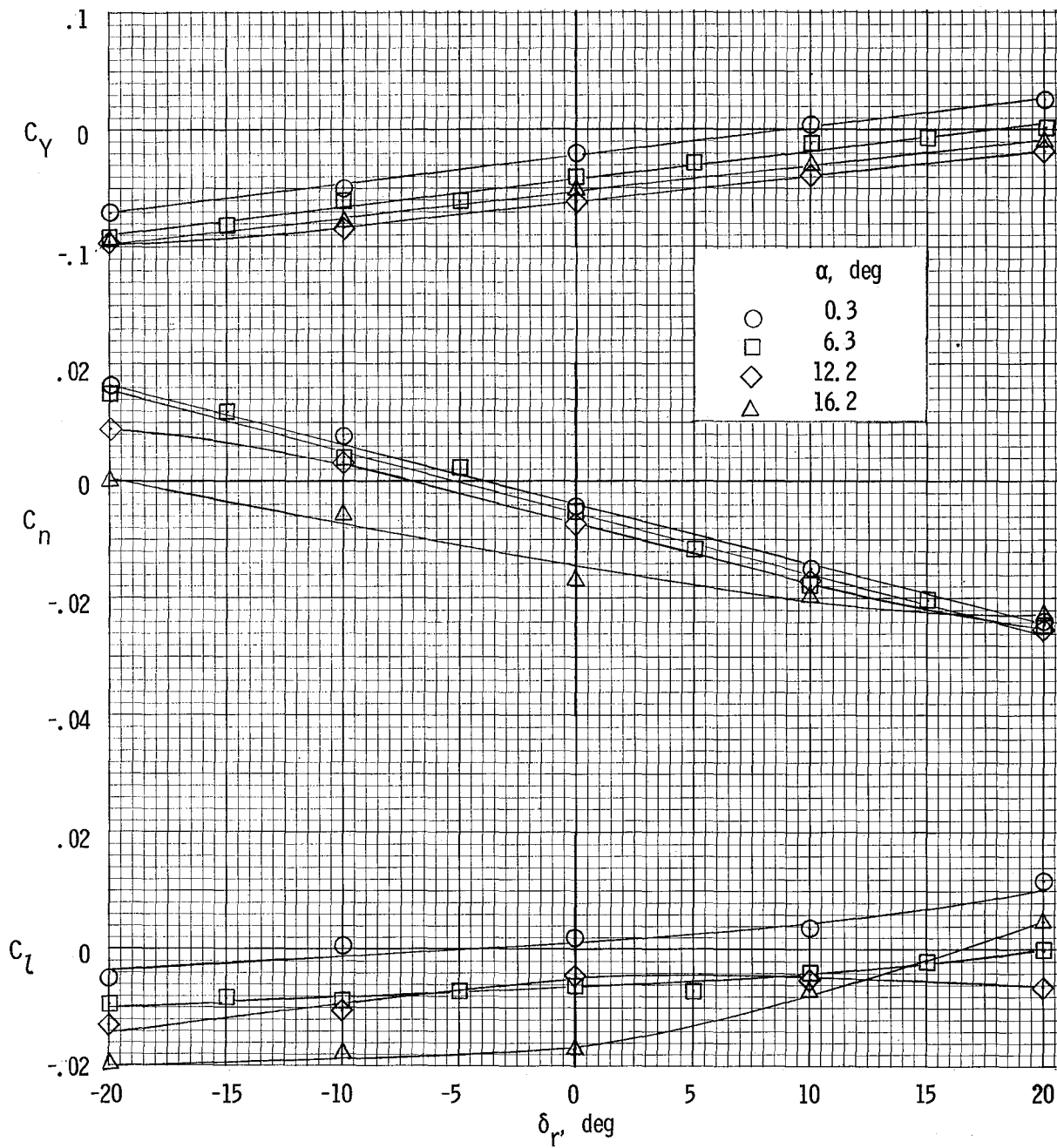
(c) $\beta = 0^0$.

Figure 33.- Continued.

(d) $\beta = -4^o$.
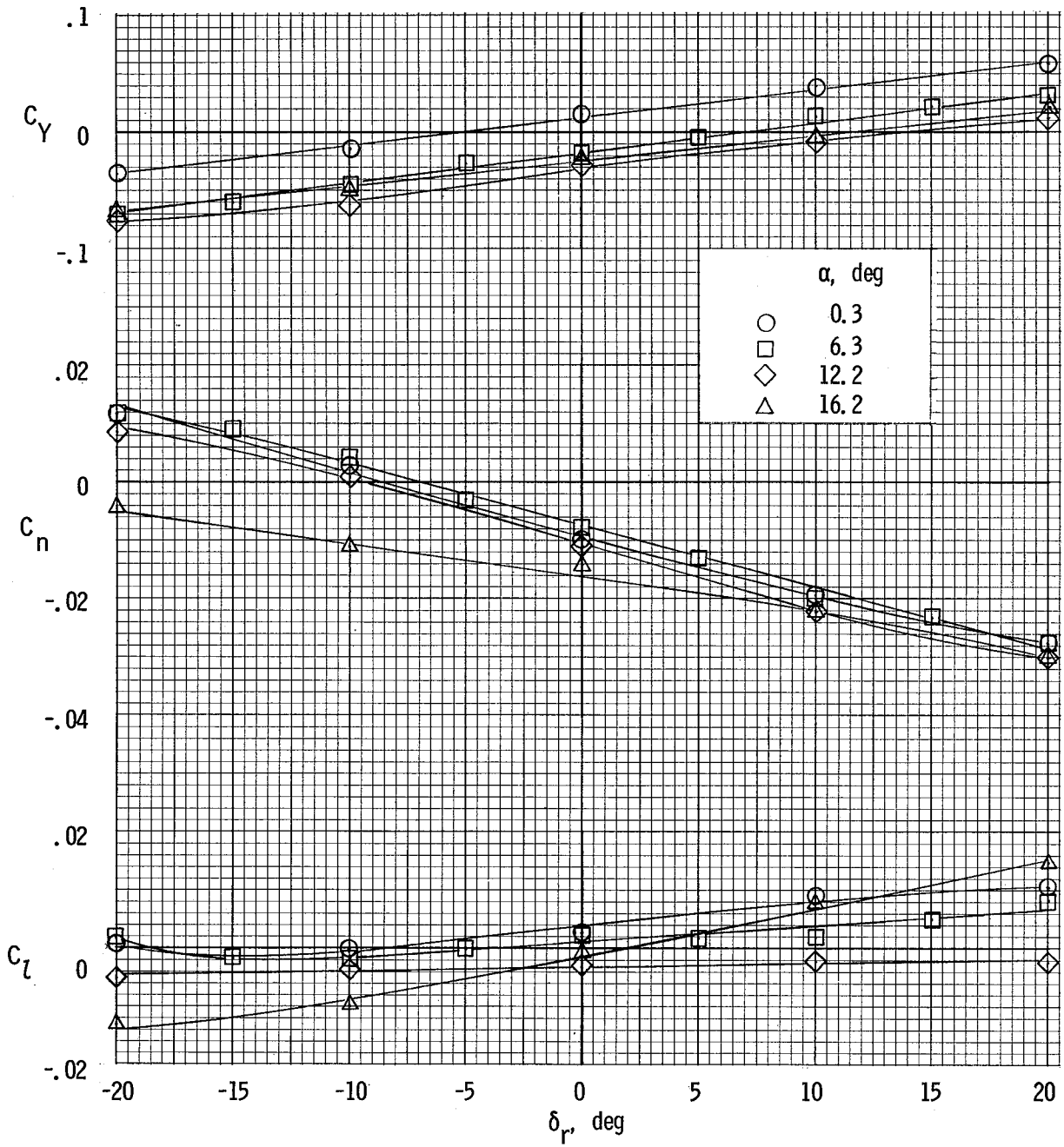
Figure 33.- Continued.

(e) $\beta = -8^0$.
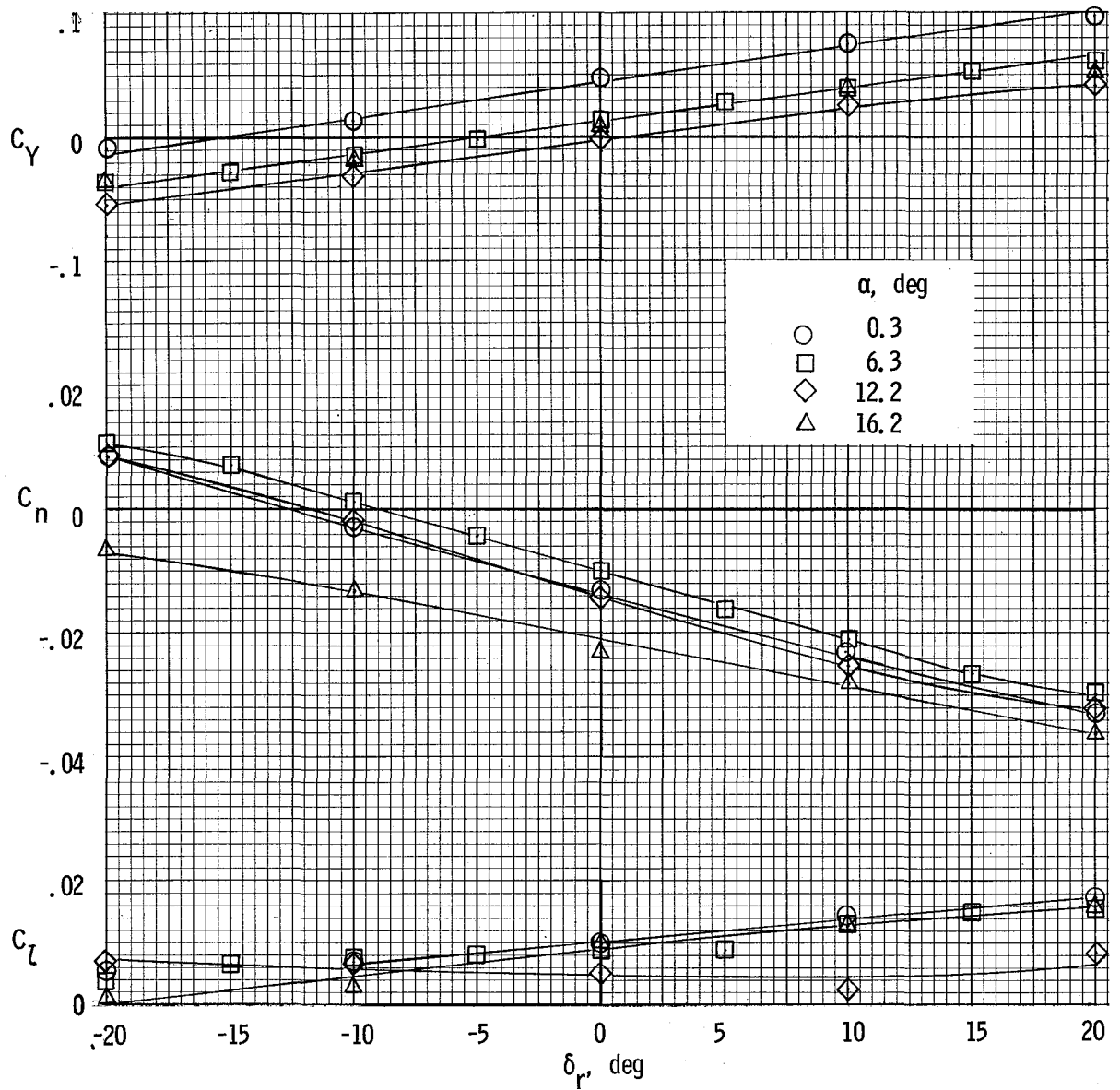
Figure 33.- Concluded.

(a) $\beta = 8^0$.
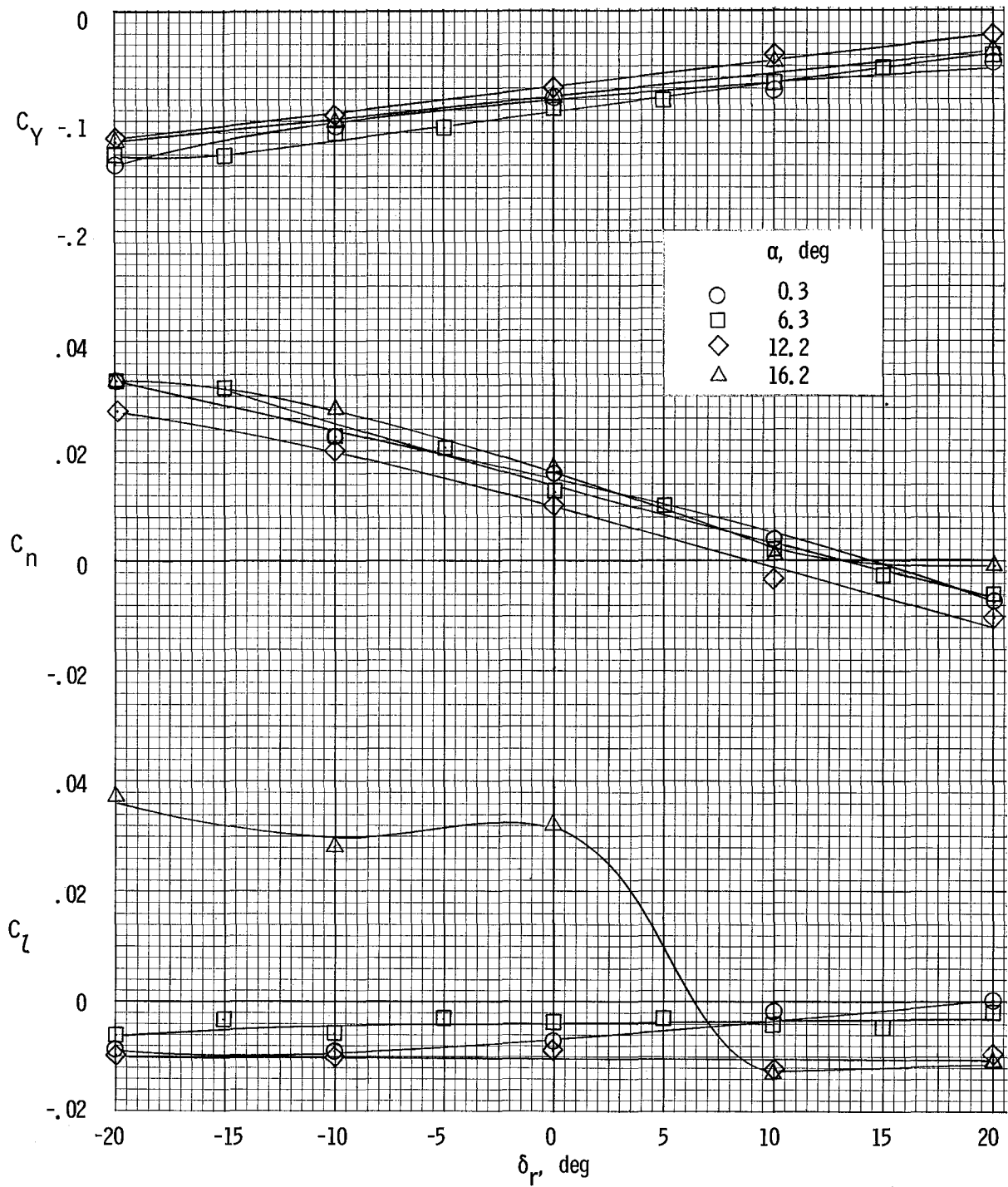
Figure 34.- Variation of lateral characteristics of airplane with rudder deflection. $\delta_f = 27^0$; $T'_c = 0$.
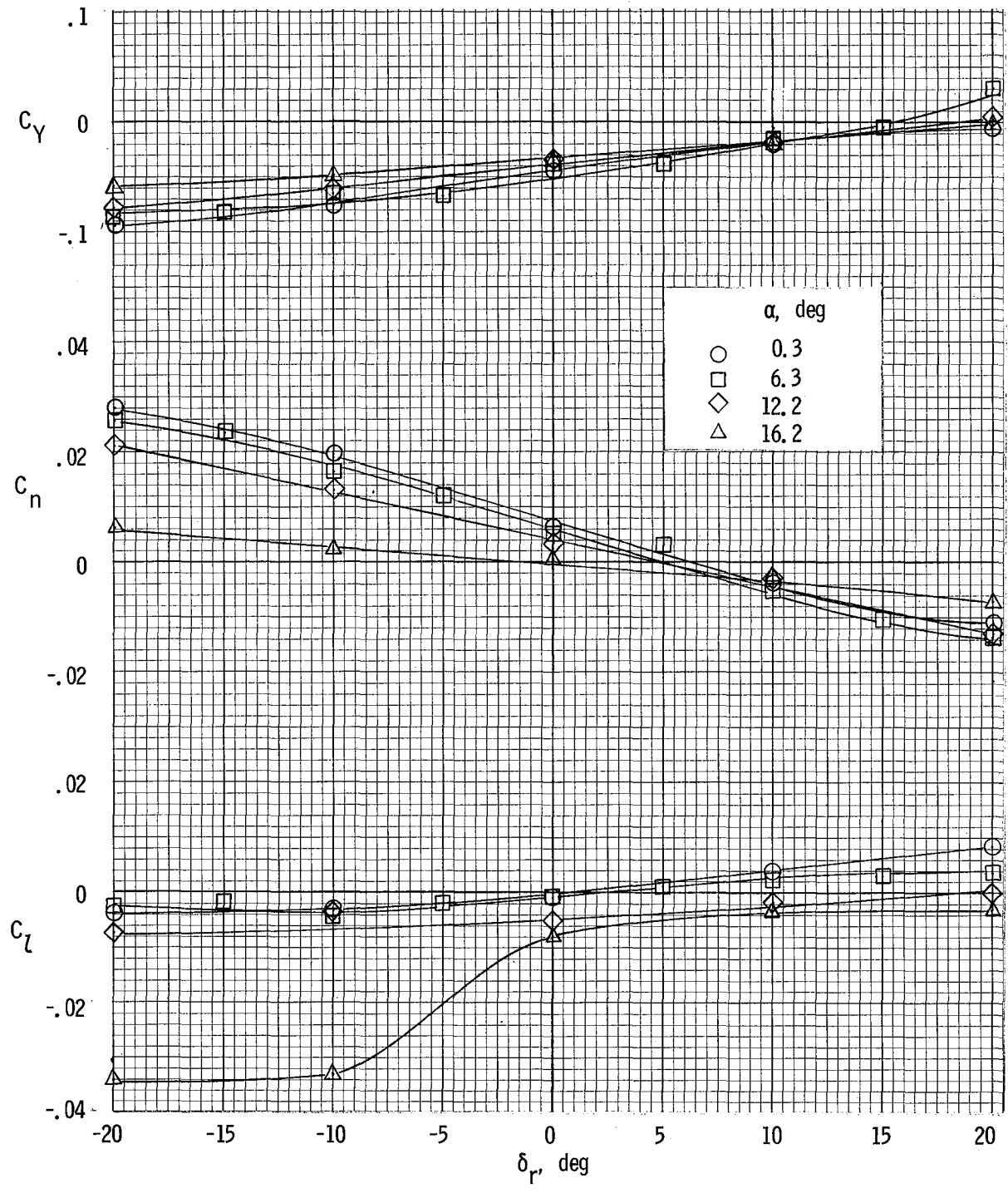
(b) $\beta = 4^\circ$.

Figure 34.- Continued.

112
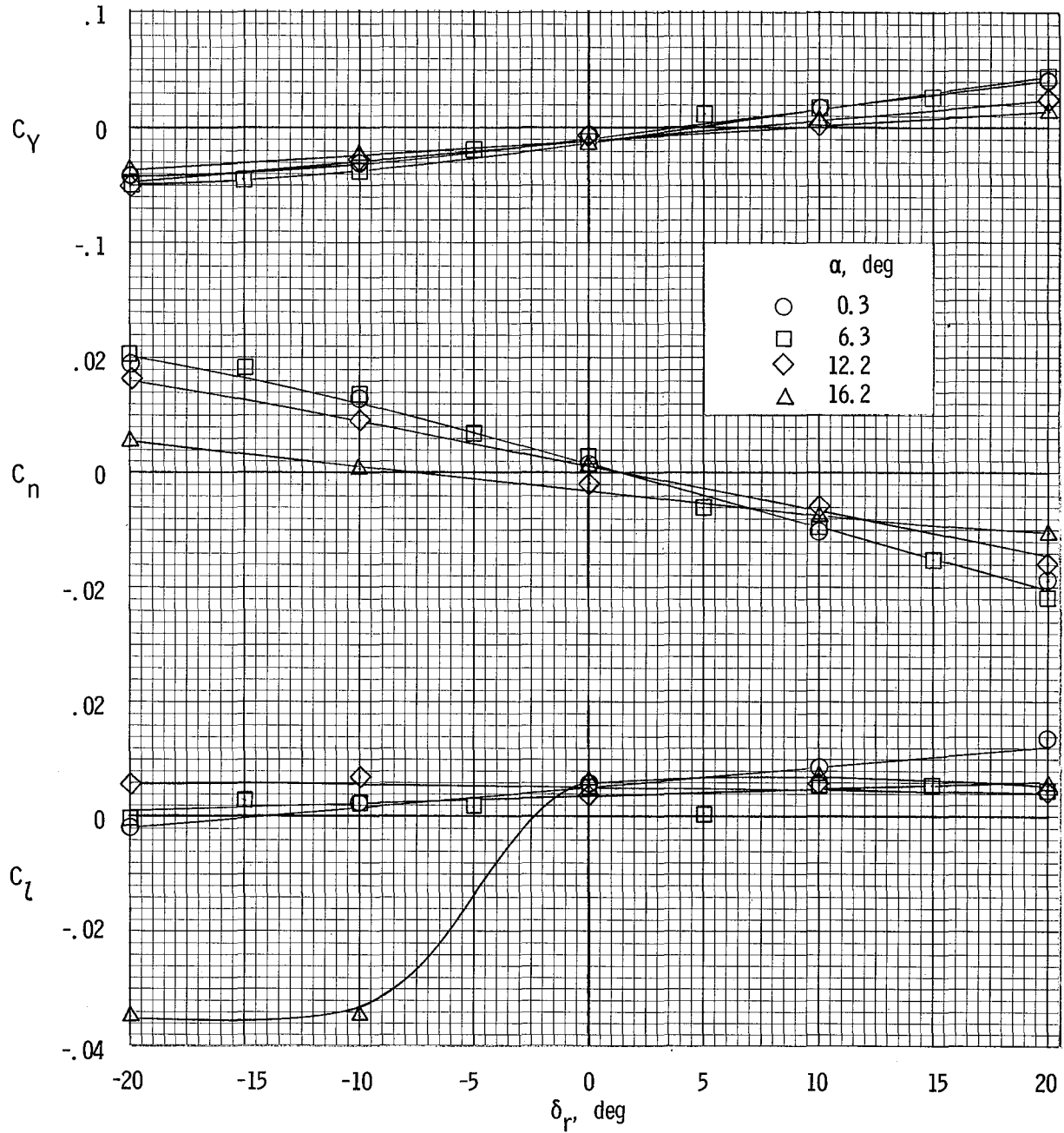
(c) $\beta = 0^\circ$.

Figure 34.- Continued.
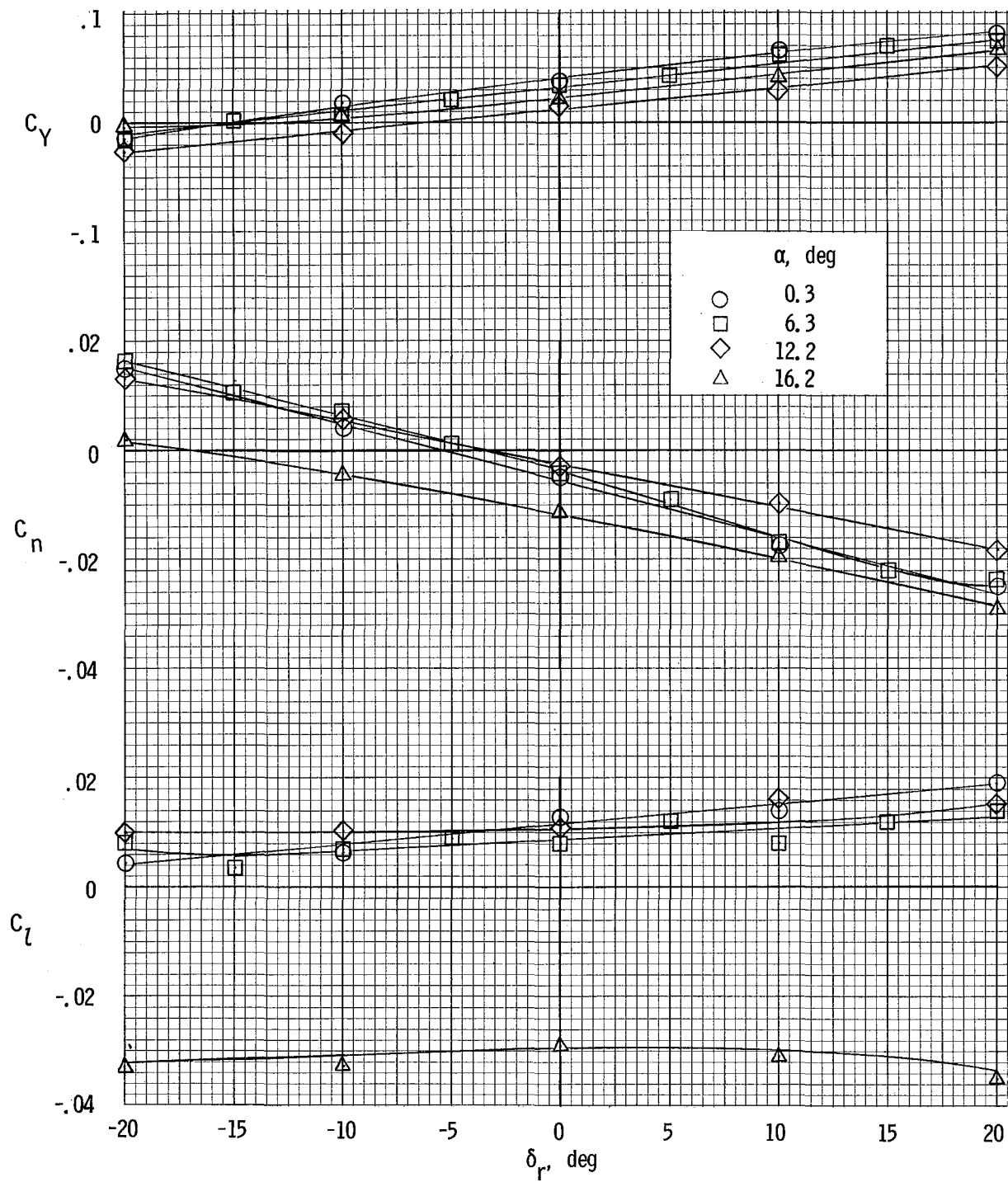
(d) $\beta = -4°$.

Figure 34.- Continued.

114
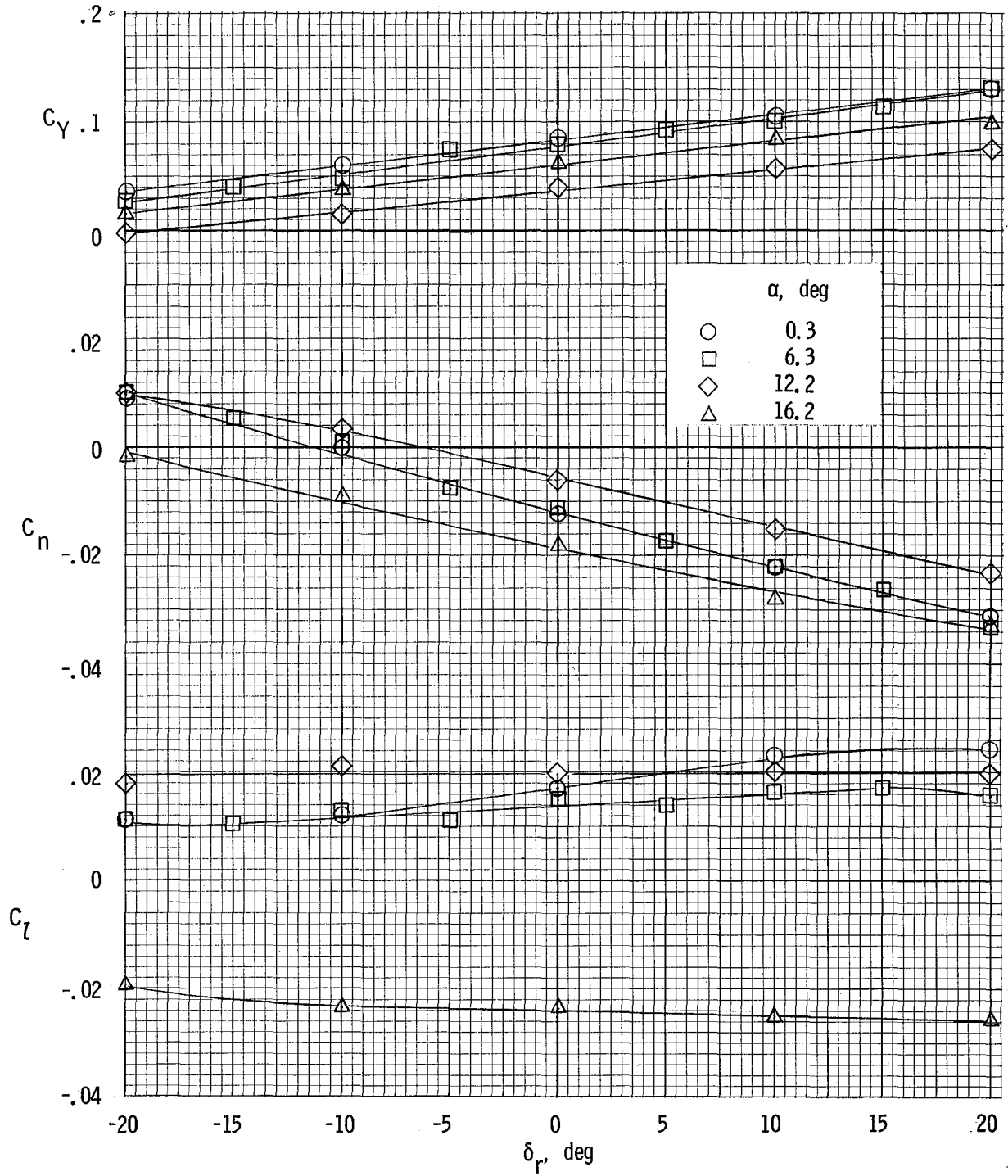
(e) β = -8°.

Figure 34.- Concluded.

(a) $\beta = 8^0$.
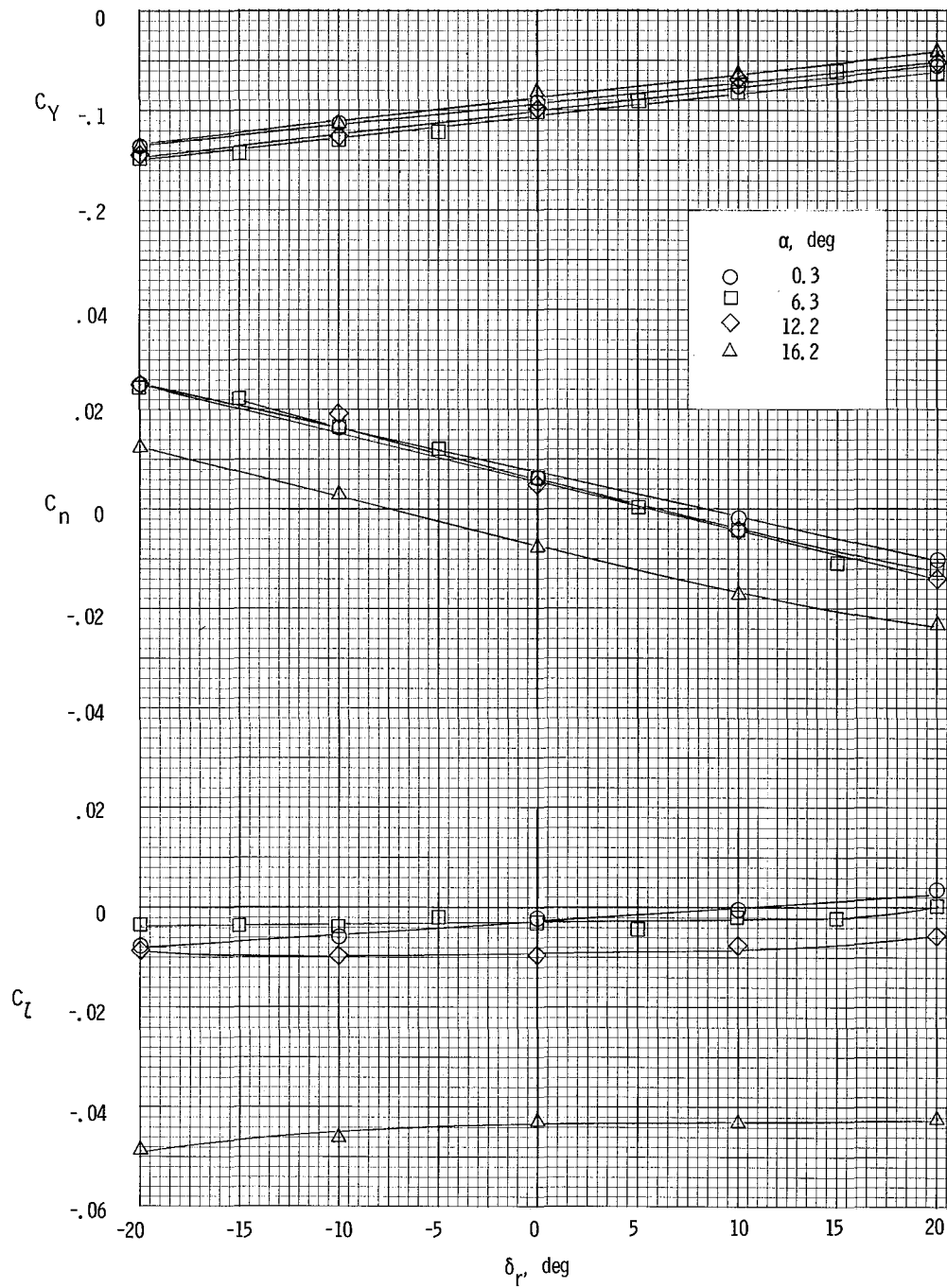
Figure 35.- Variation of lateral characteristics of airplane with rudder deflection. $\delta_f = 27^0$; $T_c' = 0.20$.
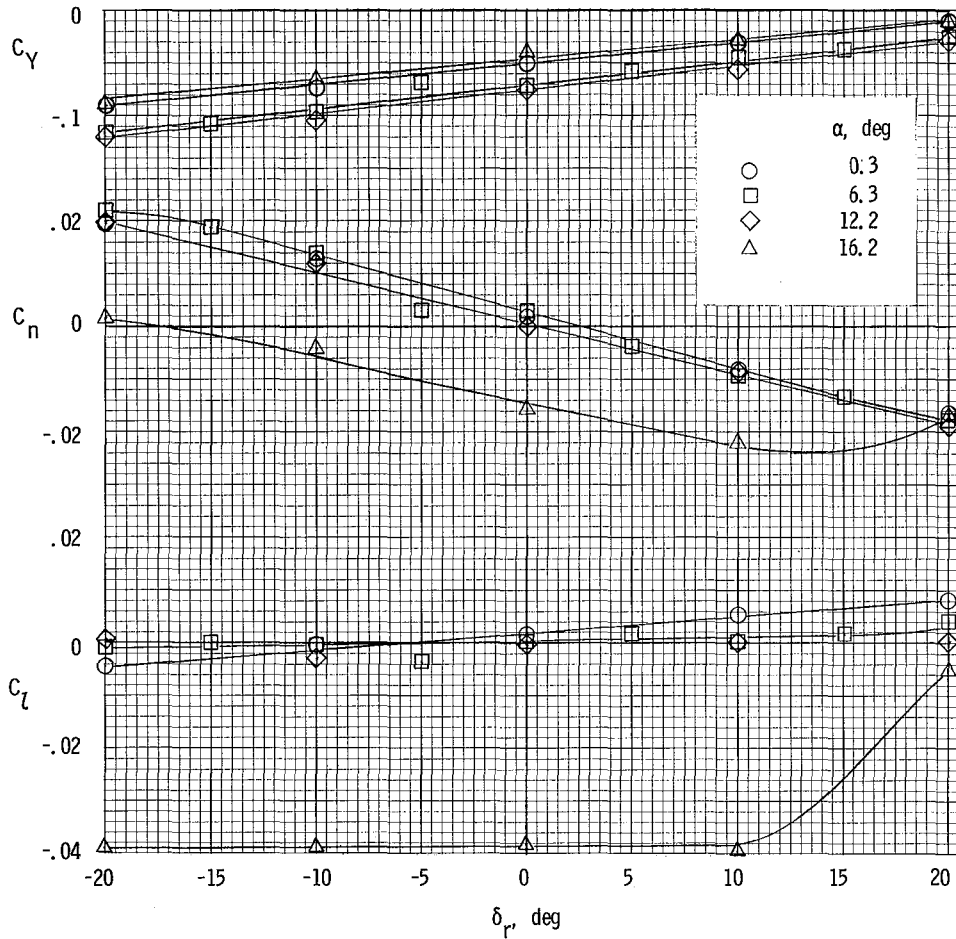
(b) $\beta = 4^\circ$.

Figure 35.- Continued.
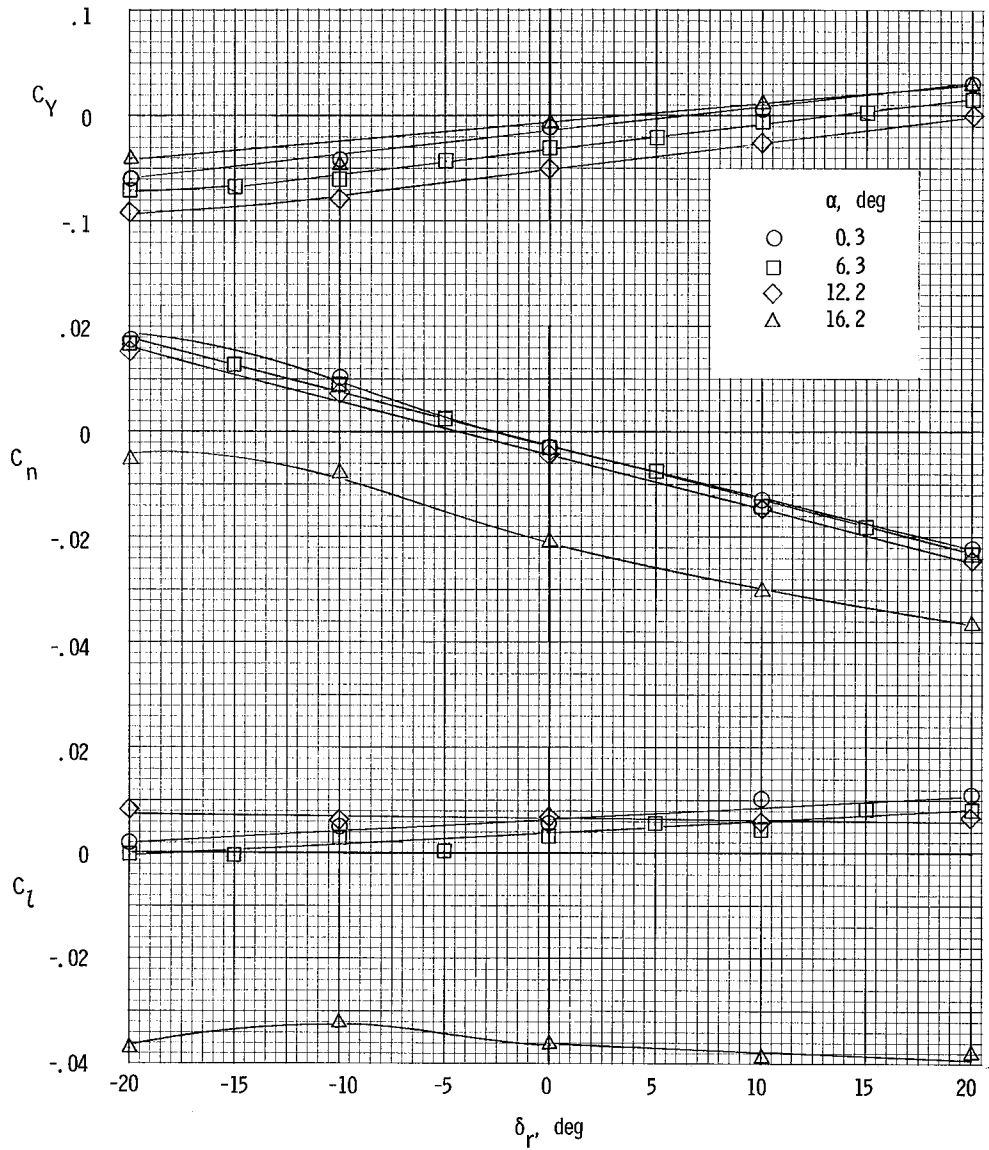
(c) β = 0°.

Figure 35.- Continued.

118
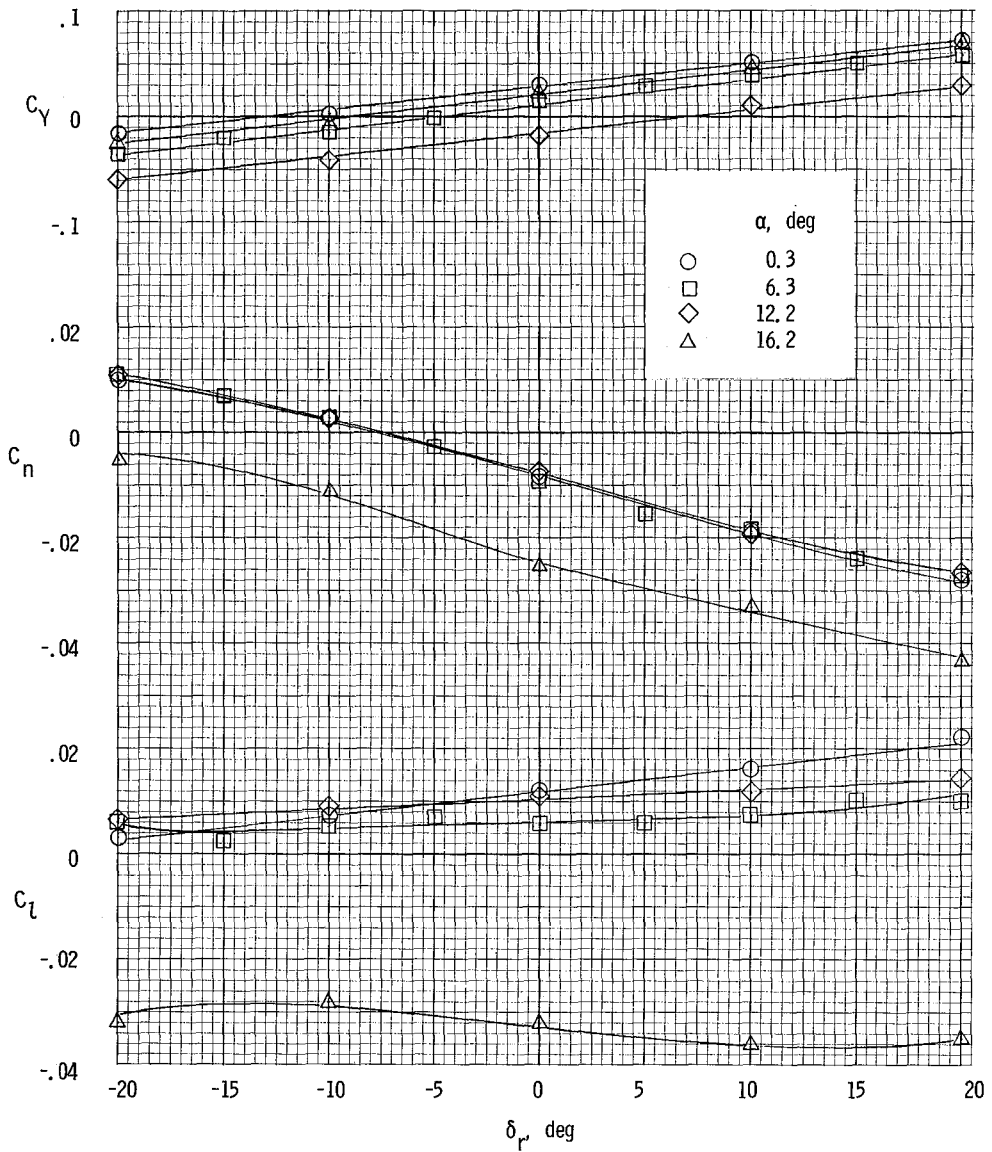
(d) $\beta = -4^\circ$.

Figure 35.- Continued.

(e) $\beta = -8^o$.
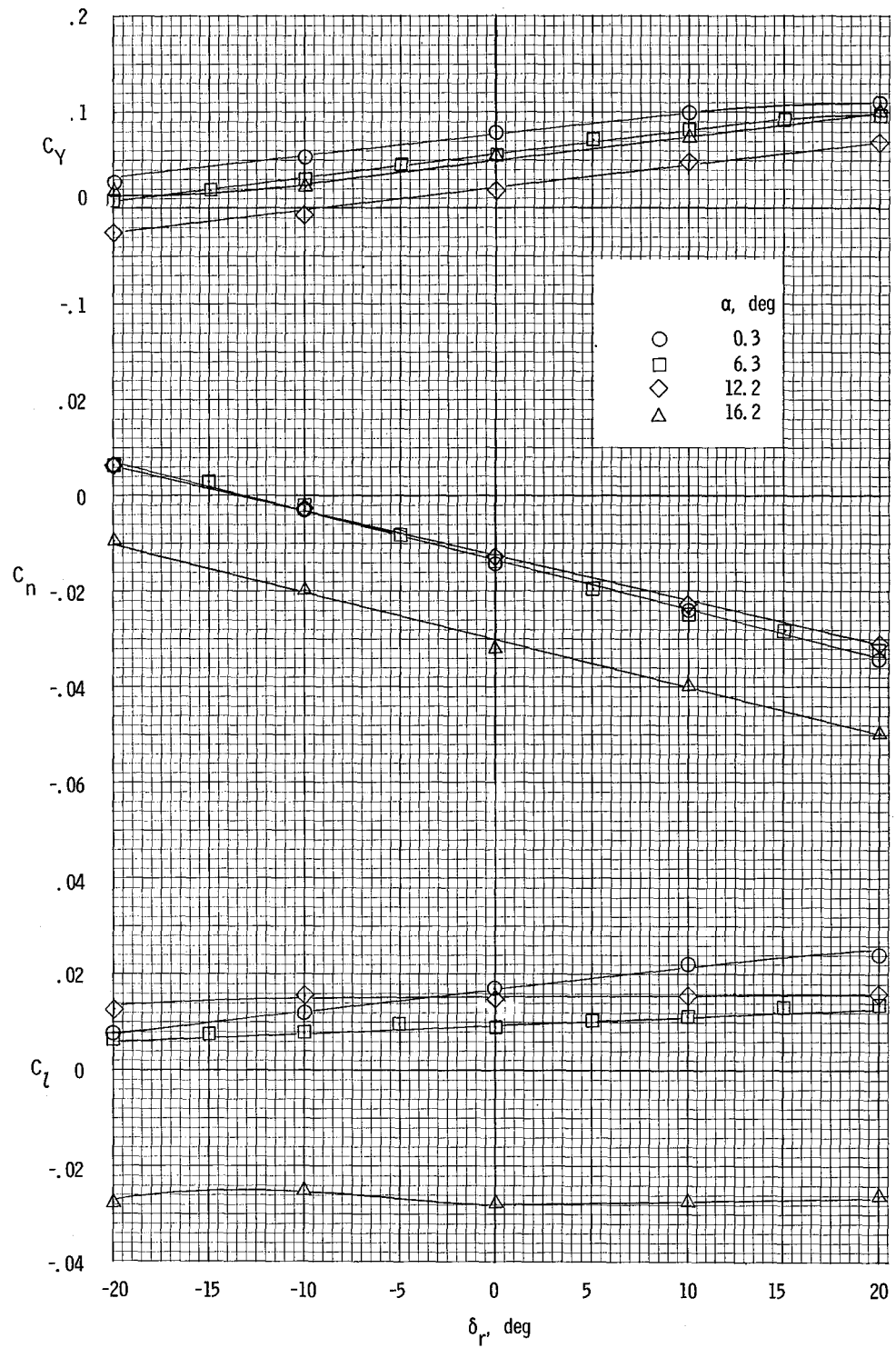
Figure 35.- Concluded.

(a) β = 8⁰.
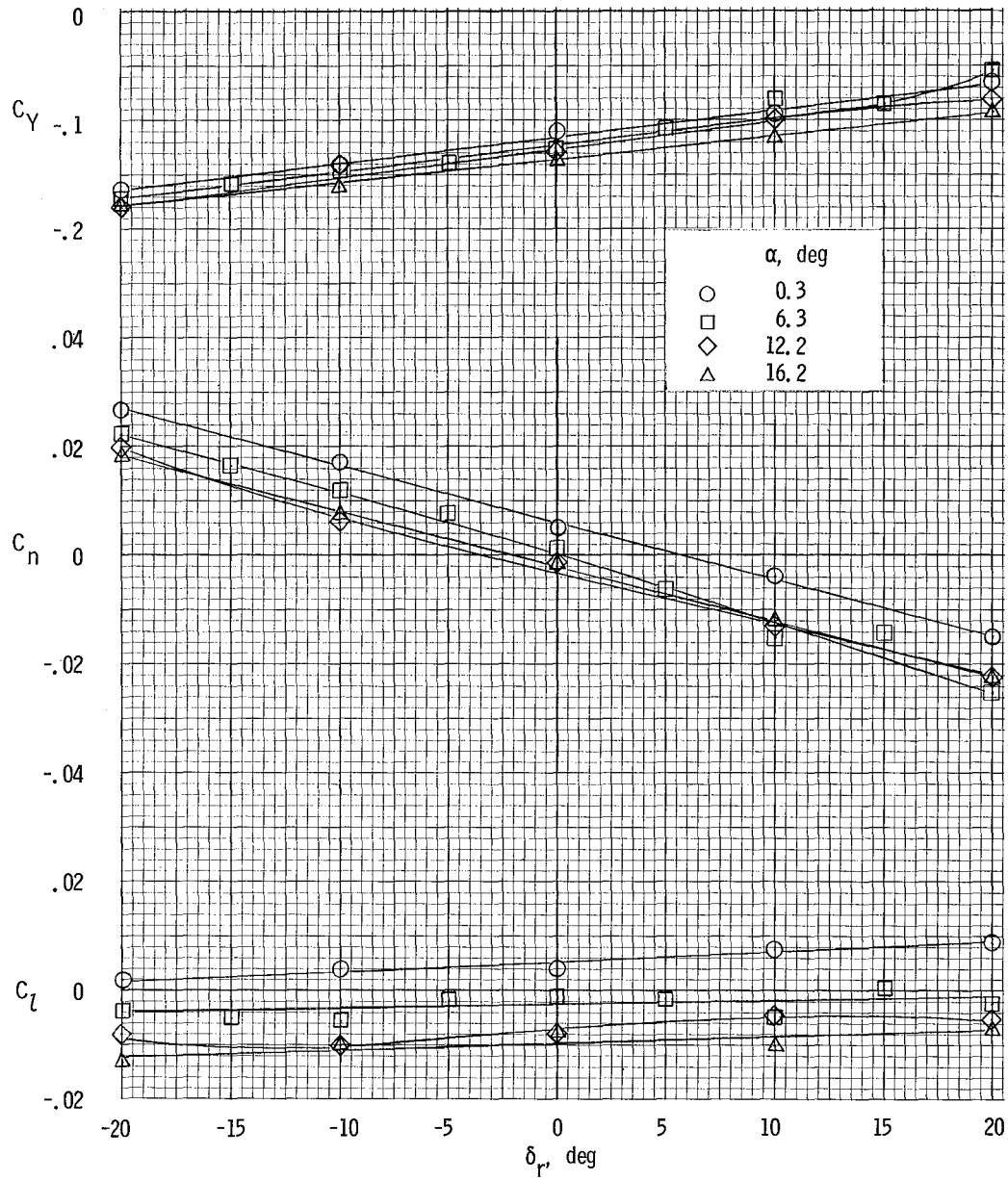
Figure 36.- Variation of lateral characteristics of airplane with rudder deflection. δ_f = 27⁰; T_c' = 0.44.

(b) β = 4°.

Figure 36.- Continued.
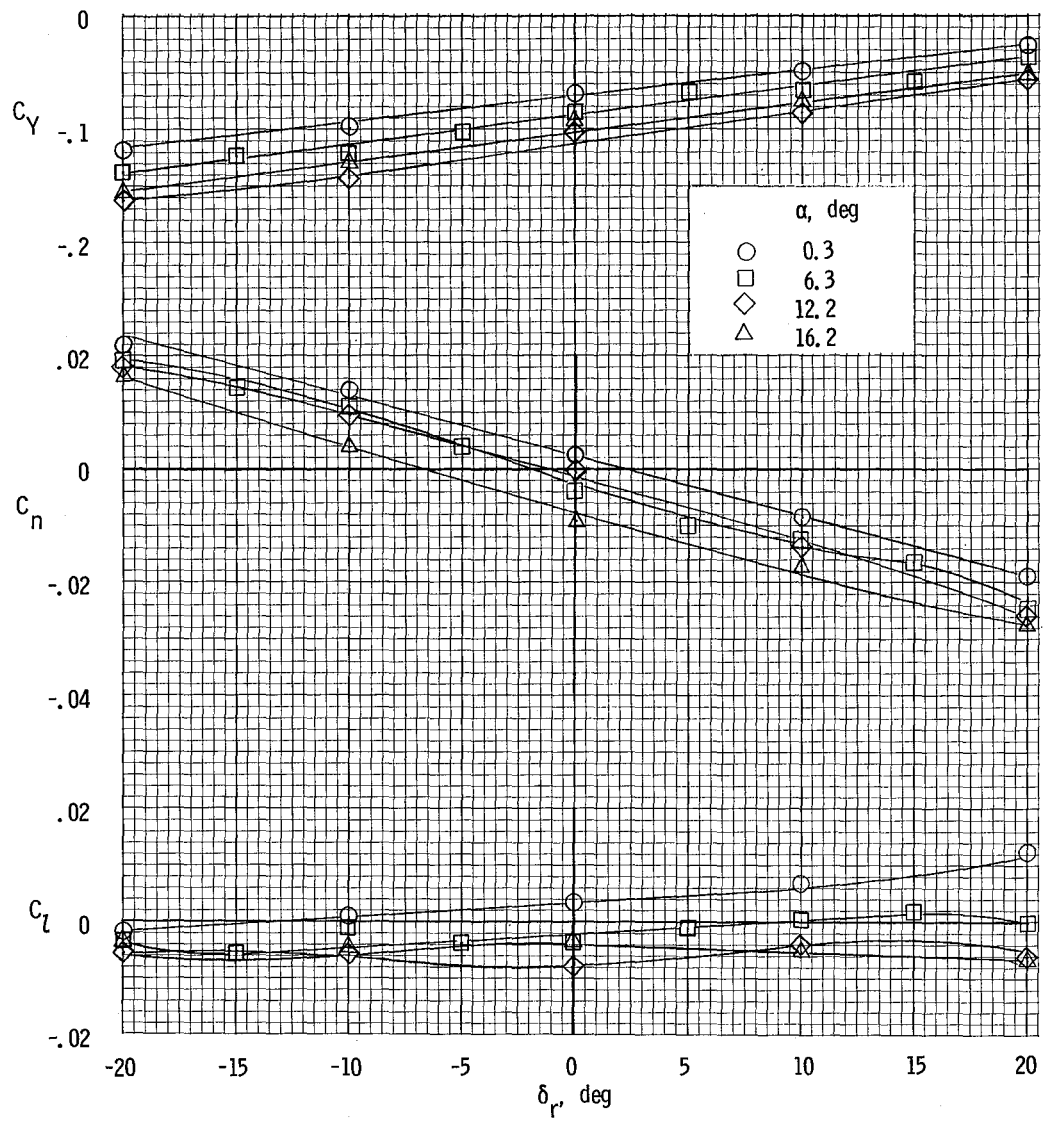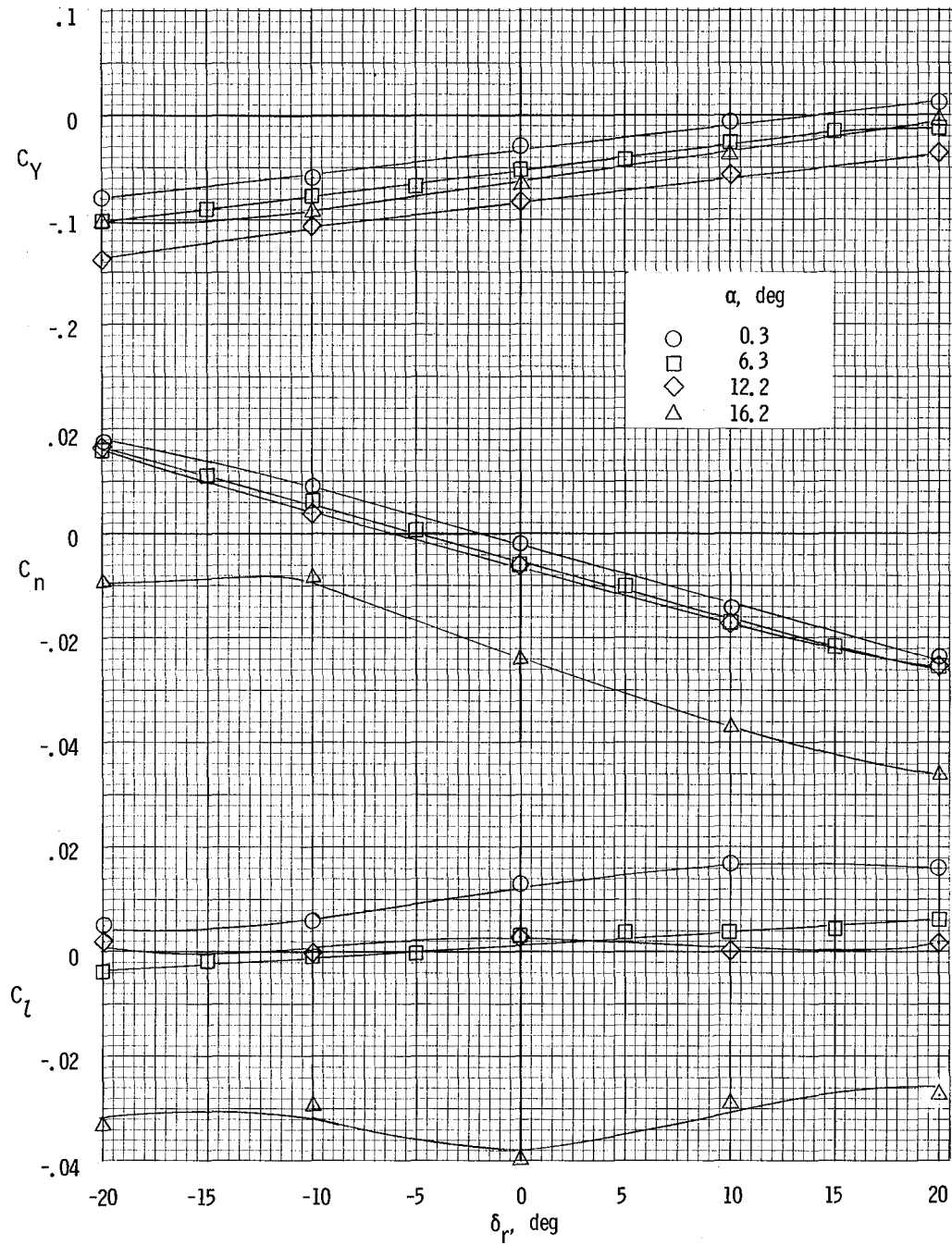
(c) β = 0°.

Figure 36.- Continued.

123

(d) β = -4°.
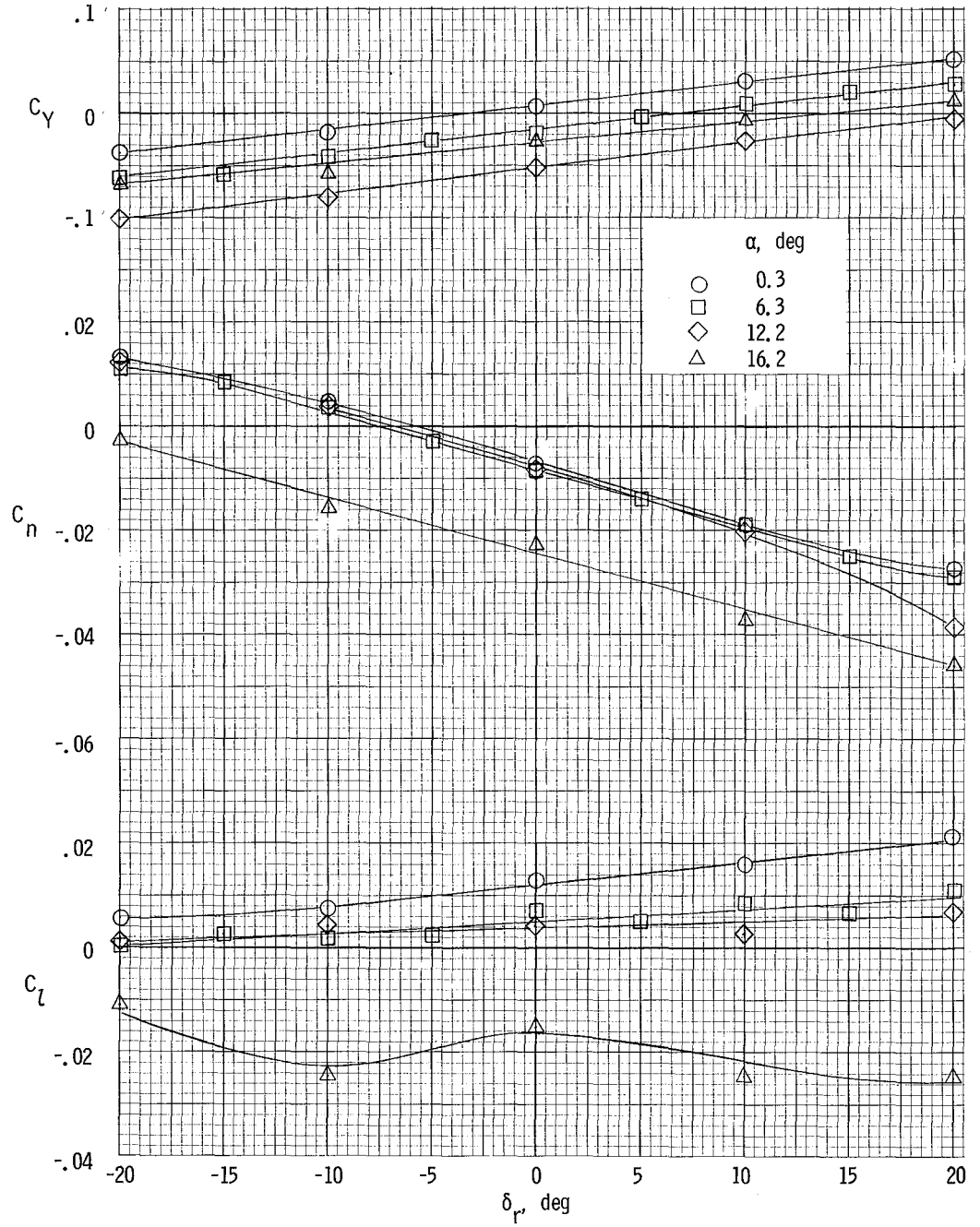
Figure 36.- Continued.

(e) $\beta = -8^0$.
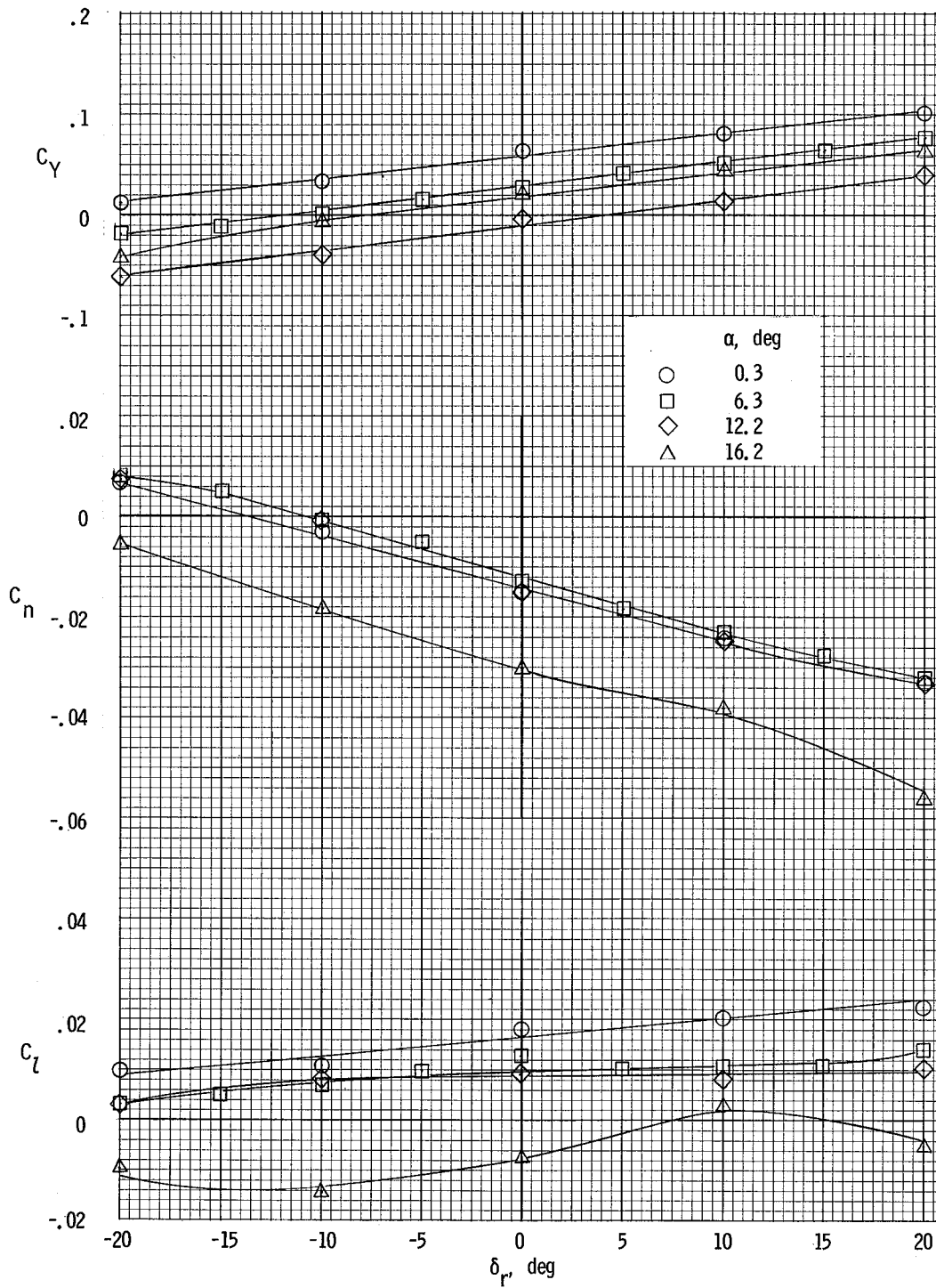
Figure 36.- Concluded.

(a) $\beta = 8^0$.
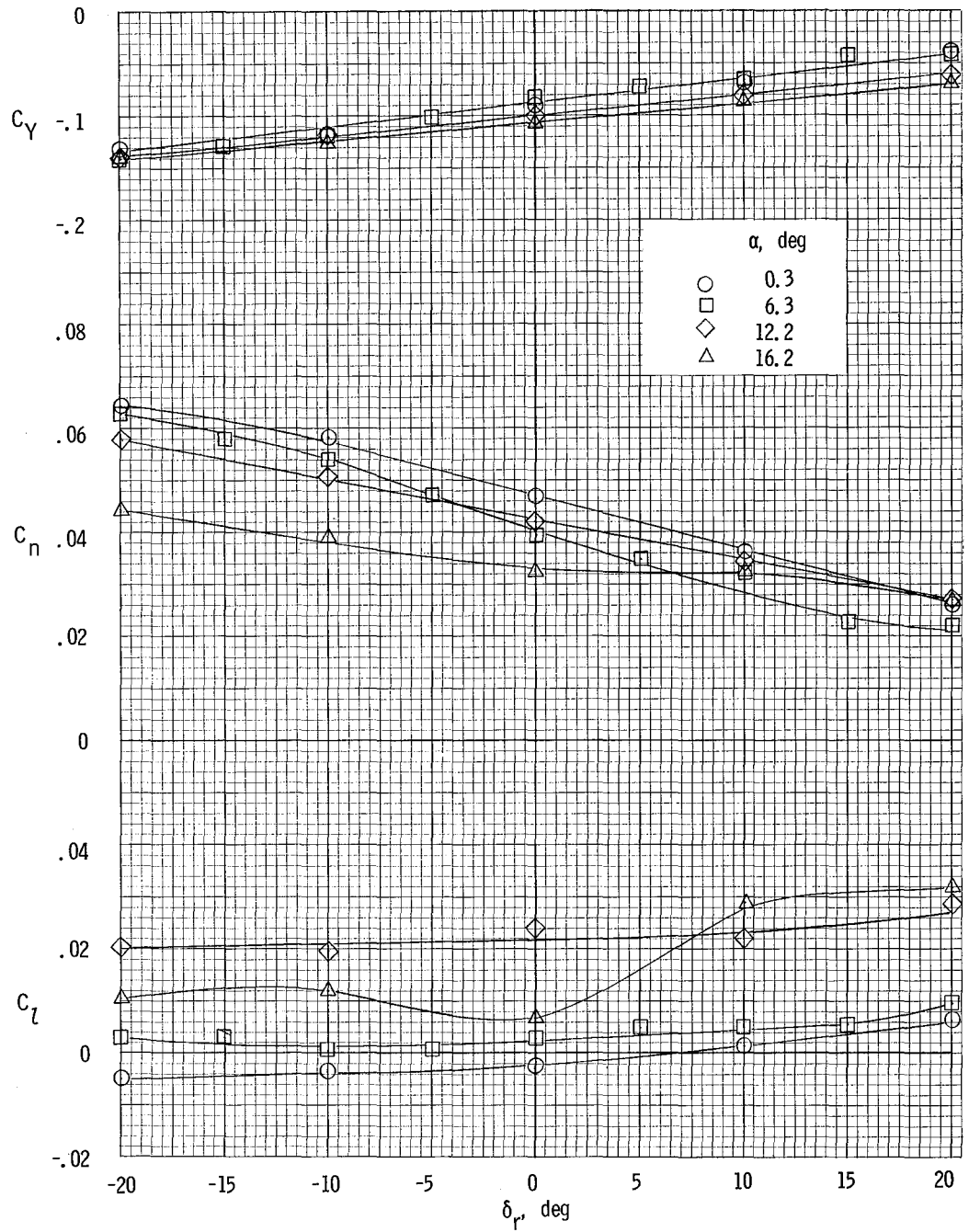
Figure 37.- Variation of lateral characteristics of airplane with rudder deflection for asymmetric power. $\delta_f = 0^0$. Left engine full; right engine feathered.
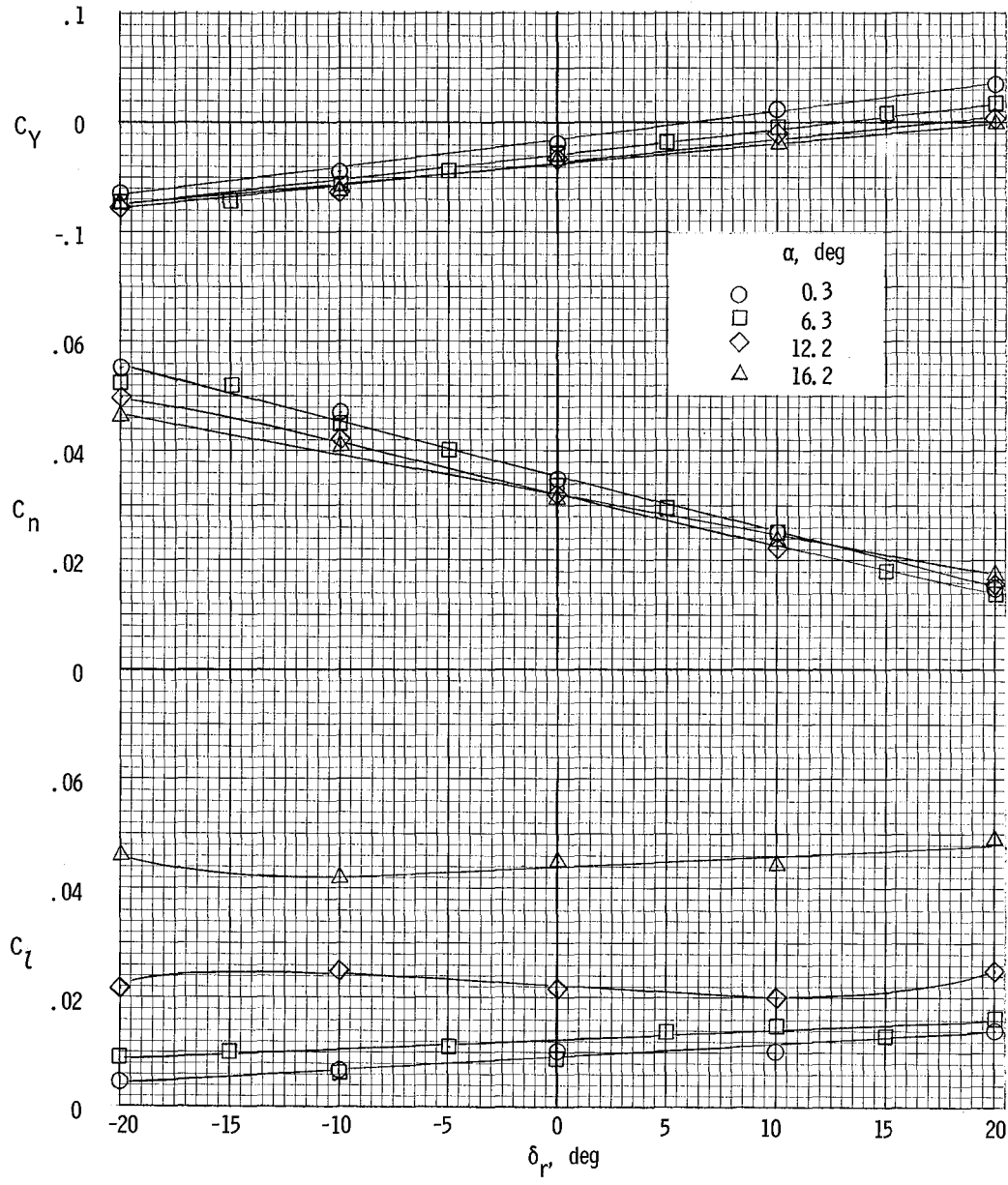
(b) $\beta = 0^0$.

Figure 37.- Continued.

(c) $\beta = -8^0$.
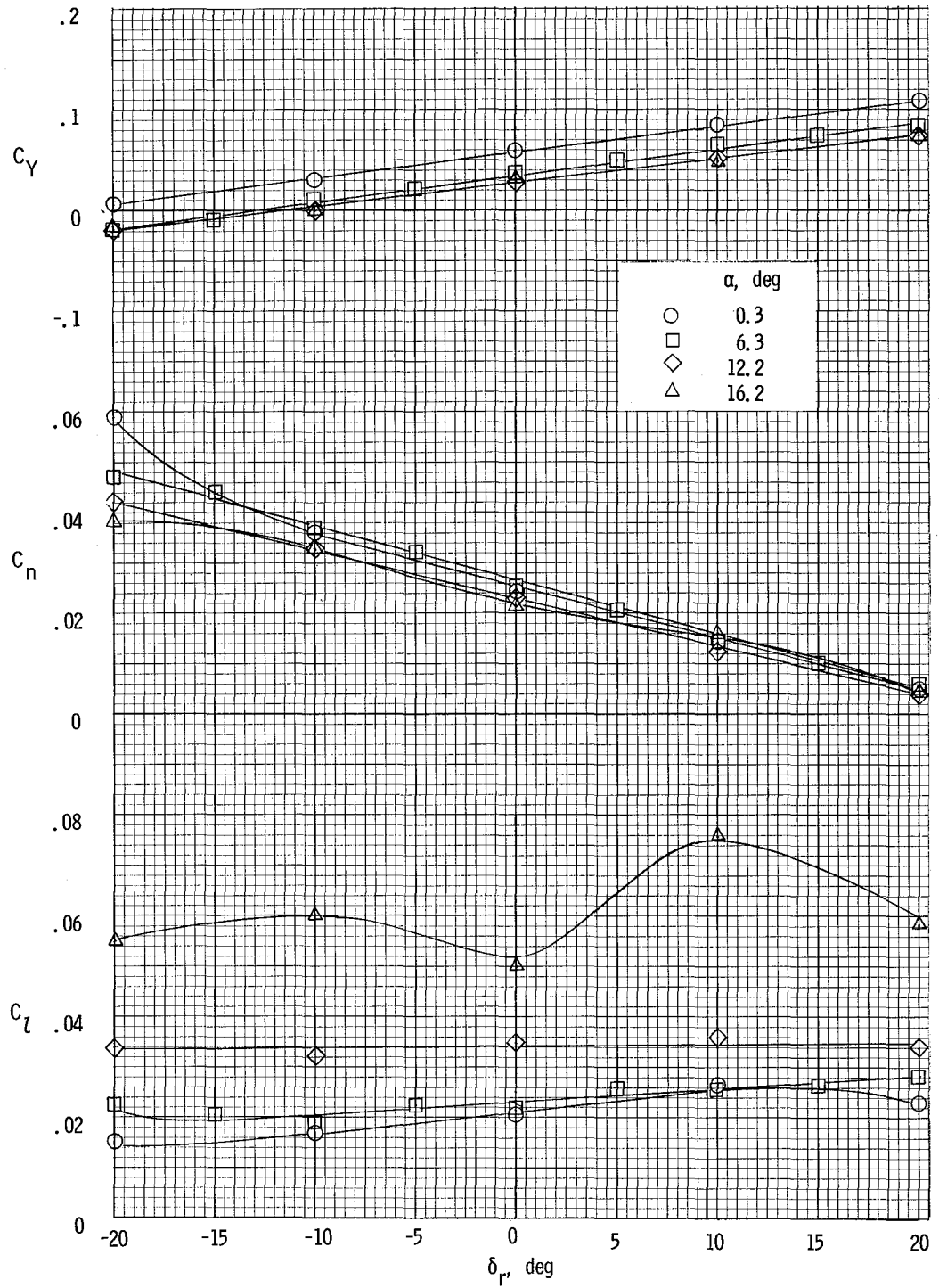
Figure 37.- Concluded.

(a) $\beta = 8^o$.
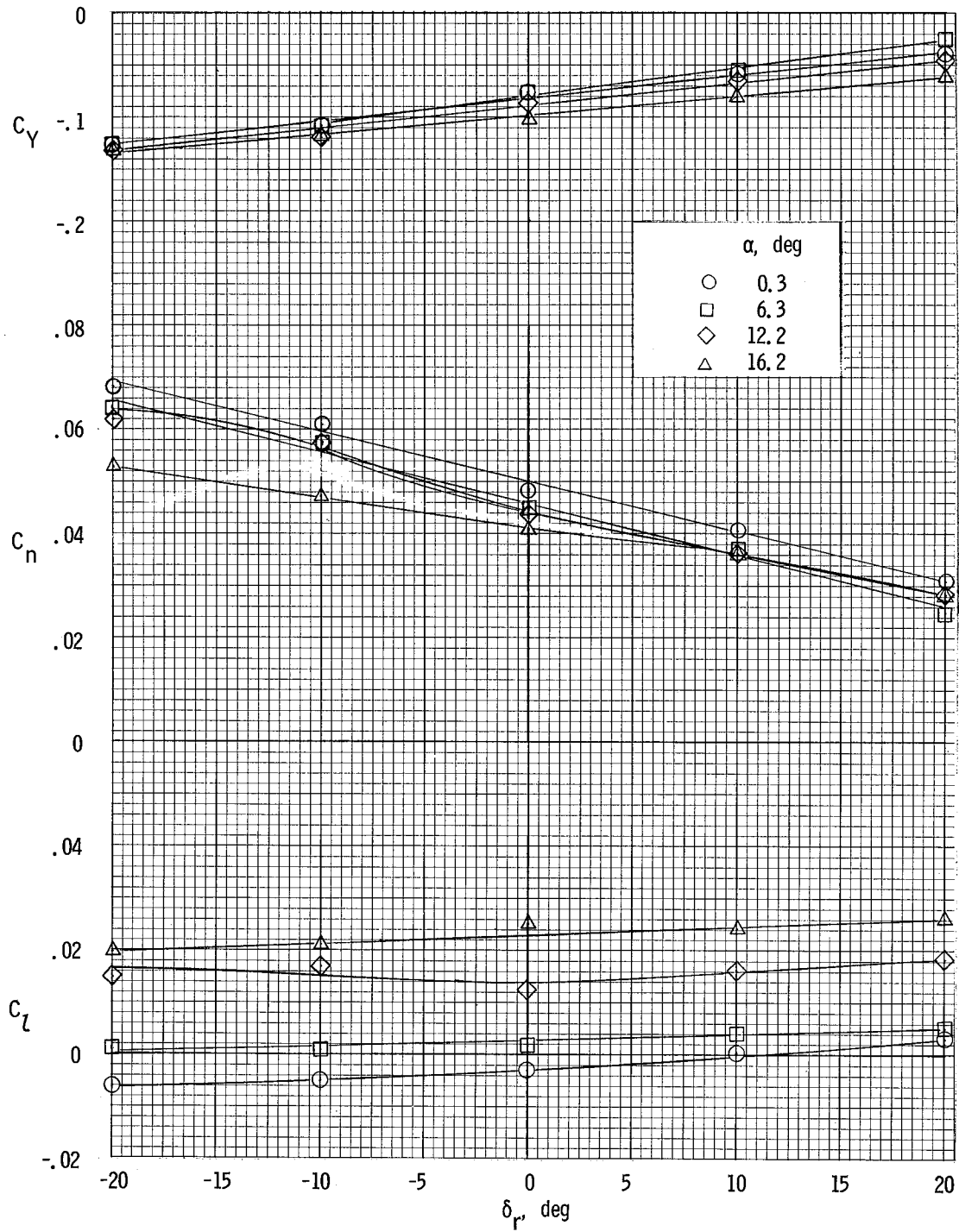
Figure 38.- Variation of lateral characteristics of airplane with rudder deflection for asymmetric power. $\delta_f = 0^o$. Left engine full; right engine windmilling.
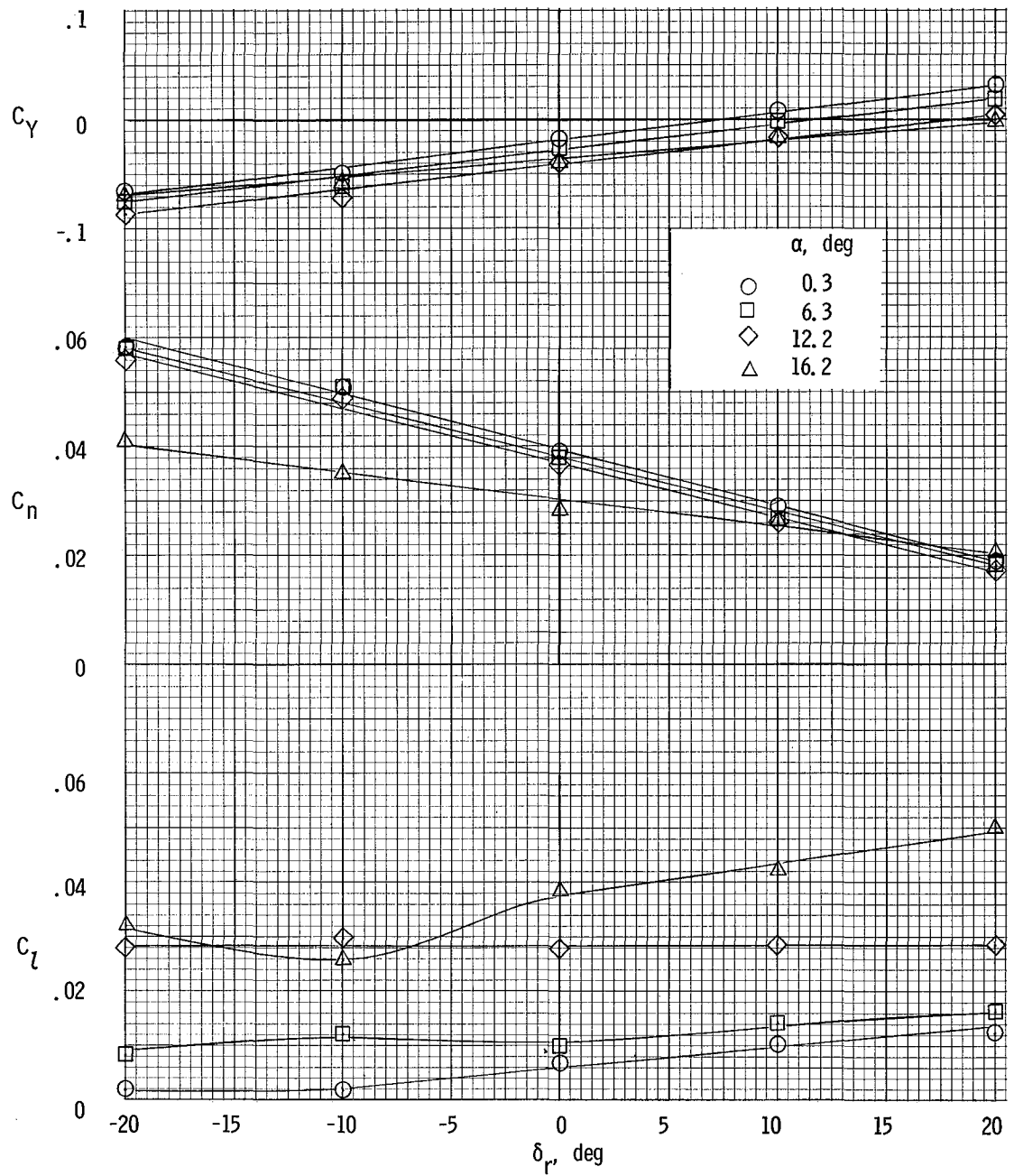
(b) $\beta = 0^0$.

Figure 38.- Continued.

130
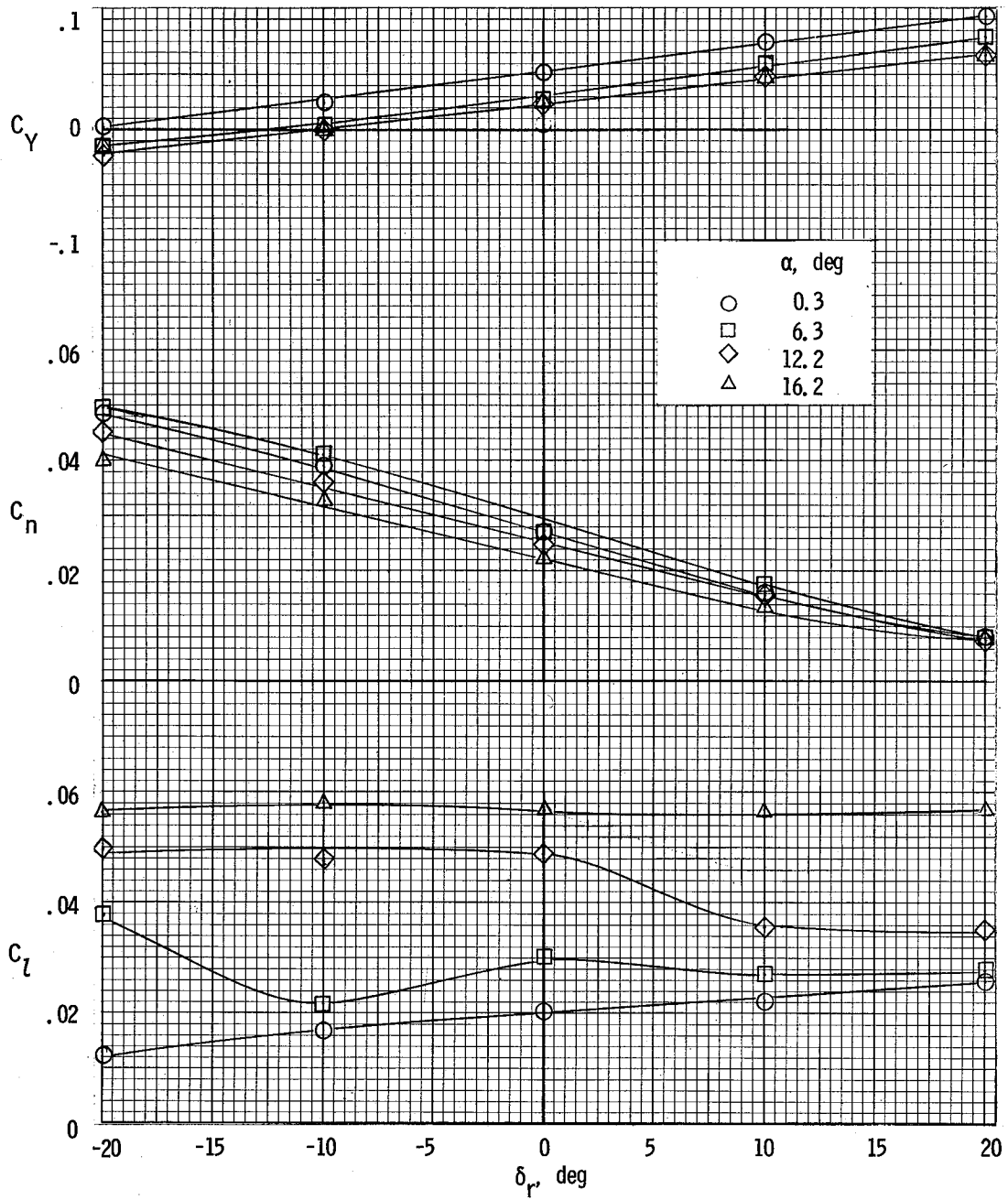
(c) β = -8°.

Figure 38.- Concluded.

(a) β = 8⁰.

Figure 39.- Variation of lateral characteristics of airplane with rudder deflection for asymmetric power. δf = 0⁰. Right engine full; left engine feathered.
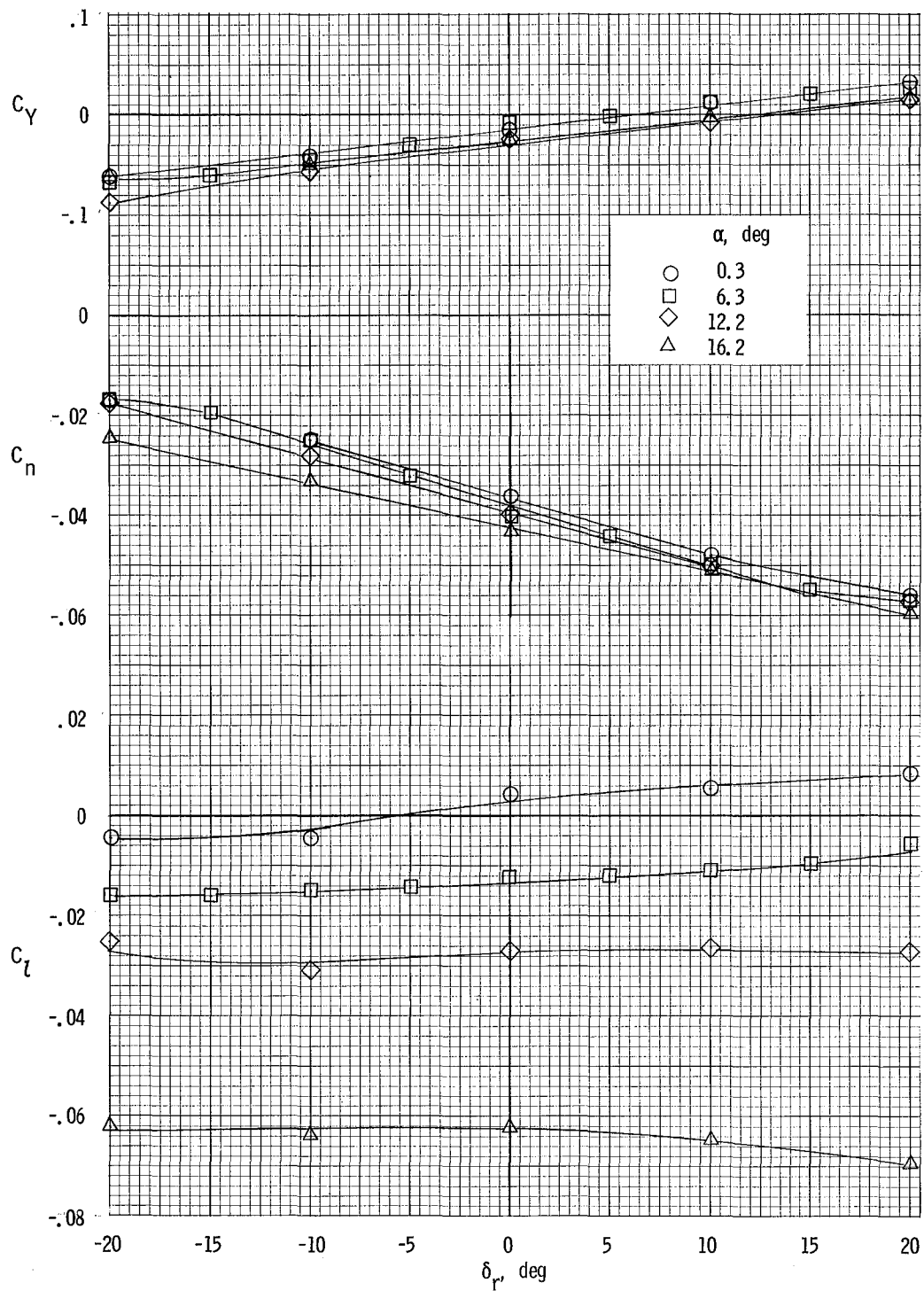
(b) β = 0°.

Figure 39.- Continued.

133

(c) $\beta = -8^0$.
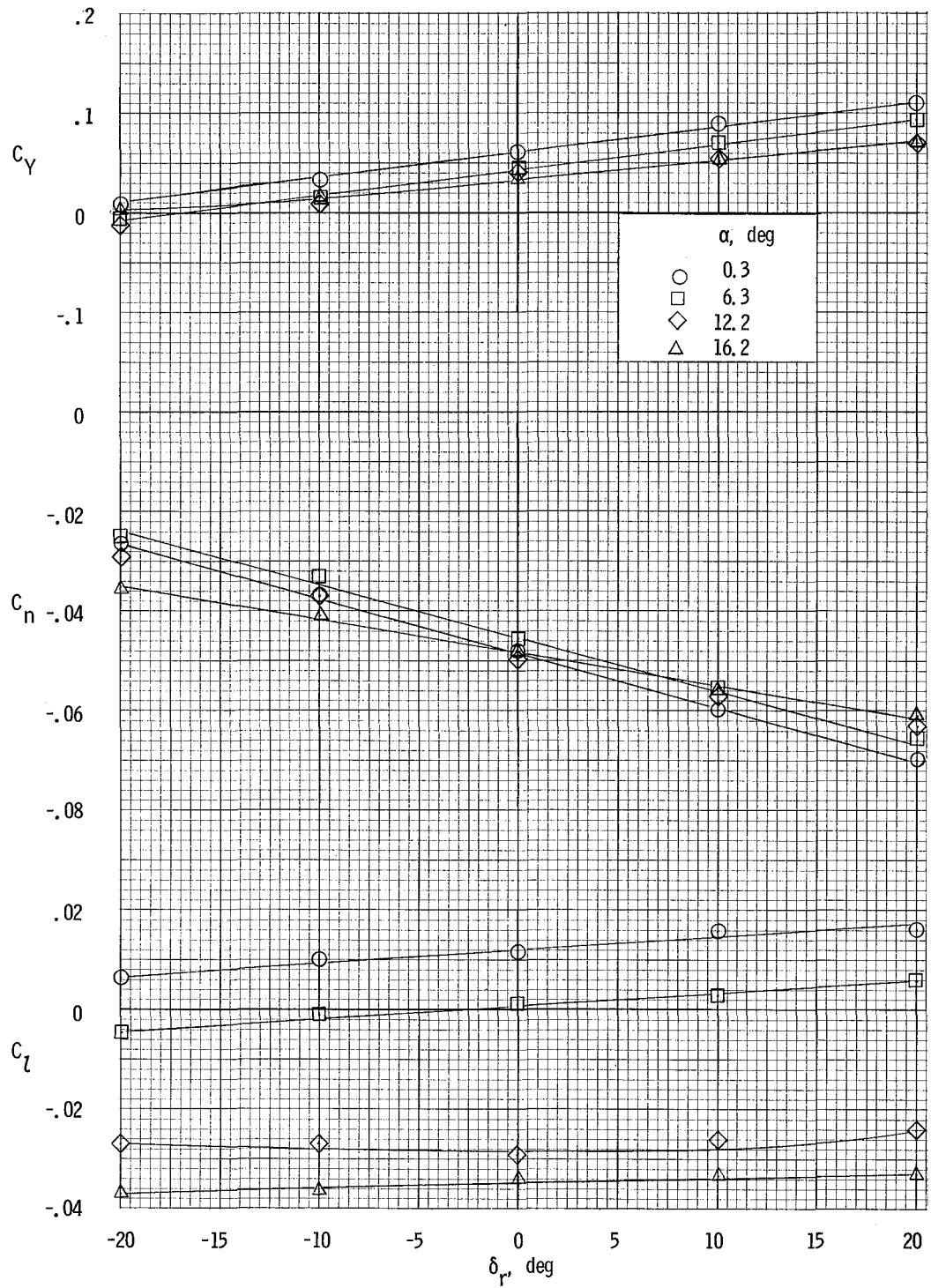
Figure 39.- Concluded.

134

(a) $\beta = 8^0$.

Figure 40.- Variation of lateral characteristics of airplane with rudder deflection for asymmetric power. $\delta_f = 0^0$. Right engine full; left engine windmilling.

(b) $\beta = 0^0$.

Figure 40.- Continued.

(c) $\beta = -8^0$.
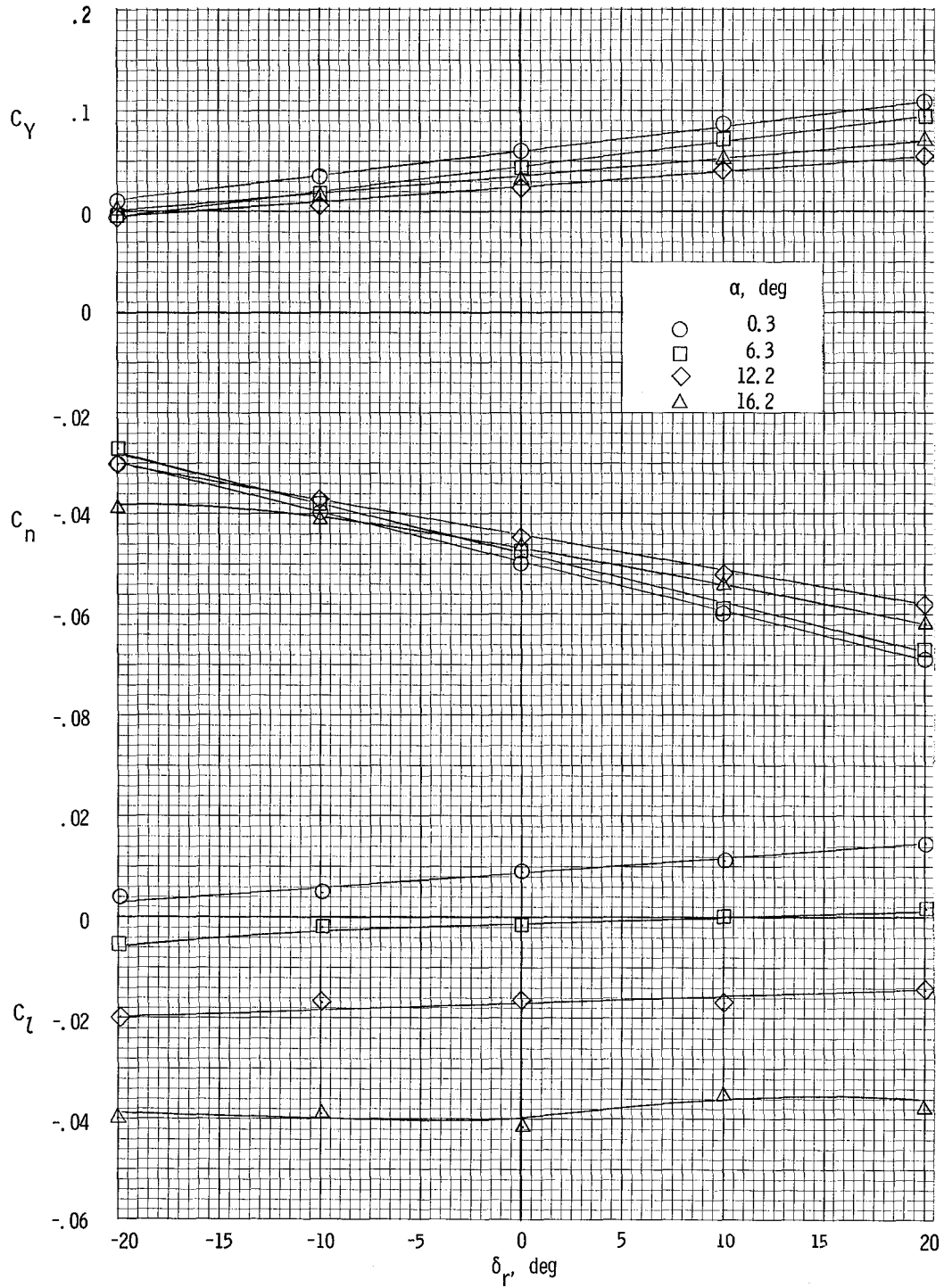
Figure 40.- Concluded.
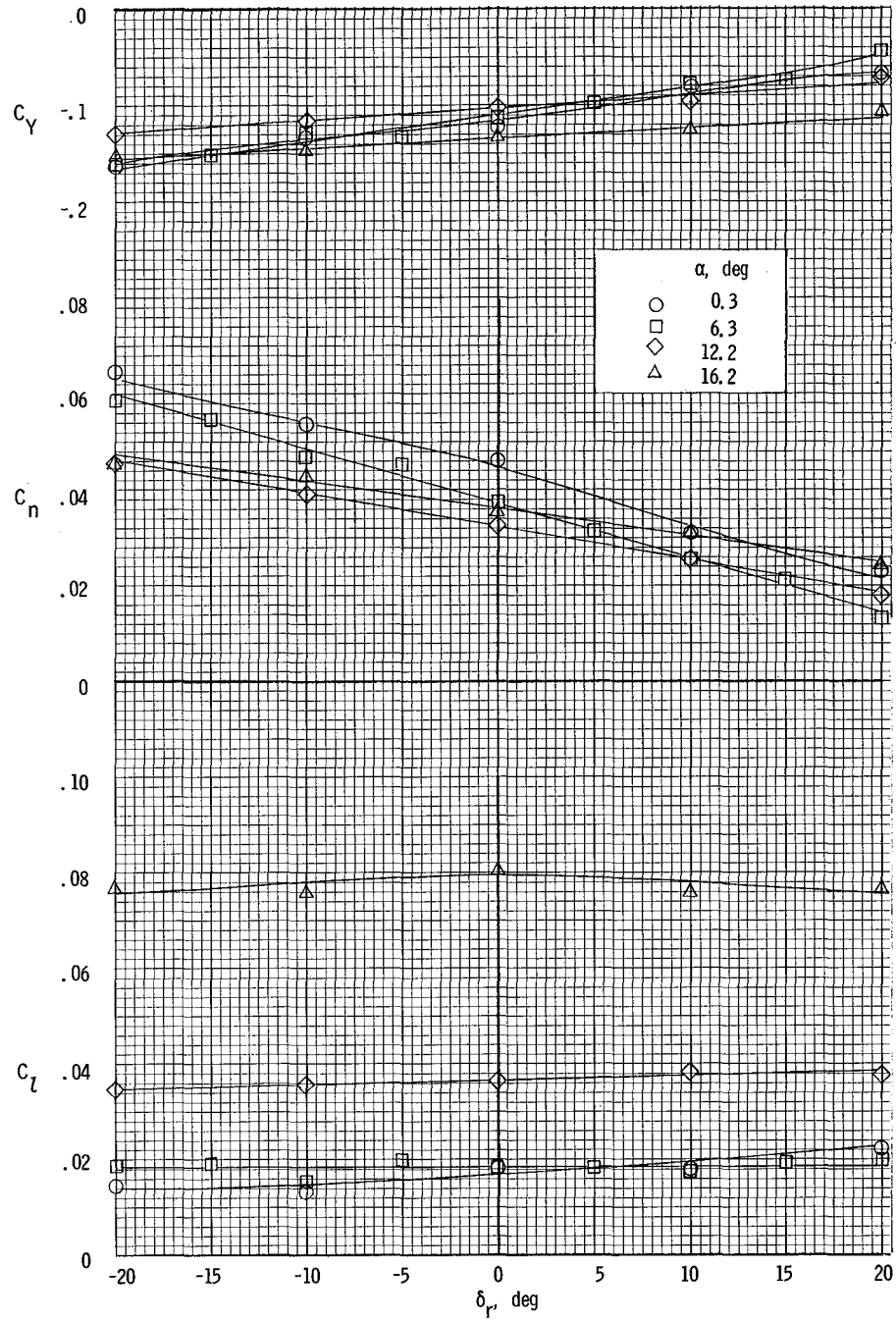
(a) β = 8°.

Figure 41.- Variation of lateral characteristics of airplane with rudder deflection for asymmetric power. δ_f = 27°. Left engine full; right engine feathered.

(b) $\beta = 0^0$.

Figure 41.- Continued.

(c) $\beta = -8^0$.
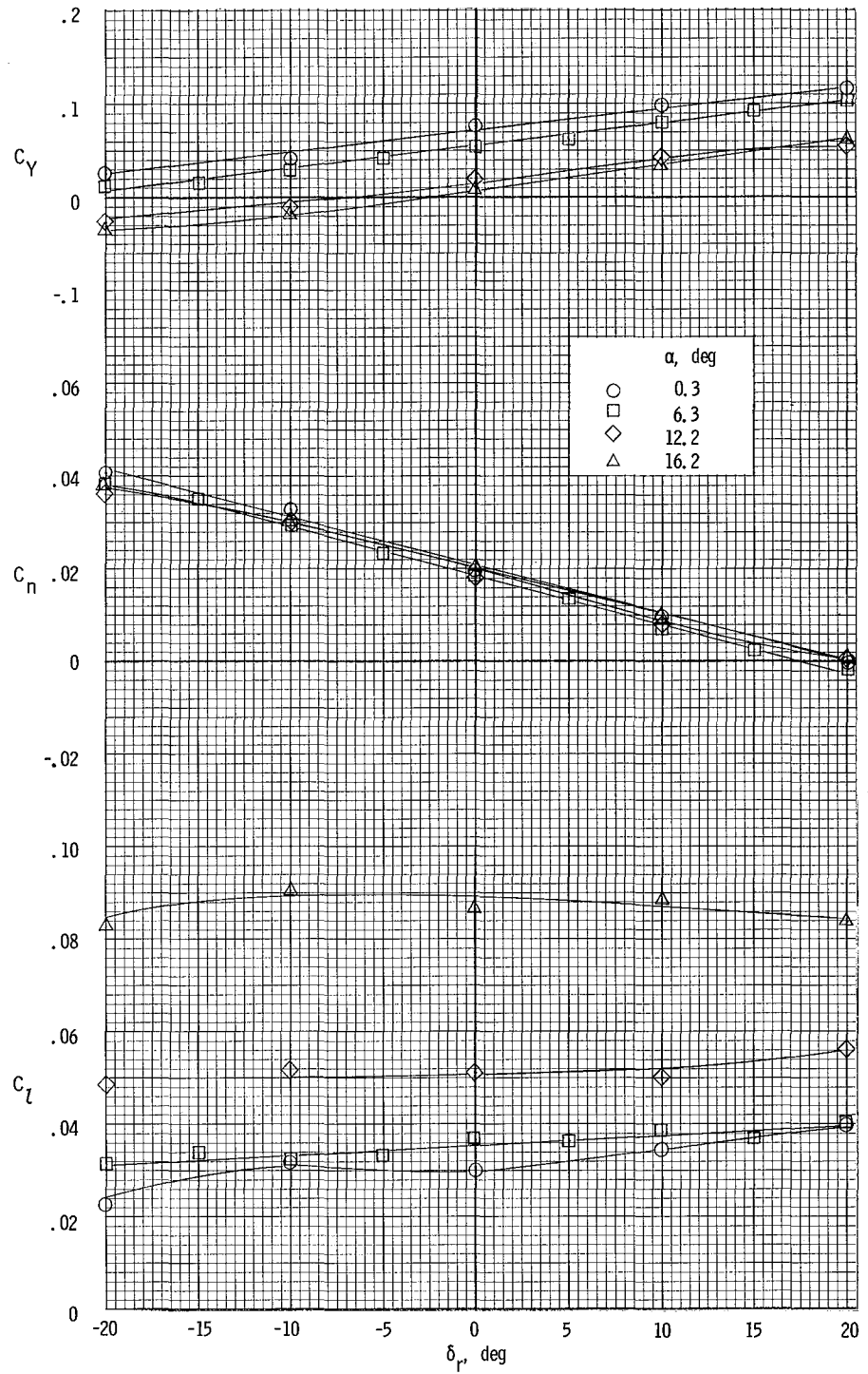
Figure 41.- Concluded.

(a) β = 8°.

Figure 42.- Variation of lateral characteristics of airplane with rudder deflection for asymmetric power. δ_f = 27°. Left engine full; right engine windmilling.

(b) $\beta = 0^0$.

Figure 42.- Continued.
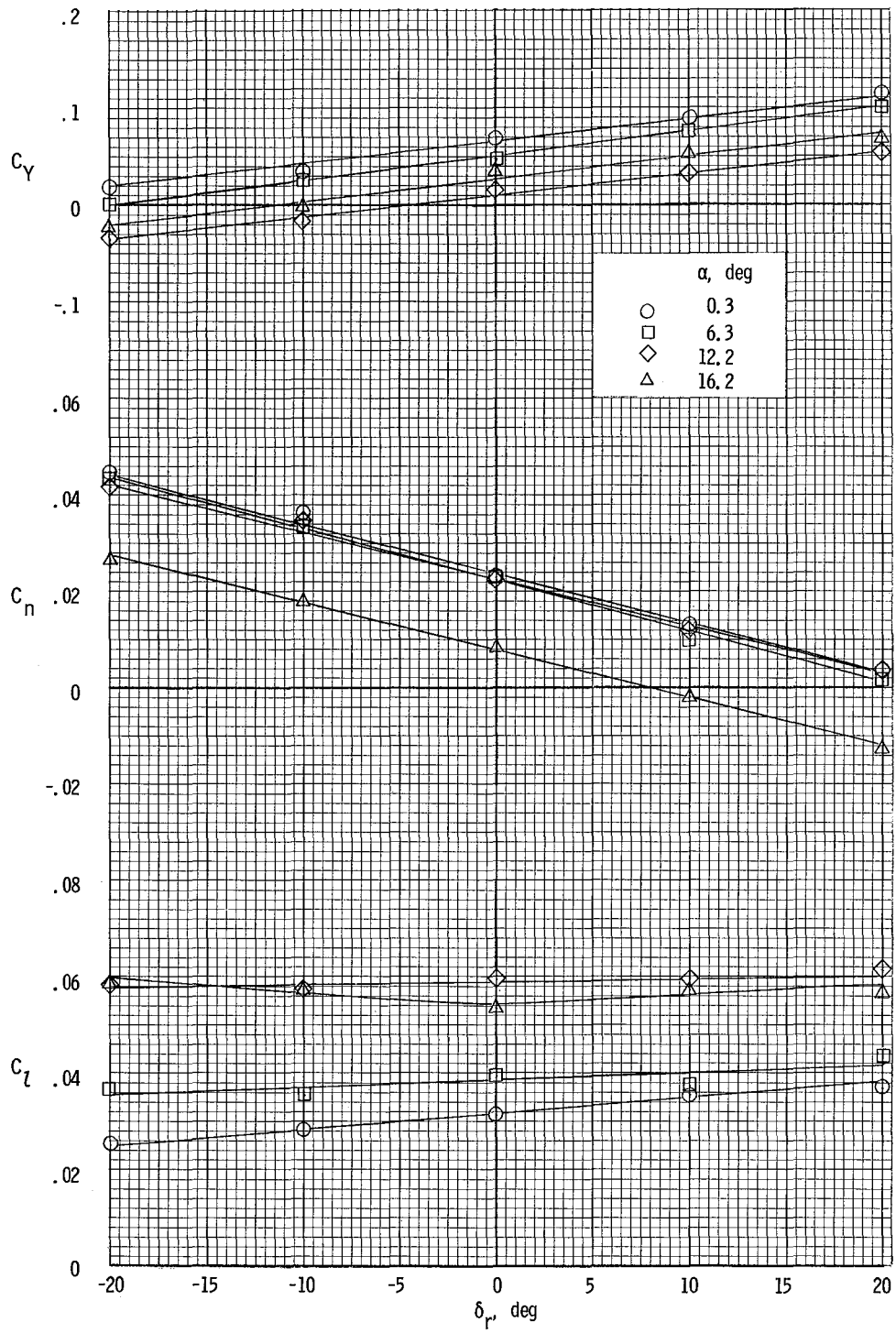
(c) $\beta = -8^0$.

Figure 42.- Concluded.

(a) $\beta = 8^0$.
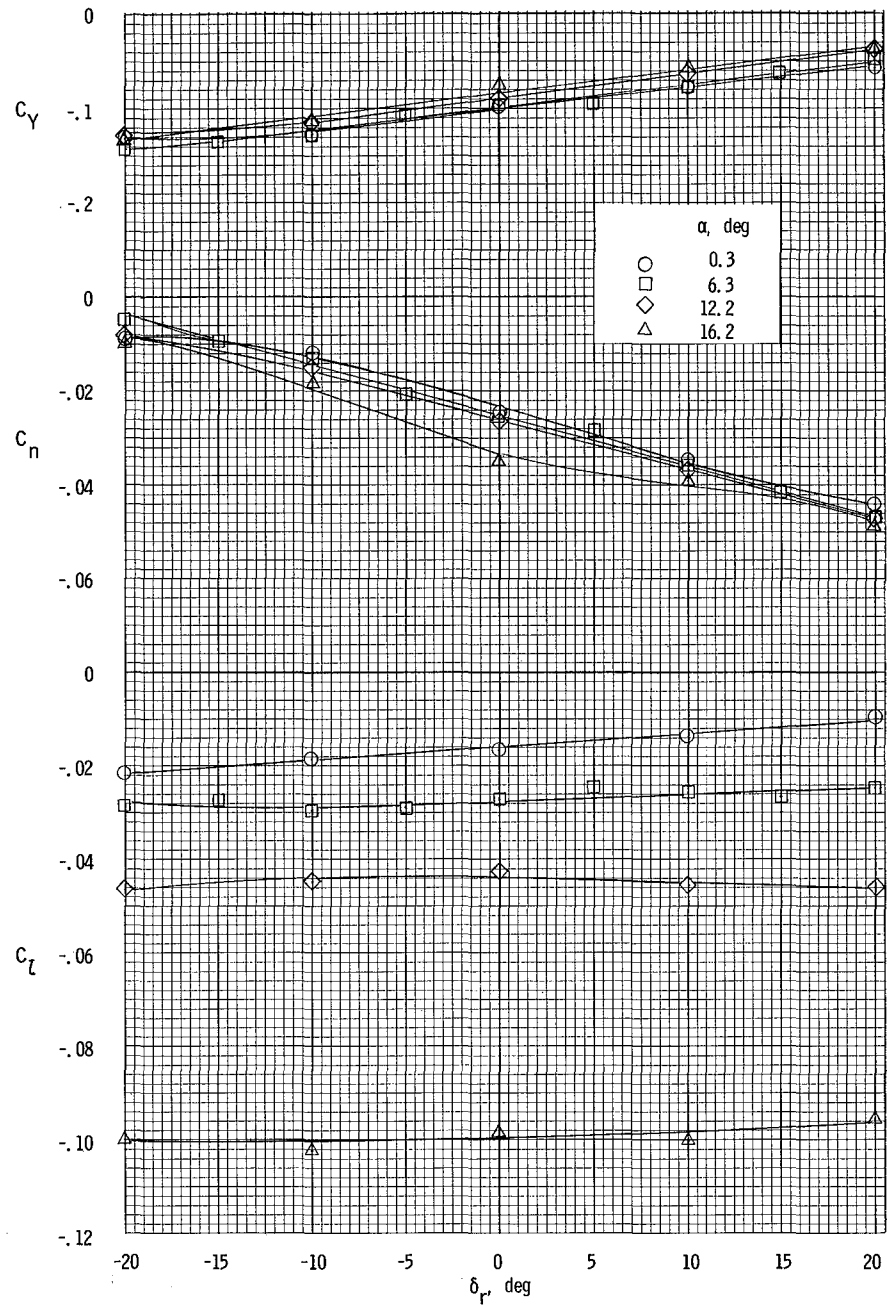
Figure 43.- Variation of lateral characteristics of airplane with rudder deflection for asymmetric power. $\delta_f = 27^0$. Right engine full; left engine feathered.

144

(b) $\beta = 0^0$.

Figure 43.- Continued.
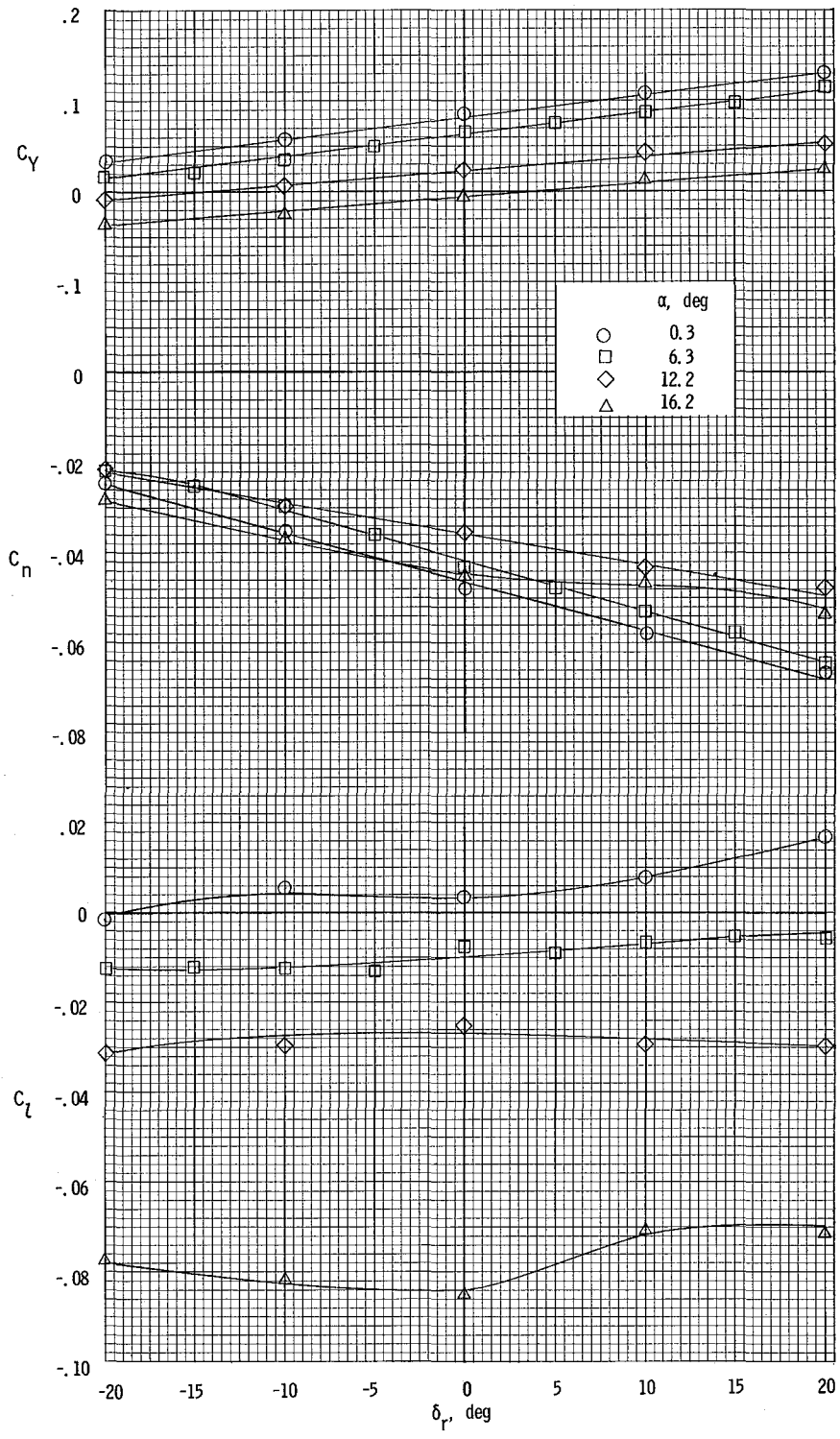
(c) $\beta = -8°$.

Figure 43.- Concluded.

(a) $\beta = 8^\circ$.

Figure 44.- Variation of lateral characteristics of airplane with rudder deflection for asymmetric power. $\delta_f = 27^\circ$. Right engine full; left engine windmilling.
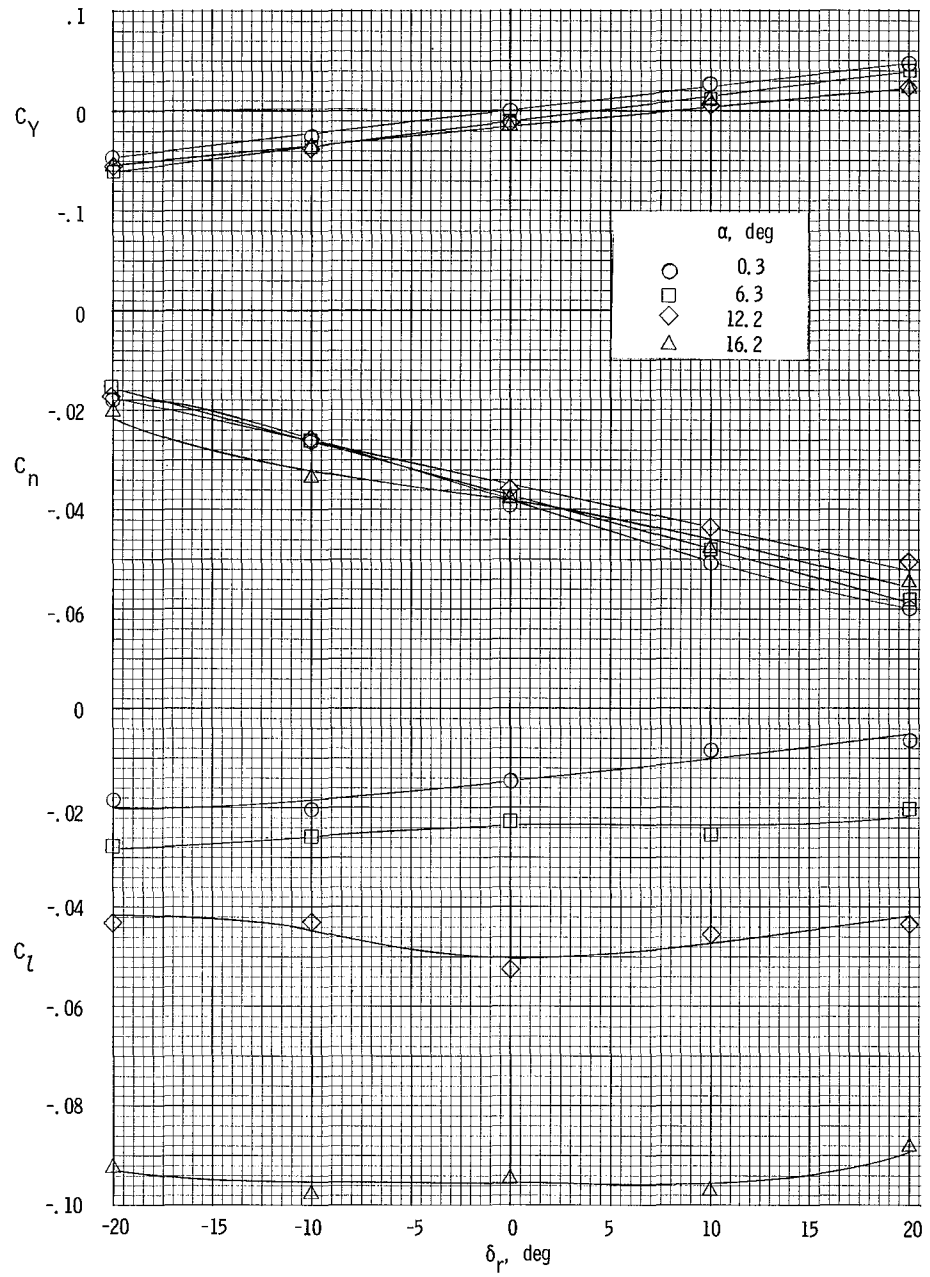
(b) $\beta = 0^\circ$.

Figure 44.- Continued.

(c) $\beta = -8^0$.
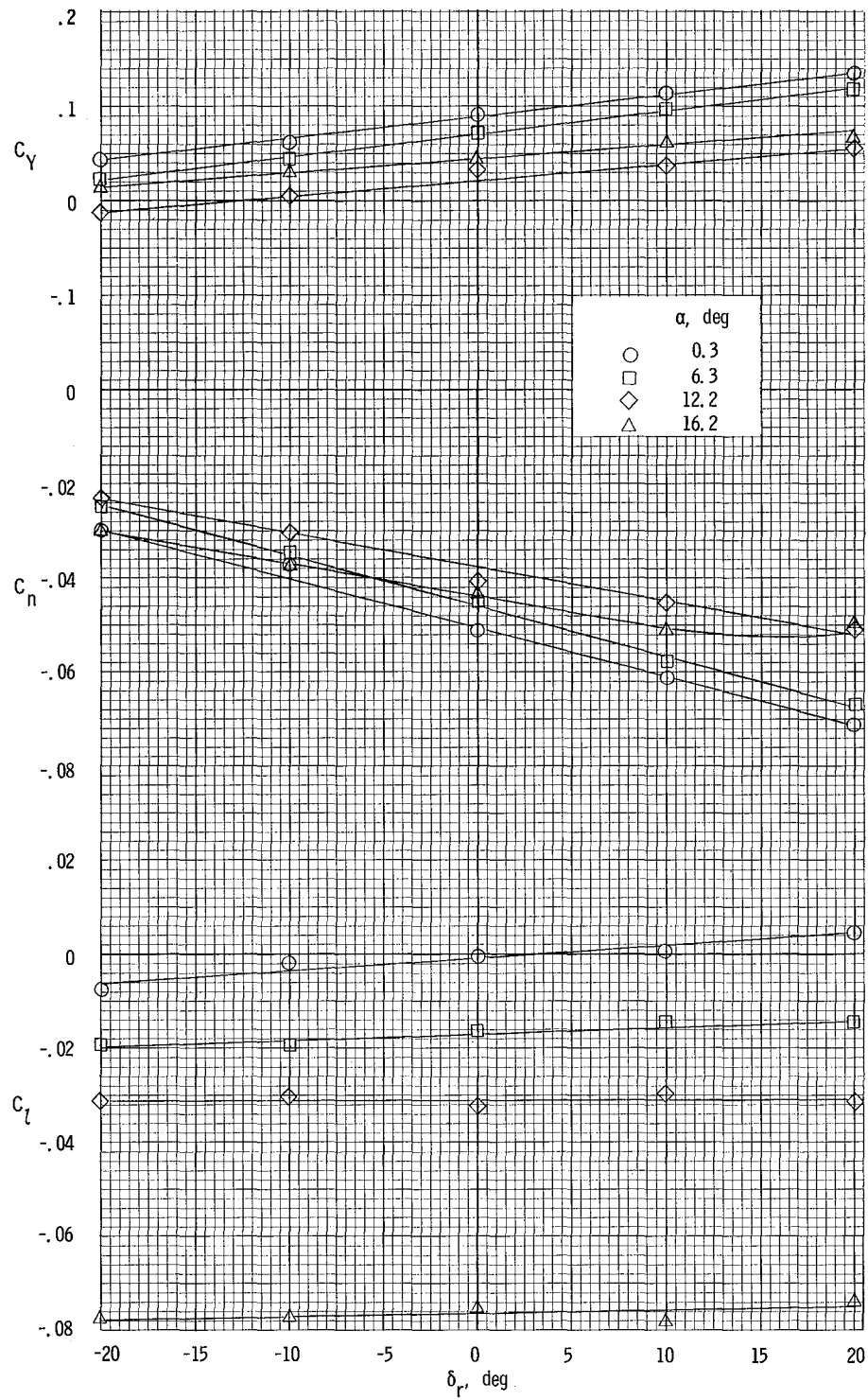
Figure 44.- Concluded.
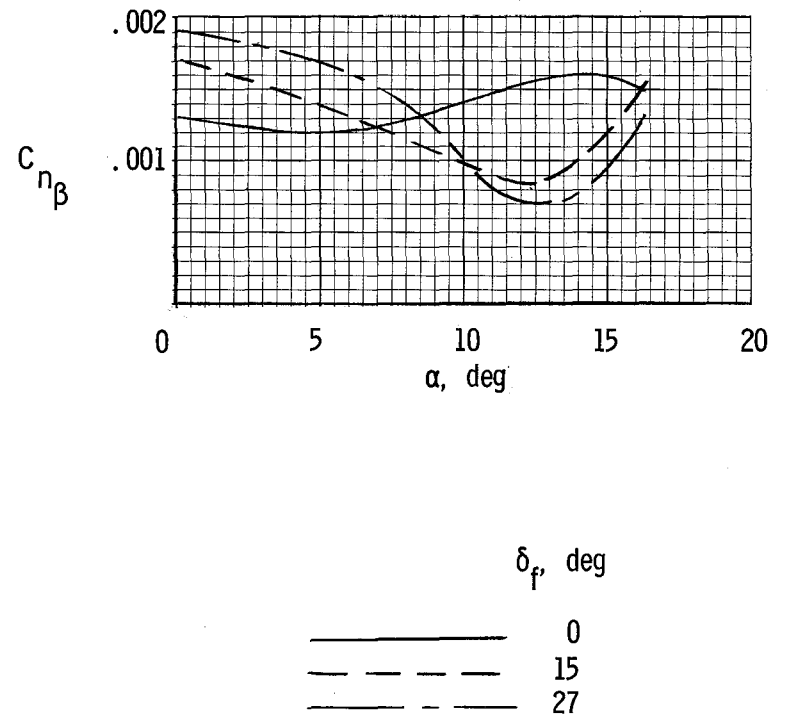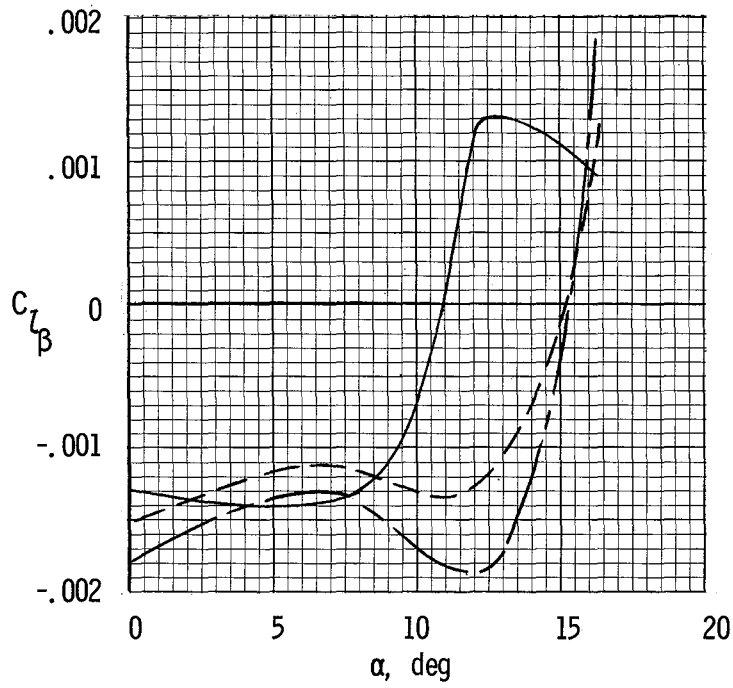
Figure 45.- Variations of effective dihedral and directional stability parameters with angle of attack. Propellers removed.
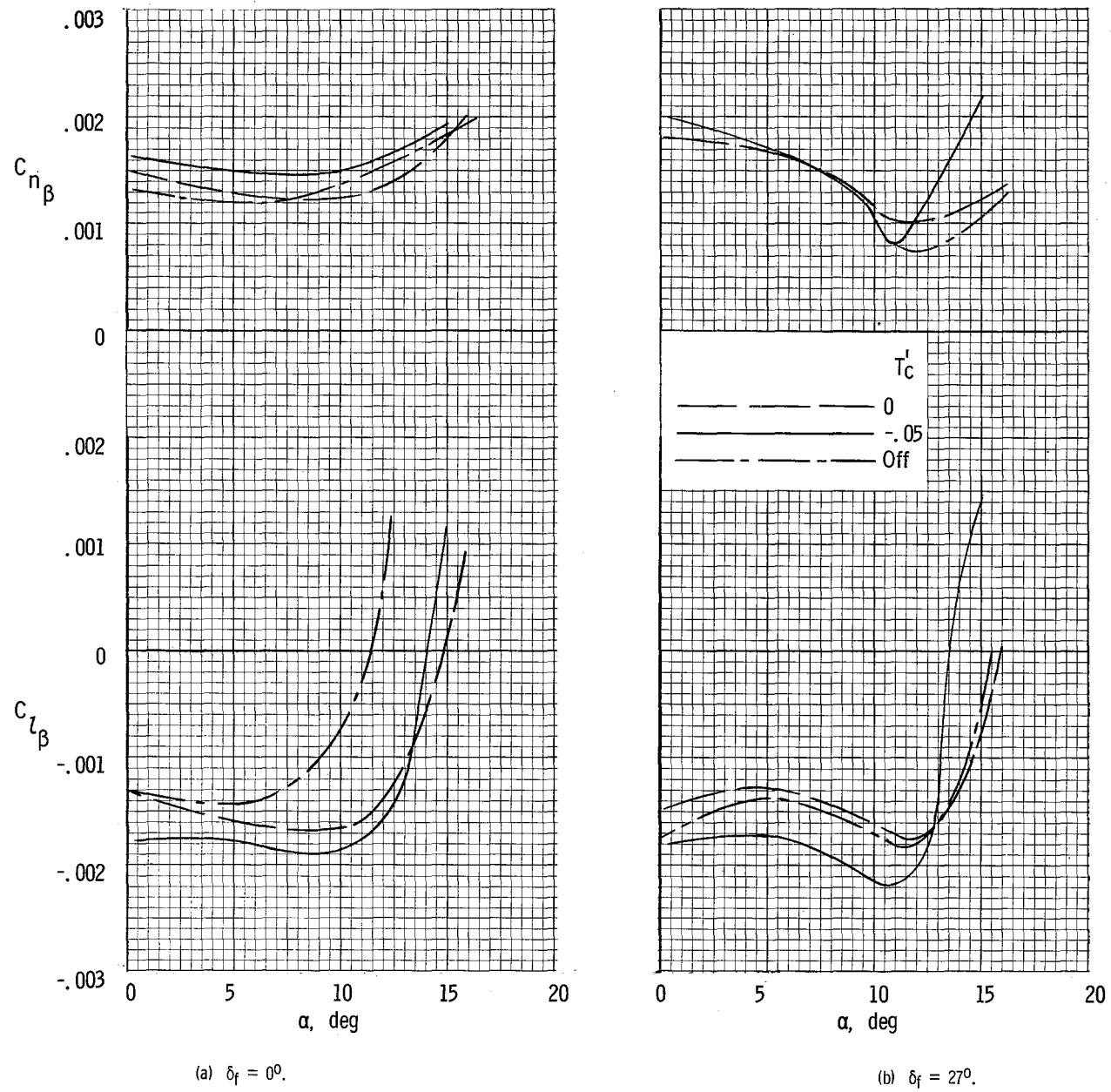
Figure 46.- Comparison of effective dihedral and directional stability parameters with windmilling propellers ($T'_c = -0.05$), zero thrust, and propellers removed.
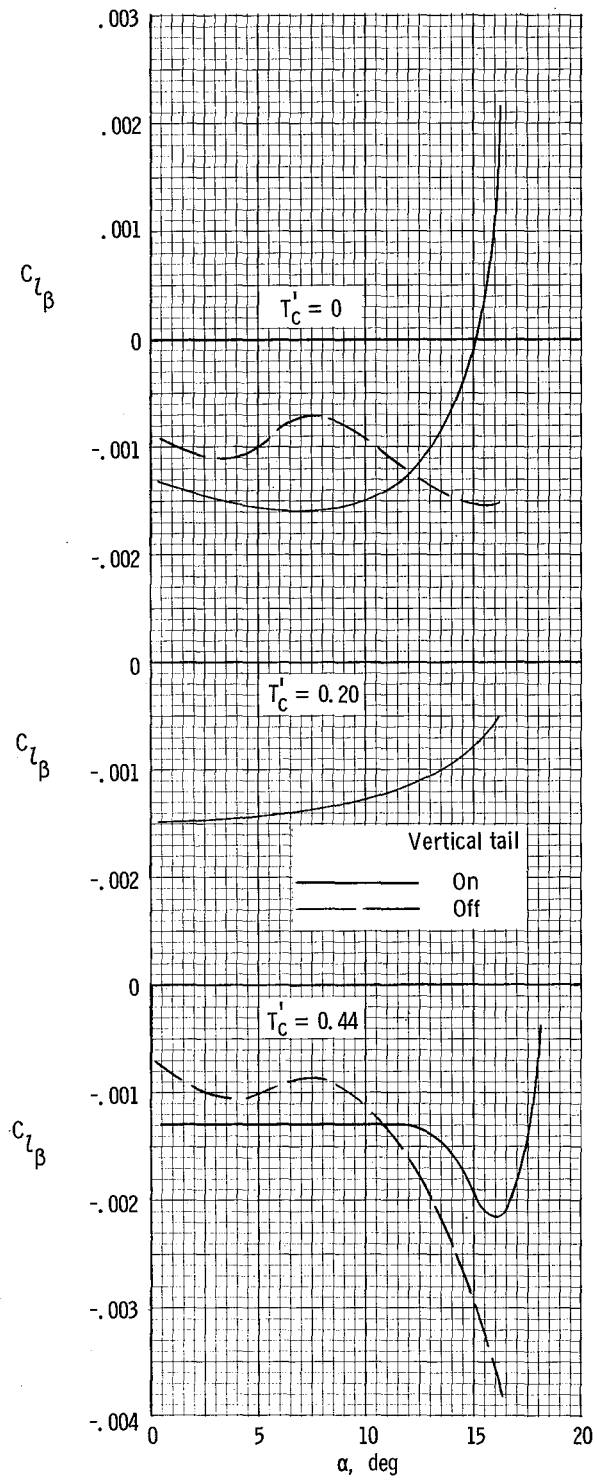
(a) $\delta_f = 0^0$.

Figure 47.- Variation of effective dihedral parameter with angle of attack for several flap deflections.

(b) $\delta_f = 15^0$.
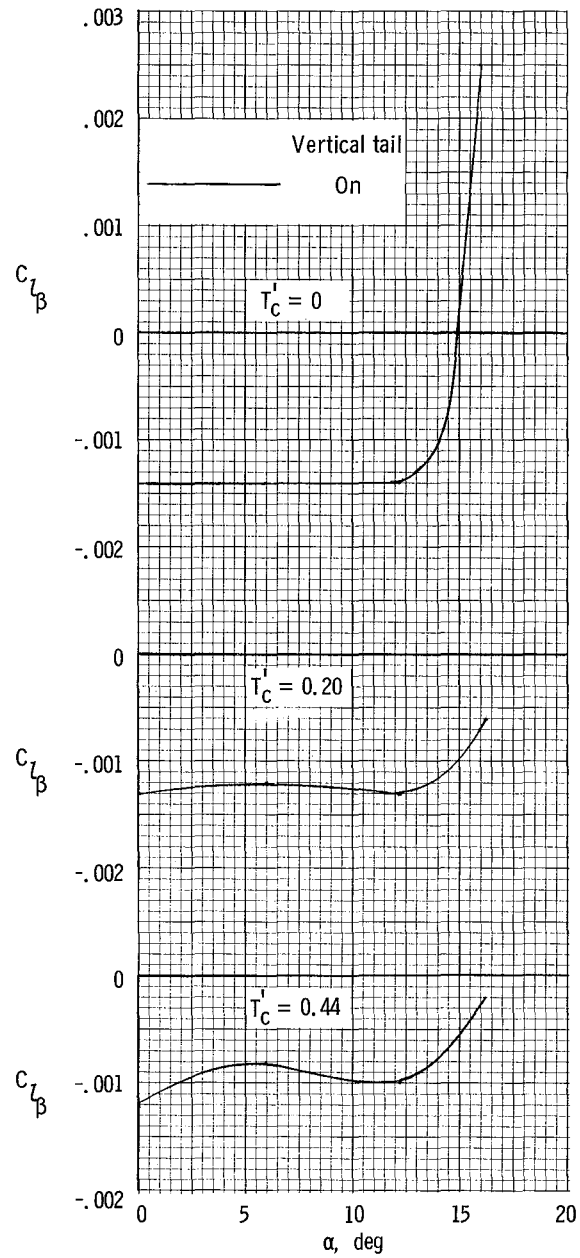
Figure 47.- Continued.

(c) $\delta_f = 27^o$.
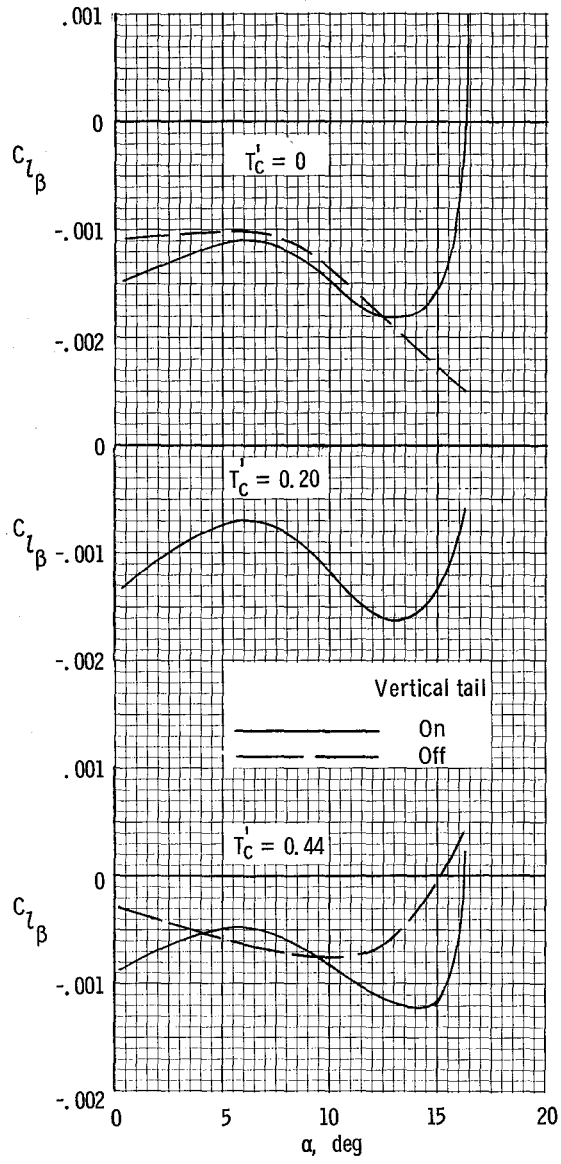
Figure 47.- Concluded.
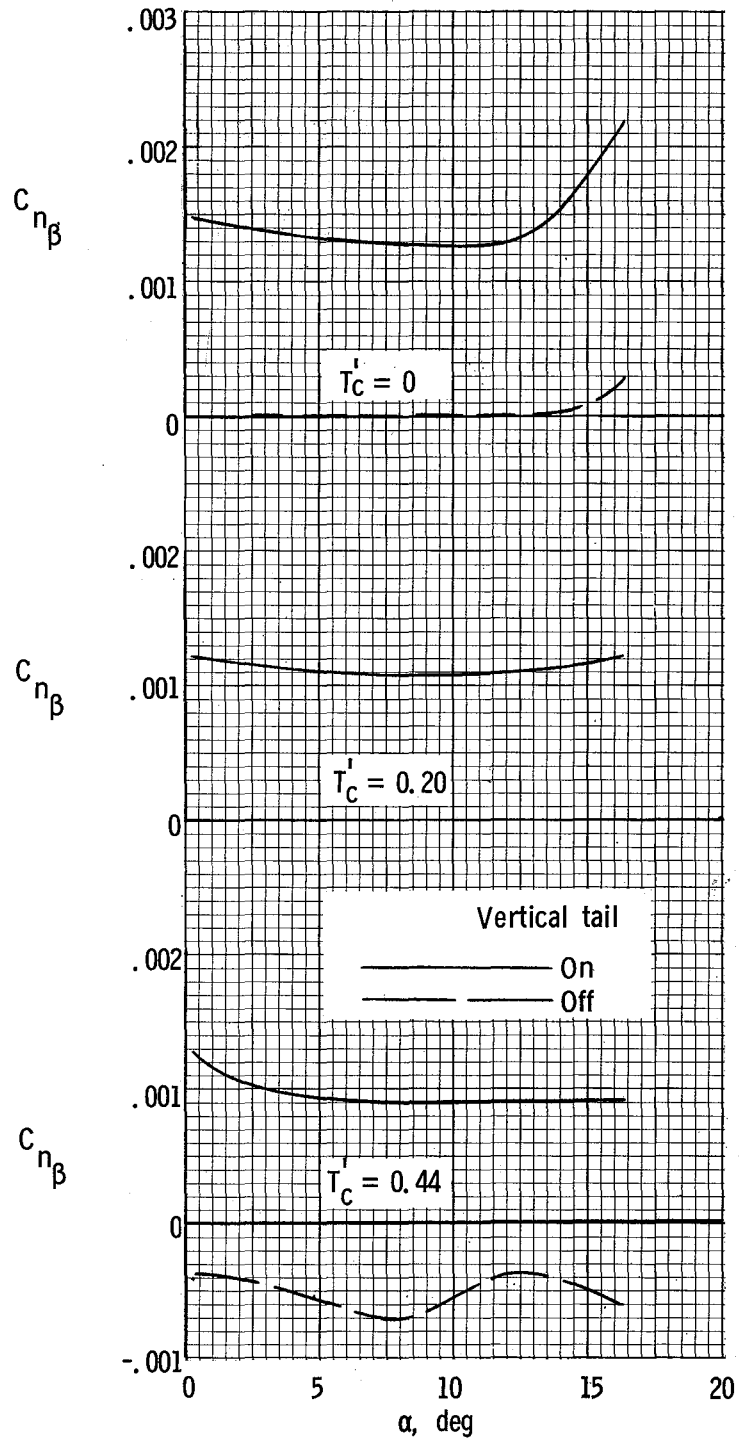
(a) $\delta_f = 0^0$.

Figure 48.- Variation of directional stability parameter with angle of attack for several flap deflections.

(b) $\delta_f = 15^o$.
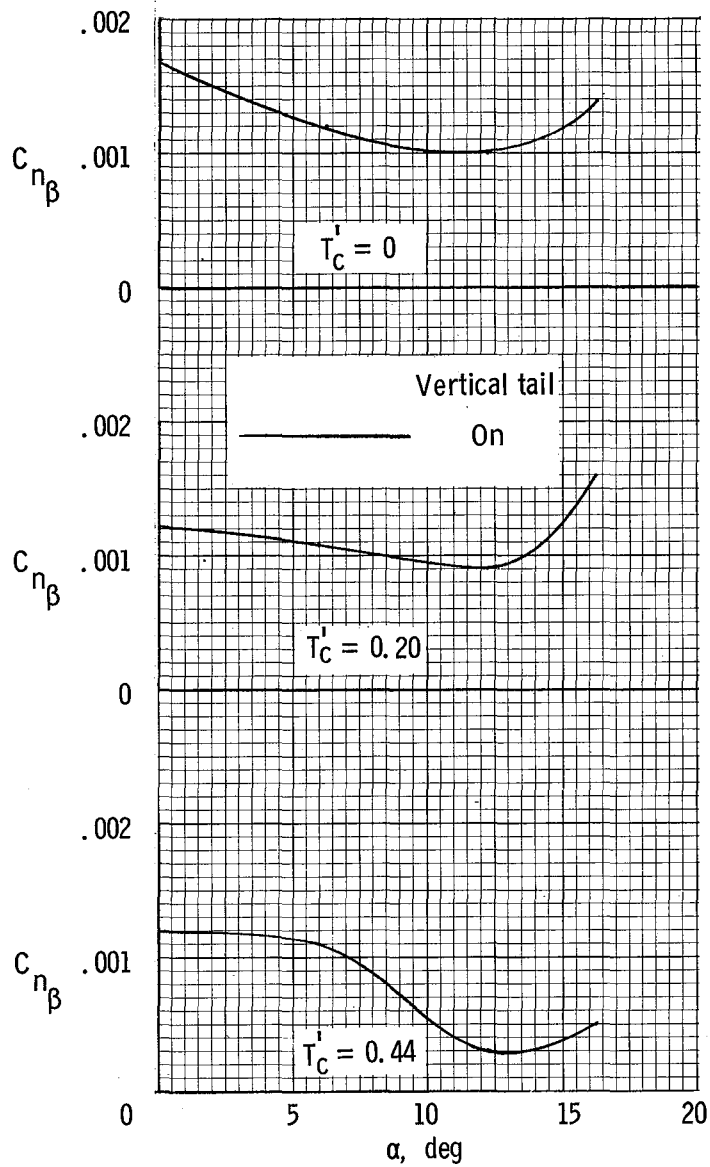
Figure 48.- Continued.

(c) $\delta_f = 27^o$.
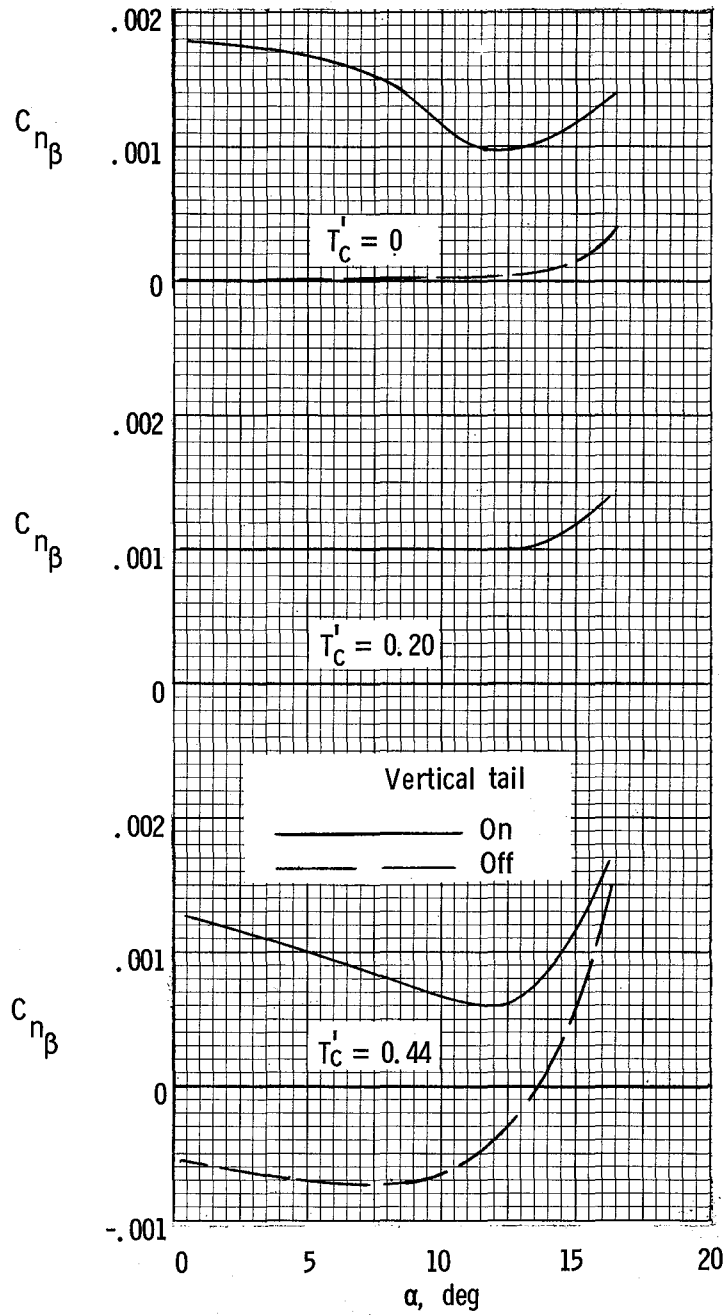
Figure 48.- Concluded.

158
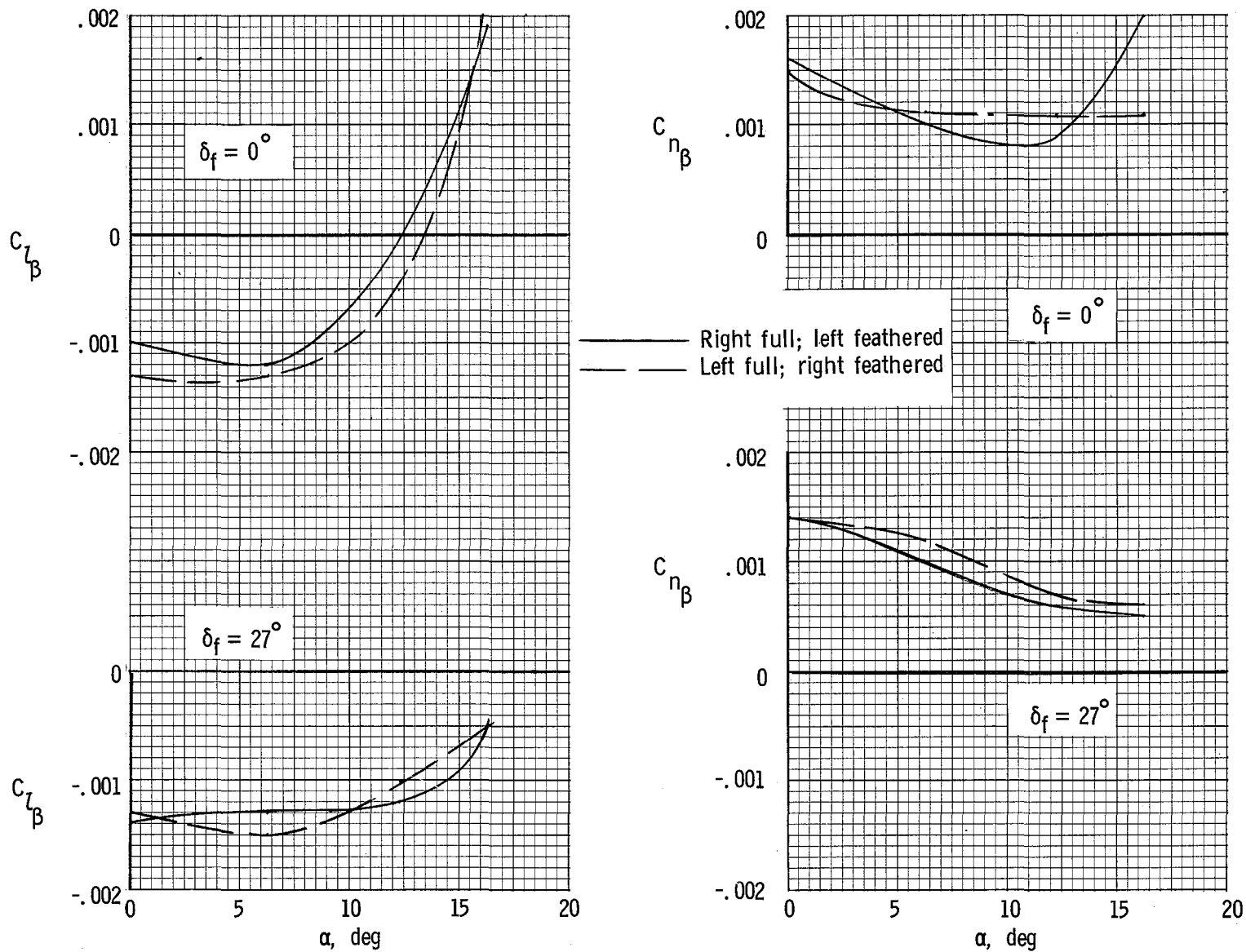
Figure 49.- Variation of lateral and directional stability parameters with angle of attack for asymmetric power.
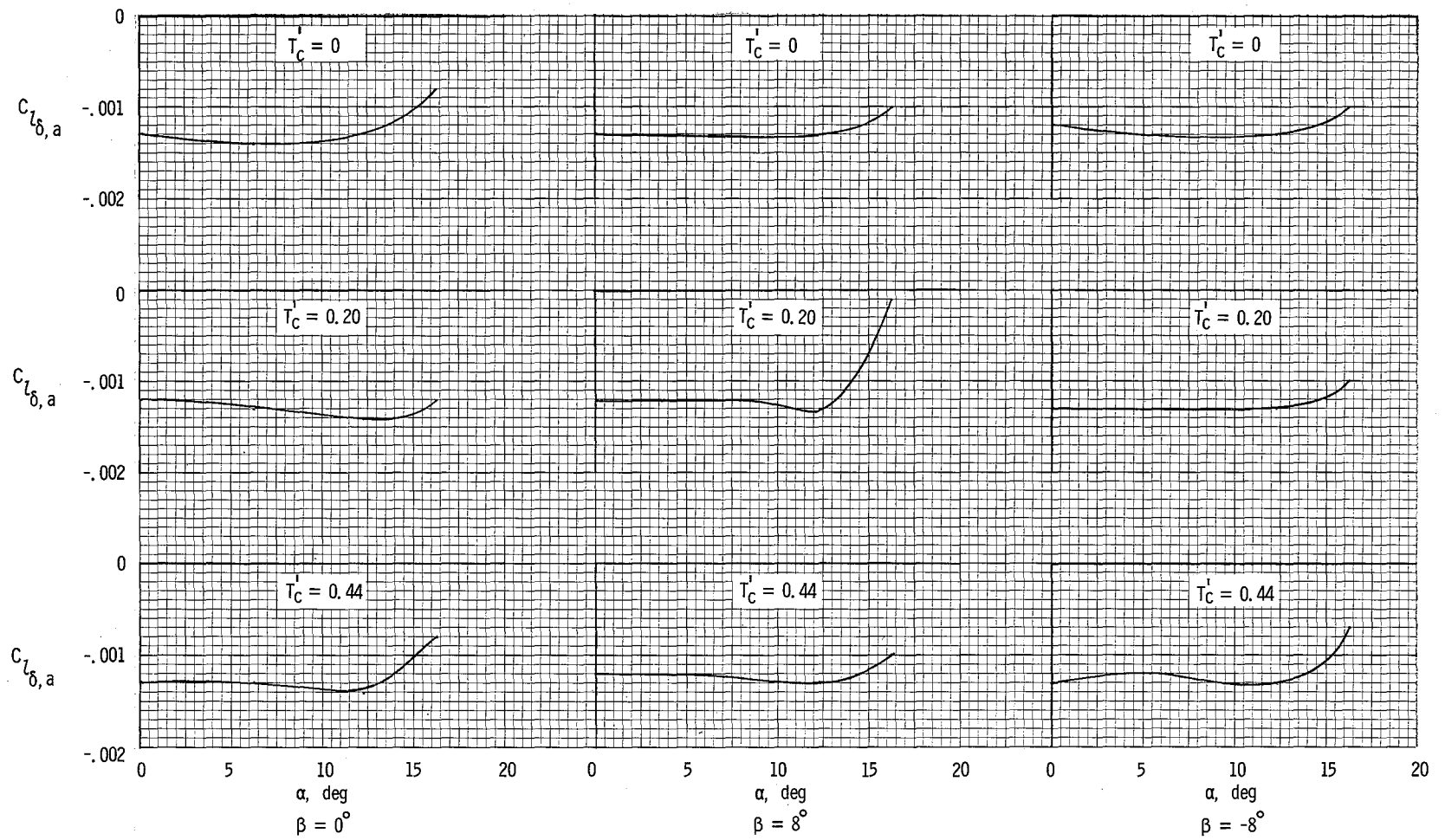
(a) $\delta_f = 0^0$.

Figure 50.- Variation of aileron effectiveness with angle of attack for several sideslip angles and flap deflections.
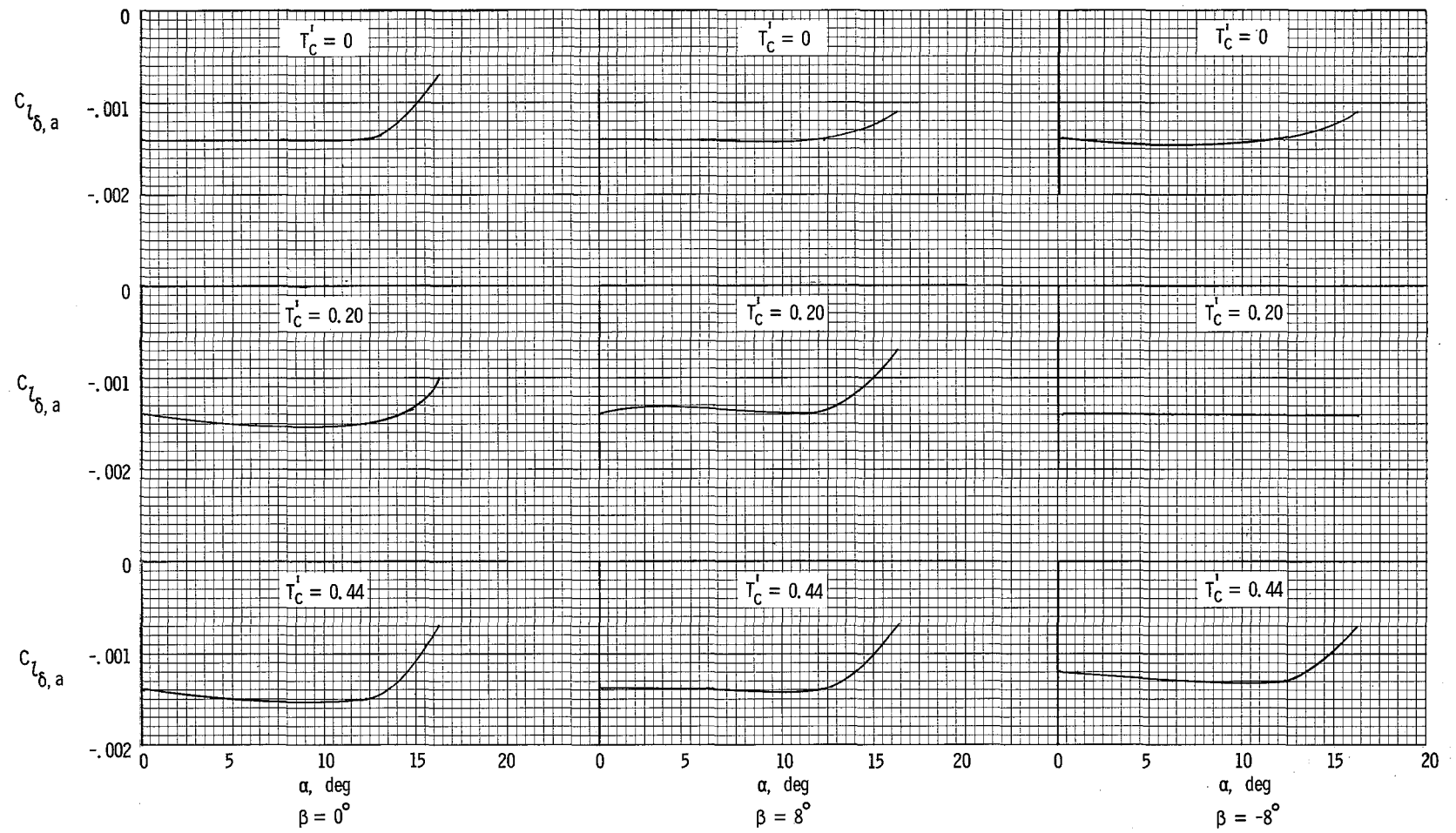
(b) $\delta_f = 27^\circ$.

Figure 50.- Concluded.
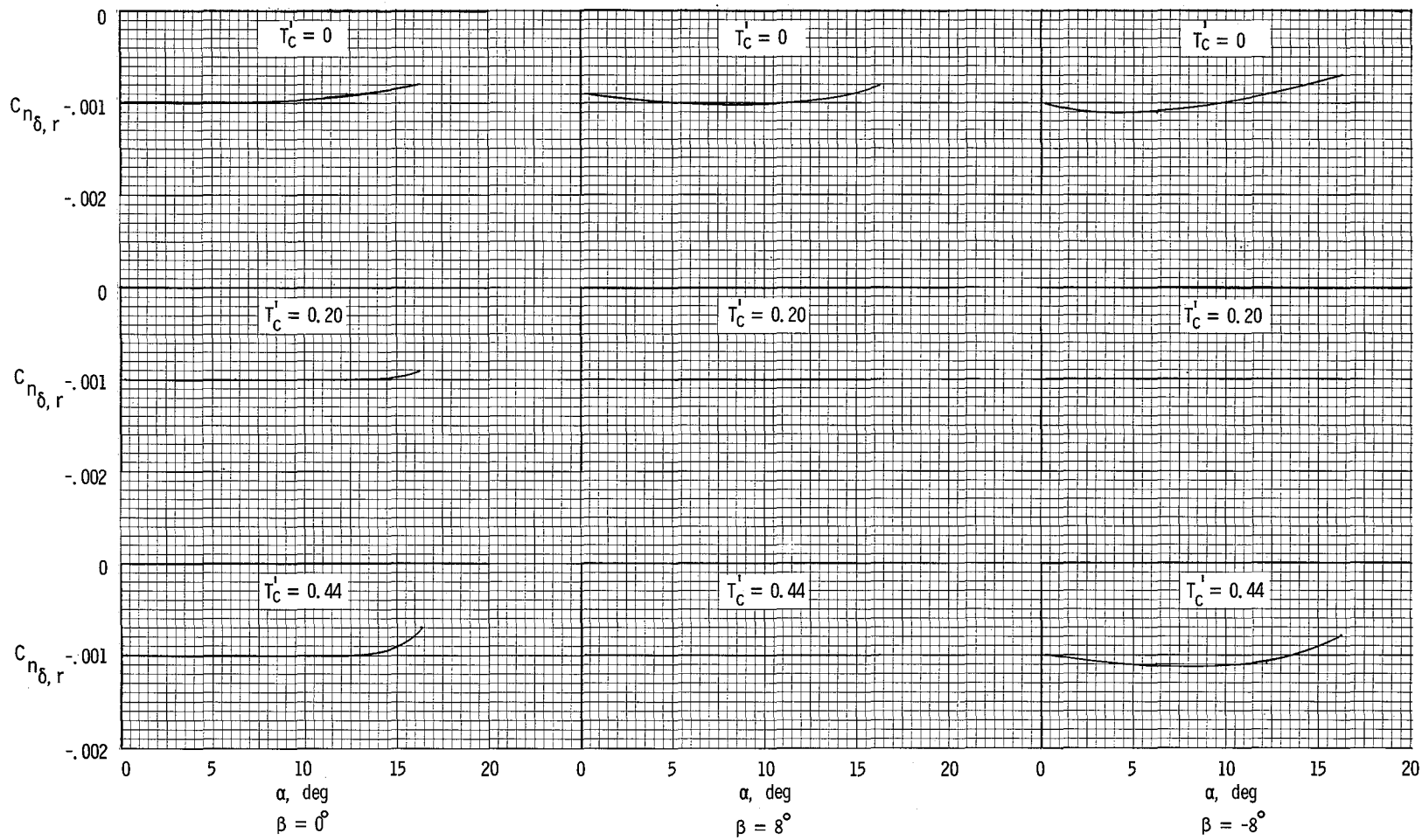
(a) $\delta_f = 0^0$.

Figure 51.- Variation of rudder effectiveness with angle of attack for several sideslip angles and flap deflections.
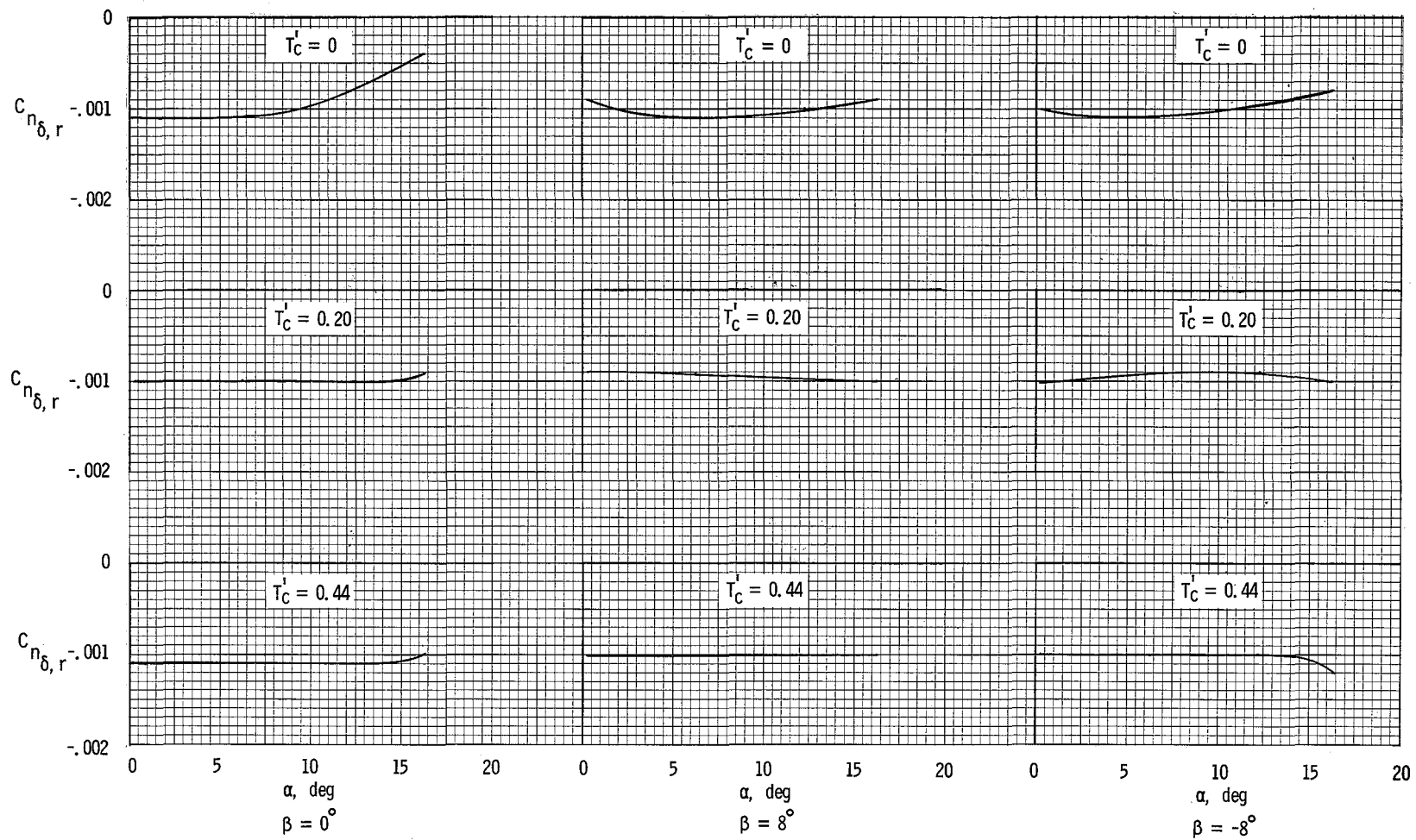
(b) $\delta_f = 27°$.

Figure 51.- Concluded.
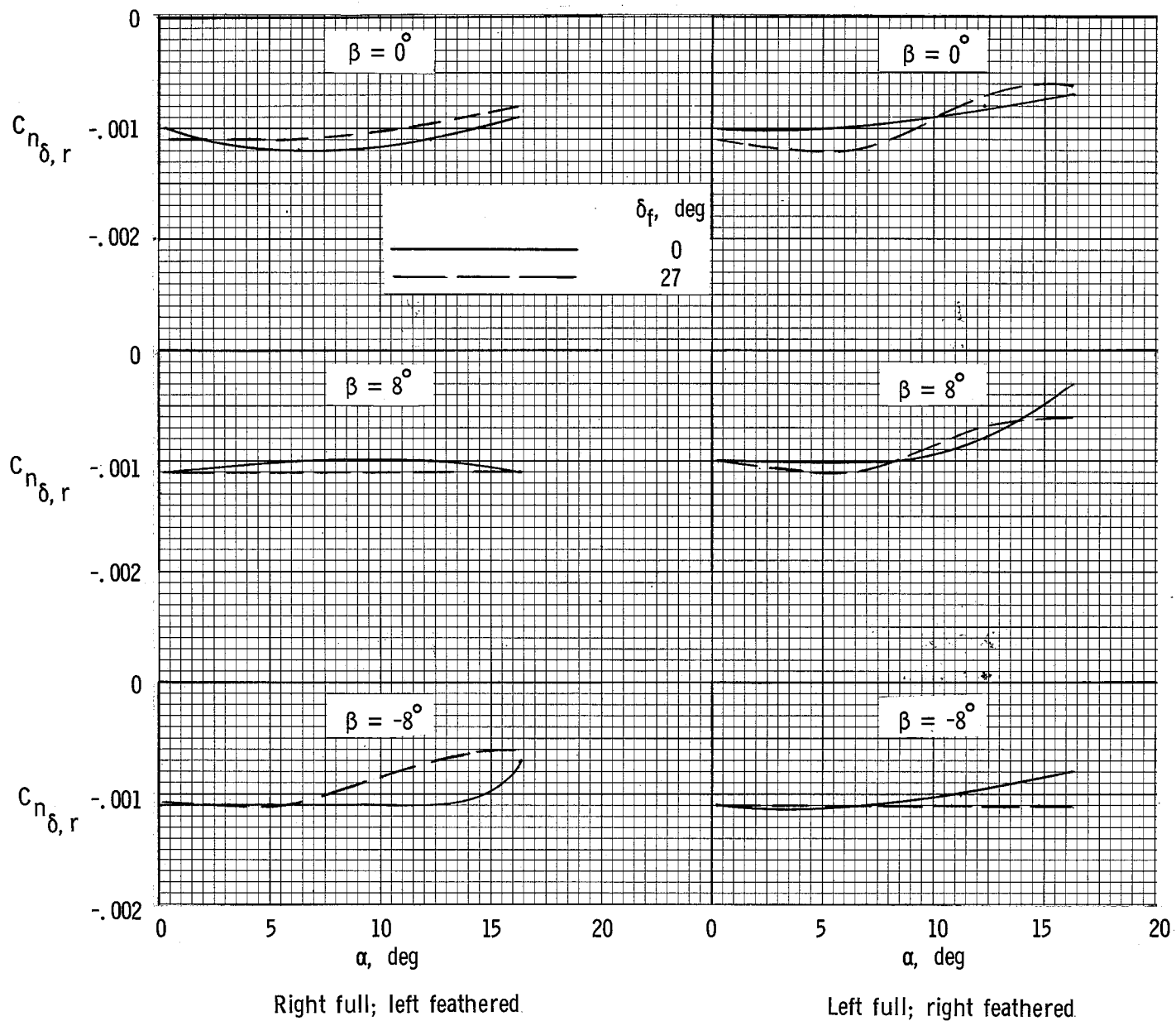
Figure 52.- Rudder effectiveness with asymmetric power.
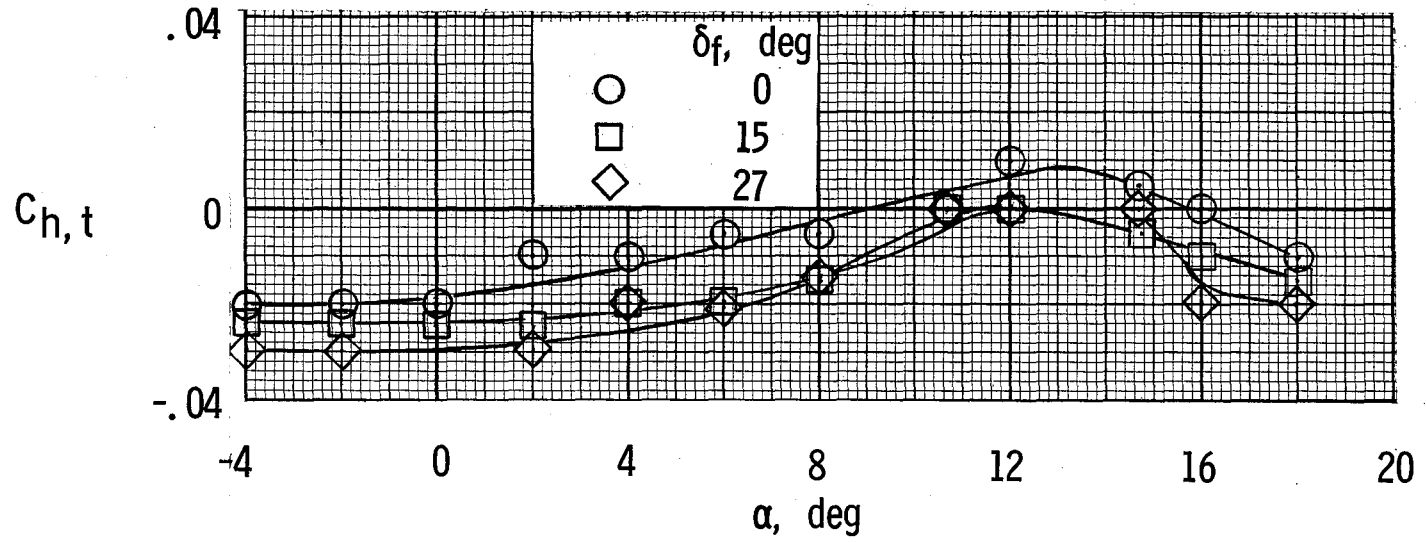
Figure 53.- Horizontal-tail hinge-moment coefficients with propellers removed.
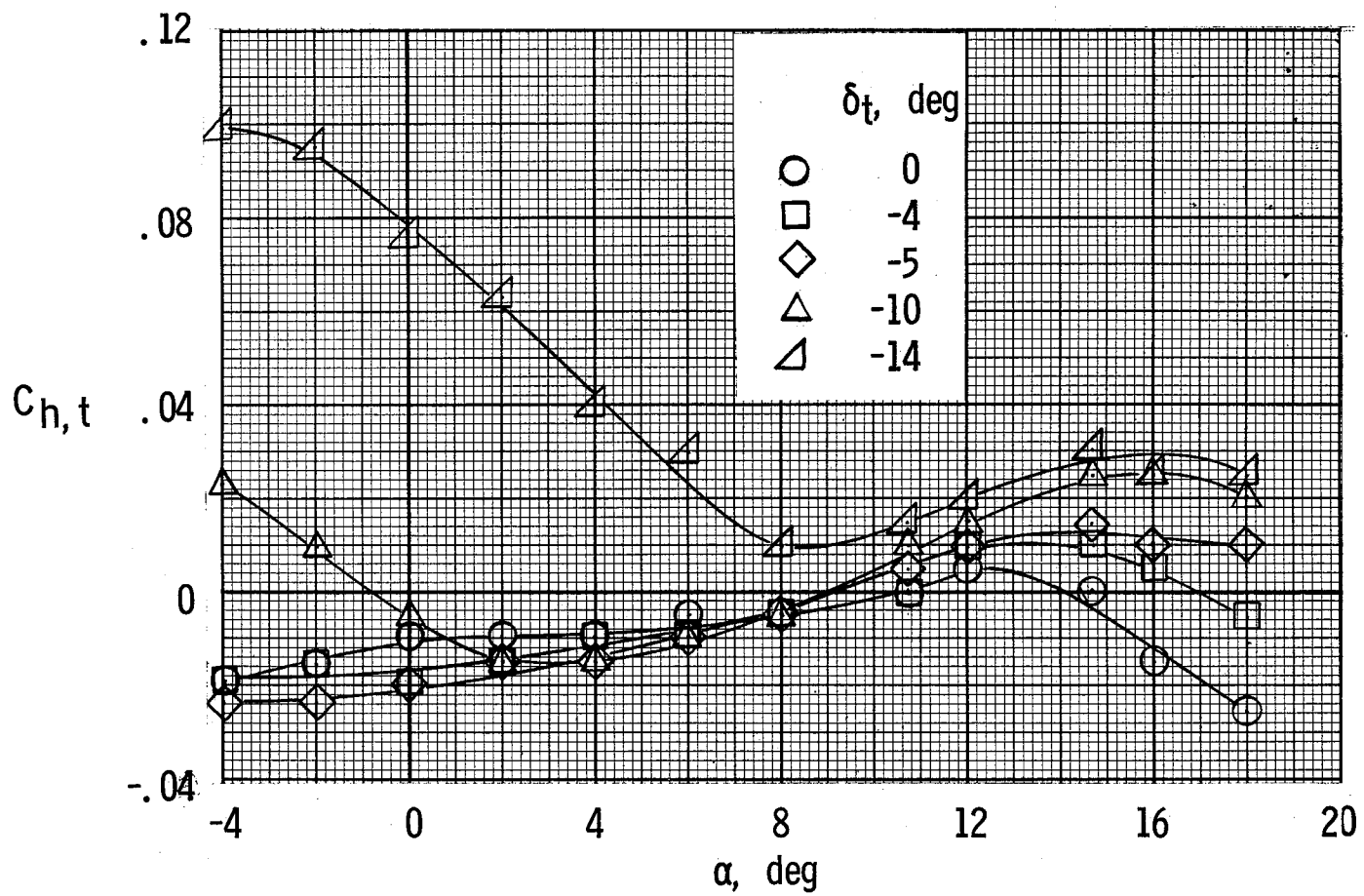
Figure 54.- Horizontal-tail hinge-moment coefficients with tab locked at zero deflection. $\delta_f = 0^0$; $T'_c = 0.20$.
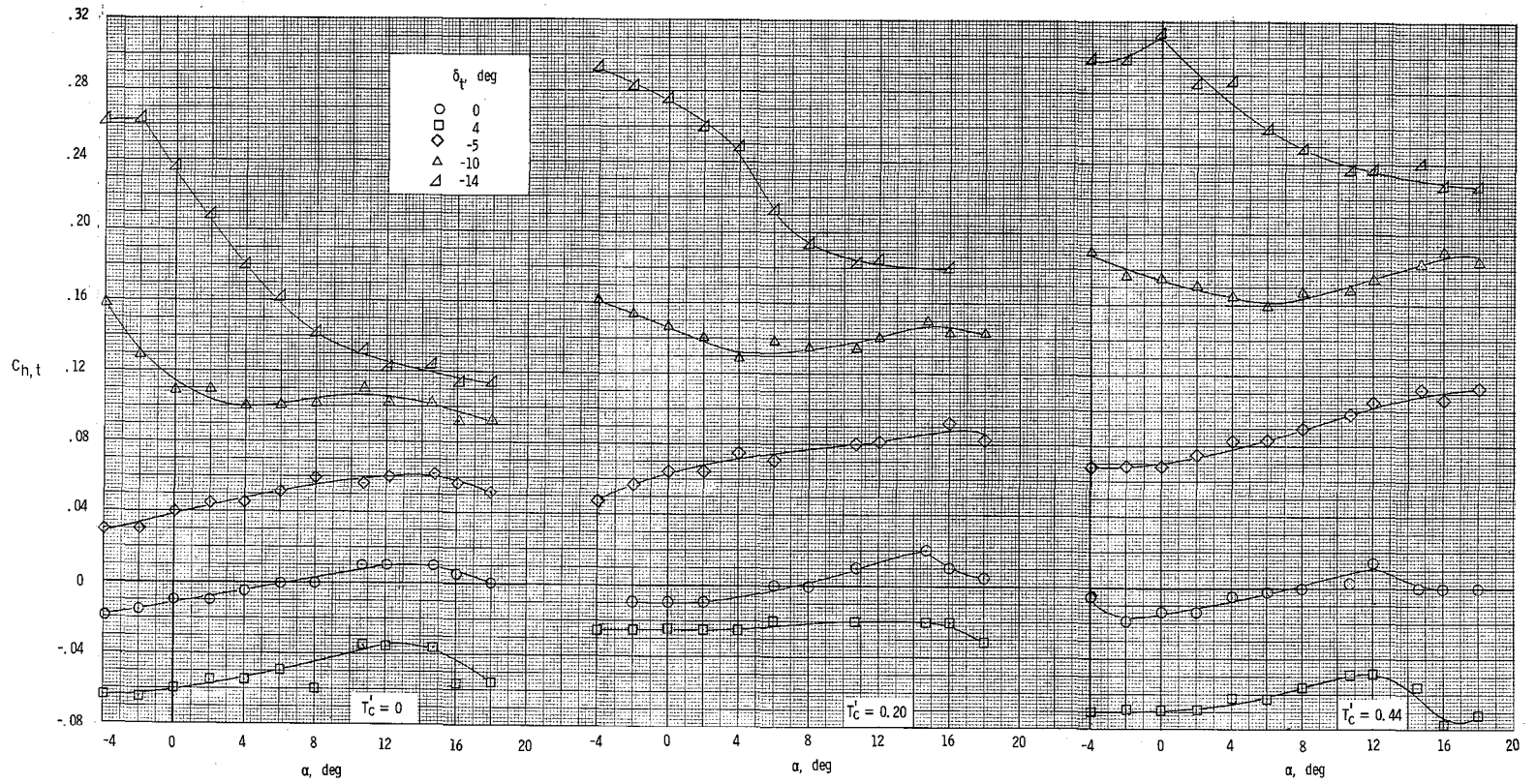
(a) $\delta_f = 0^0$.

Figure 55.- Variation of horizontal-tail hinge-moment coefficients with angle of attack for several power and flap settings.

(b) $\delta_f = 15^0$.
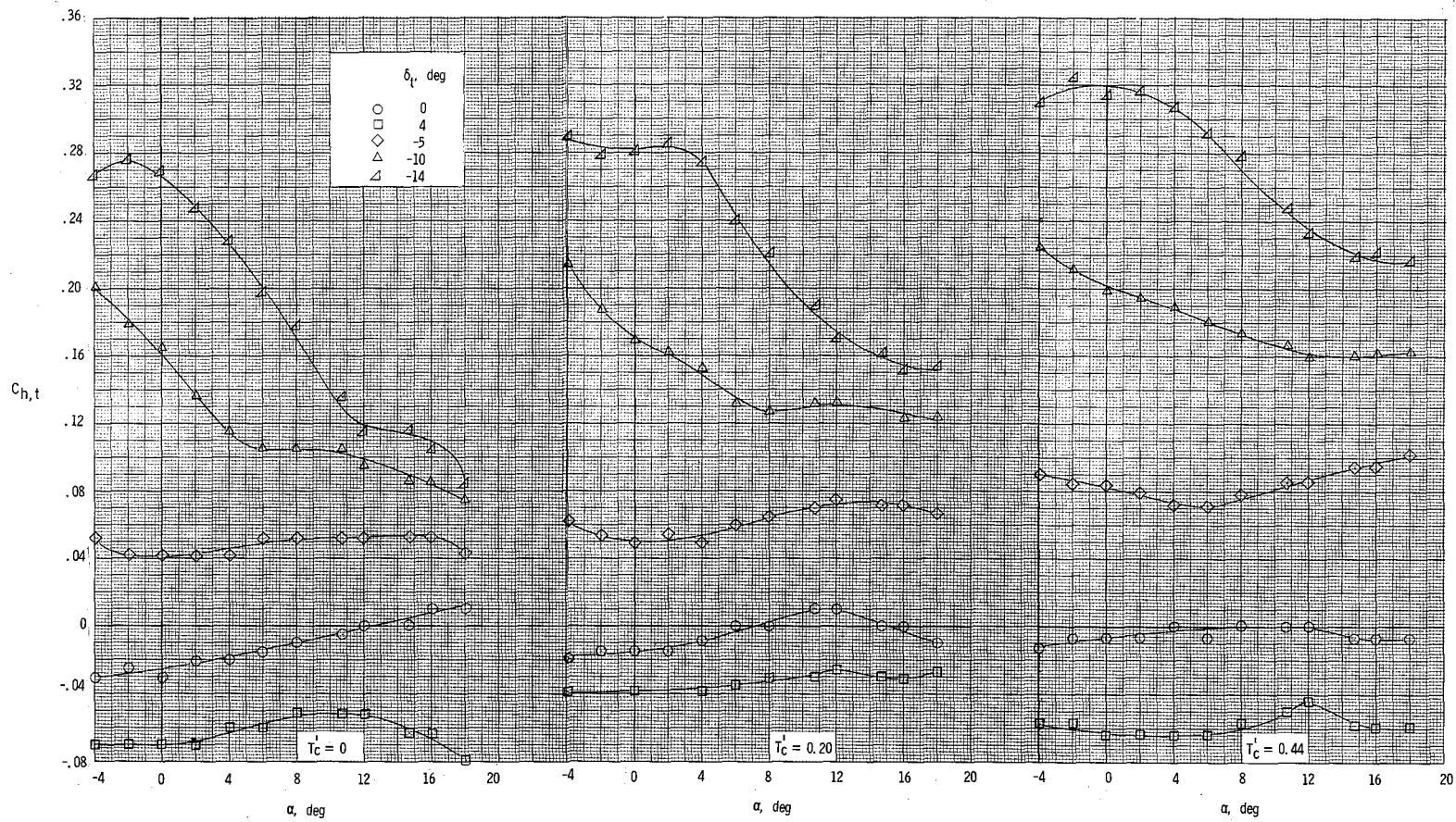
Figure 55.- Continued.
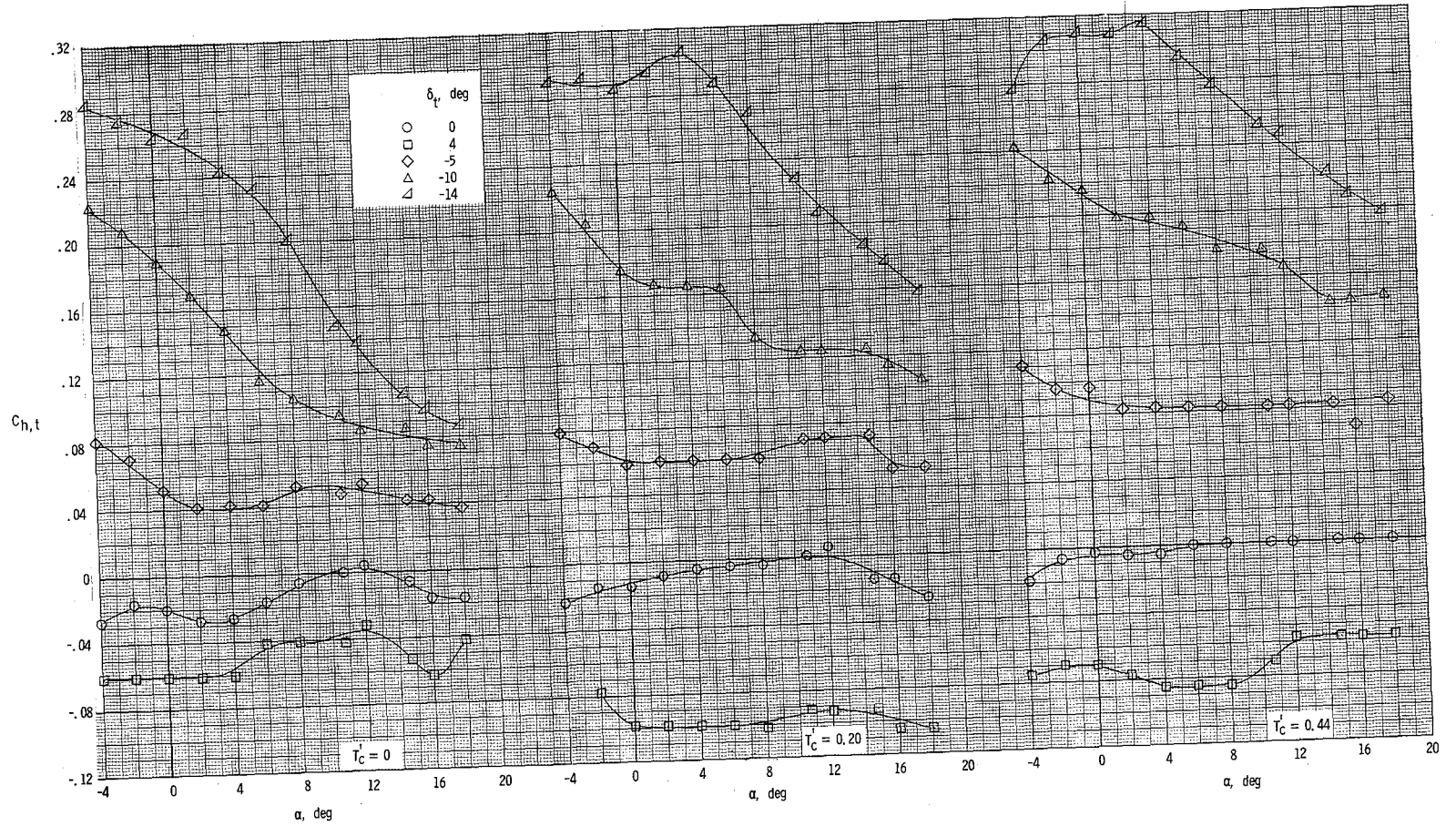
(c) $\delta_f = 27^\circ$.

Figure 55.- Concluded.
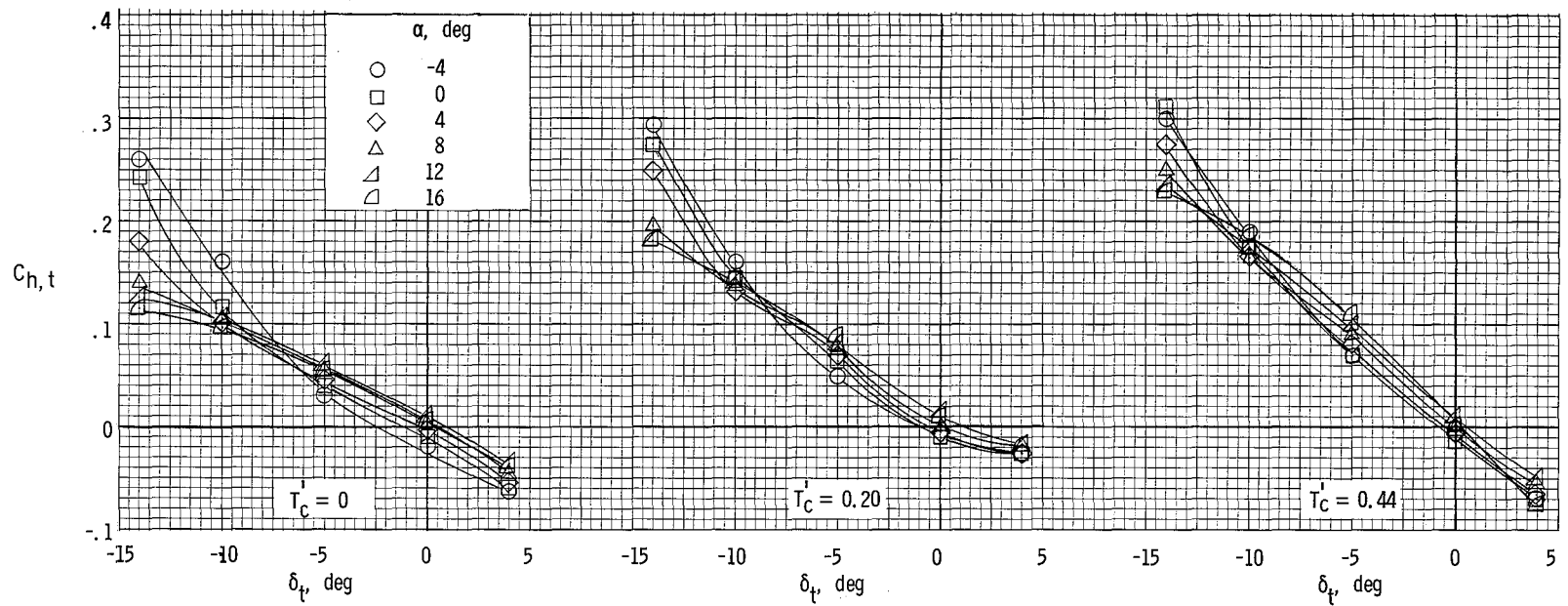
(a) $\delta_f = 0^\circ$.

Figure 56.- Variation of horizontal-tail hinge-moment coefficients with deflection angle for several power and flap settings.

(b) $\delta_f = 15^0$.
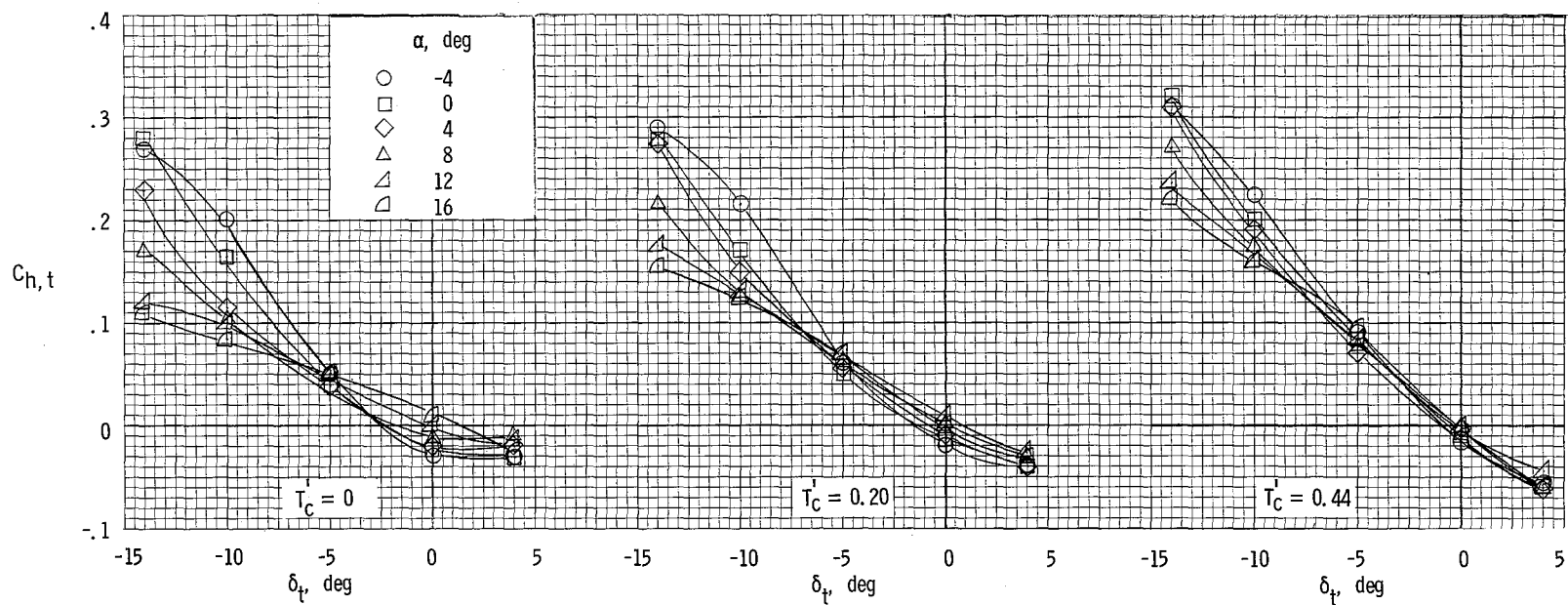
Figure 56.- Continued.
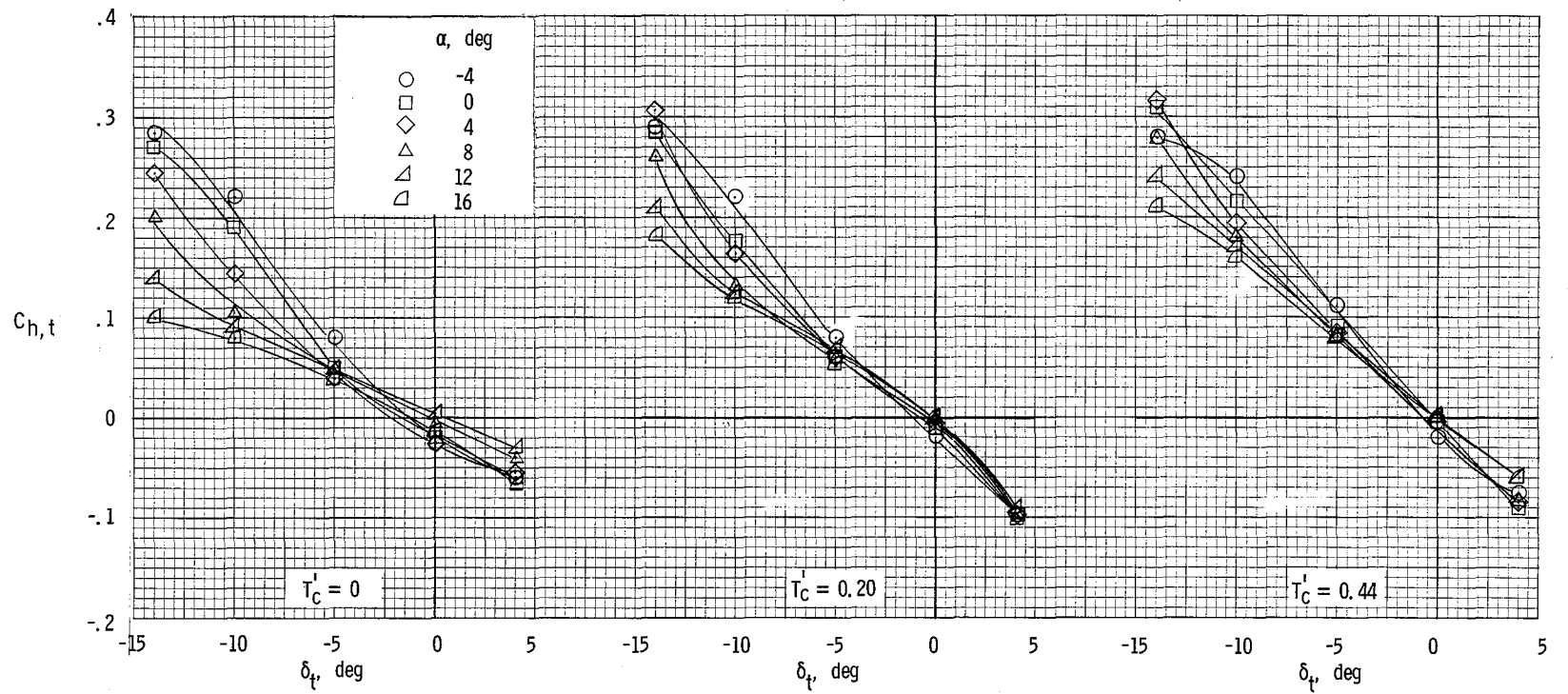
(c) $\delta_f = 27^0$.

Figure 56.- Concluded.
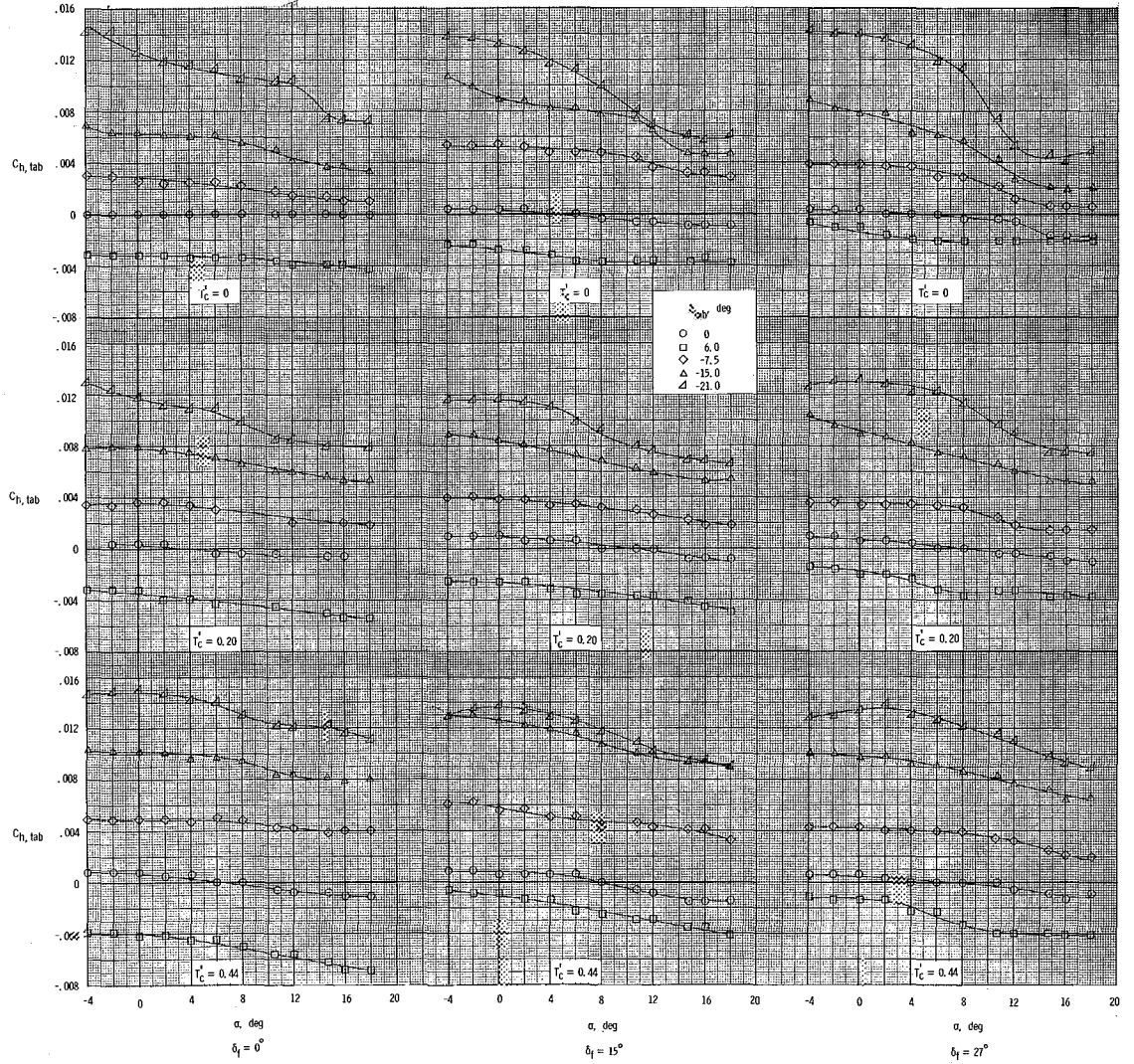
Figure 57.- Variation of horizontal-tail tab hinge-moment coefficient with angle of attack for various power and flap settings.

172

(a) $\beta = 8^0$.
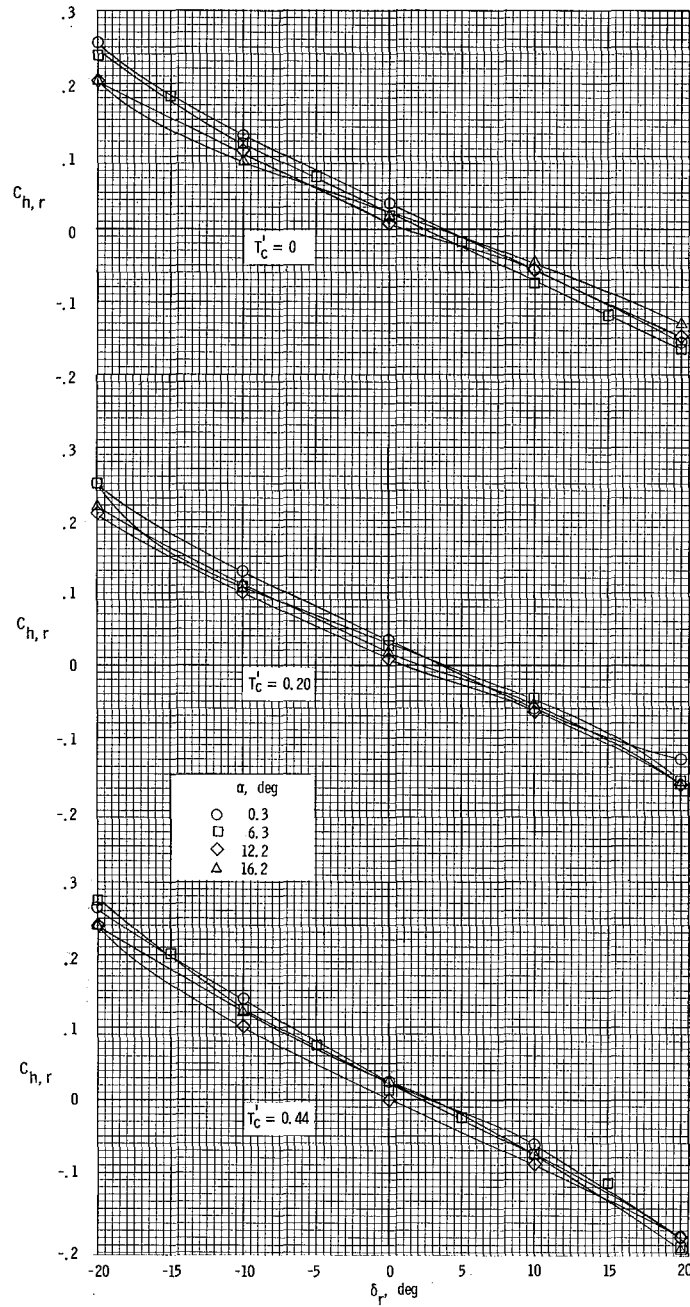
Figure 58.- Variation of rudder hinge-moment coefficients with control deflection. $\delta_f = 0^0$.
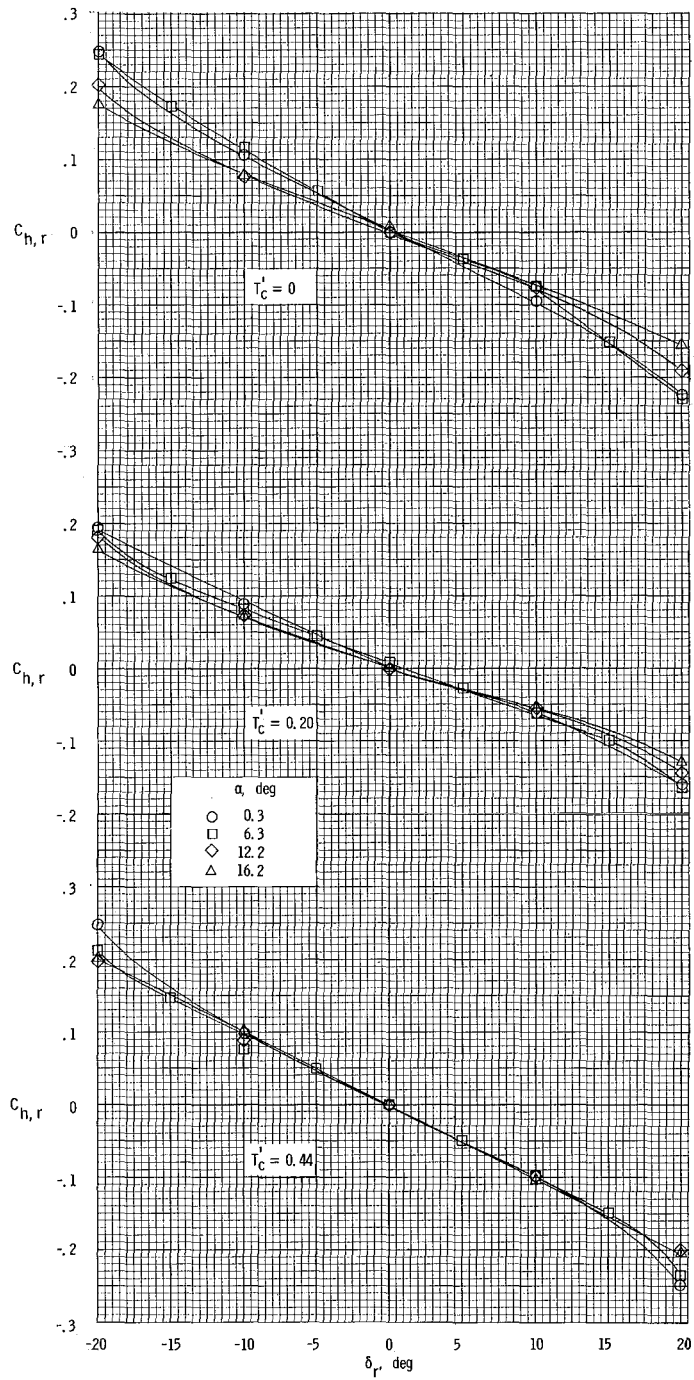
(b) $\beta = 0^0$.

Figure 58.- Continued.

(c) $\beta = -8^0$.
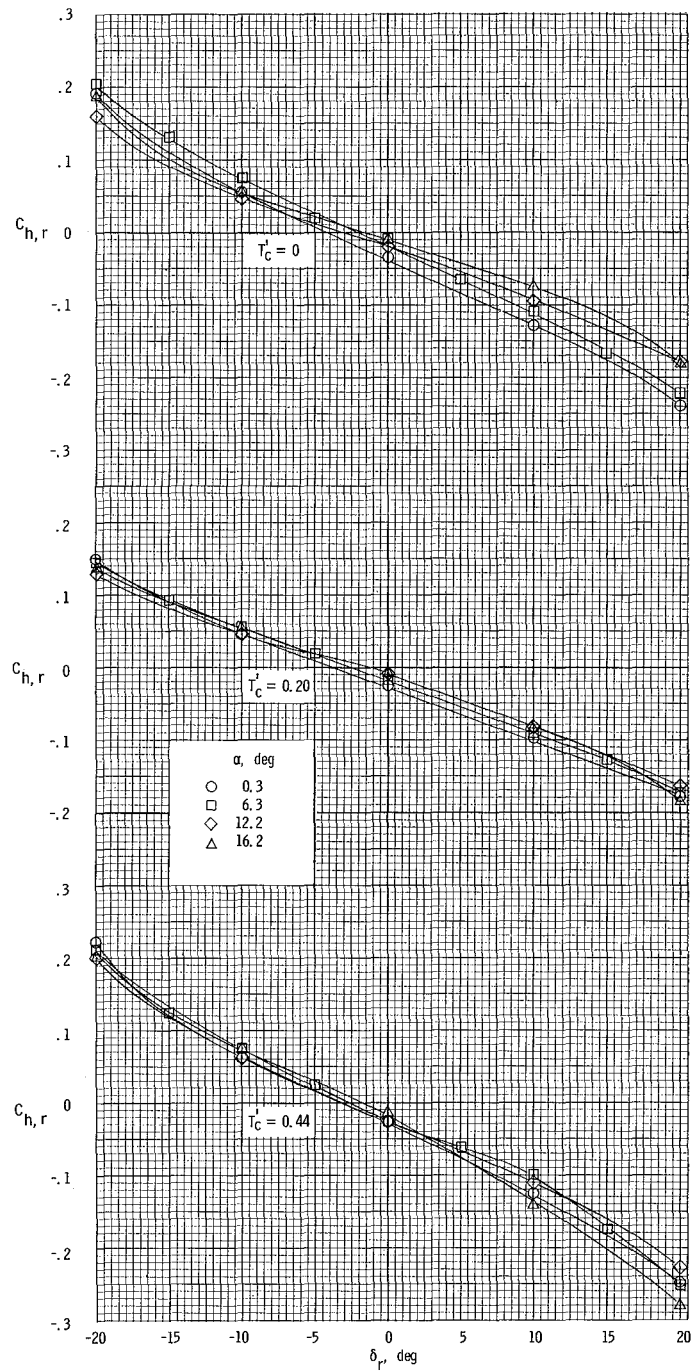
Figure 58.- Concluded.
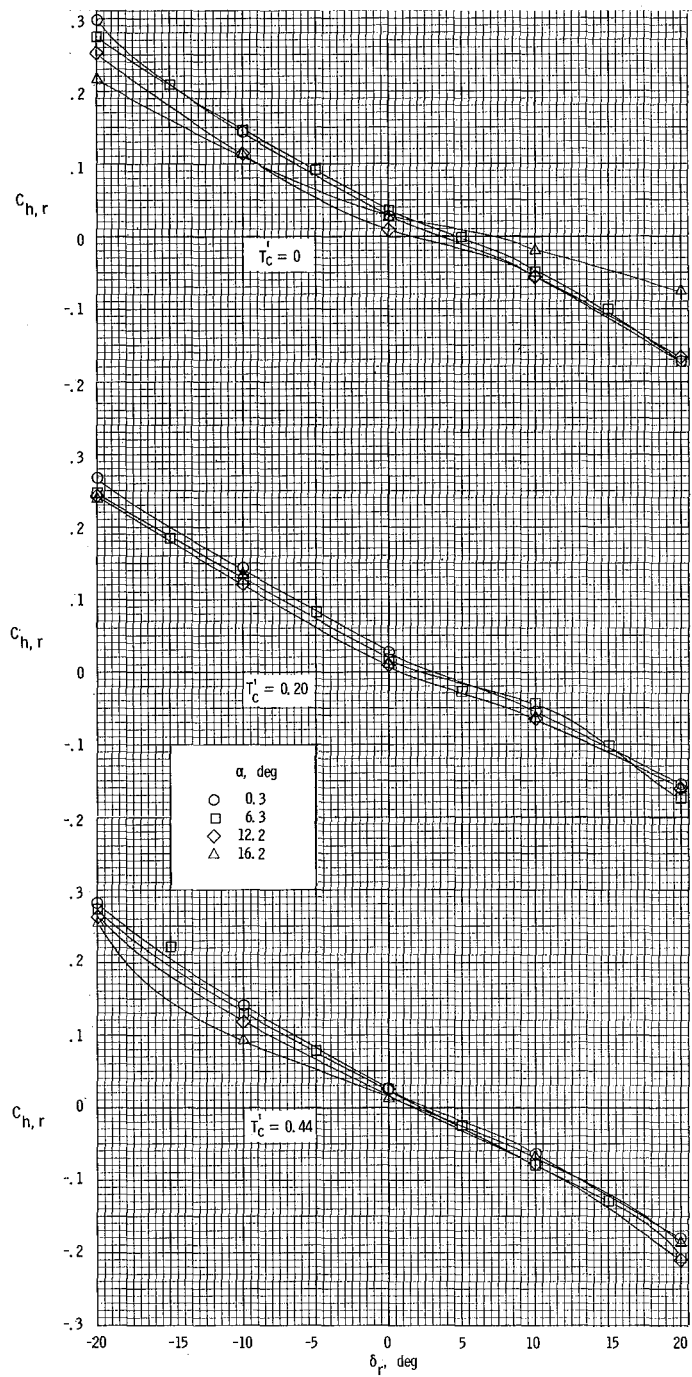
(a) $\beta = 8^\circ$.

Figure 59.- Variation of rudder hinge-moment coefficient with control deflection. $\delta_f = 27^\circ$.
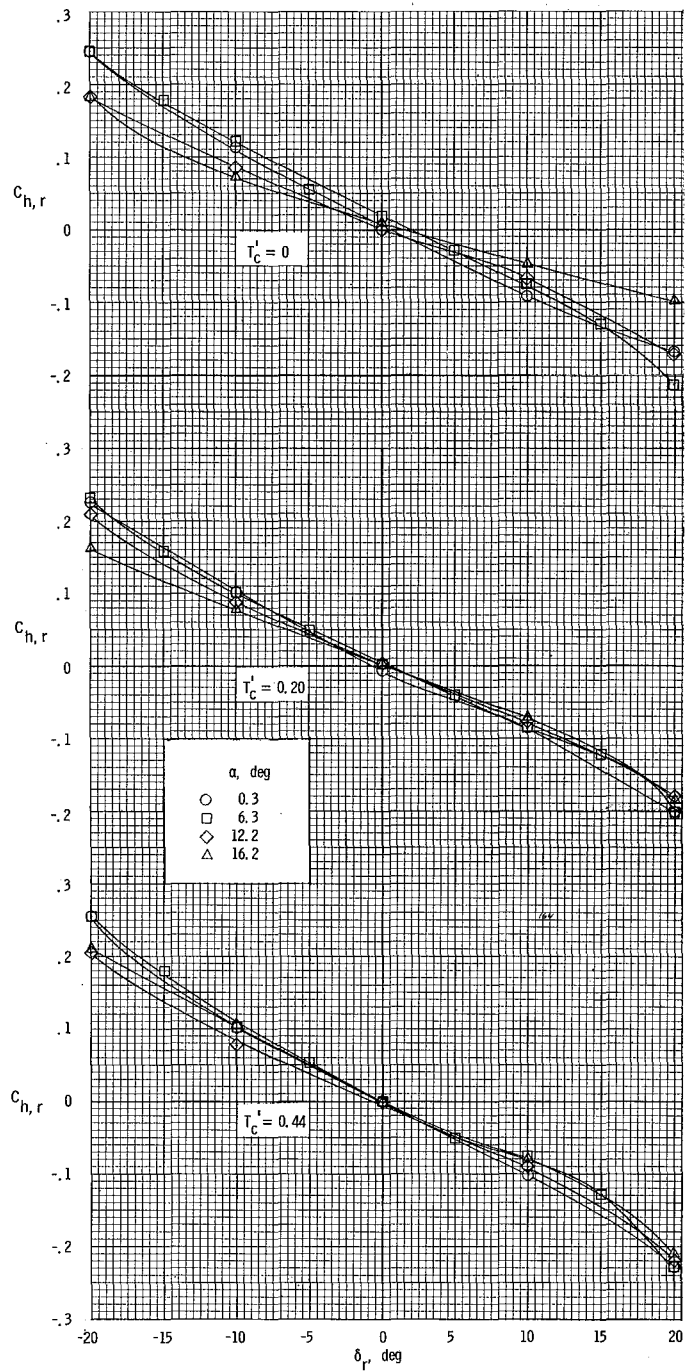
(b) β = 0⁰.

Figure 59.- Continued.

(c) $\beta = -8^0$.
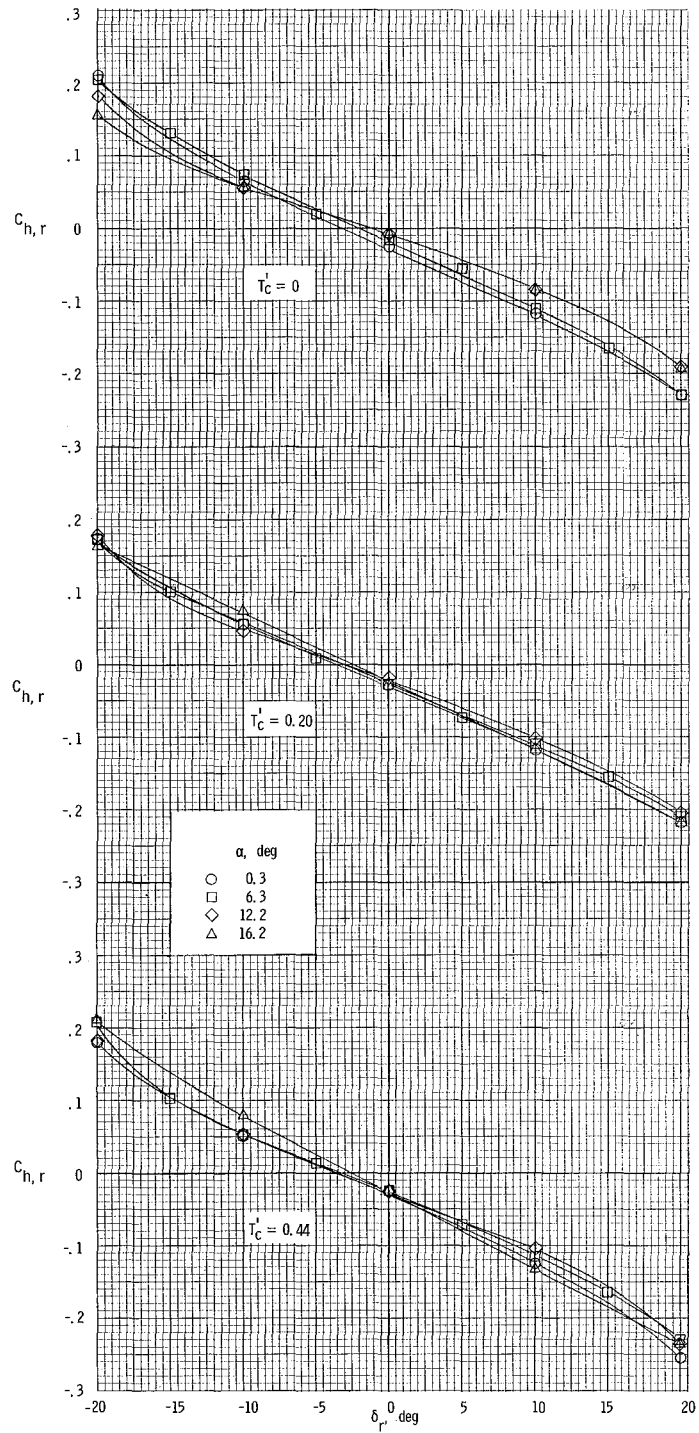
Figure 59.- Concluded.
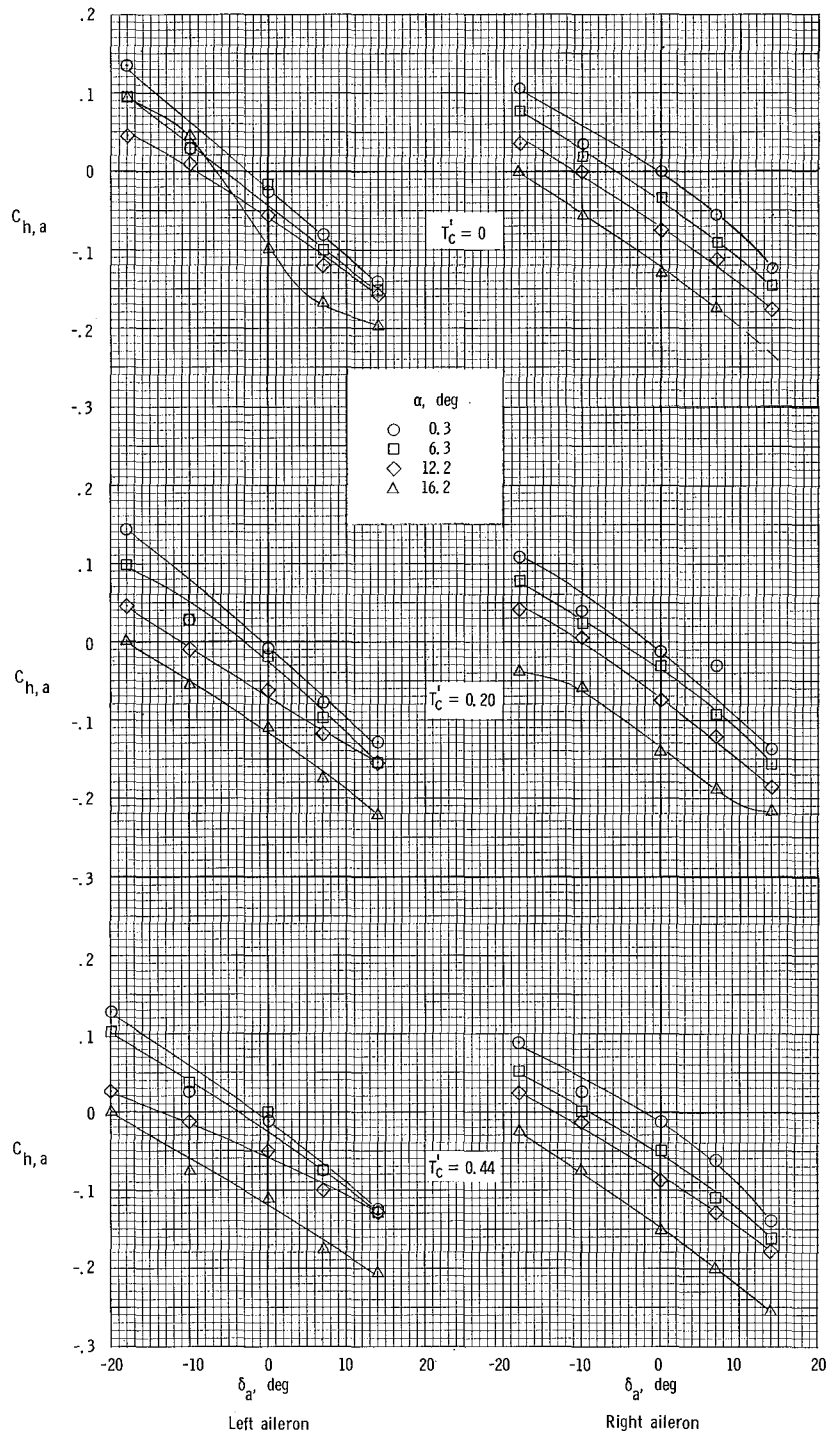
(a) $\beta = 8^0$.

Figure 60.- Variation of aileron hinge-moment coefficient with control deflection. $\delta_f = 0^0$.

179
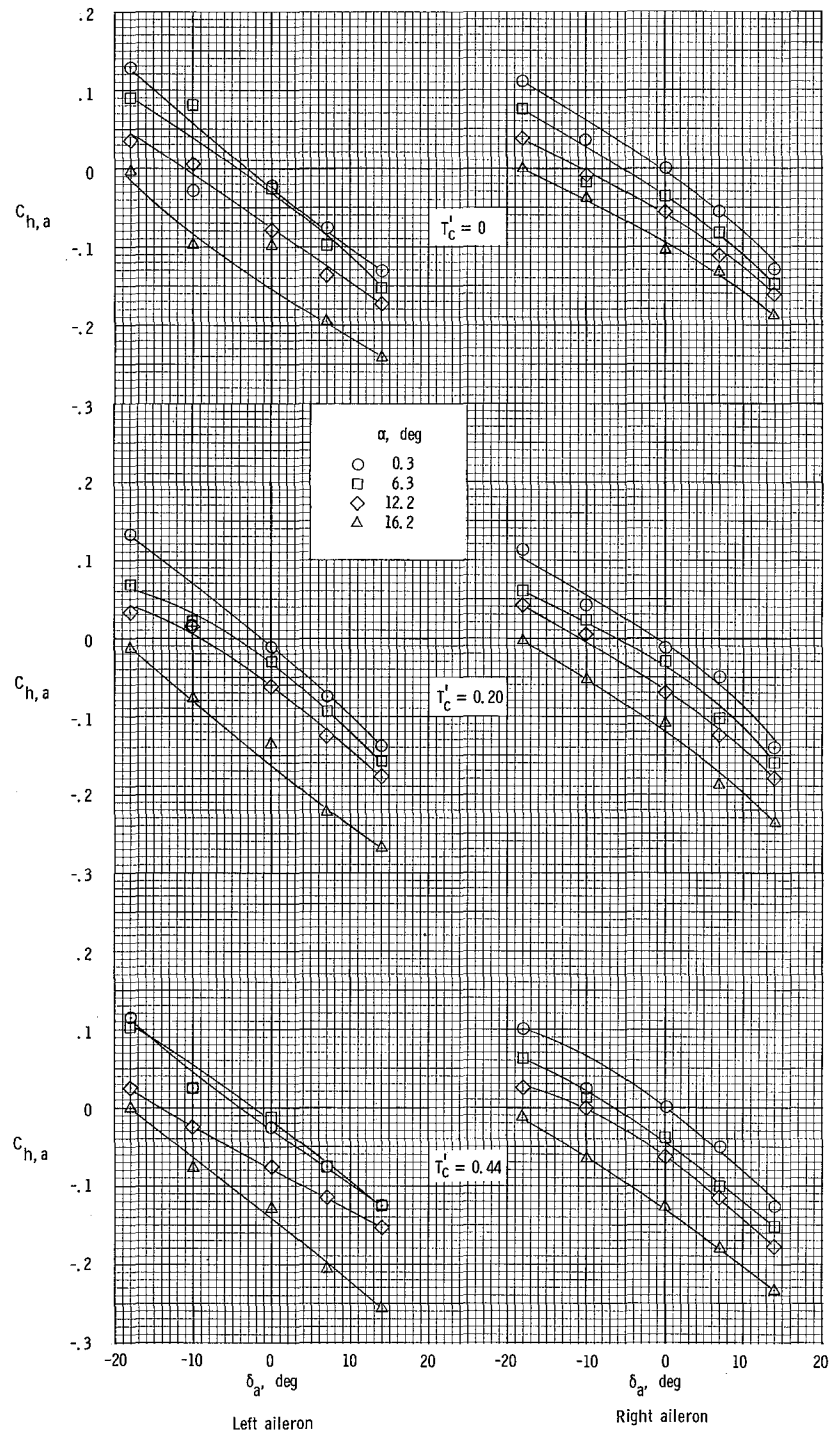
(b) $\beta = 0^0$.

Figure 60.- Continued.

(c) $\beta = -8^0$.
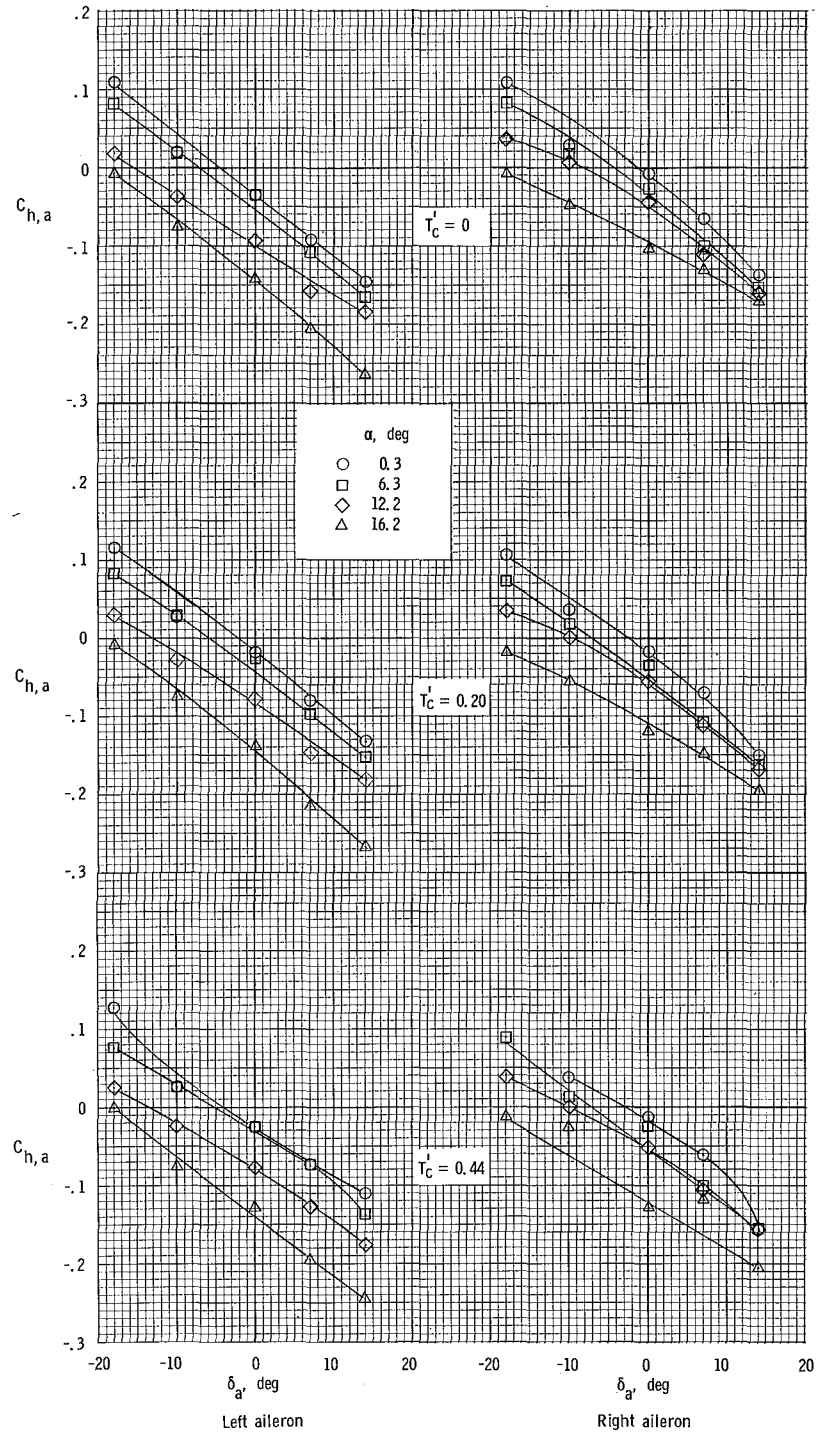
Figure 60.- Concluded.

(a) $\beta = 8^0$.
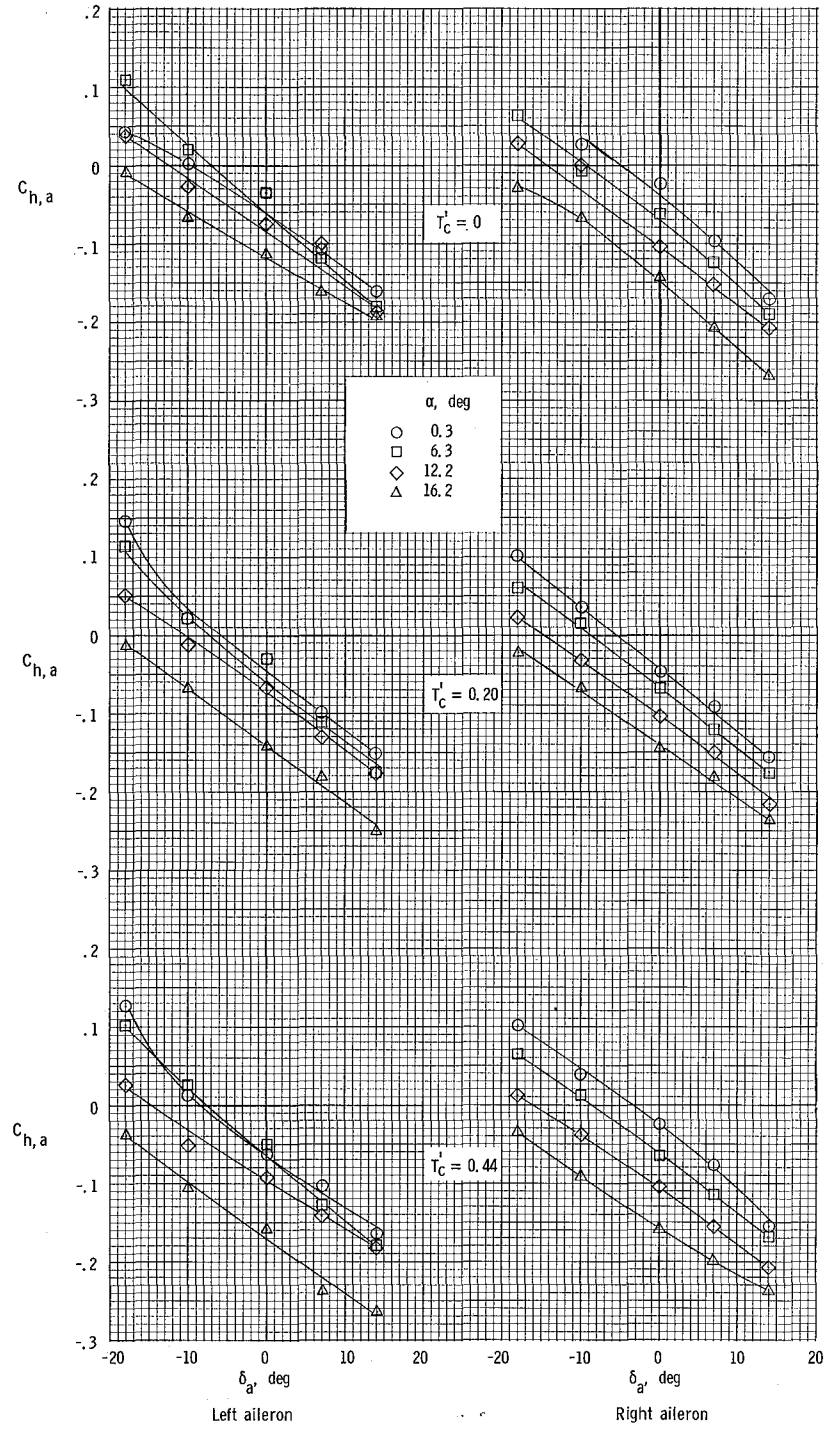
Figure 61.- Variation of aileron hinge-moment coefficient with control deflection. $\delta_f = 27^0$.
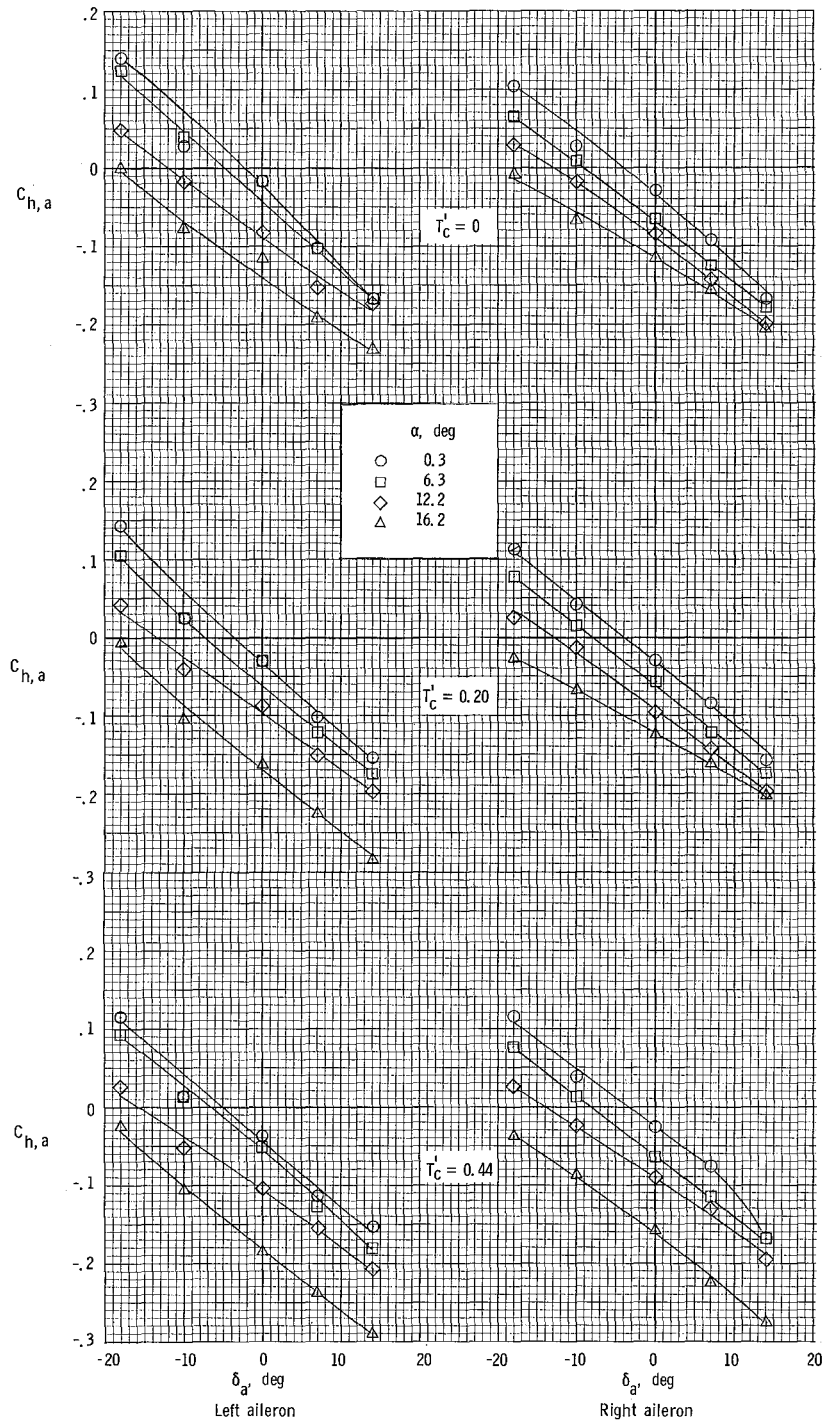
(b) $\beta = 0^0$.

Figure 61.- Continued.

(c) $\beta = -8^0$.
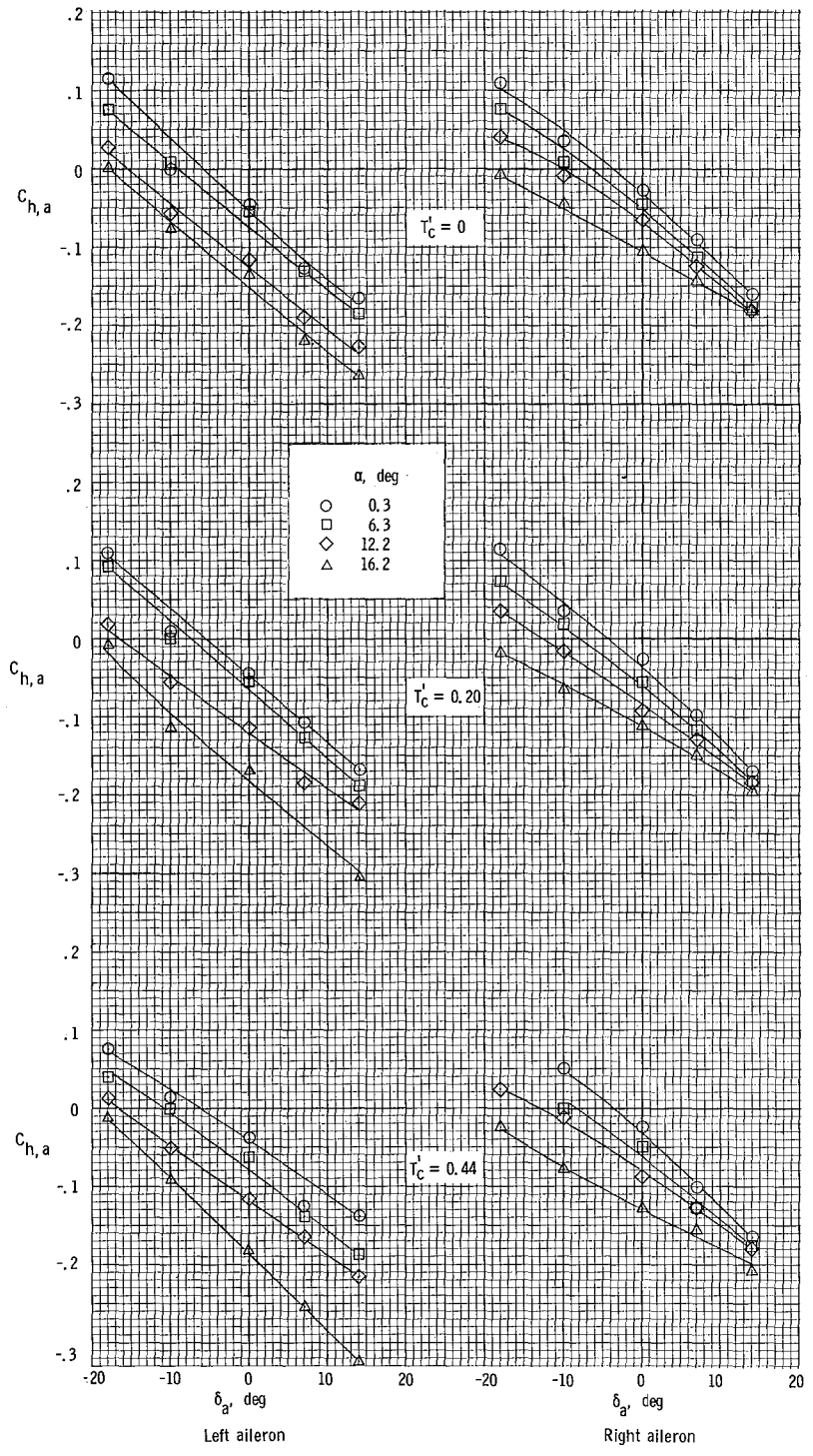
Figure 61.- Concluded.

(a) $\delta_f = 0^o$.
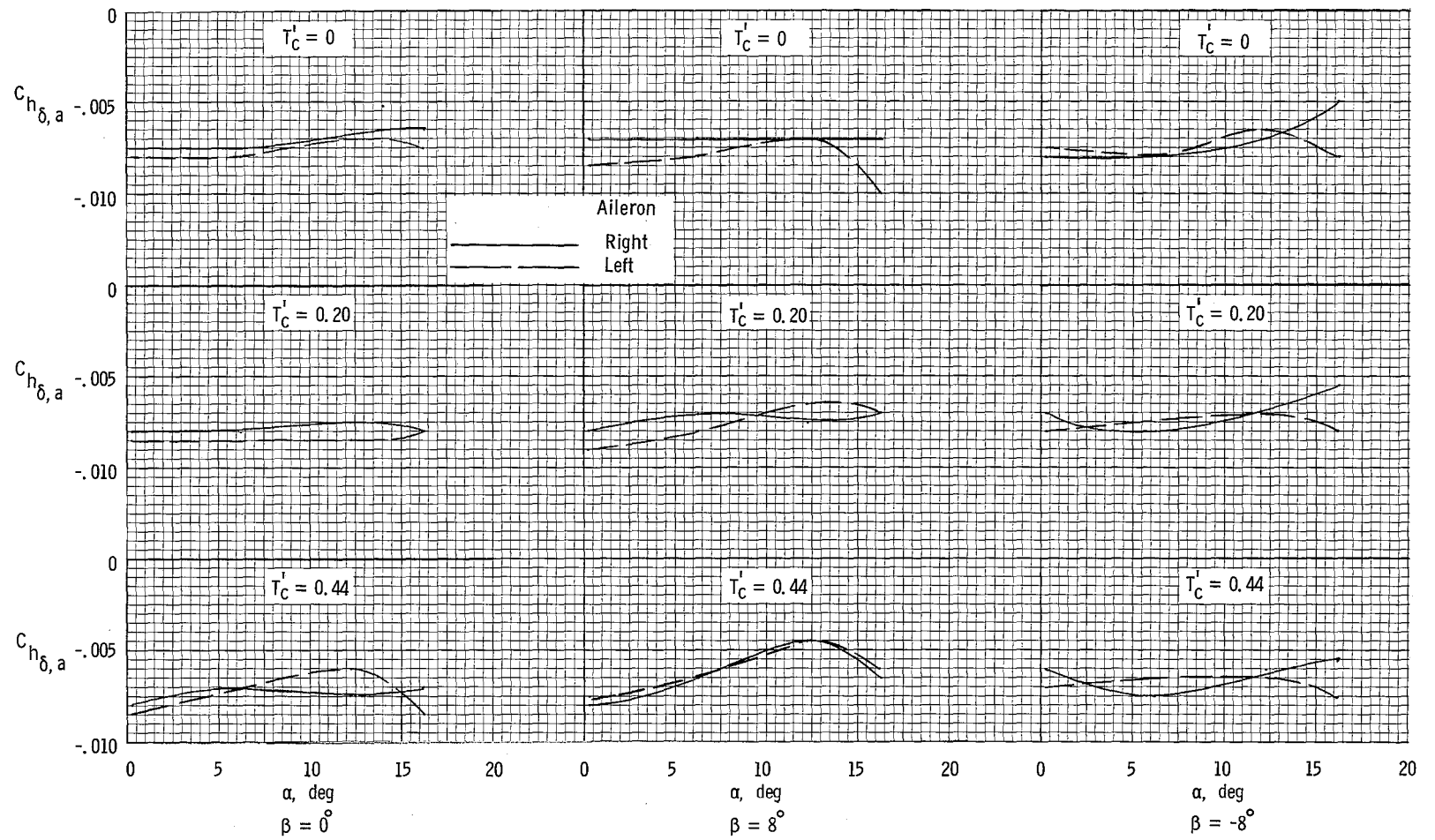
Figure 62.- Effect of sideslip and thrust coefficient on hinge-moment parameter $C_{h_{\delta,a}}$.

(b) $\delta_f = 27^o$.
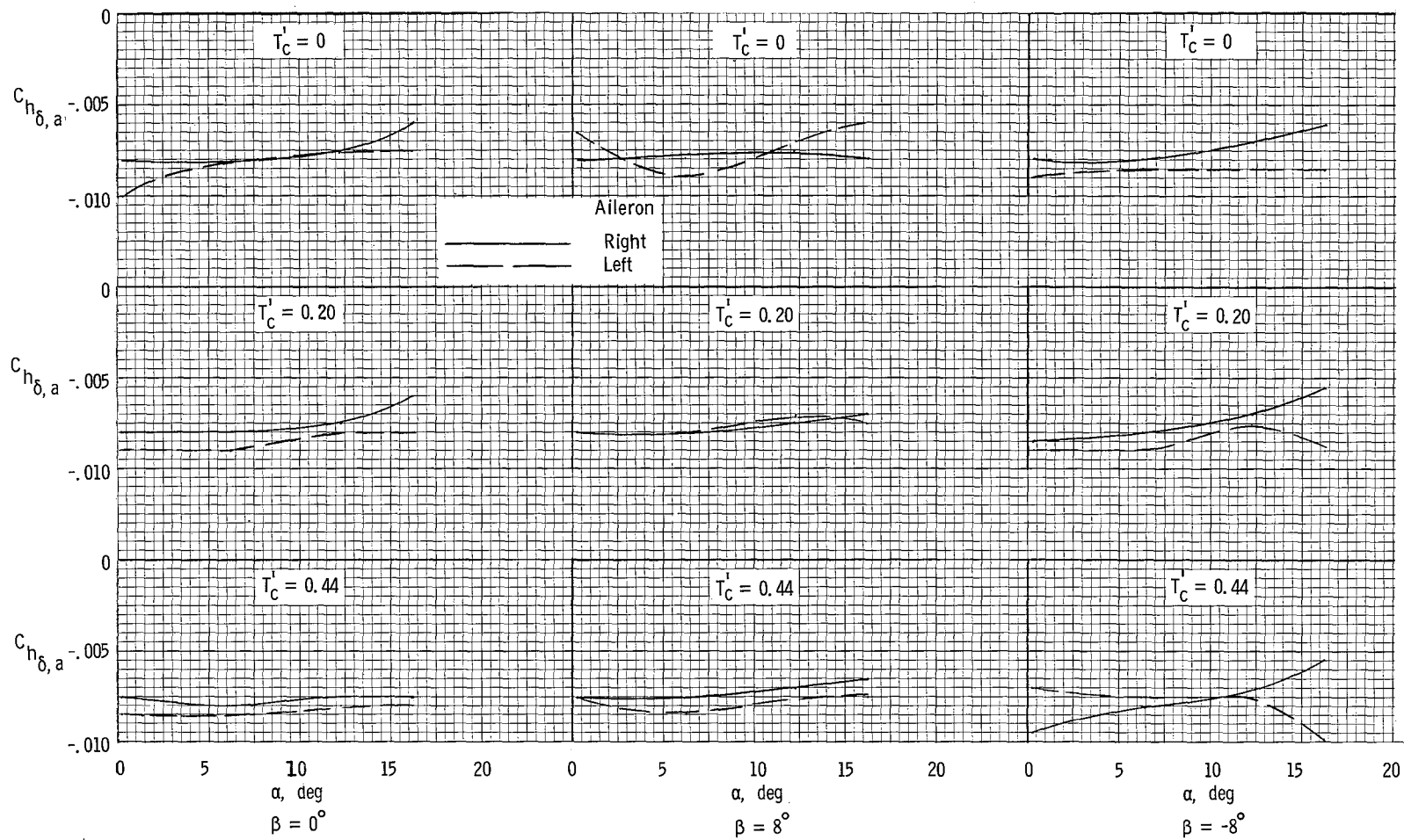
Figure 62.- Concluded.
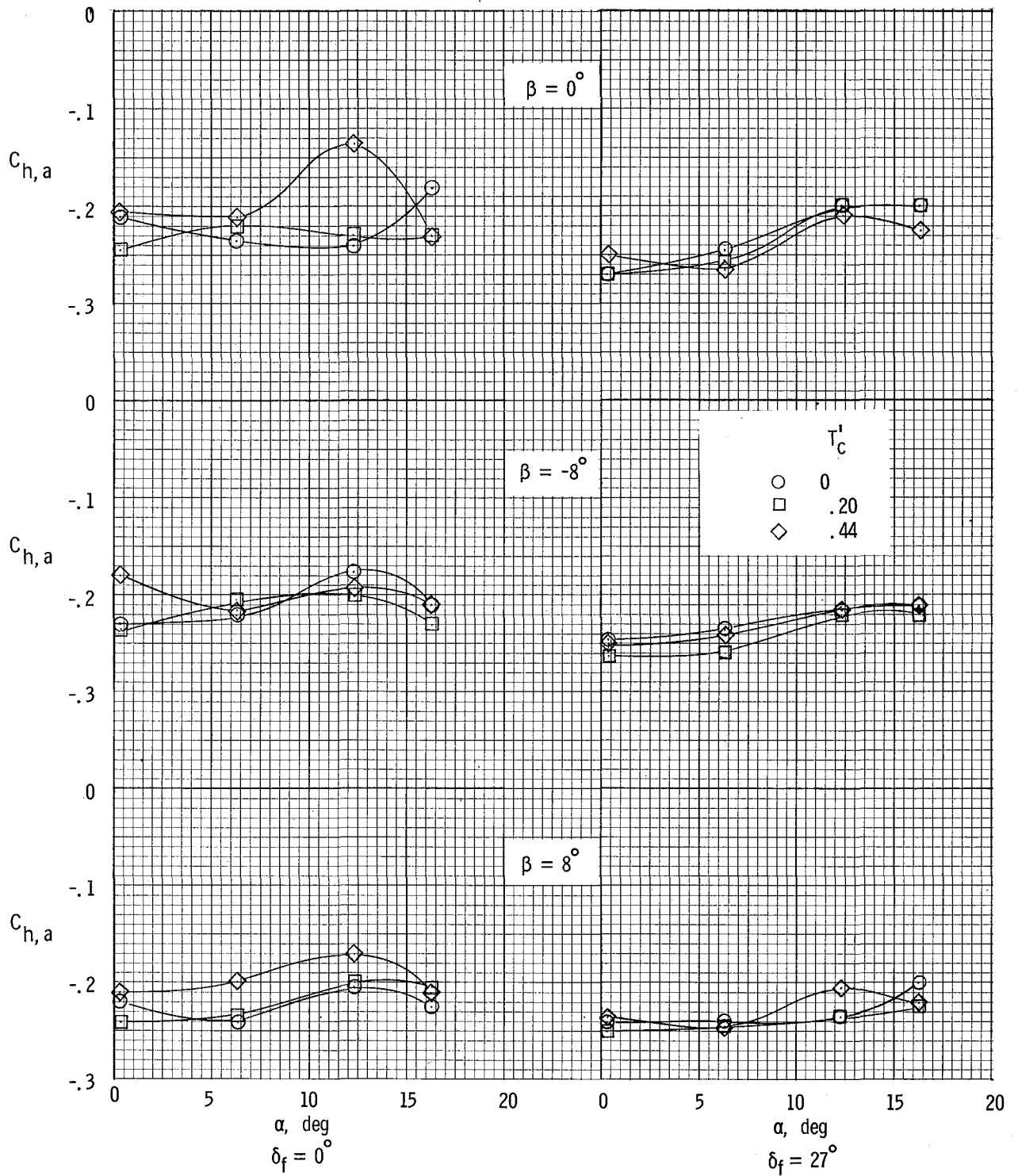
Figure 63.- Total aileron hinge-moment coefficients for full right control.
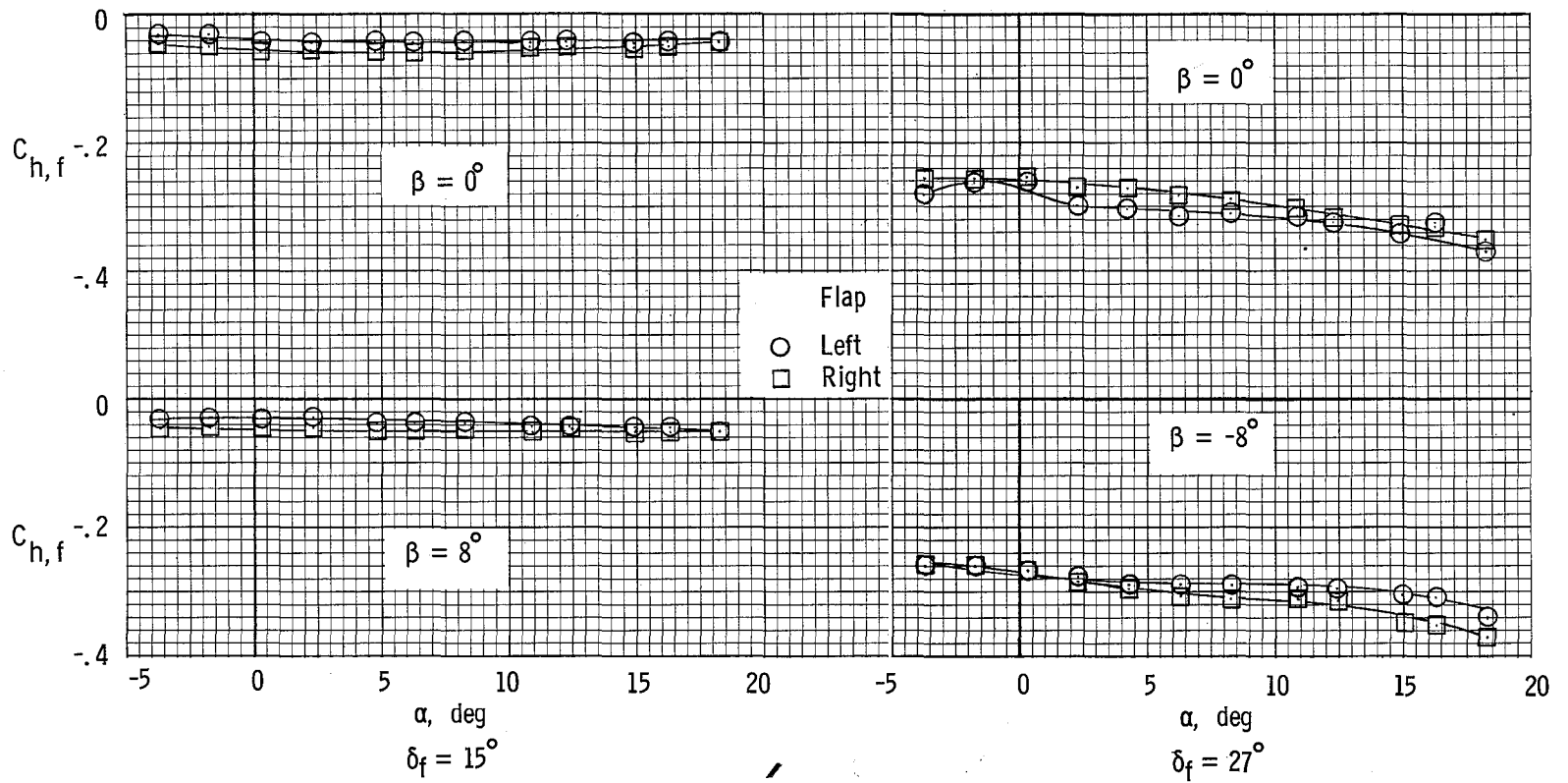
Figure 64.- Variation of flap hinge-moment coefficients with angle of attack with propellers removed.

(a) $\delta_f = 15^0$.
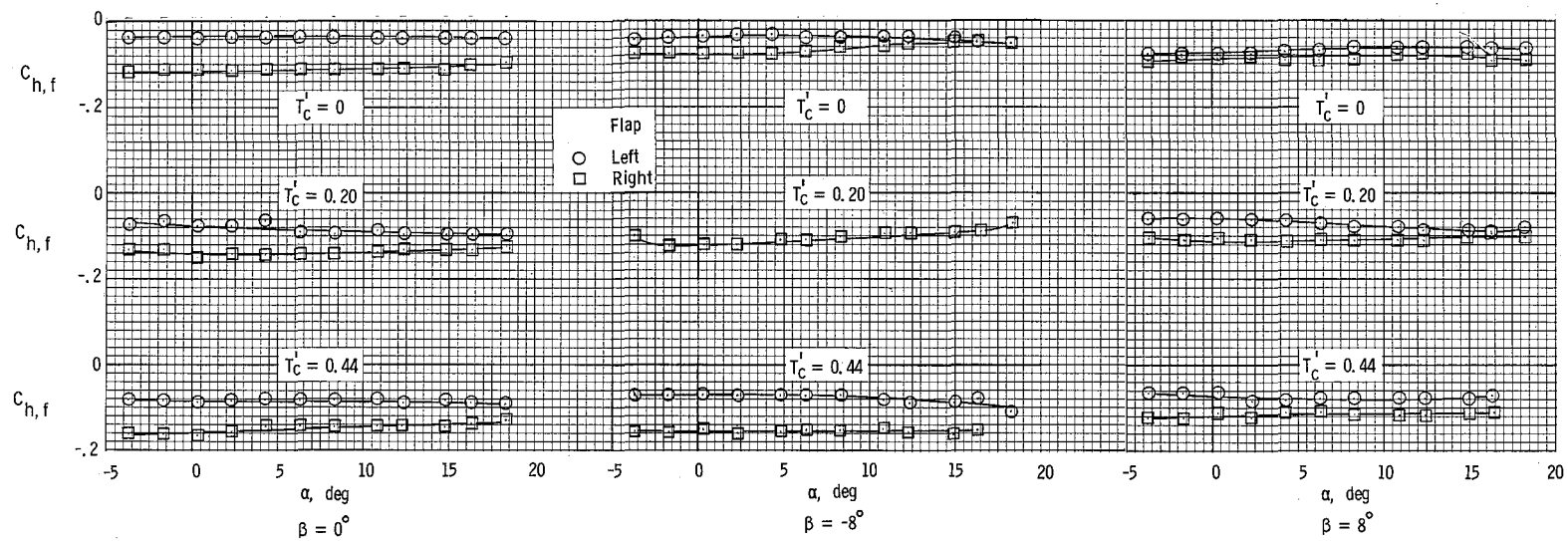
Figure 65.- Variation of flap hinge-moment coefficients with angle of attack for several thrust coefficients and sideslip angles.
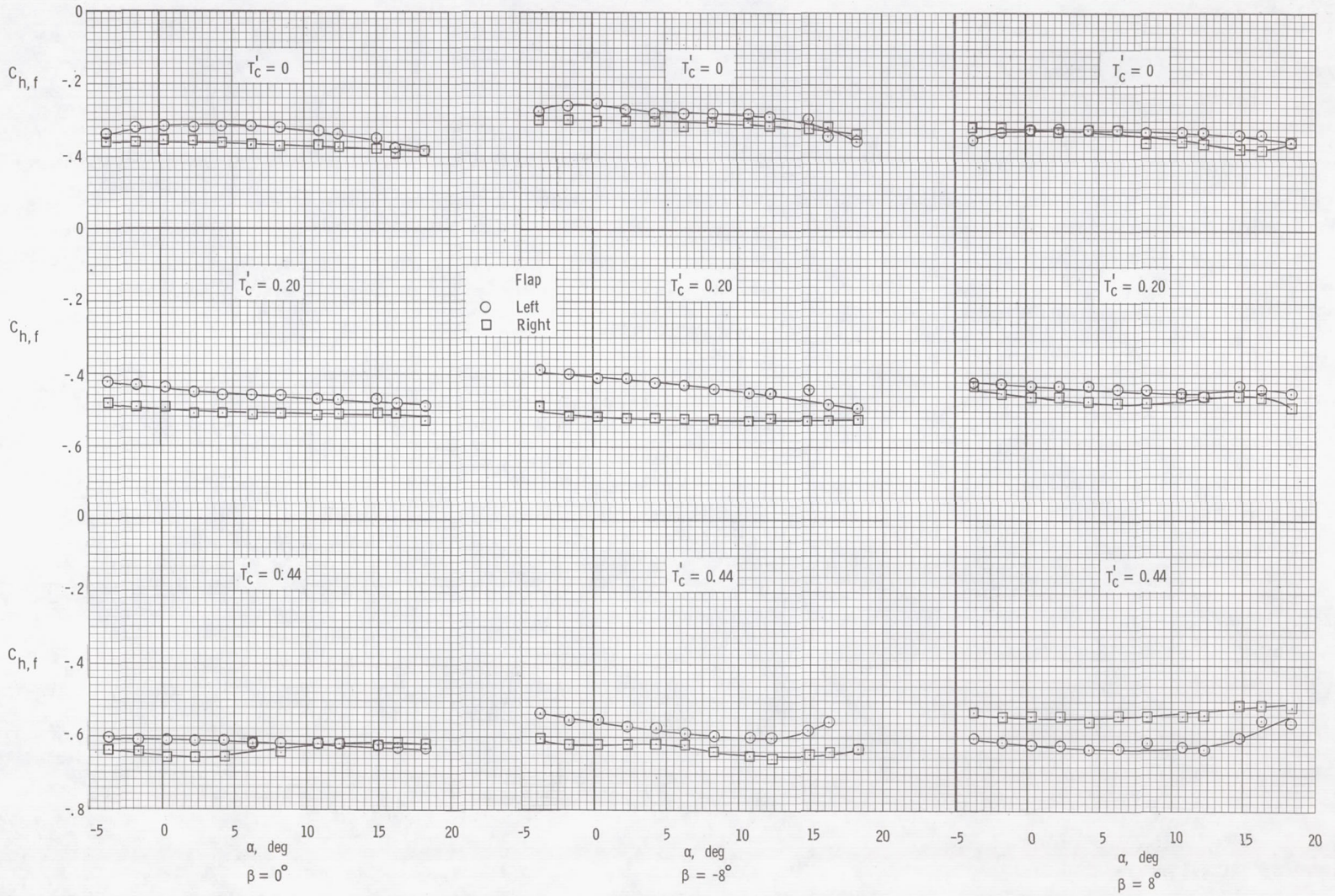
(b) $\delta_f = 27^{\circ}$.

Figure 65.- Concluded.
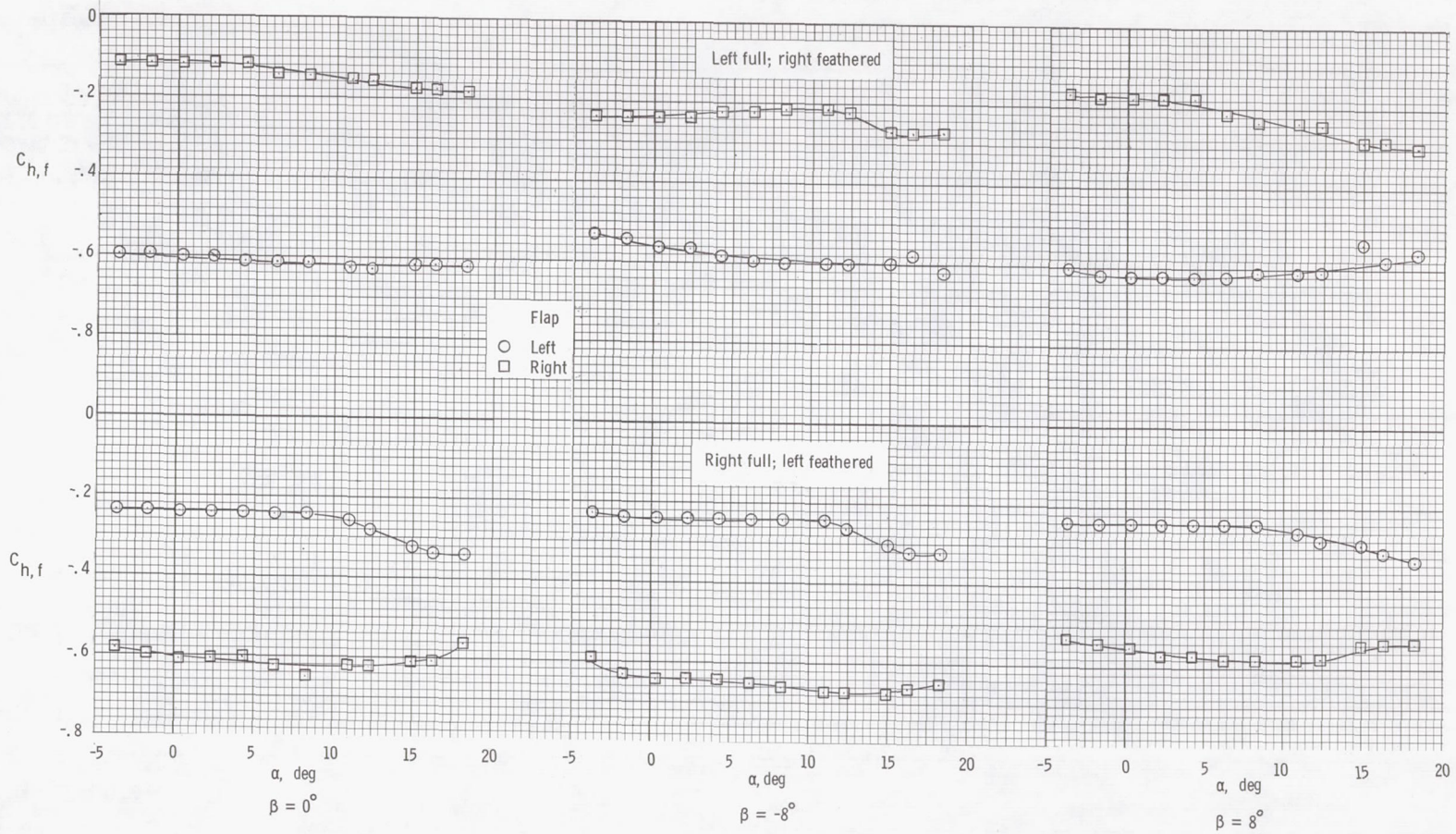
Figure 66.- Flap hinge-moment coefficients for asymmetric power. $\delta_f = 27°$.
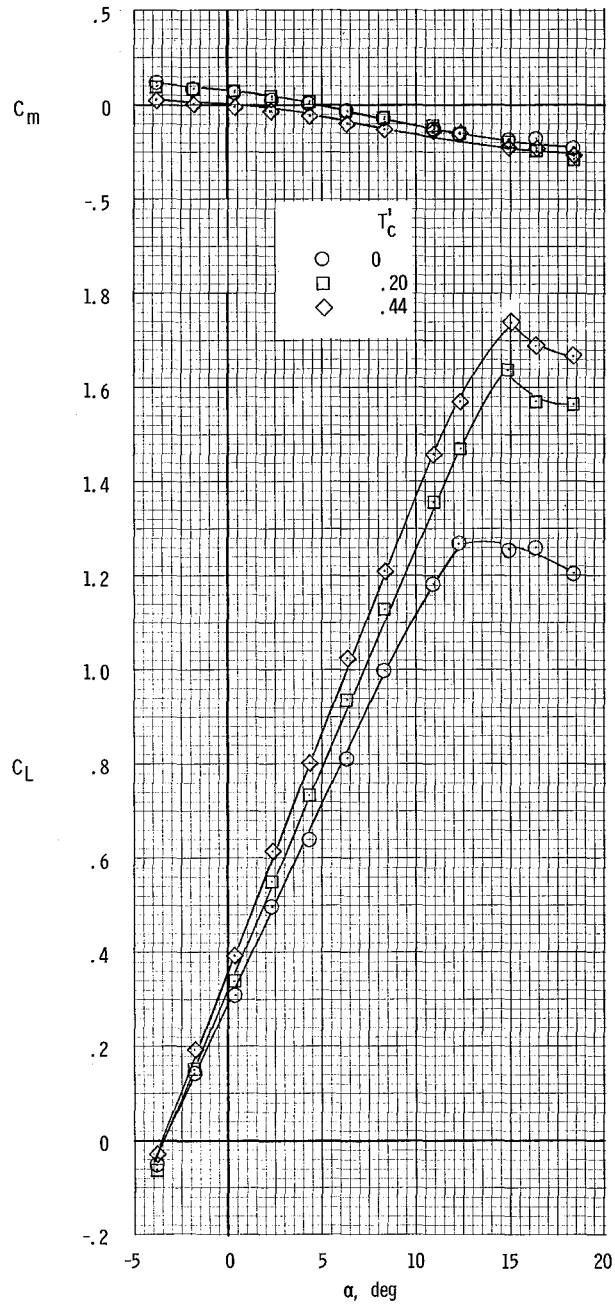
(a) $\delta_f = 0^0$.

Figure 67.- Effect of power on longitudinal characteristics. $\beta = 0^0$; $\delta_t = 0^0$.

(b) $\delta_f = 15^o$.
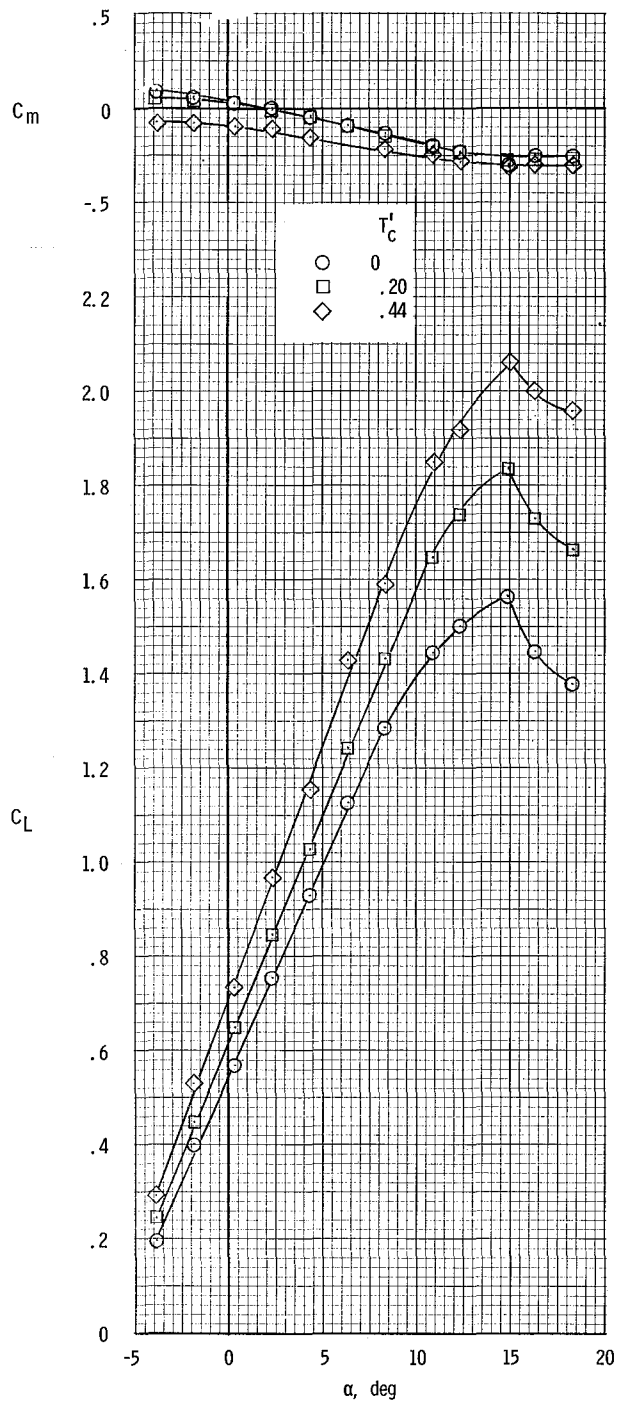
Figure 67.- Continued.

(c) $\delta_f = 27^0$.
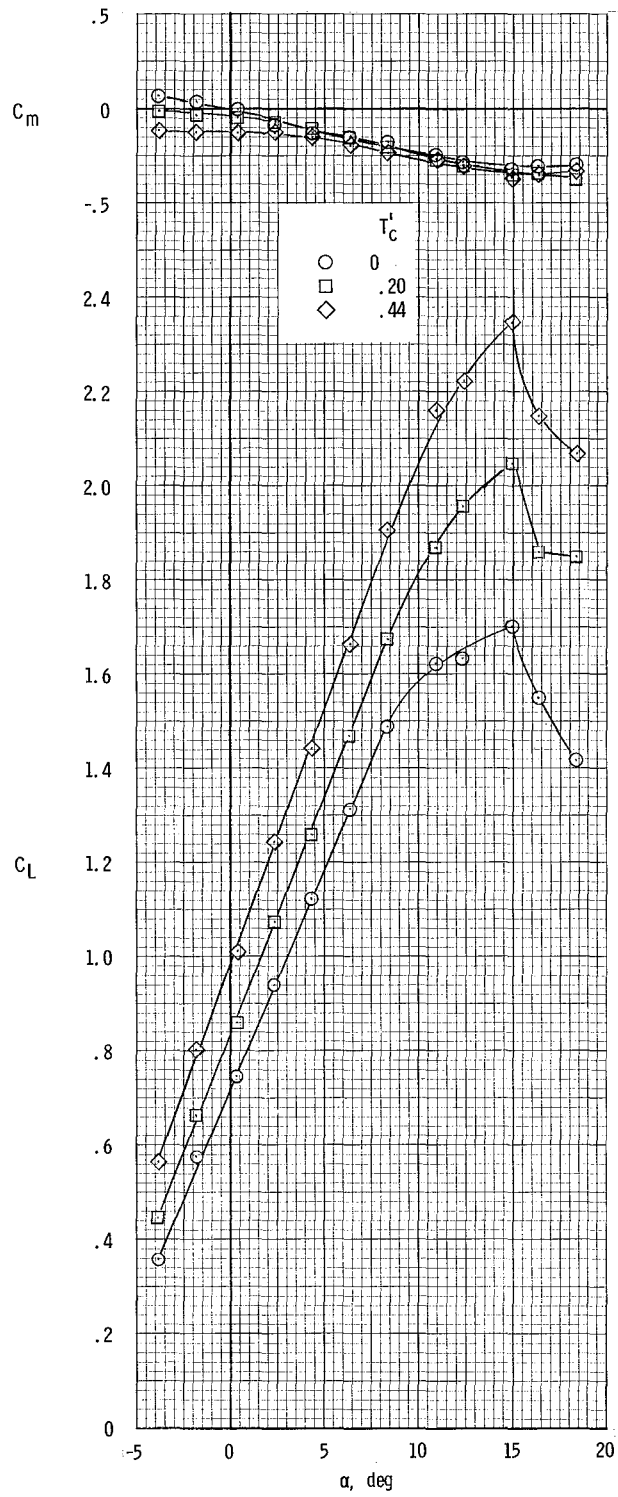
Figure 67.- Concluded.
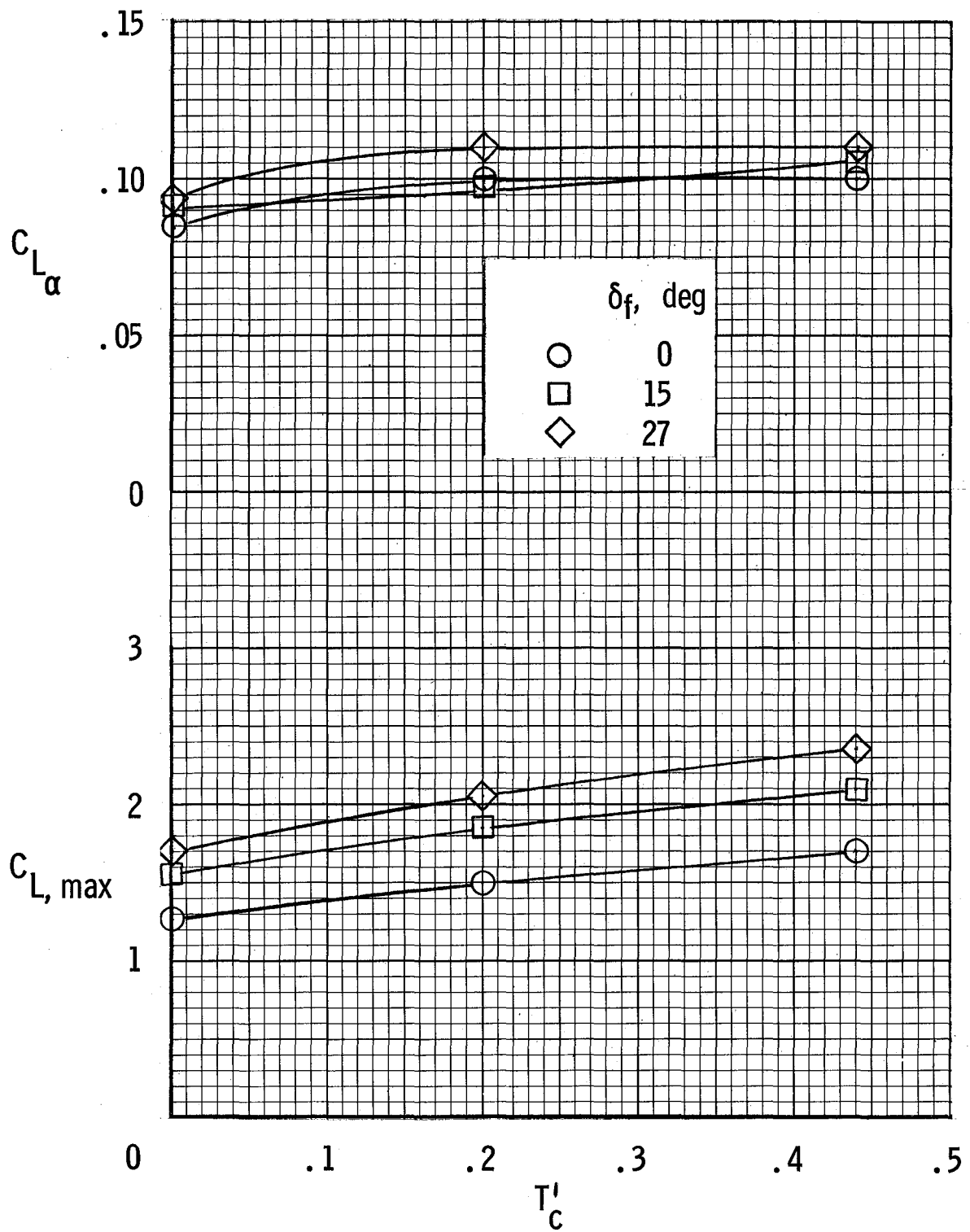
Figure 68.- Effect of power on lift-curve slope and maximum lift coefficient. $\delta_t = 0^0$.
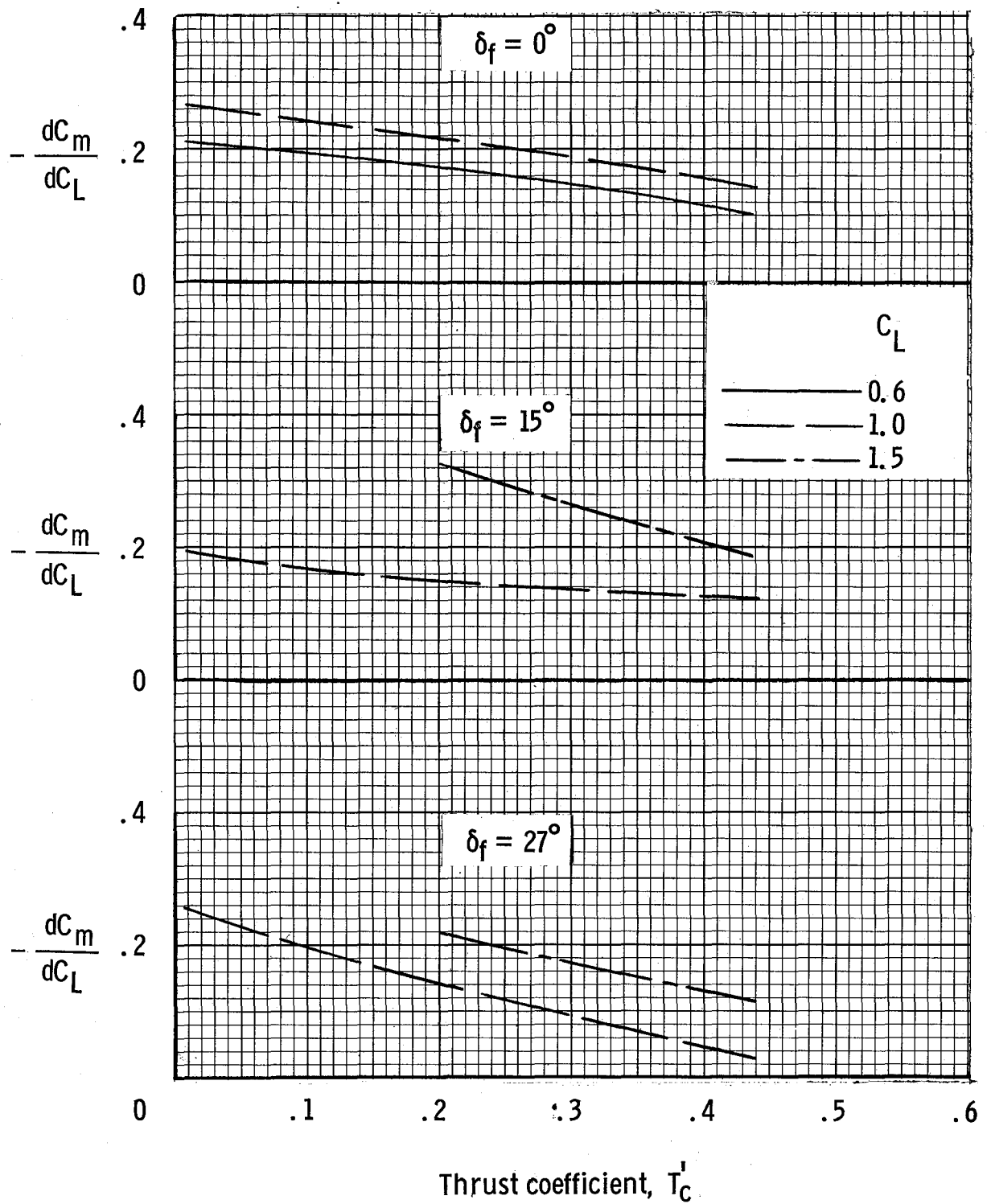
Figure 69.- Effect of power on stick-fixed longitudinal stability characteristics.
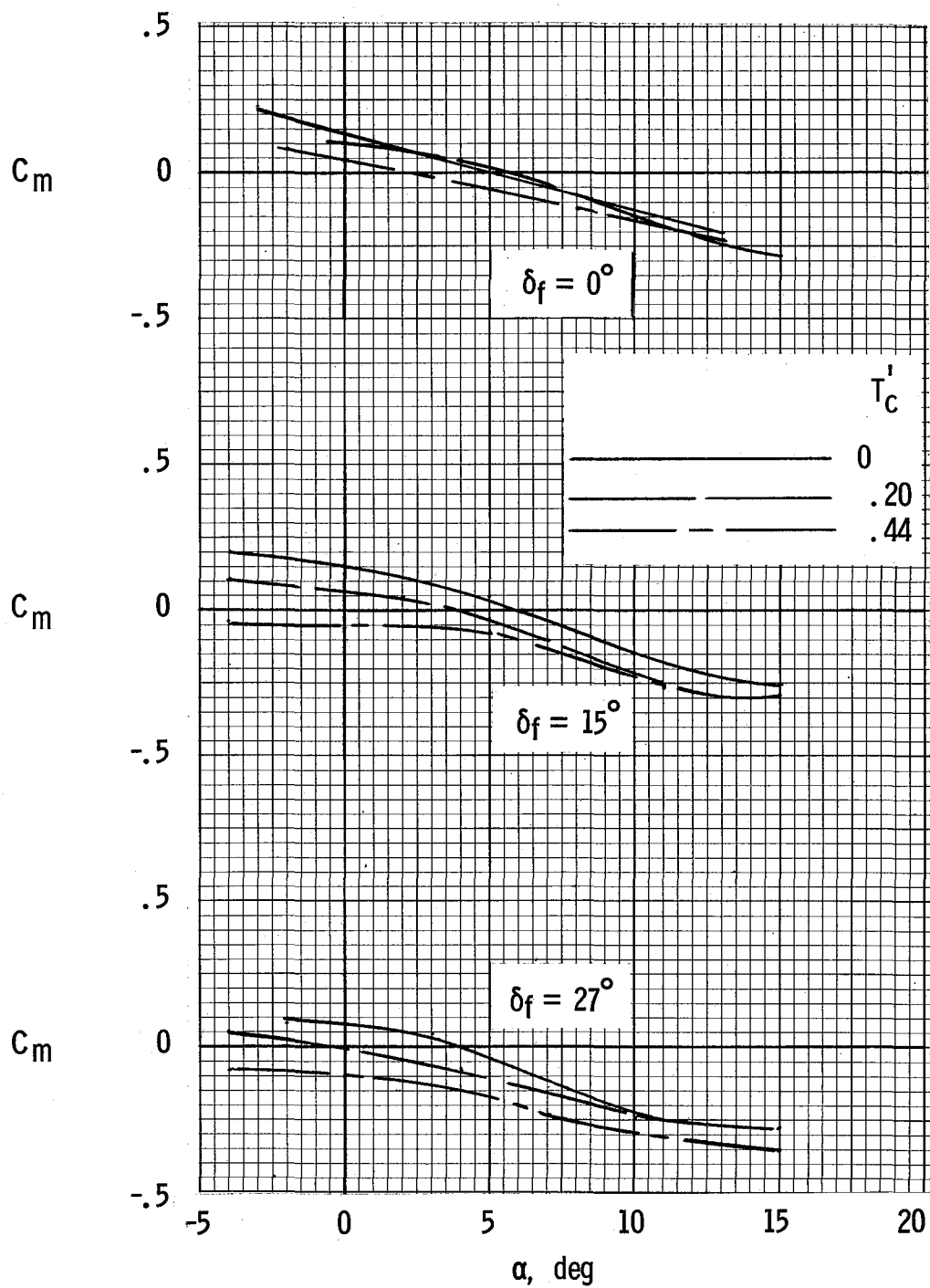
(a) Variation of stick-free pitching moment with angle of attack.

Figure 70.- Stick-free static stability characteristics.
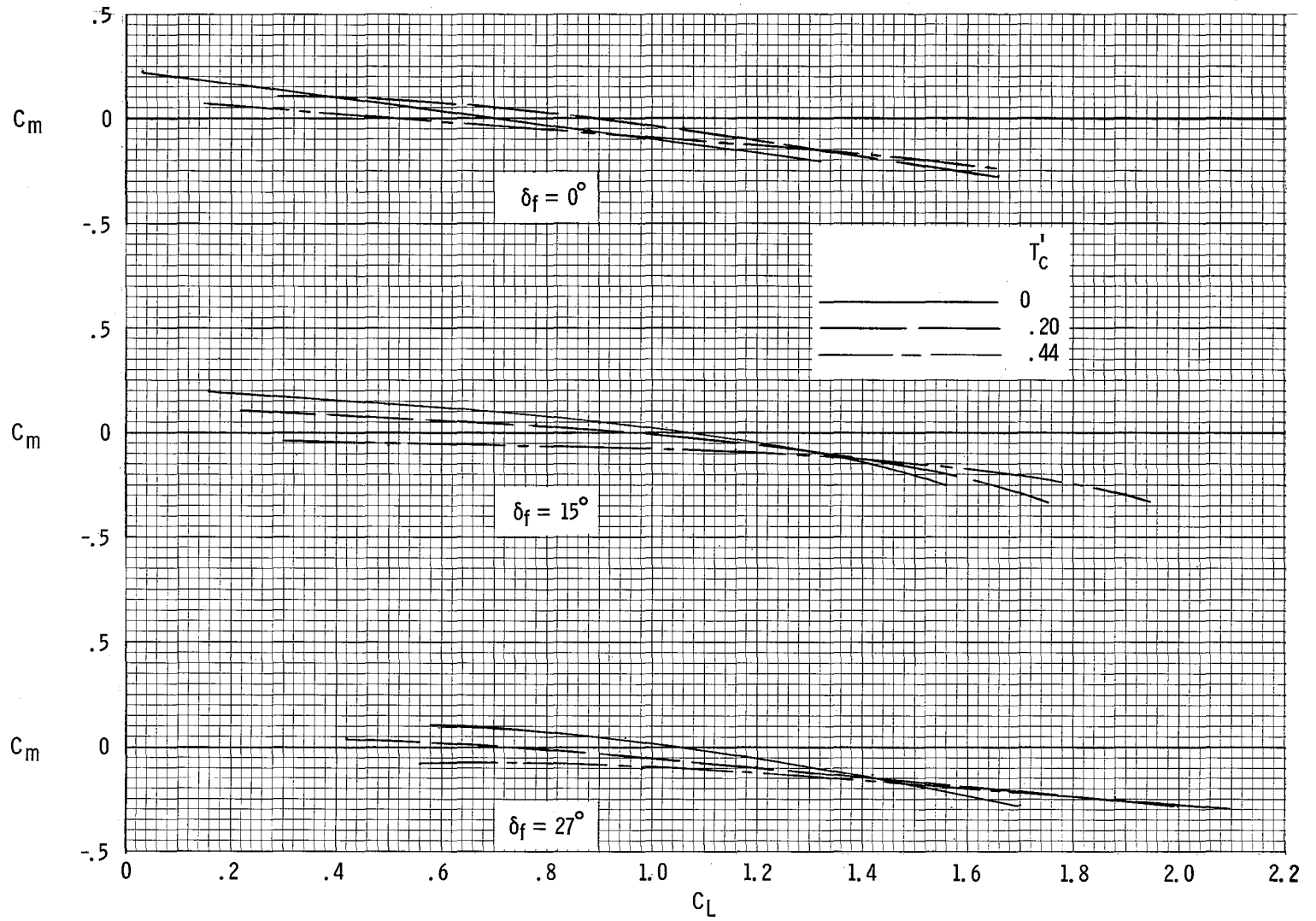
(b) Variation of stick-free pitching moment with lift coefficient.

Figure 70.- Continued.
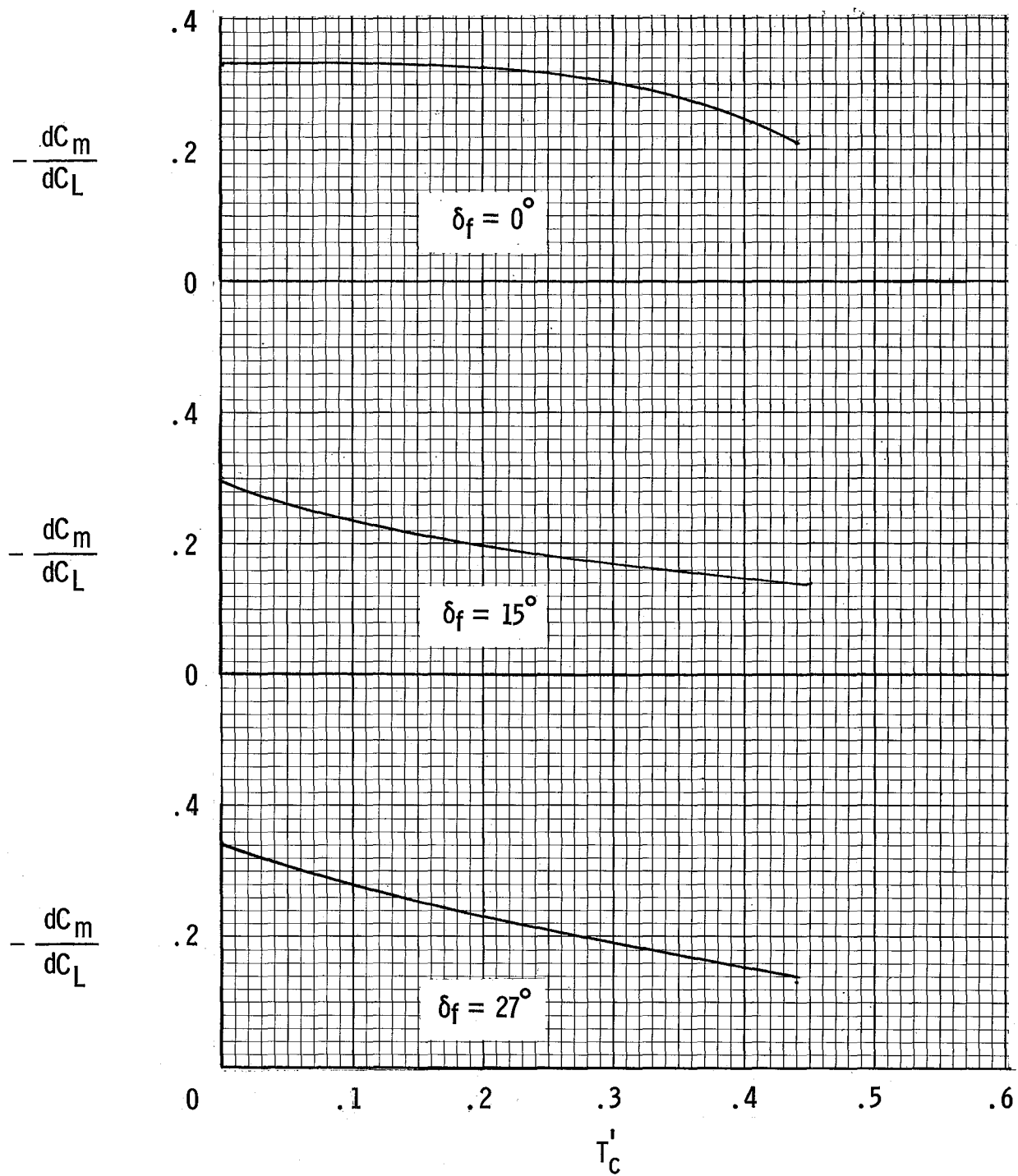
(c) Effect of power on stick-free longitudinal stability. $C_L = 1.0$.

Figure 70.- Concluded.
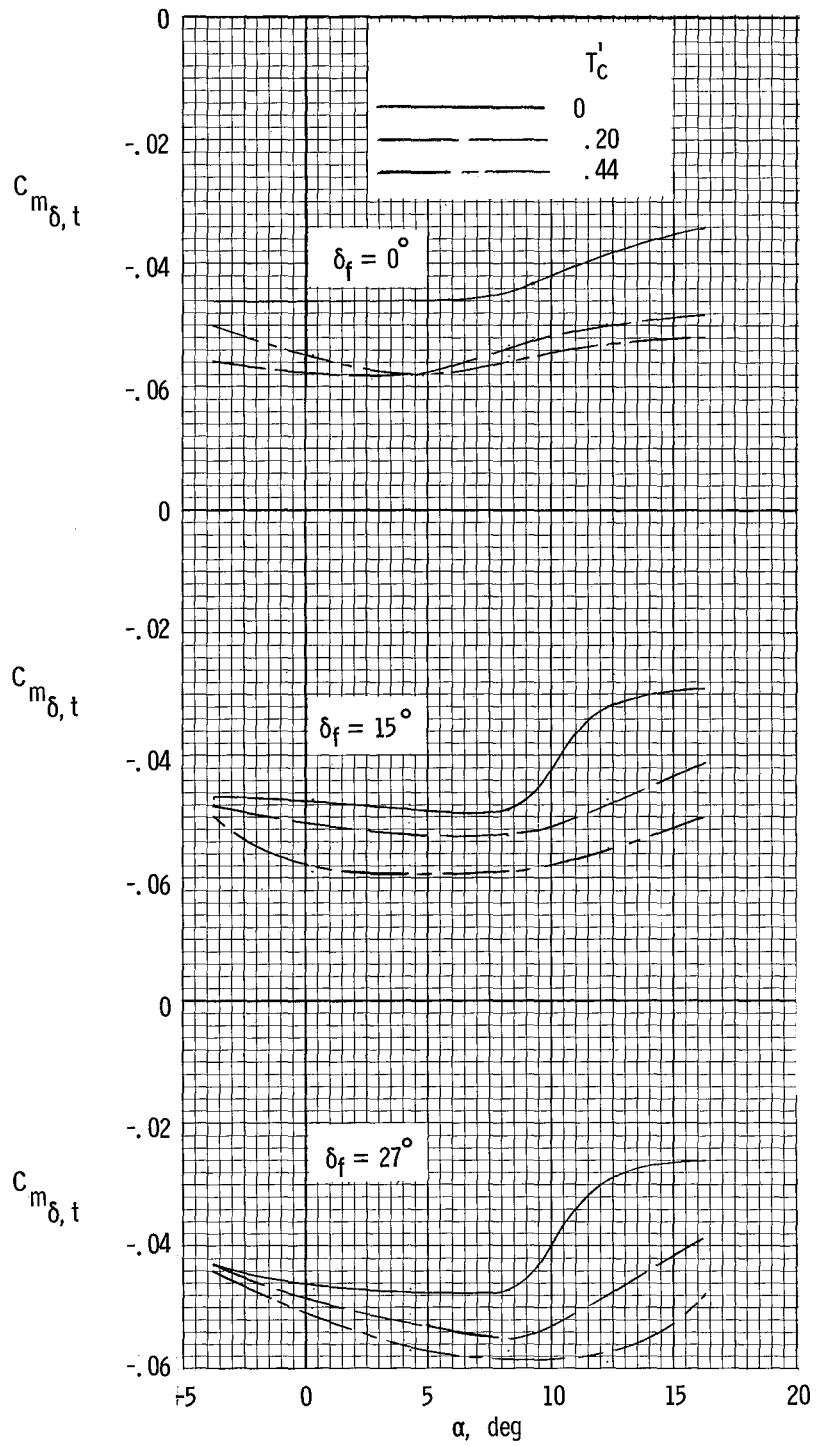
Figure 71.- Variation of horizontal-tail effectiveness with angle of attack for several power and flap settings.
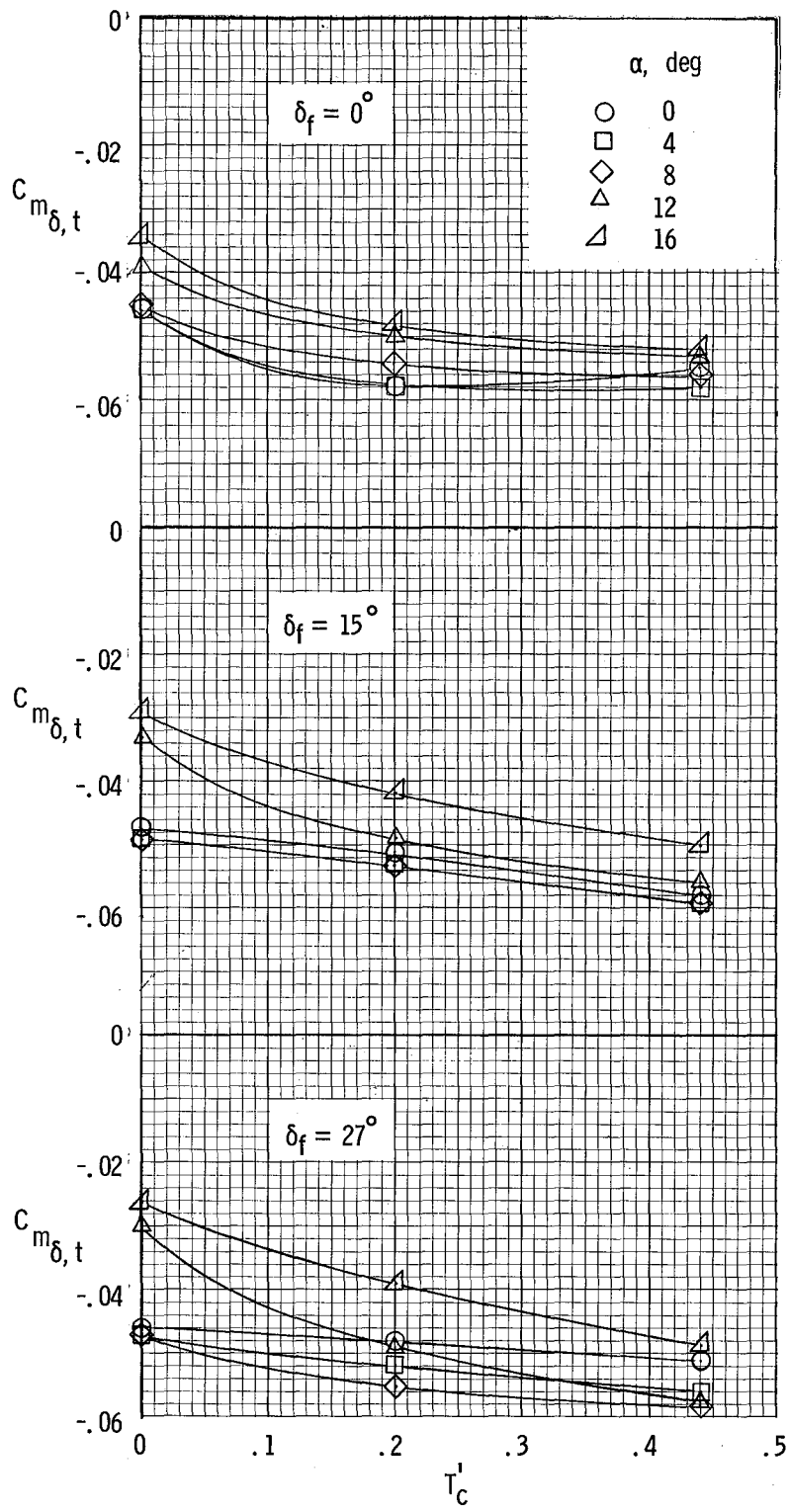
Figure 72.- Effect of power on horizontal-tail effectiveness.

ε, deg

$T'_c = 0.44$

$T'_c = 0$

$\delta_f = 0°$

$\delta_f = 15°$

$\delta_f = 27°$

α, deg

α, deg

α, deg
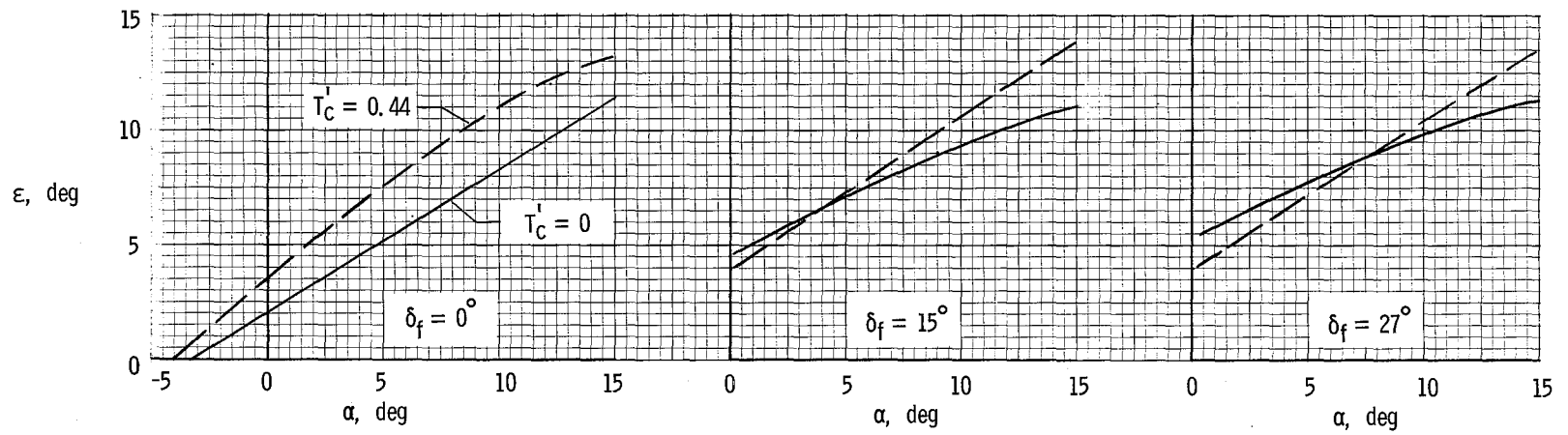
Figure 73.- Variation of downwash angle with angle of attack at horizontal tail for several flap and power conditions.
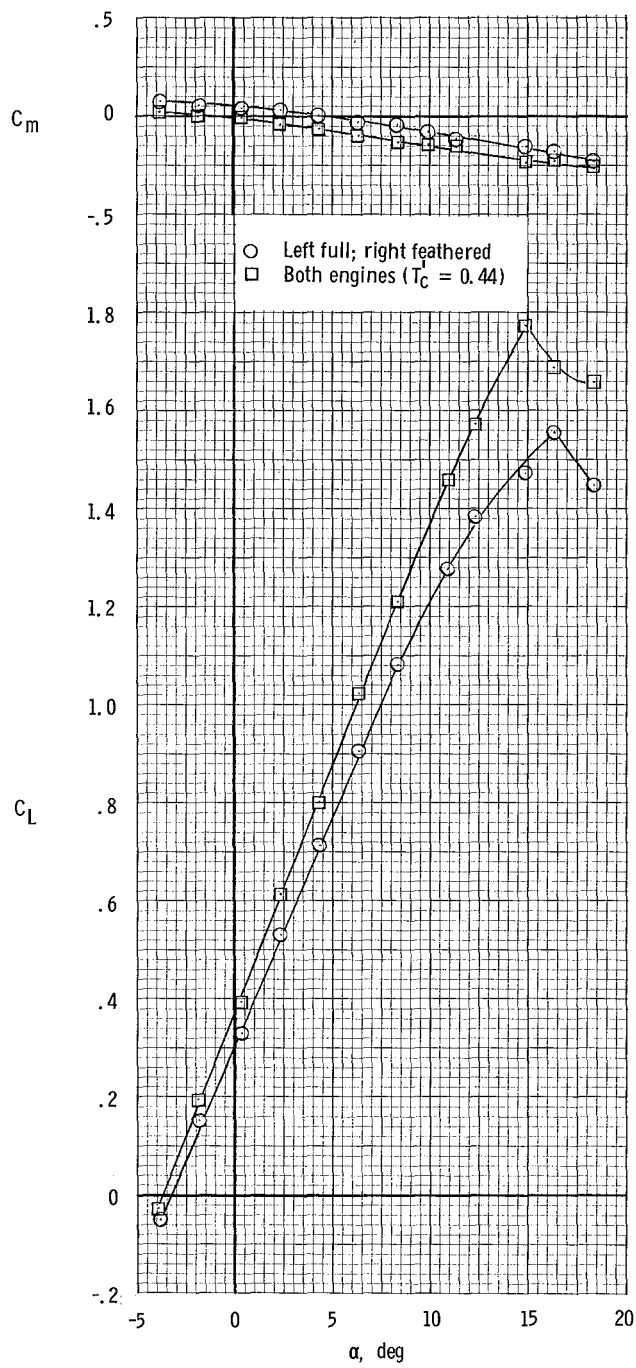
(a) $\delta_f = 0^0$.

Figure 74.- Effect of asymmetric power on longitudinal characteristics. $\beta = 0^0$; $\delta_t = 0^0$.
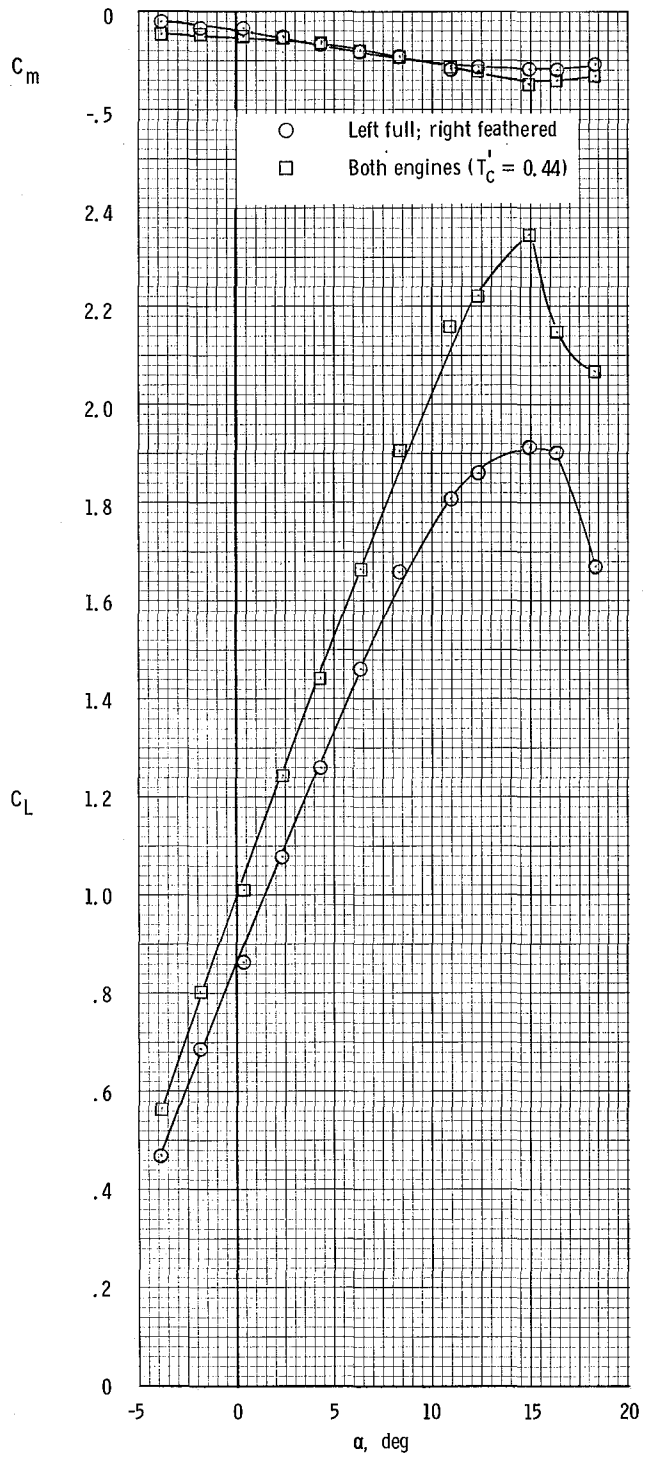
(b) $\delta_f = 27^\circ$.

Figure 74.- Concluded.
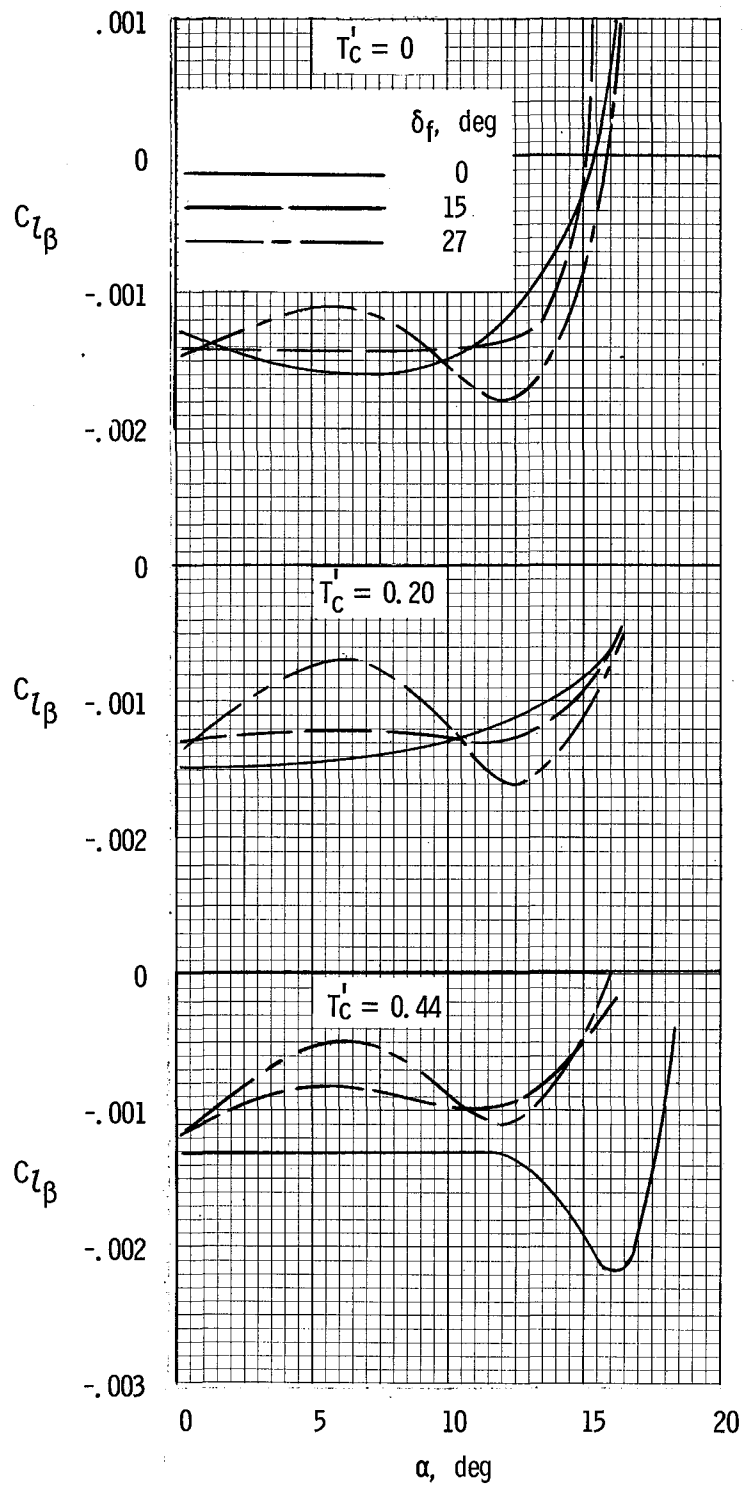
Figure 75.- Effective dihedral characteristics.

205
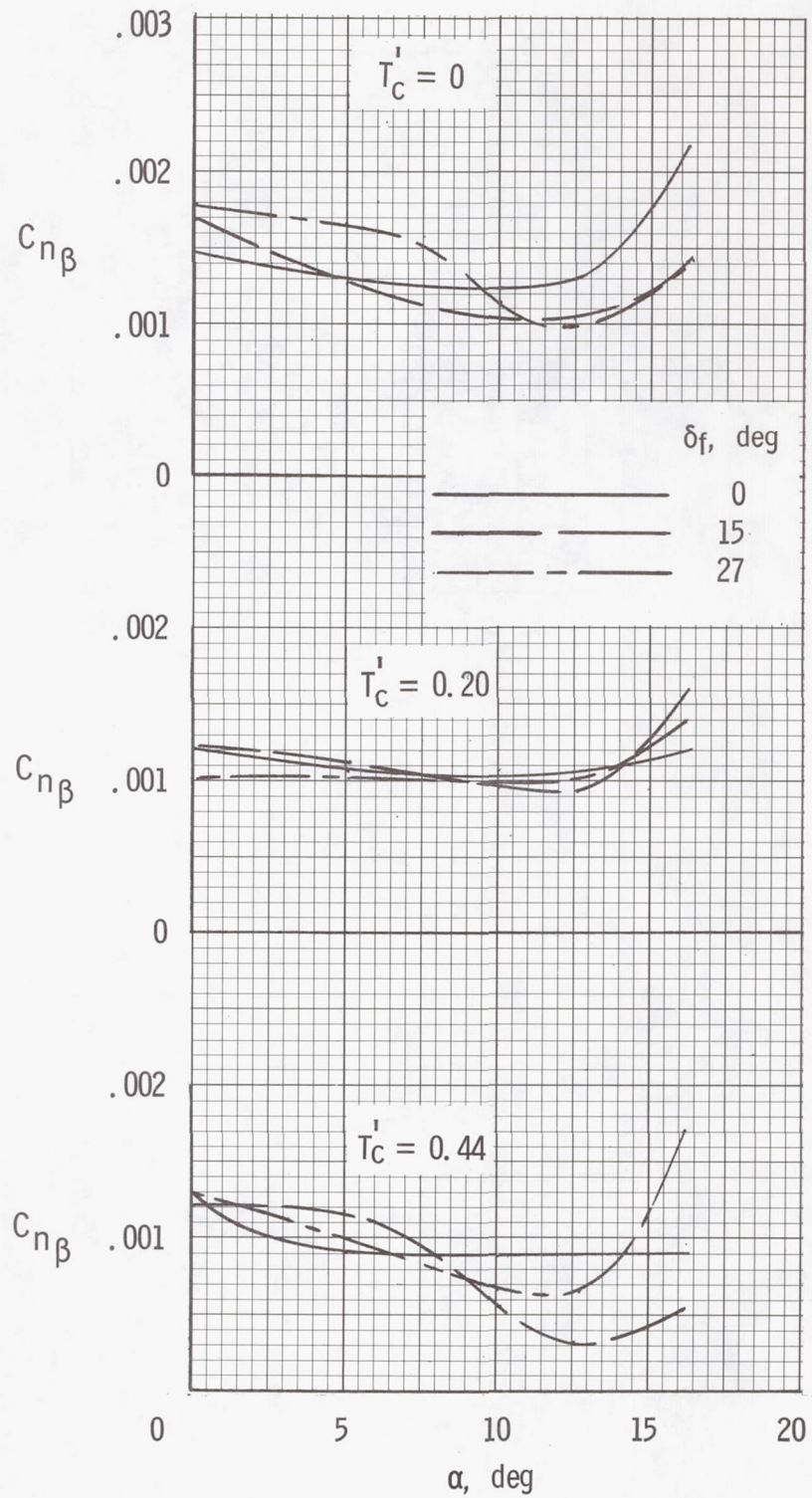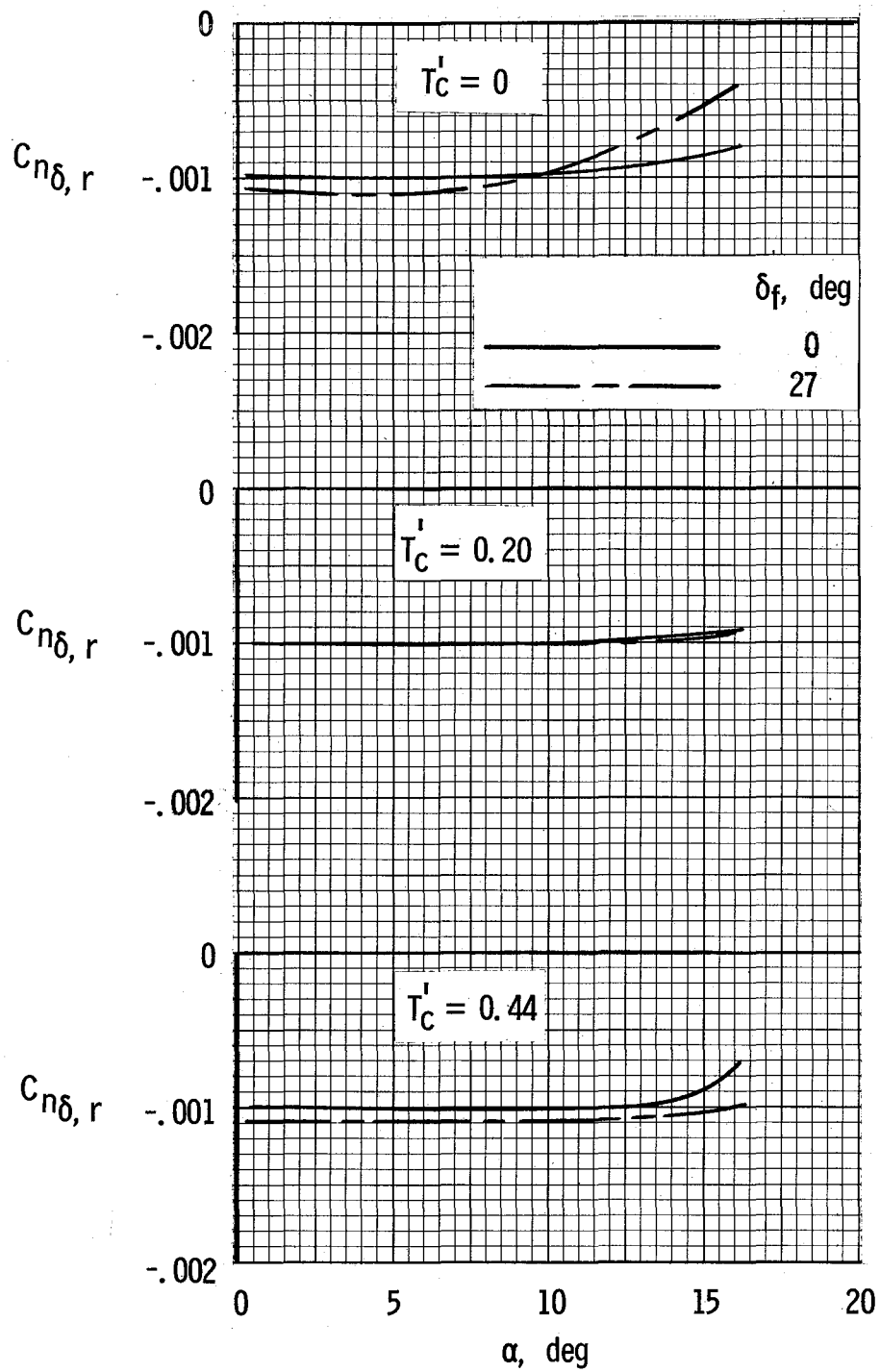
Figure 76.- Directional stability characteristics.
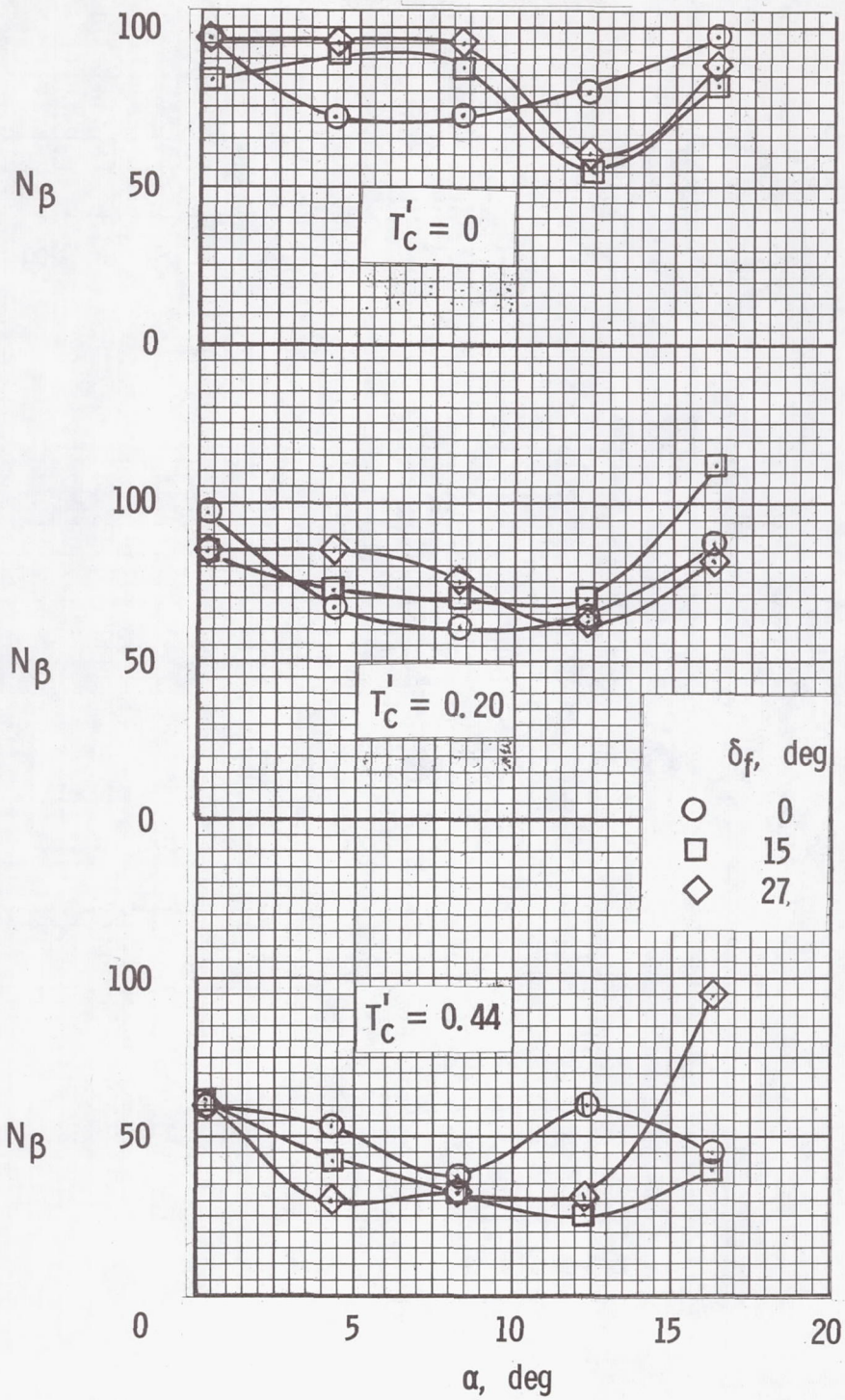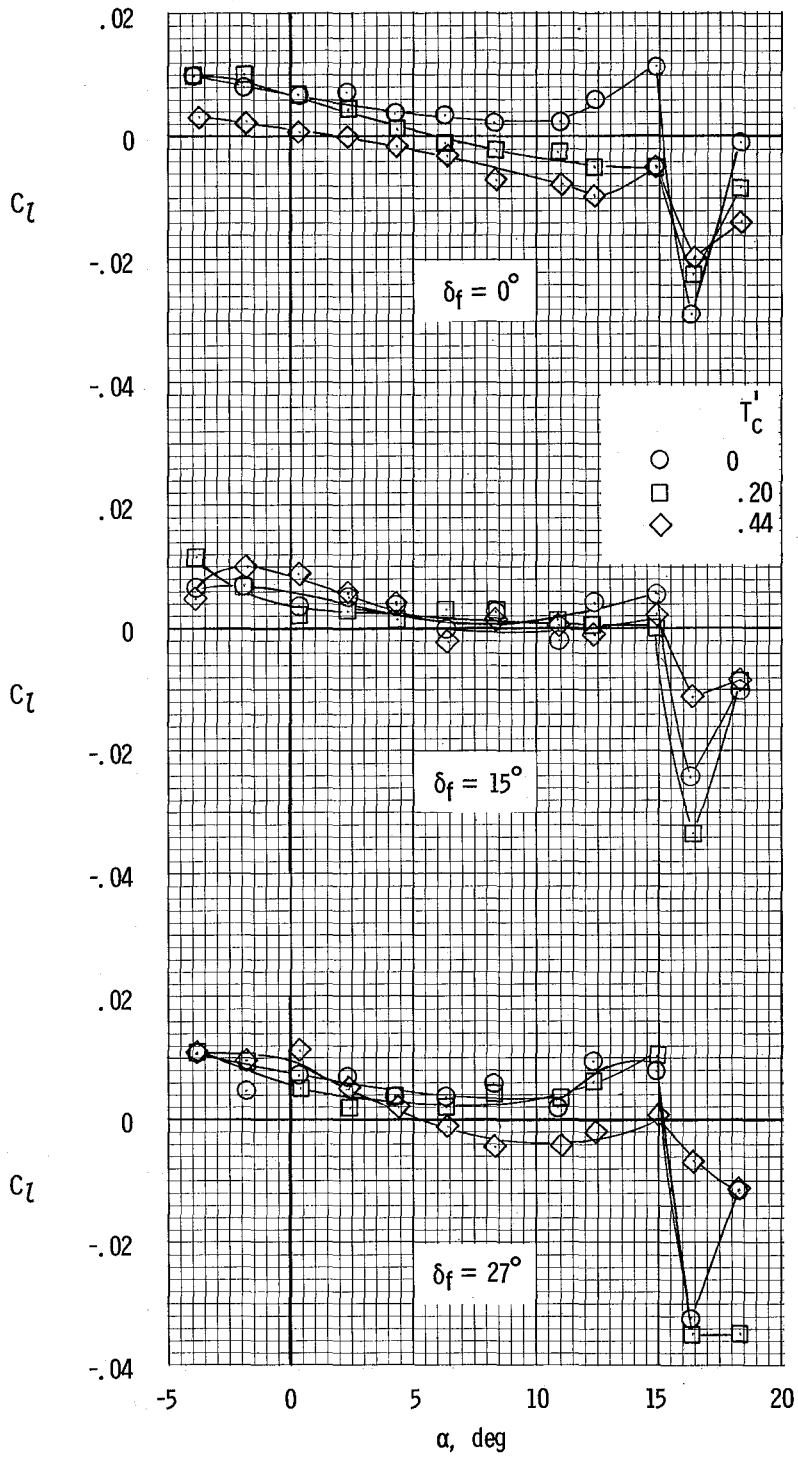
Figure 77.- Yawing-moment characteristics.
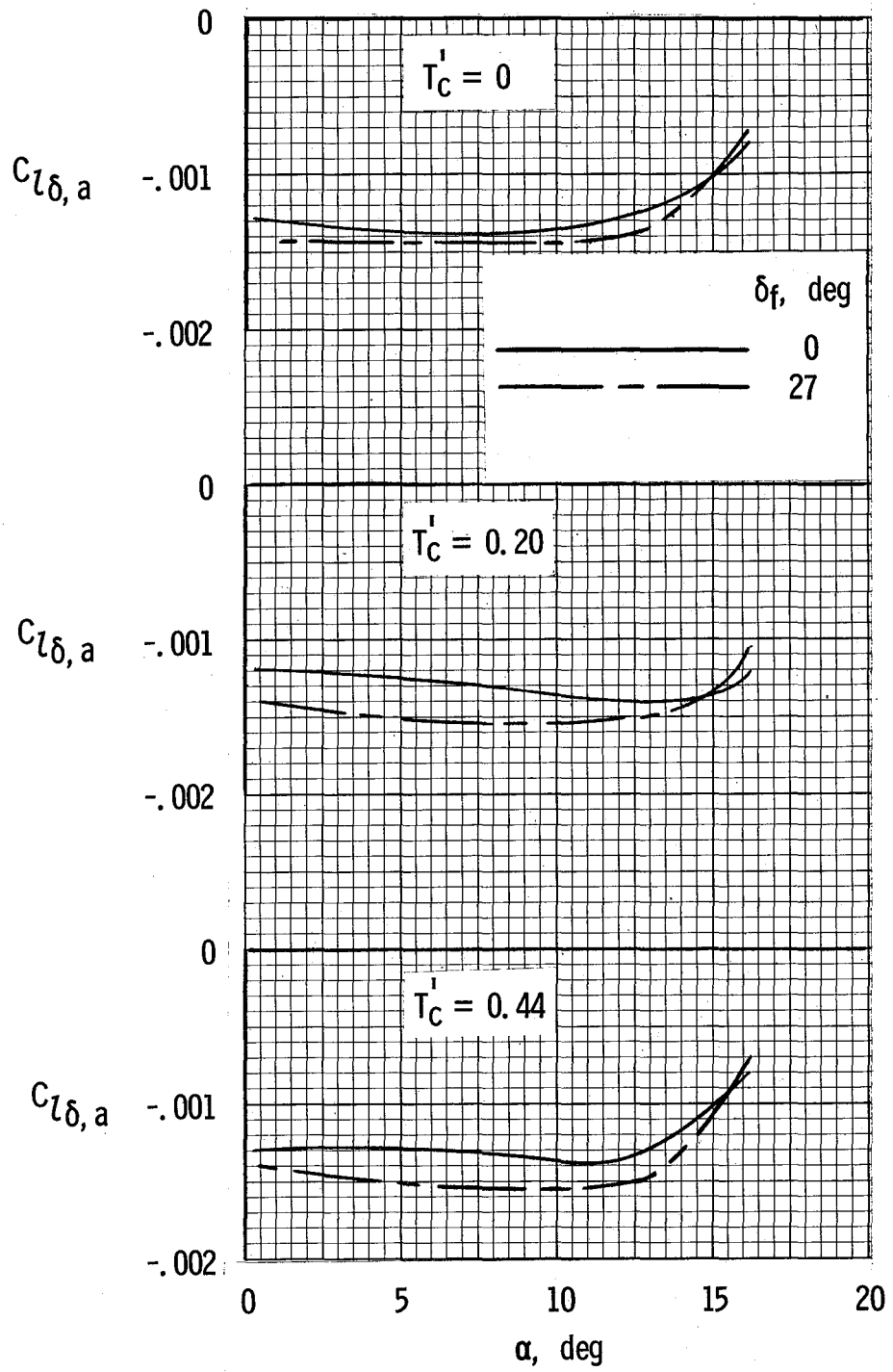
(a) Aileron effectiveness.

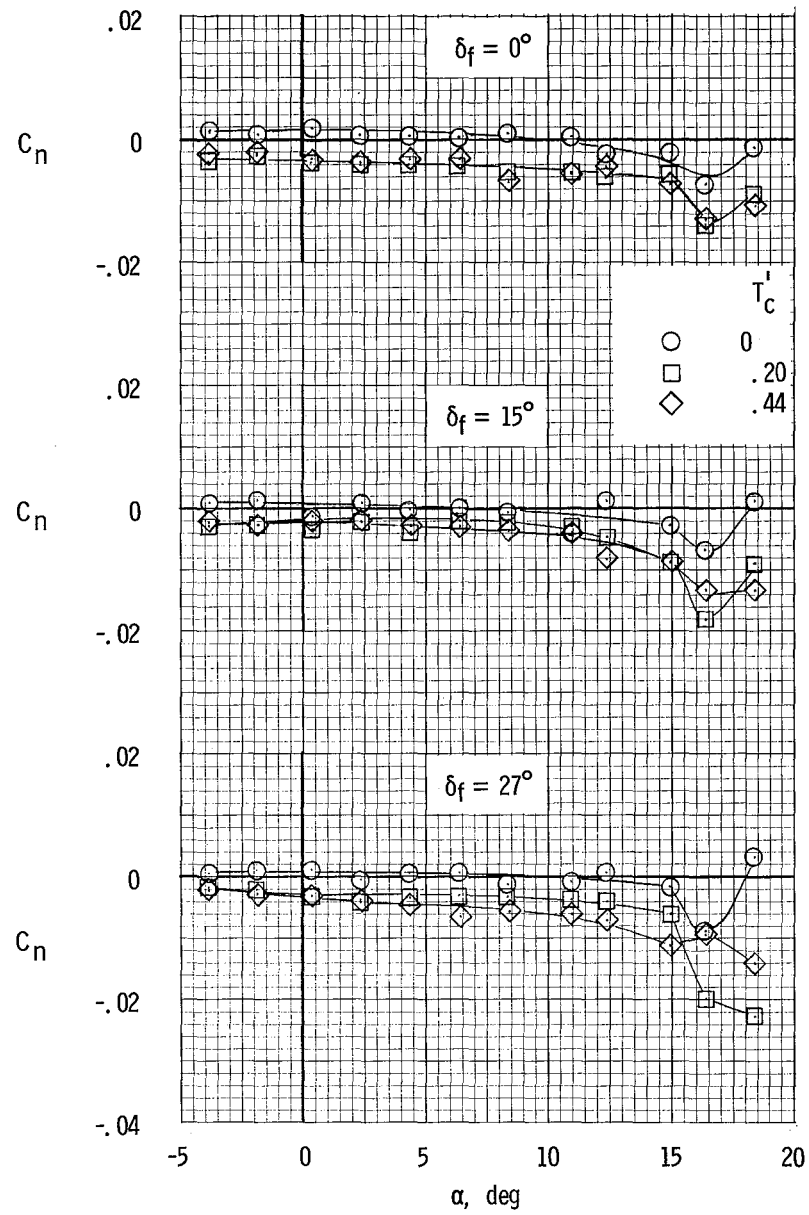Figure 78.- Aileron and rudder effectiveness with angle of attack.

(b) Rudder effectiveness.

Figure 78.- Concluded.

(a) Rolling-moment coefficients.

Figure 79.- Variations of rolling-moment and yawing-moment coefficients with angle of attack. $\beta = 0^o$.
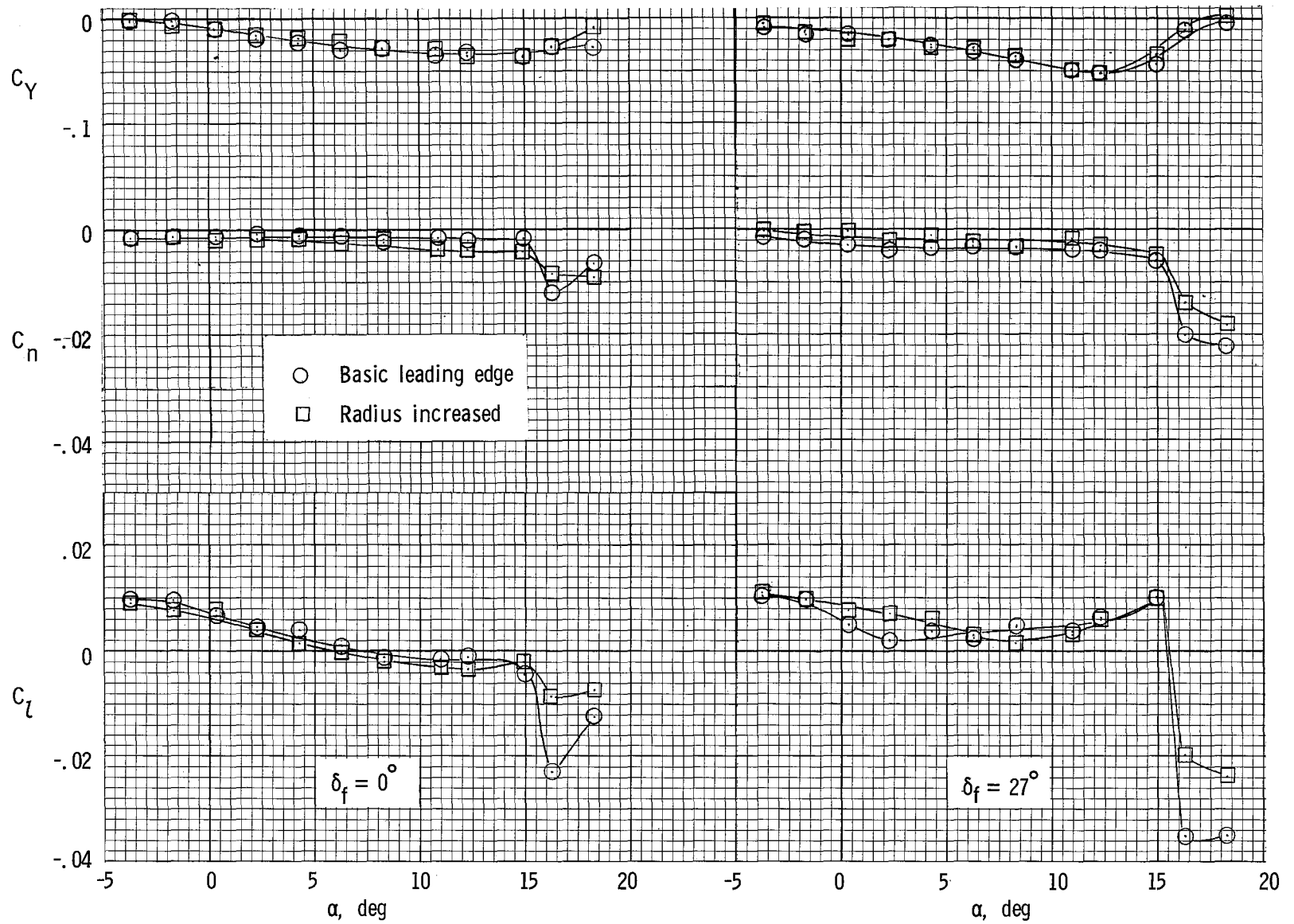
(b) Yawing-moment coefficients.

Figure 79.- Concluded.

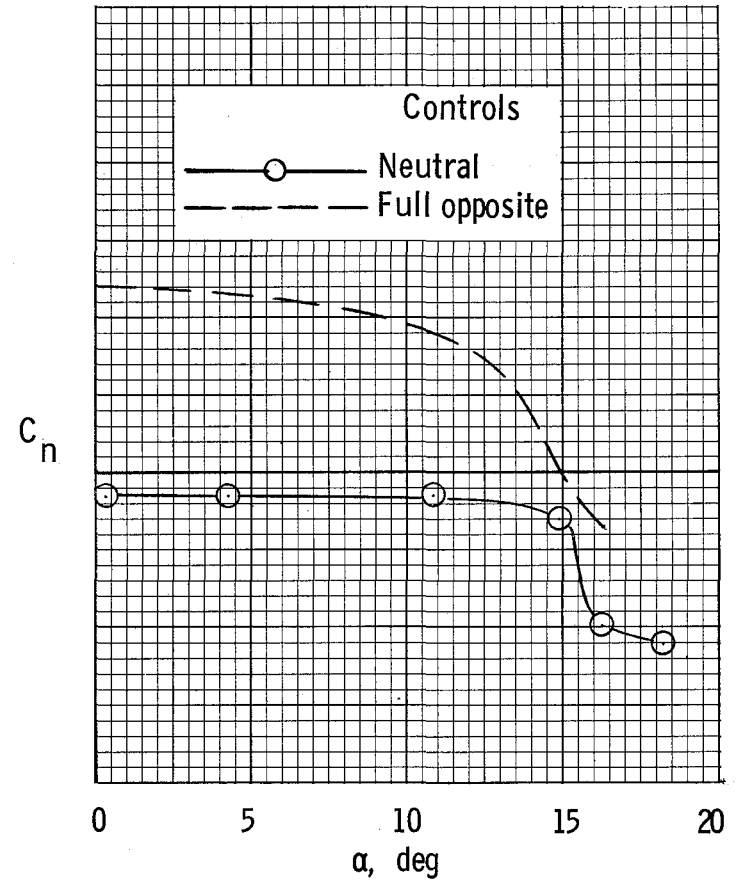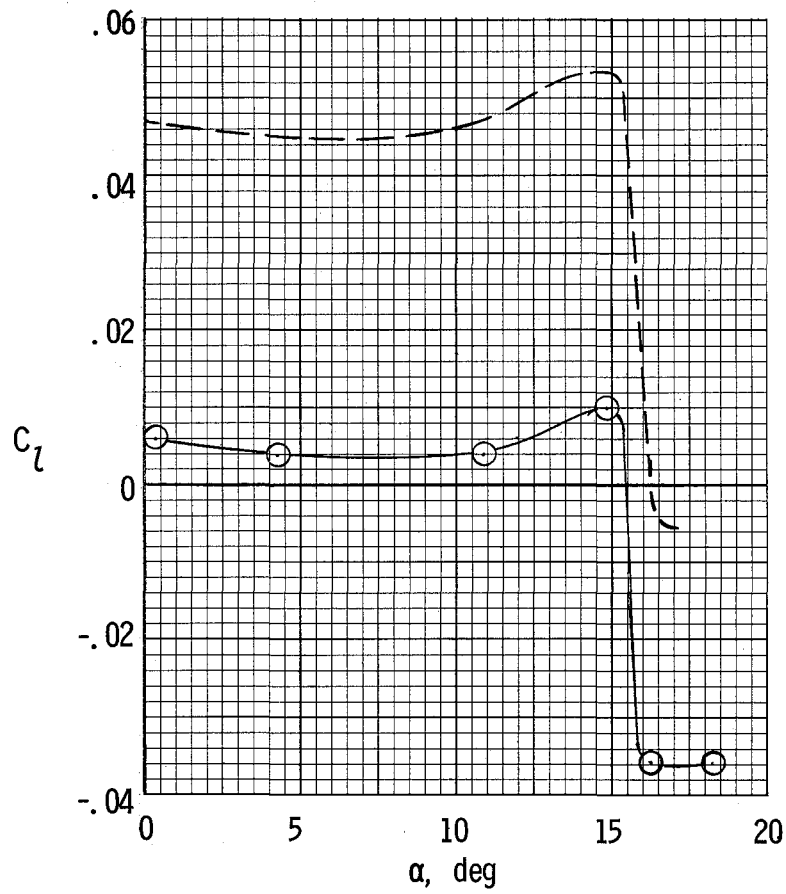Figure 80.- Effect of increase in wing leading-edge radius on lateral characteristics. $T_c' = 0.20$.

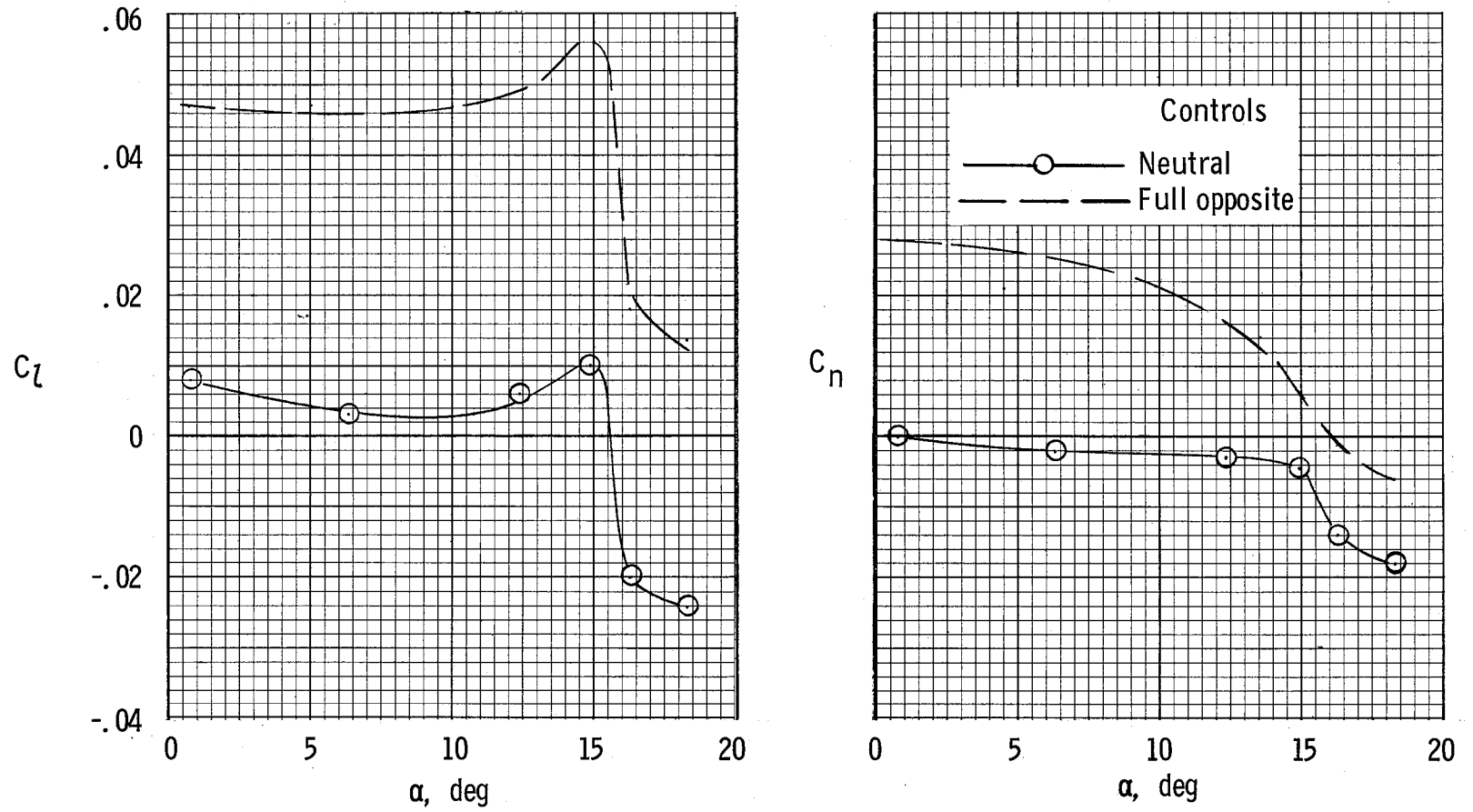Figure 81.- Control capability for overcoming lateral moments. $T_c' = 0.20$; $\delta_f = 27^0$; $\beta = 0^0$.

Figure 82.- Control capability for overcoming lateral moments. Increase in wing leading-edge radius. $T_C' = 0.20$; $\delta_f = 27^0$; $\beta = 0^0$.
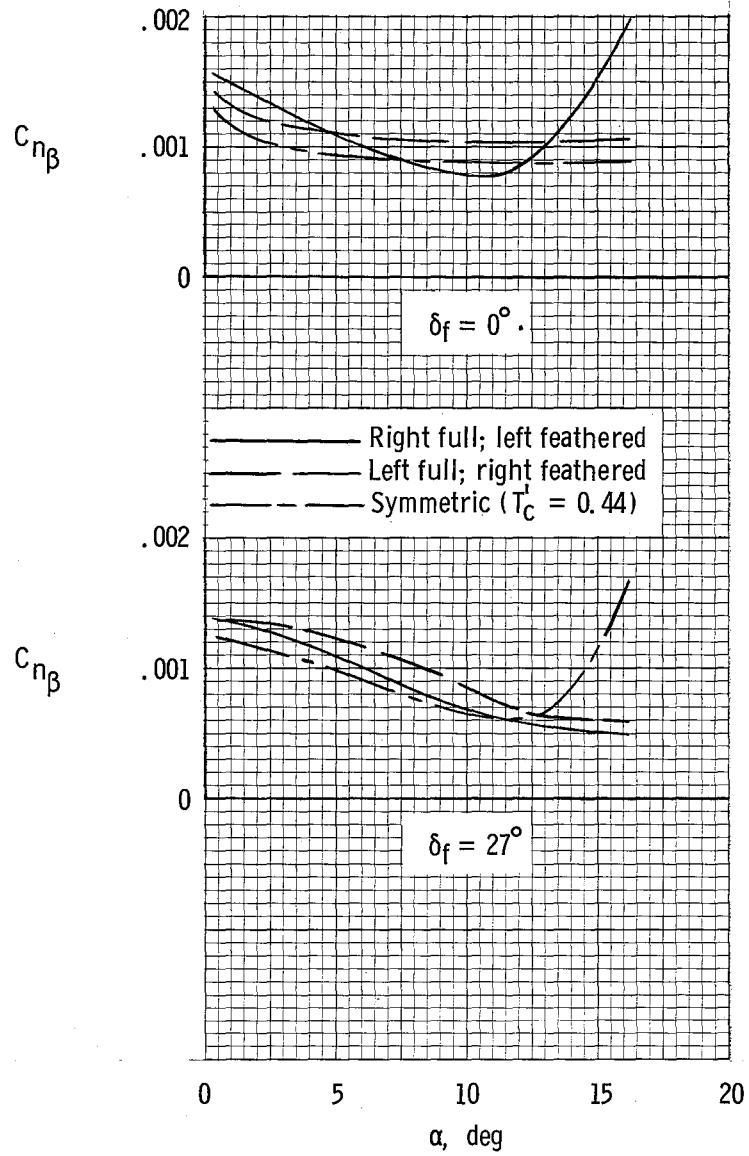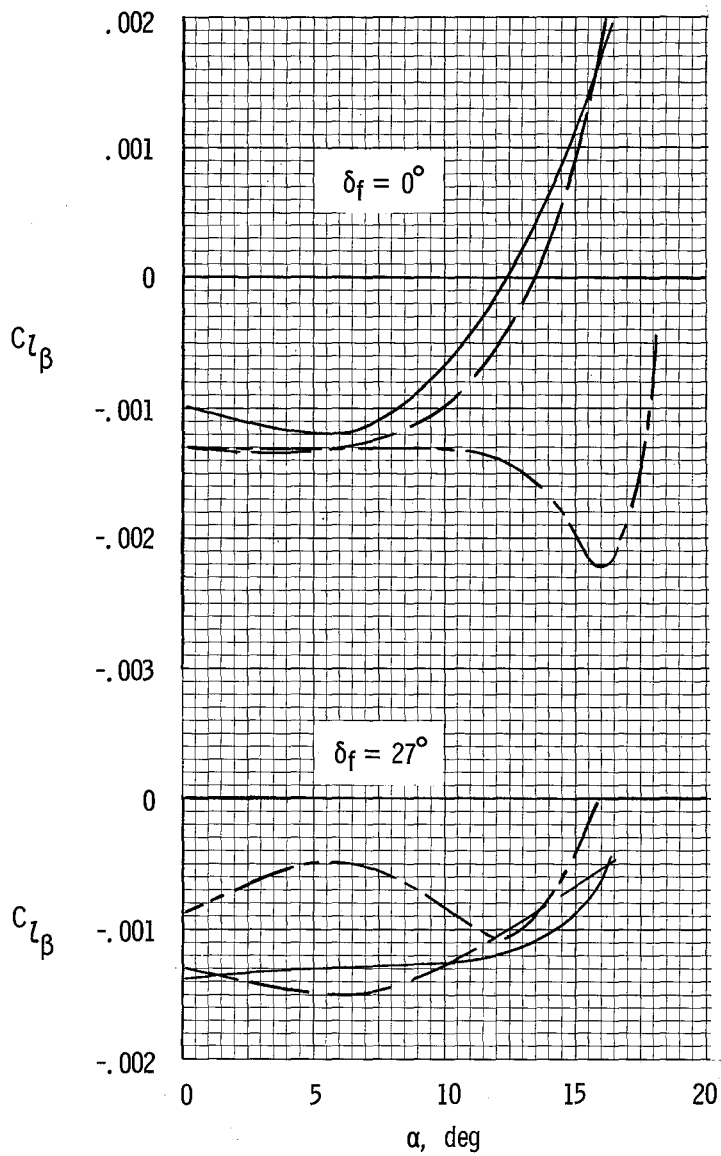
Figure 83.- Variations of effective dihedral and directional stability parameter with angle of attack. Asymmetric power.
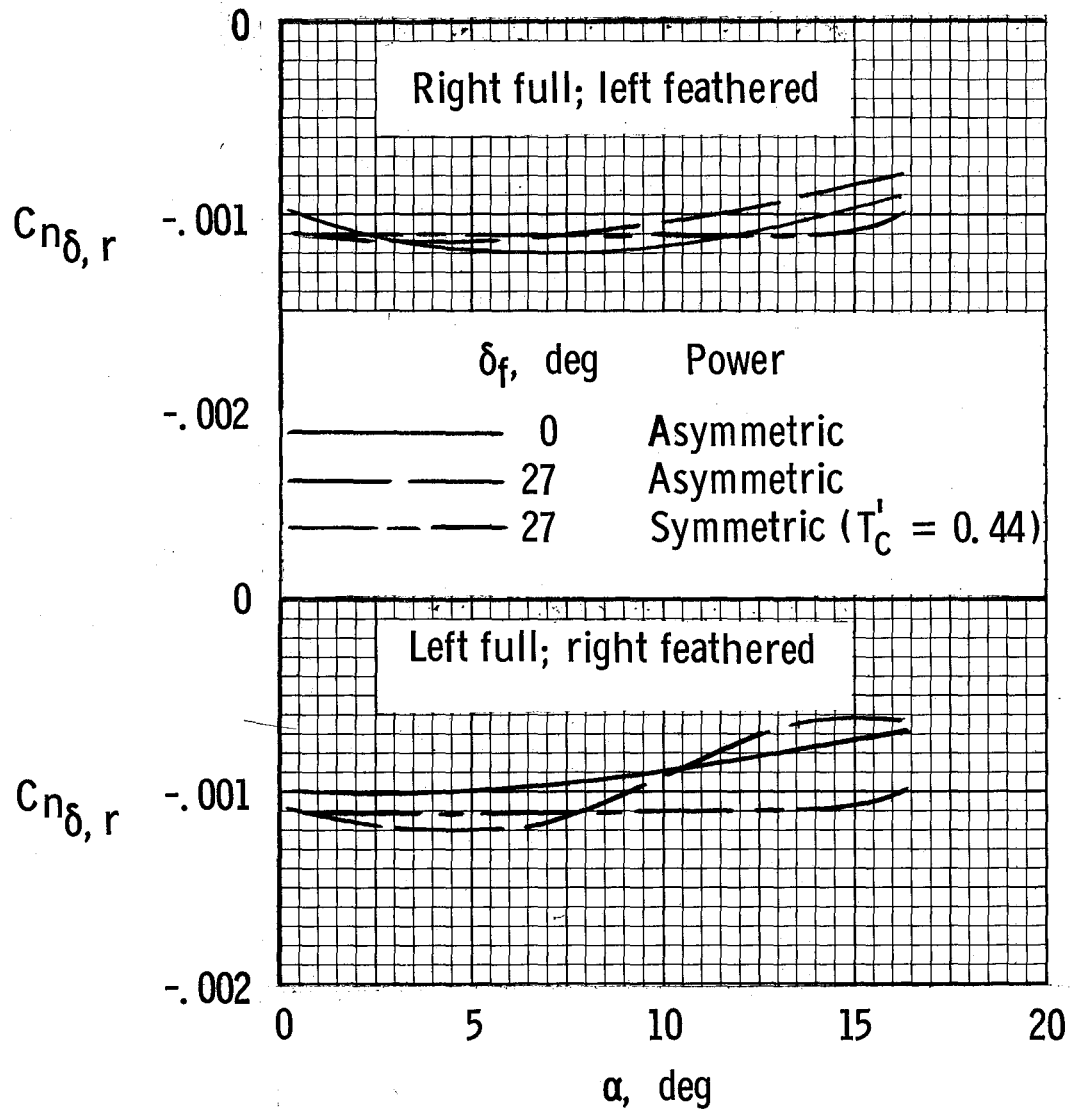
Figure 84.- Rudder effectiveness. $\beta = 0^{0}$.